

# Probing interactions of molecules and pigments on titanium dioxide surfaces for photovoltaic cells, using QCM-D

THÈSE N° 6363 (2014)

PRÉSENTÉE LE 3 OCTOBRE 2014

À LA FACULTÉ SCIENCES DE BASE

LABORATOIRE DE PHOTONIQUE ET INTERFACES

PROGRAMME DOCTORAL EN CHIMIE ET GÉNIE CHIMIQUE

ÉCOLE POLYTECHNIQUE FÉDÉRALE DE LAUSANNE

POUR L'OBTENTION DU GRADE DE DOCTEUR ÈS SCIENCES

PAR

Hauke Arne HARMS

acceptée sur proposition du jury:

Prof. V. Hatzimanikatis, président du jury  
Prof. M. Graetzel, Prof. J.-E. Moser, directeurs de thèse  
Prof. J. T. Hupp, rapporteur  
Prof. B. Kasemo, rapporteur  
Prof. F. Stellacci, rapporteur



ÉCOLE POLYTECHNIQUE  
FÉDÉRALE DE LAUSANNE

Suisse  
2014



*There are two kinds of truths: those of reasoning and those of fact. The truths of reasoning are necessary and their opposite is impossible; the truths of fact are contingent and their opposites are possible.*

Gottfried Wilhelm Leibniz (1646-1716), La Mondalogie.

To my parents.



# Abstract

Photovoltaic cells offer a sustainable way of generating electricity from sunlight, and they will be of growing economical importance for decades to come. Hybrid organic-inorganic solar cells, such as dye sensitized solar cells or perovskite solar cells, are an area of active research, and fundamental scientific advances can lead to impressive improvements of device efficiency. In this thesis, I present experimental studies on some of the fundamental properties of molecules and pigments on titanium dioxide surfaces for solar energy conversion.

Among a wide range of techniques, my main instrument is a quartz crystal microbalance with dissipation technique (QCM-D). I develop special methods of measurement, which enable the characterization of mass uptake in mesoporous systems. I apply the QCM-D technique to measure the adsorption of dye molecules, elucidate the role of the coadsorbate chenodeoxycholic acid, and I prove the reversibility of the conversion reaction between lead iodide and the organic-inorganic methylammonium lead-iodide perovskite.

In dye sensitized solar cells (DSC), dye molecules are adsorbed onto a mesoporous titanium dioxide ( $\text{TiO}_2$ ) photoanode. They fulfill several functions: they absorb light, they subsequently inject an electron into the conducting  $\text{TiO}_2$  scaffold, and the dye is then regenerated from a hole transport material infiltrating the mesoporous photoanode. Furthermore, the dye molecules form a molecular self-assembled monolayer that blocks recombination between electrons in the  $\text{TiO}_2$  conduction band and the oxidized form of the redox mediator in the hole transport material.

In the first chapter, I study the adsorption of the ruthenium-based dye Z907 by QCM-D, and demonstrate the capability of the technique to measure dye adsorption in-situ on a flat  $\text{TiO}_2$  film, as a model system, with sub-monolayer resolution. An adsorption isotherm is measured for Z907, which leads to a formal adsorption equilibrium constant of  $5.1 \cdot 10^6 \text{ M}^{-1}$  and a number density of 0.76 molecules per  $\text{nm}^2$ .

In chapter two, I extend the measurements to a system of dye and coadsorbates, where the coadsorbate is not directly accessible by optical techniques. I can thus take advantage of the QCM-D technique that measures mass uptake. All of the recent high-efficiency liquid-electrolyte DSCs do indeed use chenodeoxycholic acid as a coadsorbate, and it is of particular advantage in those that deploy organic dyes in conjunction with a one-electron redox shuttle, e.g. cobalt-based electrolytes.

I developed a method to quantify the ratio between chenodeoxycholic acid and dye molecules

---

when coadsorbed on the TiO<sub>2</sub> using a combination of QCM-D and subsequent fluorescence spectroscopy. I demonstrate this method using the example of the coadsorption of the triphenylamine dye Y123 with chenodeoxycholic acid, and find that these adsorb at a molar ratio of (1:1.8) for (Y123:cheno) on the TiO<sub>2</sub> surface. The same method is applied to porphyrin dye YD2-o-C8, ullazine dye JD21 and diketopyrrolopyrrole dye DPP17. The findings illustrate that the role of chenodeoxycholic acid depends on its specific interaction with the dye molecule.

In chapter three, I present a microscopic study on the molecular layer of the amphiphilic ruthenium-based dye Z907 adsorbed on TiO<sub>2</sub>. In collaboration with two groups at EPFL, we present in-situ atomic force microscopy images with sub-nanometer resolution in a functionally relevant liquid environment. Our results reveal changes in the conformation and the lateral arrangement of the dye molecules, depending on their average packing density on the surface. The experimental results are confirmed by molecular dynamics simulations of dyes adsorbed on the (101) facet of anatase TiO<sub>2</sub> immersed in acetonitrile solvent.

Chapter four aims to understand the QCM-D signals that are recorded on mesoporous TiO<sub>2</sub> films. Mesoporous films are employed in dye sensitised solar cells because they act as a scaffold with a very large internal surface area. This high accessible surface area makes mesoporous films and their loading with guest molecules interesting for sensing applications such as when a mesoporous film is attached to a QCM-D sensor in order to increase relative sensitivity.

For thin mesoporous films of up to 200 nm thickness, I find a regular inertial loading, which allows for an archimedic measure of molecules adsorbed inside the mesoporous matrix. For thick mesoporous TiO<sub>2</sub> films of 2 μm or thicker, I observe a particular behaviour that can be explained by the resonant coupling of the quartz crystal driving frequency to an eigenmode of the mesoporous TiO<sub>2</sub> film. My findings can be the basis for a future, systematic study in order to develop a method for sensing applications employing mesoporous films in general.

In chapter five, I contribute to the fundamental understanding of the perovskite conversion reaction between PbI<sub>2</sub> and CH<sub>3</sub>NH<sub>3</sub>PbI<sub>3</sub> perovskite. This material is central to the latest, record-breaking perovskite solar cells. Many scientists were not aware that the above conversion reaction is reversible. I prove that the back-conversion is reversible by release of methylammonium iodide from the perovskite film into selective solvents, which leads to the crystallization of PbI<sub>2</sub> on the substrate. Quantitative data is drawn from relative mass changes measured in-situ by QCM-D and complementary ex-situ techniques.

**Keywords:** Dye sensitized solar cell, DSC, quartz crystal microbalance, QCM-D, dye molecule, chenodeoxycholic acid, adsorption, molecular layer, AFM liquid phase, perovskite, conversion reaction, mesoporous film, TiO<sub>2</sub>, photovoltaic cell, solar energy conversion.

# Résumé

Les cellules photovoltaïques offrent une solution durable permettant de générer de l'électricité à partir de la lumière solaire, et l'importance économique de ces systèmes dans les années à venir est susceptible d'augmenter. Les cellules hybrides organiques-inorganiques, tels que les cellules solaires à colorant sensibilisateur ou les cellules solaires perovskite, sont un domaine où la recherche est très active. Des avancées dans la compréhension fondamentale peuvent mener à de grandes améliorations de l'efficacité de ces systèmes.

Dans cette thèse, je présente l'étude expérimentale de certaines propriétés fondamentales de molécules et pigments adsorbés à la surface de dioxyde de titane pour la conversion d'énergie solaire. Parmi les nombreuses techniques de mesure, mon instrument principal est la microbalance à cristal de quartz avec mesure de dissipation (QCM-D). Je développe une méthode spéciale de mesure qui permet la caractérisation de la masse adsorbée dans les systèmes mésoporeux. J'applique la technique QCM-D, afin de mesurer l'adsorption des molécules de colorant, d'élucider le rôle de l'acide chénooxycholique utilisé en tant que coadsorbant, et de prouver la réversibilité de la réaction de conversion entre l'iodure de plomb et le perovskite organique-inorganique.

Dans les cellules solaires à colorant sensibilisateur (DSC), les molécules de colorant sont adsorbées sur une photoanode de dioxyde de titane ( $\text{TiO}_2$ ) mésoporeux. Ces molécules remplissent plusieurs fonctions : elles absorbent la lumière, puis injectent un électron dans le réseau de  $\text{TiO}_2$  conducteur; le colorant est ensuite régénéré par un transporteur de trou infiltré dans la photoanode mésoporeuse. De plus, les molécules de colorant forment une monocouche auto-assemblée qui bloque la recombinaison entre les électrons dans la bande de conduction du  $\text{TiO}_2$  et la forme oxydée du transporteur de trou. Dans le premier chapitre, j'étudie par QCM-D l'adsorption du colorant Z907, basé sur du ruthénium, et démontre ainsi la capacité de cette technique de mesurer l'adsorption du colorant in-situ sur un film plat de  $\text{TiO}_2$ , utilisé comme système modèle, avec une résolution sub-monocouche. Une isotherme d'adsorption est mesurée pour Z907, ce qui conduit à la constante d'équilibre d'adsorption formelle de  $5.1 \cdot 10^6 \text{ M}^{-1}$  et à la densité de 0.76 molécules par  $\text{nm}^2$ .

Tous les électrolytes liquides récents dans les DSCs hautement efficaces utilisent l'acide chénooxycholique comme coadsorbant, qui est difficile à détecter. Cheno est une molécule d'un grand avantage dans les DSC utilisant des colorants organiques et un médiateur redox à un seul électron tel que les électrolytes au cobalt.

---

Dans le deuxième chapitre, j'ai développé une méthode pour quantifier le ratio entre l'acide chénodéoxycholique et les molécules de colorant coadsorbées sur le  $\text{TiO}_2$  en utilisant la combinaison de la technique QCM-D et de la spectroscopie de fluorescence. Je démontre l'efficacité de cette méthode en utilisant l'exemple de la coadsorption du colorant triphénylamine Y123 avec l'acide chénodéoxycholique, et montre que ces molécules s'adsorbent avec un ratio molaire de (1:1.8) pour (Y123:cheno) à la surface du  $\text{TiO}_2$ . La même méthode est ensuite appliquée au colorant porphyrine YD2-o-C8, au colorant ullazine JD21 et au colorant diketopyrrolopyrrole DPP17. Ces expériences montrent que le rôle de l'acide chénodéoxycholique dépend de son interaction spécifique avec la molécule de colorant.

Dans le troisième chapitre, je présente une étude microscopique dans la couche moléculaire du colorant amphiphile basé au ruthénium Z907, adsorbé sur le  $\text{TiO}_2$ . En collaboration avec deux autres groupes de l'EPFL, nous présentons des images de microscopie à force atomique in-situ avec une résolution sub-nanométrique dans un environnement liquide, comparable au système fonctionnel complet. Nos résultats révèlent le changement de la conformation et de l'arrangement latéral des molécules de colorant, dépendant de leur densité à la surface. Les résultats expérimentaux sont confirmés par des simulations de dynamique moléculaire pour du colorant adsorbé sur la facette (101) du  $\text{TiO}_2$  anatase immergé dans le solvant acétonitrile.

Le quatrième chapitre a pour but la compréhension des signaux QCM-D mesurés sur les films de  $\text{TiO}_2$  mésoporeux. Les films mésoporeux sont employés dans les DSCs car ils agissent comme une matrice avec une surface interne très large. Cette très grande surface accessible les rend intéressants pour les applications reliées aux senseurs. Par exemple, lorsque le film mésoporeux est attaché à un senseur QCM-D de façon à augmenter la sensibilité relative. Pour des films mésoporeux jusqu'à 200 nm, je trouve un recouvrement inertiel régulier, ce qui permet une mesure d'Archimède des molécules adsorbées dans la matrice mésoporeuse. Pour des films mésoporeux de 2  $\mu\text{m}$  ou plus épais, j'observe un comportement particulier qui peut être expliqué par le couplage résonant de la fréquence du cristal de quartz avec un eigenmode du film de  $\text{TiO}_2$  mésoporeux. Ces découvertes peuvent servir de base pour une future étude systématique dans le but de développer une méthode pour des applications de senseurs.

Dans le chapitre cinq, je contribue à l'avancée fondamentale dans la compréhension de la réaction de conversion entre le  $\text{PbI}_2$  et le perovskite  $\text{CH}_3\text{NH}_3\text{PbI}_3$ . Ce matériau est central dans les dernières cellules à très haute efficacité, basées sur des perovskites. De nombreux scientifiques n'étaient pas conscients du fait de la réversibilité de la réaction. Je prouve que la réaction est réversible par relâchement de  $\text{CH}_3\text{NH}_3\text{I}$  par le perovskite dans des solvants sélectifs, ce qui mène à la cristallisation du  $\text{PbI}_2$  sur le substrat. Des données quantitatives sont extraites des changements de masse relative mesurés in-situ par QCM-D ainsi que par des techniques complémentaires ex-situ.

**Mots-clés:** Cellule solaire à colorant, DSC, couche moléculaire, microbalance à cristal de quartz, QCM-D, adsorption, AFM, perovskite,  $\text{TiO}_2$ , film mésoporeux, cellule photovoltaïque.



# Zusammenfassung

Solarzellen bieten eine Möglichkeit zur nachhaltigen Energiegewinnung. Sie wandeln Sonnenlicht in elektrischen Strom um, und ihre wirtschaftliche Bedeutung wird in Zukunft weiter wachsen. Solarzellen auf der Basis von organisch-anorganischen Hybridmaterialien, beispielsweise Farbstoffsolarzellen oder Perowskitsolarzellen, sind neue Materialien, die einen großen Kostenvorteil gegenüber der existierenden Siliziumtechnologie bieten, und sie sind Gegenstand aktueller Forschung. Neue, fundamentale Erkenntnisse über ihre mikroskopische Morphologie und Zusammensetzung bilden oft die Grundlage für erhebliche Verbesserungen der Effizienz von organisch-anorganischen Solarzellen.

Meine Arbeit widmet sich der Erforschung ebendieser wissenschaftlichen Grundlagen, die direkte Auswirkungen auf die technische Anwendung haben. In einer breiten Palette von experimentellen Techniken ist mein Hauptinstrument eine Schwingquartzmikrowage mit Dissipationsmessung (QCM-D), die der Messung kleinster Massenänderungen an dünnen Filmen dient. Ich messe die Adsorption von Farbstoffmolekülen und trage zu einem besseren Verständnis der Rolle von Coadsorbaten bei. Ich entwickle spezielle Messmethoden, die die Interpretation von QCM-D Experimenten zur Adsorption an mesoporösen Filmen ermöglichen. Des Weiteren zeige ich die Reversibilität der Konversion von Bleiodid zu organisch-anorganischem Metylammonium Bleiodid Perowskit.

Die Grundlage einer Farbstoffsolarzelle wird von einer molekularen Farbstoffschicht gebildet, welche an der internen Oberfläche einer mesoporösen Titandioxid-Photoanode ( $\text{TiO}_2$ ) adsorbiert ist. Die Schicht von Farbstoffmolekülen erfüllt mehrere Funktionen: Der Farbstoff absorbiert Licht, und kann daraufhin ein Elektron ins Leitungsband des  $\text{TiO}_2$  abgeben. Der dann oxidierte Farbstoff wird mithilfe eines Elektrolyten regeneriert, mit dem die mesoporöse Photoanode gefüllt ist. Darüber hinaus verhindert die geschlossene Schicht von Farbstoffmolekülen die Rekombination von Elektronen aus dem Leitungsband des  $\text{TiO}_2$  mit der oxidierten Form des RedOx-Paares im Elektrolyten.

Im ersten Kapitel untersuche ich die Adsorption des Ruthenium-Farbstoffs Z907 an flache  $\text{TiO}_2$  Filme, die als idealisiertes Modellsystem dienen, und an denen die Möglichkeit demonstriert wird, mit der Empfindlichkeit der QCM-D Technik molekulare sub-Monolagen aufzulösen. Anhand einer Adsorptionsisotherme ermitteln wir eine Teilchendichte von 0.76 Molekülen pro  $\text{nm}^2$ , sowie einen formellen Langmuir-Sorptionskoeffizienten von  $5.1 \cdot 10^6 \text{ M}^{-1}$ .

---

In den meisten hocheffizienten Farbstoffsolarzellen wird die Gallsäure Chenodesoxycholsäure (Cheno) als Coadsorbat verwendet, um Aggregation von Farbstoffmolekülen zu verhindern, und um die Ladungsträgerrekombination zwischen Titandioxid und dem Elektrolyten zu unterbinden. Cheno ist jedoch durch optische Methoden nur schwer als Adsorbat zu detektieren, und es fehlen effiziente Nachweismethoden, um die Funktionsweise von Cheno zu erforschen. Im zweiten Kapitel entwickle ich eine indirekte Nachweismethode die QCM-D mit Fluoreszenzmessungen kombiniert, um das molare Verhältnis von verschiedenen Farbstoffen und Cheno im adsorbierten molekularen Film zu bestimmen. Im Beispiel der Coadsorption vom Triphenylamin-Farbstoff Y123 mit Cheno ermittele ich ein molares Verhältnis von (1:1.8) von Y123 zu Cheno. Die genaue Rolle von Cheno hängt jedoch spezifisch vom Farbstoff ab.

Im dritten Kapitel präsentiere ich eine mikroskopische Studie des Ruthenium-Farbstoffs Z907 nach Adsorption an eine anatase  $\text{TiO}_2$  Oberfläche. Dies sind die Ergebnisse einer Kollaboration mit zwei Gruppen an der EPFL. Wir nutzen Rasterkraftmikroskopie, um in-situ Aufnahmen des adsorbierten Farbstoffs in einem relevanten flüssigen Lösungsmittel mit sub-Nanometer-Auflösung zu erhalten, und wir beobachten eine Konformationsänderung der Farbstoffmoleküle in Abhängigkeit von ihrer Packungsdichte an der  $\text{TiO}_2$  Oberfläche. Unsere Ergebnisse werden unabhängig durch molekulardynamischen Simulationen bestätigt.

In Kapitel vier zeige ich QCM-D Experimente mit mesoporösen Filmen auf der Sensoroberfläche. Mesoporöse Filme werden in Farbstoffsolarzellen benutzt, weil die Filme eine große interne Oberfläche zur Adsorption von Farbstoffmolekülen bieten. Diese große interne Oberfläche ist gleichermaßen für generelle Anwendungen in der Sensorik von Bedeutung. Ich demonstriere, dass die gesamte Masse des Films gemessen wird, und somit ein archimedisches Maß adsorbierter Moleküle innerhalb des Films darstellt. Außerdem beobachte ich bei mesoporösen Filmen von mehr als  $2 \mu\text{m}$  Dicke eine Resonante Kopplung zwischen einer Eigenfrequenz des Films und der treibenden Frequenz des Schwingquartzes.

Im fünften Kapitel präsentiere ich einen Beitrag zum fundamentalen Verständnis der Konversion zwischen Bleiodid und Methylammonium Bleiodid Perowskit. Dieses Perowskit-Material ist von zentraler Bedeutung als Pigment in Perowskit-Solarzellen, die in den vergangenen zwei Jahren aufgrund von großen Effizienzsteigerungen Aufsehen erregt haben. Ich zeige, dass die oben erwähnte Konversion reversibel ist, indem Methylammonium Iodid mithilfe selektiver Lösungsmittel aus dem Perowskit-Material herausgelöst wird, während Bleiodid auf dem Substrat re-kristallisiert. Die zeitaufgelösten quantitativen QCM-D Messungen werden durch komplementäre ex-situ Messungen bestätigt.

**Schlüsselwörter:** Farbstoffsolarzelle, Schwingquartzmikrowaage, QCM-D, Farbstoffmolekül, Chenodesoxycholsäure, Adsorption, molekulare Schicht, Rasterkraftmikroskopie, Perowskit, Konversion, mesoporöse Filme, Titandioxid, Solarzelle, Photovoltaik.

# Contents

<b>Abstract / Résumé / Zusammenfassung</b>	<b>v</b>
<b>Introduction</b>	<b>1</b>
Motivation . . . . .	1
World energy outlook and solar energy conversion . . . . .	2
Overview of thesis . . . . .	4
Dye sensitized solar cells . . . . .	6
Solar spectrum and Shockley-Queisser limit . . . . .	7
Principle device characterization . . . . .	8
Operation principle of a dye sensitized solar cell . . . . .	11
The titanium dioxide surface . . . . .	12
Binding modes of the dye to anatase TiO <sub>2</sub> . . . . .	13
Dye adsorption and desorption processes . . . . .	14
Quartz crystal microbalance with dissipation monitoring (QCM-D) . . . . .	16
Sauerbrey equation . . . . .	16
Dissipation and contact with liquid . . . . .	17
QCM-D measurement technique . . . . .	19
Sensor preparation . . . . .	22
<b>1 The adsorption of ruthenium complex Z907 on flat, compact TiO<sub>2</sub> by QCM-D</b>	<b>25</b>
1.1 Z907 adsorption on flat, compact TiO <sub>2</sub> by QCM-D . . . . .	27
1.1.1 Principle Z907 dye adsorption and solvent baseline . . . . .	27
1.1.2 Z907 adsorption isotherm . . . . .	31
1.1.3 Confirmation of QCM-D results by complementary techniques . . . . .	34
1.2 Kinetics of Z907 dye adsorption and desorption . . . . .	36
1.2.1 Notations: adsorption and desorption rates for the Langmuir equation . . . . .	36
1.2.2 Desorption dynamics . . . . .	37
1.2.3 Adsorption dynamics . . . . .	40
1.3 Conclusion . . . . .	42
<b>2 Coadsorption of chenodeoxycholic acid and various types of donor – <math>\pi</math>-bridge – acceptor dyes</b>	<b>45</b>
2.1 Introduction to coadsorbates in dye-sensitized solar cells . . . . .	45
2.2 Chenodeoxycholic acid and triphenylamine dye Y123 . . . . .	46

## Contents

---

2.2.1	Experimental procedure . . . . .	46
2.2.2	Cheno and triphenylamine dye Y123 . . . . .	48
2.3	Coadsorption with porphyrin dye YD2-o-C8, ullazine dye JD21, and diketopyrrolopyrrole dye DPP17 . . . . .	53
2.3.1	Cheno and porphyrin dye YD2-o-C8 . . . . .	53
2.3.2	Cheno and ullazine dye JD21 . . . . .	54
2.3.3	Cheno and diketopyrrolopyrrole dye DPP17 . . . . .	57
2.4	Conclusion . . . . .	60
<b>3</b>	<b>Microscopic characterization of amphiphilic ruthenium complexes adsorbed on anatase titanium dioxide</b>	<b>63</b>
3.1	Introduction to direct microscopic investigation of molecular adsorbate layers	63
3.1.1	Experimental and computational methods . . . . .	64
3.2	Local probe by non-contact atomic force microscopy in liquid phase . . . . .	66
3.3	Classical molecular mechanics simulations by computing an ensemble of dye molecules adsorbed on anatase titanium dioxide . . . . .	72
3.4	Conclusion . . . . .	79
<b>4</b>	<b>QCM-D with mesoporous titanium dioxide films</b>	<b>81</b>
4.1	Introduction mesoporous films and QCM-D . . . . .	81
4.1.1	General . . . . .	81
4.1.2	Sample preparation and characterisation . . . . .	84
4.2	Dye loading of thin mesoporous TiO <sub>2</sub> films of 60 nm to 200 nm thickness . . . . .	86
4.2.1	QCM-D on thin mesoporous TiO <sub>2</sub> and fluorescence spectroscopy . . . . .	86
4.2.2	Liquid volume trapped inside thin mesoporous TiO <sub>2</sub> by QCM-D . . . . .	94
4.3	Mesoporous films of more than 2 $\mu$ m thickness . . . . .	100
4.3.1	QCM-D throughout the deposition of mesoporous TiO <sub>2</sub> films . . . . .	100
4.3.2	QCM-D during dye adsorption on 10 $\mu$ m thick mesoporous TiO <sub>2</sub> . . . . .	103
4.3.3	Resonant coupling to a 10 $\mu$ m thick mesoporous TiO <sub>2</sub> film . . . . .	106
4.4	Conclusion . . . . .	112
<b>5</b>	<b>Conversion of thin lead iodide films to perovskites by exposure to methylammonium iodide</b>	<b>115</b>
5.1	Introduction to perovskites in photovoltaic devices . . . . .	115
5.1.1	General introduction . . . . .	115
5.1.2	Perovskite structure . . . . .	117
5.1.3	Methylammonium lead iodide perovskites for photovoltaic applications and their synthesis by conversion from lead-iodide salt . . . . .	118
5.1.4	Sample preparation and characterisation . . . . .	121
5.2	Overview of the conversion and back-conversion . . . . .	123
5.2.1	Quantitative overview by QCM-D . . . . .	123
5.2.2	Elemental analysis by ICP-MS . . . . .	126
5.2.3	Morphology by SEM . . . . .	128

5.2.4	Structural analysis by XRD . . . . .	129
5.2.5	Effect of PbI <sub>2</sub> morphology on QCM-D signals . . . . .	133
5.3	Repetitive conversion and back-conversion between CH <sub>3</sub> NH <sub>3</sub> PbI <sub>3</sub> and PbI <sub>2</sub> . .	137
5.3.1	Repetitive conversion by QCM-D . . . . .	137
5.3.2	Repetitive conversion by SEM and XRD . . . . .	138
5.4	Details of the back-conversion process . . . . .	142
5.5	Conclusion . . . . .	146
	<b>Bibliography</b>	<b>160</b>
	<b>Acknowledgements</b>	<b>161</b>
	<b>Curriculum Vitae and list of publications</b>	<b>163</b>



# Introduction

## Motivation

I have always found pleasure in following my curiosity: exploring new places, understanding fundamental processes in detail, and developing new ideas and applications. Yet in order to direct my curiosity to a specific domain over the duration of a doctorate, I needed a sustainable inspiration. I found this in the domain of solar-energy conversion, and it has been satisfying to make a contribution to the emerging problem of power consumption, limited resources and environmental pollution. Dye sensitized solar cells are an inspiring topic for me in that a dye molecule is used to harvest sunlight, which is a beautiful allegory of natural photosynthesis.

The domain of hybrid and organic photovoltaic cells is a great scientific playground at the interface of Physics and Chemistry, and the field takes advantage of very recent technological advances in the characterisation and control of nano-scale morphology of materials. Working across these disciplines entails great satisfaction for me, because it provides a broader scientific horizon.

My research aims to understand the fundamental details of the molecules and pigments adsorbed on a metal oxide surface. In the domain of hybrid and organic photovoltaics, a better understanding of fundamental processes can eventually enable large performance improvements of the solar cell.

### World energy outlook and solar energy conversion

Photovoltaic solar cells enable the harvesting of sustainable electrical power from sunlight. Today, fossil or nuclear fuels supply most of our energy consumption. These are limited resources, and their use has adverse effects on our environment. Available solar cells are either expensive or of low efficiency. New types of solar cells may be more efficient and cheaper to produce. But a fundamental understanding of the basic physics and chemistry is needed in order to produce better solar cells.

The current global electrical power demand is satisfied by providing an electrical energy of 5.8 TW [48]. To put this into perspective, a simple home in Switzerland has an electrical power consumption of 10 000 kWh per year, which corresponds to an energy demand of 1.4 kW on average. A unit of one TW corresponds to one billion kW. Until the year 2035, the global electrical energy demand is expected to rise to 9.7 TW. Most of the electrical energy is provided by the consumption of fossil fuels, notably coal and gas for electricity generation [48]. To put this into context, the total global primary energy demand is 40 TW today, and will rise to 54 TW by the year, which includes heating, industrial processes and transportation <sup>1</sup>.

Fossil fuels, in particular oil and gas, are limited resources that will become expensive as well-accessible fields are depleted. Resources of fossil fuels are also subject to geopolitical tensions. By contrast, it is possible to install capacity for renewable sources such as wind and solar-energy in most locations globally and, subject to demand, to the required level of supply. Solar-energy is a relatively cheap and clean alternative. Further, renewable sources are independent of suppliers of fossil fuels, which may be of strategic importance. However, such changes may often be at odds with short- and medium-term economic interests of established power suppliers and their lobbies. Thus, their implementation requires both political leadership as well as carefully balanced economic incentives for both industry and households. In the economical and political context, price tags also provide a means to steer consumption.

Lately, the growing public awareness of both, climate change caused by carbon dioxide emission and the risks related to nuclear fission, has pressed several European governments to adopt new energy policies for change [1]. Despite the unfortunate surge in coal consumption, this change in energy policy is driving a demand for sustainable and renewable energy, most importantly for wind and solar. Of these, solar power represent the largest untapped source of renewable energy with a practical terrestrial global solar potential value of about 600 TW [39], a fraction of the 17000 TW of solar energy that strikes the surface of the Earth. By comparison, the global potential of wind power is only 14 TW [81, 71, 18].

---

<sup>1</sup>Estimated from the current electricity generation of 21420 TW h in the year 2010, and the projected electricity generation of 26640 TW h for the year 2035. The total primary energy demand was 13000 Mtoe in 2010 and is estimated to be 17500 Mtoe in 2035. 1 Mtoe is 11.63 TW h, and the annual energy consumption in TW h is displayed in values of average power consumption in TW for easier comparison to solar power. All values are taken from pages 50 and 183 the IEA Energy Outlook 2012 [48].



In principle, photovoltaic installations have a unique advantage in that they do not need to be centralised facilities, but can be an integrated part of the existing infrastructure of a building. Thus, they can be installed in a decentralised manner, which implies that electricity is actually produced close to the place where it is needed. Furthermore, the use of building-integrated photovoltaic panels does not waste any agricultural land and creates synergies in the use of space. It is important to realize that fertile land is one of mankind's most valuable resources, and that it should neither be used for solar parks nor for excessive production of biofuels.

The most-commonly seen rooftop photovoltaic devices are polycrystalline silicon solar cells. Power-conversion efficiencies of the best commercially-available silicon modules are around 21% [111], whereas the best single-crystalline silicon solar cell reaches 25.0% in the laboratory. Silicon solar cells have been developed over the last 50 years, but only became a widespread sight on private rooftops across Europe since 2000, following government-led public promotion, economic incentives and a major decrease in investment cost. Conventional silicon photovoltaic cells are expensive to manufacture because their production process is energy-intensive, and temperatures of up to 1500°C are required to melt and process silicon. Relatively large quantities of the purified material are needed, and silicon solar cells are often referred to as first-generation photovoltaic technology.

So-called second-generation photovoltaic technology refers to thin-film technologies based on materials that deliver better performance while using smaller material quantities. Examples are gallium-arsenide-based solar cells or copper indium gallium selenite (CIGS)-cells. However, many of the elements used in second-generation solar cells are rare or toxic, and are subject to fluctuations in market prices for the supply of materials used in their production. More recent, third-generation solar cells refer to technologies that are highly efficient and potentially of low cost. They include tandem and multi-junction solar cells, which can overcome the Shockley-Queisser limit [108]. The highest efficiency without light-concentration today is 38.8% for a five-junction solar cell, based on GaInP and GaInAs materials [87]. However, the latter does require delicate processing of expensive materials, and will probably not be feasible for mass production.

Organic and hybrid organic-inorganic photovoltaic technologies are more recent technologies that offer the prospect of lower-temperature production using cheap and abundant materials. Multi-junction solar cells based on cheap, non-toxic organic materials are already available on the market, and their current record efficiency is about 12.0% [87]. They are an important demonstration of the feasibility of third-generation solar cells. Dye sensitized solar cells [91] have a significant advantage over conventional photovoltaic technologies in that they excel when operating in low light conditions or at elevated temperatures; in both situations they have been demonstrated to outperform commercial silicon solar cells.

The current focus of both commercial and academic research for first- and second-generation photovoltaic cells is centred on cost-reductions to the production process. However, gains in device efficiency are only small, and will be the result of delicate engineering and optimisation.

By contrast, third-generation solar cells are an area of active research, and fundamental scientific advances can lead to impressive improvements of device efficiency. Further, the active exchange and the curiosity-driven element of academic research in the development of third-generation photovoltaic cells has promoted many alternative approaches and a readiness to try new materials and ideas from related domains. For example, the last two years have seen a rapidly increasing use of perovskite based pigments for solar energy conversion, which have been readily incorporated into existing device architectures, and led to a surge in efficiency to 17.9% [87].

In dye sensitized solar cells, a molecular layer of dye molecules adsorbed on a conducting scaffold is central to light absorption and to the generation of electrical current. In this thesis I investigate the adsorption of molecular layers in model systems of dye sensitized solar cells. My findings bring a better understanding of the molecular arrangement and composition, which may eventually lead to the production of more efficient and long-term stable solar cells. Further, I bring new insight into material conversion reactions in perovskite pigments.

### Overview of thesis

Each chapter of this thesis contains a specific introduction that describes the underlying problematic, which is studied within it. Each chapter equally has a detailed conclusion at its end, which presents the results in their context and gives an outlook on future development. For the remainder of this introduction, I give an overview that puts the different chapters into context to each other. This section is followed by an introduction to the dye sensitized solar and to the quartz crystal microbalance with dissipation technique.

In dye sensitized solar cells, dye loading of the supporting semiconductor scaffold is crucial for performance and affects it in three ways. First, the amount of dye determines the amount of light that can be harvested and is directly related to photocurrent. The more dye there is, the more light can be absorbed. Second, the photoexcited dye has to inject a charge into the semiconductor scaffold and needs to be regenerated by the redoxmediator in the electrolyte. It is therefore mandatory to have only a monolayer of dye and to avoid aggregation in multilayers. Third, the dye acts as a blocking layer that prevents recombination between the injected charge in the semiconductor and the oxidized form of the redox couple in the electrolyte. Hence the monolayer needs to be as dense as possible. The organized self-assembly of a dye monolayer and co-adsorbates have a paramount influence on the cell efficiency.

In order to elucidate the different properties of the dye-coadsorbate layer, our primary analytical technique will be a quartz crystal microbalance with dissipation monitoring (QCM-D) that enables quantitative in-situ mass-uptake monitoring on  $\text{TiO}_2$  surfaces. We basically measure three quantities: The adsorbed area mass, quantifying adsorbed dye and additives on flat surfaces; kinetics of mass change, quantifying time-resolved data on flat and porous films; measurement of dissipation, monitoring viscoelastic properties of adsorbed layers and of the overlying liquid.

QCM-D can resolve the adsorption kinetics on flat surfaces that we study as an idealised system, thus separating the actual adsorption process from diffusion processes that would dominate in porous films. Understanding processes on flat films is also crucial for direct comparison with complementary microscopic studies using AFM or STM.

We collaborate partners at EPFL and beyond, who are actively interested in exploring the complementary microscopic side of dye adsorption. Combining the qualitative microscopic information and the quantitative in-situ information obtained by QCM-D and optical measurements, we shall develop a more complete understanding of the adsorbed dye layer and its consequences on the performance of the dye sensitized solar cell.

In addition to adsorbed molecular layers, we try to gain a better understanding of methyl ammonium lead iodide perovskite films deposited on titanium dioxide. The hybrid perovskite film is commonly applied by a two-step sequential deposition: first, a lead iodide film is deposited from solution by spin-coating of a titanium dioxide substrate; subsequently, the lead-iodide film is exposed to a methyl ammonium iodide source, for example a solution of the latter in isopropanol, which leads to incorporation of the methyl ammonium iodide into the film and the conversion of the salt into the perovskite material. We want to gain a better understanding of the conversion reaction, starting from its kinetics and the amount of material converted. We furthermore investigate heterogeneity in the material composition of the perovskite film.

In the application of a dye sensitized solar cells as well as in perovskite-based solar cells, a mesoporous  $\text{TiO}_2$  film is often key, because it provides a large surface area. In our research we explore the use of mesoporous  $\text{TiO}_2$  films on QCM-D sensor crystals with two objectives in mind: first, we want to investigate systems that are as close as possible to application for dye sensitized solar cells or for scaffolds supporting catalysts. Second, the large surface area results in an increased relative sensitivity and is thus of interest for sensing applications in general.

### Dye sensitized solar cells

Dye sensitized solar cells (DSCs) provide a possibility to harvest sustainable, renewable and cheap electrical power from sunlight. Lately, the growing public awareness of both, climate change caused by carbon dioxide emission and the risks related to nuclear fission, has pressed government to adopt new energy policies for change [1]. This is driving a demand for sustainable and renewable energy. Of these, solar power represent the largest untapped source of clean energy with a practical terrestrial global solar potential value that is estimated to be about 600 TW, a fraction of the  $1.7 \cdot 10^5$  TW of solar energy that strikes the surface of the Earth [39].

Mesoscopic dye sensitized solar cells [91] could become more attractive commercially than conventional silicon solar cells thanks to their lower environmental and material cost as well as the possibility of roll-to-roll processing. However, challenges remain in terms of module efficiency (Sony module  $\eta = 10\%$ ) and long term stability which could prevent break-through commercialization. Module efficiency can be limited by reproducibility of the cells photovoltage and current. Additionally, long-term stability could be limited by dye desorption or by corrosion by the electrolyte. In both cases, the state of the self-assembled dye monolayer plays a crucial role. Incomplete monolayers will lead to a drop in photovoltage and current compared to a dense layer. It is therefore desirable to gain a better understanding of the mechanism of dye adsorption and desorption and how it can be controlled.

A. and E. Bequerel first discovered the photoelectric effect in 1839 in an electrochemical cell that relied on the intrinsic absorption of silver halide [9], paving the way for silver photography. Vogel was the first who sensitized silver halides in 1873 [117], thus extending the sensitivity over the entire visible spectrum. Cyanin dyes were used as they adsorbed strongly on the silver halide surface in the form of H- and J-aggregates [81]. The concept of sensitization was transferred back to electrochemical cells and by Moser in 1887 [80]. It was not until 1968 that Gerischer brought this type of sensitization of electrochemical cells to a larger audience [38], showing that the resulting photovoltage was due to electron injection from the dye to the semiconductor. There were more implementations of this principle, notably for water oxidation by Wright in 1979 [3] and on colloidal surfaces by Desilvestro et al. [21]. In 1991 O'Regan and Grätzel [91] presented a new type of electrochemical cell, based on a bulk heterojunction of mesoporous titanium dioxide ( $\text{TiO}_2$ ) and a redox mediator in a liquid electrolyte that delivered a power conversion efficiency of 7.1%, the first dye sensitized solar cell.

Since then, efficiency improvement was mainly related to the synthesis of new sensitizers like the black dye [84]. Recently, organic donor- $\pi$ -bridge-acceptor and porphyrin dyes with exceptionally high extinction coefficients [11] coupled with the use of a  $\text{Co}^{(II/III)}$  redox shuttle have shown their potential for record efficiencies [31, 133, 76]. Porphyrins are known to form

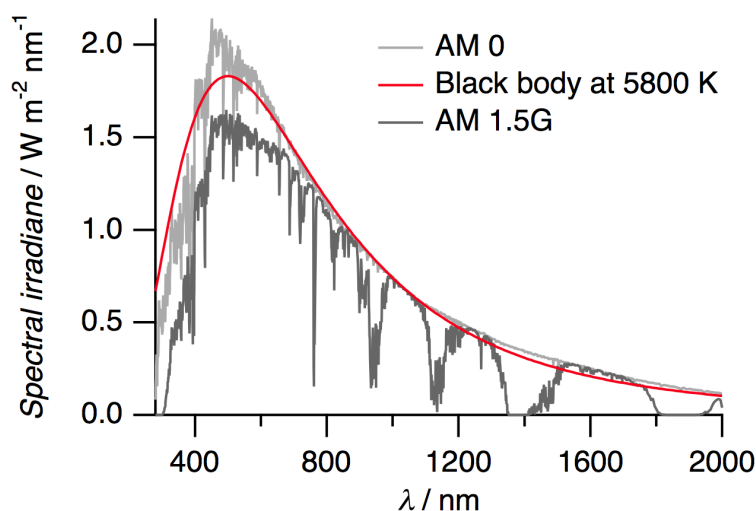


Figure 1 – Standard solar reference radiation AM 1.5G, extraterrestrial radiation AM 0, and black body radiation for  $T = 5800$  K. Solar spectra and graphic taken from [89, 126].

H- and J-aggregates on the  $\text{TiO}_2$  surface [58], and they are just one example of reorganization of the dye on the  $\text{TiO}_2$  surface. The processes that influence adhesion of each of these dyes and their interplay are rarely addressed [7, 15] and need to be clarified.

### Solar spectrum and Shockley-Queisser limit

The Sun is the primary source of energy for all life on Earth. The spectral irradiation of the Sun is shown in figure 1, featuring three different representations. The AM 0 spectrum corresponds to the irradiation that is measured outside the atmosphere of the Earth. The AM 1.5G spectrum corresponds to a standardized spectrum, representing the irradiation at the surface of the earth at sea level at an incident angle of  $48^\circ$ , as defined by the American Society for Testing of Materials [2]. AM stands for air mass coefficient, and the standardized AM 1.5G spectrum takes into account the absorption and scattering by the constituents of our atmosphere, and it is the standard spectrum that is used for the testing and certification of solar cells. It corresponds more or less to the irradiation on a sunny summer day at noon in Switzerland. The red curve in figure 1 shows the irradiation of a black body of a temperature of 5800 K, according to Planck's black body radiation [94], which is a good approximation of the irradiation of the sun. The integral of the curve gives the total incident irradiance, or the power per area, that is delivered by the Sun to the Earth. Outside the atmosphere, this incident energy current is  $J_{\text{AM } 0} = 1366 \text{ W m}^{-2}$ , and for the standardized terrestrial spectrum AM 1.5G

$$J_{\text{AM } 1.5\text{G}} = 1000 \text{ W m}^{-2} \quad . \quad (1)$$

However, there are fundamental limitations on how much of this incident energy can be

converted to useful forms of energy. For classical photovoltaic devices, Shokley and Queisser have calculated a detailed balance limit of the maximum power conversion efficiency in 1961 [108]. They assumed an ideal p-n single-junction device with an energy band gap  $E_g$ , in which every photon of a larger energy than the bandgap  $h\nu \geq E_g$  will be absorbed and create an electron-hole pair. Their model further assumes that there is only radiative recombination between electrons and holes, that the photovoltaic cell behaves like a black-body absorber, and that the device shows no series resistance, i.e. perfect charge extraction.

The Shockley-Queisser limit can be estimated on the basis of three mechanisms. First, the most fundamental limitation is the Carnot efficiency which describes the thermodynamic limit of the conversion of thermal energy from a heat sink of a given temperature (the sun or its radiation temperature) to usable energy, or work, at another heat sink (the solar cell). For a solar cell at room temperature, the Carnot efficiency allows for a free energy conversion efficiency of 77%. Second, the power extraction is made under non-equilibrium conditions, which can be described by a van't Hoff's isotherm and gives a yield of approximately 91% for visible light. Third, the largest loss is due to the fact of using only a single junction to absorb polychromatic light. The bandgap  $E_g$  imposes an upper limit to the photovoltage of the device, and simultaneously the photocurrent is limited by the fact that all light of an energy lower than the bandgap is not absorbed. This means that only 44% of the solar spectrum is integrated. The three contributions together give the Shockley-Queisser limit, which is around 31% for at ambient temperature.

The Shockley-Queisser limit can be overcome in particular by the use of multi-junction solar cells, and in general, the Carnot-efficiency can be improved by the use of concentrator cells at elevated temperatures. However, elevated temperatures will equally enhance radiative recombination. A detailed description of the operation principle of photovoltaic devices and loss mechanisms has been given by Würfel [128].

### Principle device characterization

The terms of photovoltage, photocurrent, and the power conversion efficiency have been mentioned in the previous section. These parameters of device performance are usually addressed by current-voltage measurements (I-V curves), and by a measurement of the incident-photon to current conversion efficiency (IPCE), which is the spectrally resolved external quantum efficiency. Beyond this, there exist a small number of different techniques, notably time-resolved optical spectroscopy and electrochemical impedance spectroscopy, to access different parameters of the processes inside the cell, the interested reader can consult references [41] and [39] for a good introduction and overview. Much of this technical introduction is based on the very instructive PhD thesis of Sophie Wenger [126].

**Current-voltage characteristics and power conversion efficiency** The electronic characteristics of a solar cell can be described in a simplified manner by the equivalent circuit shown in figure 2. Under illumination, the photovoltaic cell produces a current  $I_{ph}$ . In the dark, the

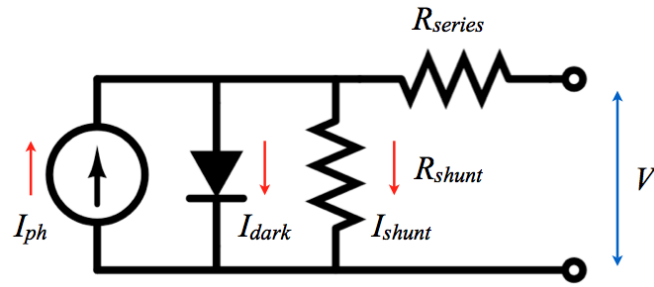


Figure 2 – Equivalent circuit of a solar cell. Graphic taken with permission from [126].

the solar cell behaves like a diode, and shows a dark current  $I_{\text{dark}}$  under forward bias. Charge recombination gives rise to a shunt resistance  $R_{\text{shunt}}$  and the associated current  $I_{\text{shunt}}$ . The series resistance  $R_{\text{series}}$  contains the resistance at the contacting interfaces, all bulk resistance, including the electrodes. The total measured current can be described by

$$I = I_{\text{ph}} - I_{\text{dark}} - I_{\text{shunt}} = I_{\text{ph}} - I_{\text{s}} \cdot \left( e^{\frac{e \cdot V}{m k_B T}} - 1 \right) - \left( \frac{V + I \cdot R_{\text{series}}}{R_{\text{shunt}}} \right) , \quad (2)$$

with the saturation current  $I_{\text{s}}$ , the applied bias voltage  $V$ , and the ideality factor  $m$ . If we neglect the last term ( $R_{\text{shunt}} \gg R_{\text{series}}$ ), which is small in an ideal solar cell, we can describe the current-voltage characteristics by a simplified expression

$$I = I_{\text{ph}} - I_{\text{s}} \cdot \left( e^{\frac{e \cdot V}{m k_B T}} - 1 \right) . \quad (3)$$

This description delivers simple expressions for the short-circuit current  $I_{\text{sc}}$  and the open-circuit voltage  $V_{\text{oc}}$ :

$$I_{\text{sc}} = I_{\text{ph}} \text{ for } V = 0, \text{ and} \quad (4)$$

$$V_{\text{oc}} = \frac{m k_B T}{e} \cdot \ln \left( \frac{I_{\text{ph}}}{I_{\text{s}}} + 1 \right) \text{ for } I = 0 . \quad (5)$$

Typical current-voltage characteristics (I-V curve) are displayed in figure 3. The figure furthermore shows the power output  $P = I \cdot V$  as a function of voltage (red line). The maximum power point,  $P_{\text{max}} = I_{\text{max}} \cdot V_{\text{max}}$ , is usually characterized by the fill factor

$$FF = \frac{I_{\text{max}} \cdot V_{\text{max}}}{I_{\text{sc}} \cdot V_{\text{oc}}} . \quad (6)$$

The most cited parameter of a solar cell however, is its solar to electric power conversion efficiency  $\eta$ , which is the ratio of the incident solar power  $P_{\text{solar}}$  to the maximum power out-

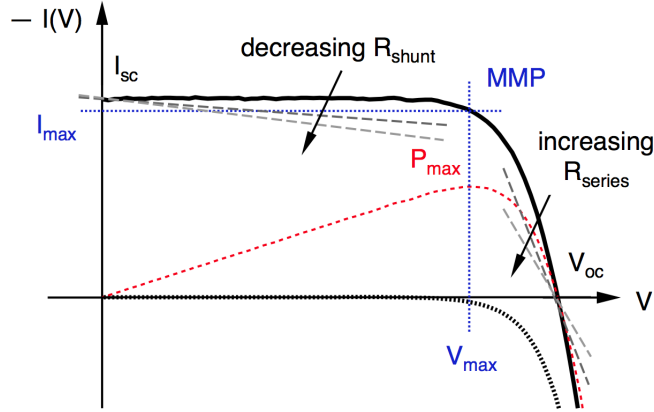


Figure 3 – Typical current-voltage characteristics (I-V curve) of a solar cell. The solid black curve corresponds to the cell under illumination, and the dotted curve is its diode behaviour in the dark. The red curve shows the power output  $P = I \cdot V$  and indicates the maximum power point via  $P_{max}$ . The dashed lines on the side illustrate the influence of the series resistance and the shunt resistance on the curve. Graphic taken with permission from Wenger [126].

put  $P_{max}$  of the photovoltaic cell:

$$\eta = \frac{P_{max}}{P_{solar}} = \frac{I_{max} \cdot V_{max}}{P_{solar}} = \frac{FF \cdot I_{sc} \cdot V_{oc}}{P_{solar}} \quad (7)$$

The notation of the applied bias voltage with a positive sign, and of the measured solar cell current with a negative sign is a convention that is consistent with the traditional description of a diode.

**External quantum efficiency** The external quantum efficiency (EQE) is often also called the incident photon to current conversion efficiency (IPCE), which depends on the energy of the incident photon. The underlying parameter is the spectral response  $SR(\lambda)$  of the solar cell, which is the ratio of the current generated to the incident power. The units of the spectral response  $SR(\lambda)$  are  $A W^{-1}$ , and the external quantum efficiency is its quantized, dimensionless equivalent

$$EQE(\lambda) = SR(\lambda) \cdot \frac{hc}{e\lambda} \quad (8)$$

$h$  is Planck's constant,  $c$  is the speed of light,  $e$  is the elementary charge, and  $\lambda$  is the wavelength of the incident light.

The  $EQE$  relates to the short circuit current density  $J_{sc}$  via the the incident photon flux  $\phi(\lambda)$



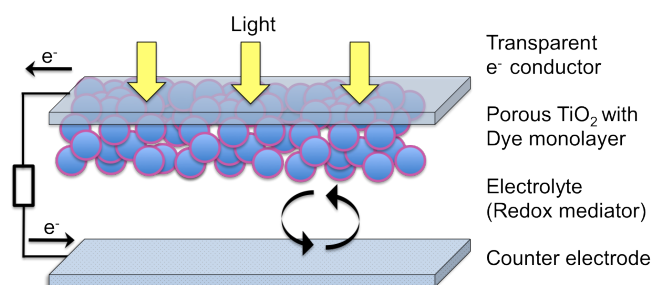


Figure 4 – Schematic device structure of a dye-sensitized solar cell (DSC).

and the integral over all wavelengths

$$J_{sc} = \int e \cdot EQE(\lambda) \cdot \phi \lambda \, d\lambda \quad . \quad (9)$$

### Operation principle of a dye sensitized solar cell

In its most simple form, a dye sensitized solar cell (DSC) converts sunlight into electricity. The principle device structure is shown in figure 4. At the heart of the DSC lies a self-assembled monolayer of dye molecules is adsorbed to a photoanode of mesoporous  $\text{TiO}_2$ . The mesoporous photoanode is infiltrated with an electrolyte containing the redox shuttle. This active part of the cells are sandwiched between two fluorine-doped tin oxide glass substrates using a polymeric Surlyn spacer and sealant. The counter electrode is usually coated with platinum which helps to regenerate the oxidized form of the redox mediator.

The energy levels and timescales for the competing processes are illustrated in figure 5. In contrast to a conventional p-n junction solar cell, the functions of light absorption and charge carrier transport are separated. As a result, there should be no exciton recombination inside the  $\text{TiO}_2$  itself. In a first step, the dye in its ground state  $S_0$  absorbs light and is promoted to an excited state  $S_0^*$ . From the excited state, the dye injects an electron into the conduction band of the  $\text{TiO}_2$  on the timescale of 50 fs - 10 ps and thereby becomes oxidized  $S^+$ . The dye is subsequently regenerated within 0.1  $\mu\text{s}$  - 30  $\mu\text{s}$  by the reduced form of the redox mediator and thereby has regained its initial state  $S_0$ . The then oxidized form of the redox mediator diffuses to the counter electrode where it is regenerated. The electrons in the conduction band of the  $\text{TiO}_2$  diffuse to the FTO-glass anode by a trapping-detrapping mechanism on the 0.1 ms-10 ms timescale [81].

Loss mechanisms are indicated by the dashed lines in figure 5. Relaxation of the excited state ( $S^* \rightarrow S$ ) occurs on the timescale of 10 ns while recombination of electrons from the conduction band with the oxidized form of the dye takes around 0.5 ms. Judging from their

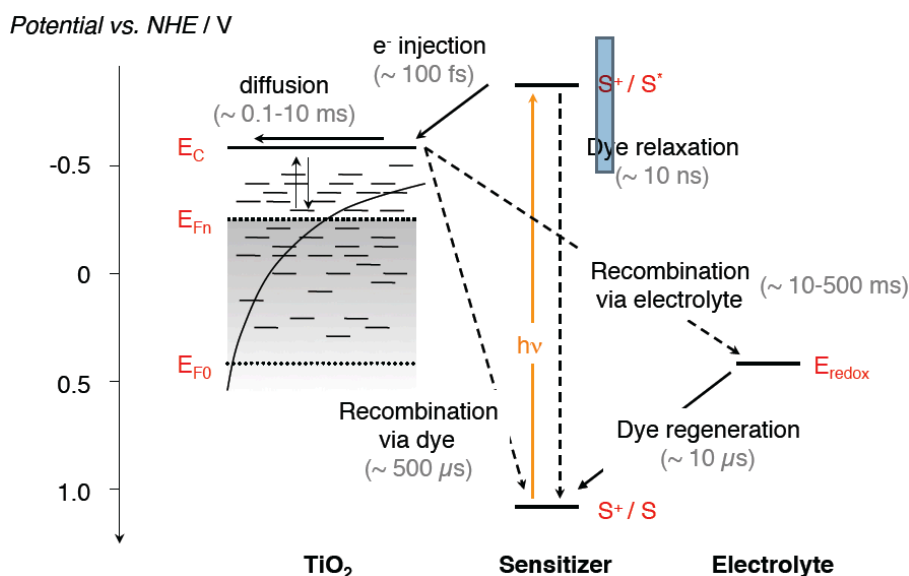


Figure 5 – Schematic energy diagram and time scales of the different processes in a DSC. Graphic taken with permission from Wenger [126].

timescales, these loss mechanisms are negligible against the corresponding forward processes of electron injection and regeneration of S<sup>+</sup>. However, recombination between the electron from the TiO<sub>2</sub> conduction band and the oxidized form of the redox mediator in the electrolyte occur at a timescale of 10 ms - 500 ms and can thus compete with the diffusive transport of the electron in the TiO<sub>2</sub> that can take up to 10 ms. As a result, this loss mechanism can be influenced by the blocking abilities of the adsorbed molecular layer, consisting of dye molecules and coadsorbates [39, 81, 126].

### The titanium dioxide surface

In DSCs, a mesoporous TiO<sub>2</sub> film with a large internal surface area forms the basis of the photoanode. In liquid-electrolyte DSCs, the film typically has a thickness 8-15 μm and consists of anatase TiO<sub>2</sub> particles of 20 nm particle size with an average pore size of 23 nm and a porosity is 58% after TiCl<sub>4</sub> post-treatment, according to BET measurements. For a typical 10 μm thick mesoporous TiO<sub>2</sub> film, the surface area is increased by three orders of magnitude compared to the projected surface area. Figure 6(a) shows a SEM micrograph of a typical mesoporous TiO<sub>2</sub> film.

In the DSC, the mesoporous TiO<sub>2</sub> is usually deposited not directly on the conductive fluorine-doped tin oxide (FTO) substrate, but on an underlayer of thin, compact TiO<sub>2</sub>. This underlayer can be deposited by various methods, usually by spray-pyrolysis, TiCl<sub>4</sub> pre-treatment or atomic layer deposition, and fulfils two main functions. First, it prevents direct contact between the hole transport material (the electrolyte) and the FTO. Second, it does improve the adhesion and the contact of the mesoporous TiO<sub>2</sub> to the substrate. Furthermore, the mesoporous TiO<sub>2</sub> film is often subjected to a TiCl<sub>4</sub> post-treatment, with the aim of improving material

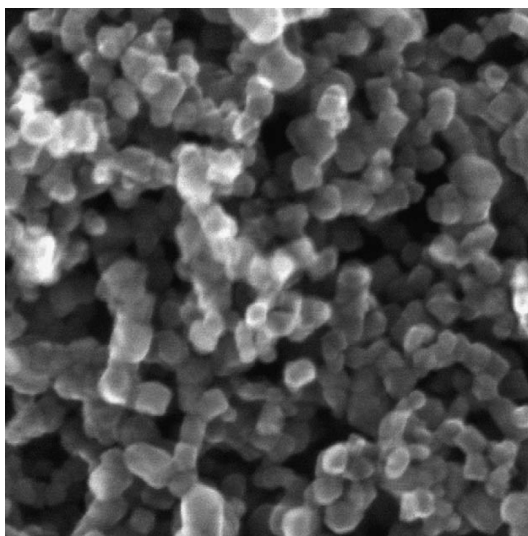


Figure 6 – SEM micrograph of a mesoporous TiO<sub>2</sub> film of 20 nm sized anatase particles.

purity on the surface and creating necking connections between the TiO<sub>2</sub> nanoparticles.

TiO<sub>2</sub> anatase has a bandgap of 3.2 eV (rutile: 3.0 eV), leading to a low intrinsic light absorption which is advantageous since positive charges inside the film would form recombination sites for electrons injected by the dye. The most prevalent facet on the traditional anatase nanoparticles is the thermodynamically most stable (101) facet [39]. However, the predominance of certain facets can be controlled during the synthesis of the TiO<sub>2</sub> nanoparticles by using facet-specific, growth-inhibiting adsorbates like hydrofluoric acid [130].

For the QCM-D measurements, flat TiO<sub>2</sub> films will be used for most of the studies, which can be used as a model system. A thorough review on TiO<sub>2</sub> surfaces has been made by Diebold in 2003 [22].

### **Binding modes of the dye to anatase TiO<sub>2</sub>**

All of the dyes presented in this thesis bind to the TiO<sub>2</sub> surface via a carboxylate group. For anatase TiO<sub>2</sub>, the thermodynamically most stable facet is the (101) facet, which should be predominant in all of the examples presented here. The most favourable anchoring sites for the carboxylate groups are the low-coordinated titanium atoms (5-fold, Ti<sup>5c</sup>) [105]. Nevertheless, there are several surface sites available for adsorption on the TiO<sub>2</sub>, and some dyes possess more than one carboxylate group, allowing in principle for different binding geometries. For one carboxylate group, there are three different known coordination types to the metal oxide: monodentate, bidentate-bridging, and bidentate-chelating, see figure 7.

For the most simple form of a carboxylate group binding to the single-crystalline anatase TiO<sub>2</sub> (101) surface, acetic acid has been shown to bind via a dissociative bidentate-bridging to two neighbouring Ti<sup>5c</sup> sites. This was the result of an scanning tunnelling microscopy (STM)

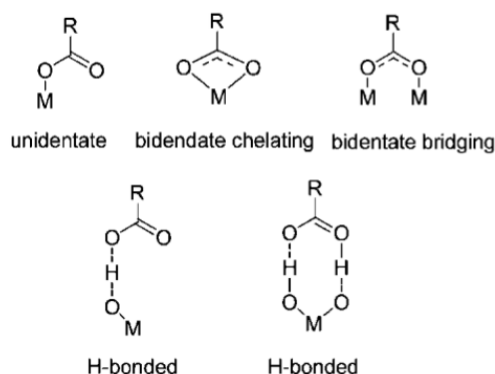


Figure 7 – Different coordination types of a carboxylate group to a metal oxide surface.

study by Grinter et al. [34], performed on an anatase single crystal in ultra high vacuum. For the investigation of a more realistic system, Schiffmann and Baiker [105] have performed a very comprehensive study, combining theoretical computations using density functional theory and an experimental ATR-IR study. They investigated dyes with several binding groups of different protonation, i.e. N3, N719, and N712, similar to an experimental study by Nazeer et al. [83]. Remarkably, the computations considered the presence of the solvent acetonitrile in detail on the surface, and Schiffmann et al. found that the protonation of the TiO<sub>2</sub> surface can strongly influence the relative stabilities of different binding configurations. The latter could induce conformational transitions from double bidentate-bridging to mixed bidentate/monodentate. Earlier computations by Shklover et al. [107] suggest that an ester-like monodentate binding is possible, however, later experimental ATR-IR studies by Gao, Humphrey-Baker et al. [33] show no evidence for this type of binding in the actual dye sensitized solar cell.

### Dye adsorption and desorption processes

The most important model for monolayer adsorption is the Langmuir adsorption model (1913-1918). It is a simple analytic model that describes reversible adsorption of monolayers of gas. Although it has limitations in the description of realistic, non-ideal situations, it is of great practical importance for its simplicity and for its pedagogic value. We intend to use it later as a starting point for interpretation of our data. This summary uses the notations used by Masel [74].

We regard an adsorbate molecule  $A_g$  that can react with an empty site  $S$  to form an adsorbed complex  $A_{ad}$



We follow Langmuir's original kinetic derivation since we will actually be able to observe these

elementary processes in our data.  $r_{ad}$  is the rate of adsorption,  $r_d$  is the rate of desorption which are given by

$$r_{ad} = k_{ad}P_A[S] \quad (11)$$

$$r_d = k_d[A_{ad}] \quad (12)$$

where  $P_A$  is the partial pressure of  $A$  over the surface,  $[S]$  is the concentration of bare sites in  $\frac{\text{number}}{\text{cm}^2}$ ,  $[A_{ad}]$  is the surface concentration of  $A$  in  $\frac{\text{molecules}}{\text{cm}^2}$  and  $k_{ad}$  and  $k_d$  are the adsorption and desorption rate constants respectively. At equilibrium adsorption and desorption rates are the same so that  $r_{ad} = r_d$  yields

$$\frac{[A_{ad}]}{P_A[S]} = \frac{k_{ad}}{k_d} =: K_{eq}^A \quad (13)$$

$K_{eq}^A$  is the Langmuir equilibrium adsorption constant. Considering only one single adsorbate species, the total concentration of sites is  $[S_0] = [S] + [A_{ad}]$ . When defining the coverage  $\theta_A = \frac{[A_{ad}]}{S_0}$  we yield the Langmuir adsorption isotherm

$$\theta_A = \frac{K_{eq}^A P_A}{1 + K_{eq}^A P_A} \quad (14)$$

The same mechanism holds true for competitive nondissociative adsorption. For example, for two species  $A$  and  $B$

$$\theta_A = \frac{K_{eq}^A P_A}{1 + K_{eq}^A P_A + K_{eq}^B P_B} \quad \text{and} \quad \theta_B = \frac{K_{eq}^B P_B}{1 + K_{eq}^A P_A + K_{eq}^B P_B} \quad (15)$$

Note that the Langmuir adsorption model is not necessarily correct for dye adsorption on the  $\text{TiO}_2$  surface, since we do not have free sites in vacuum, but always a replacement of other molecules, and because the adsorbed dye will interact with adjacent molecules.

## Quartz crystal microbalance with dissipation monitoring (QCM-D)

The quartz crystal microbalance with dissipation monitoring (QCM-D) can be used to measure mass and viscosity changes on a surface in liquid environment in real time. The shift of the resonance frequency and of its dissipation is measured in order to obtain the area mass of a rigidly adsorbed species, or the viscoelastic properties of an adsorbed soft layer and the overlying liquid. In recent years, QCM-D has become a popular technique for label-free sensing of biomolecules by preparing sensor surfaces with specific receptor molecules.

### Sauerbrey equation

The conventional quartz crystal microbalance is a well-known technique to measure mass uptake on a sensor, and it is predominantly used to measure deposition rates in evaporators or for other deposition techniques. The technique was first quantitatively described by Sauerbrey in 1959 [103].

$\alpha$ -quartz is a piezoelectric crystalline material, and it will undergo a shear-thickness movement if a voltage is applied across a plate of  $\alpha$ -quartz that is cut in its AT-direction, see figure 8 (a) for illustration. The AT-direction is at an angle of  $39^\circ$  with respect to the Y-axis of  $\alpha$ -quartz, see reference [103] for details. If the applied voltage is modulated, the crystal can be driven to undergo oscillations, and the driving frequency can be adapted to drive the crystal efficiently at its resonance frequency, which primarily depends on the quartz material properties and its dimensions. The resonance frequency  $f_0$  for a shear thickness oscillation is given by

$$f_0 = \frac{v_t}{2 \cdot t_q} \quad . \quad (16)$$

Here,  $v_t$  is the transversal sound velocity of  $\alpha$ -quartz ( $v_t = 3.34 \cdot 10^4 \text{ m s}^{-1}$ ), and  $t_q$  is the thickness of the quartz plate. If an additional small mass  $\Delta \hat{m}$  is homogeneously distributed and rigidly attached to the quartz plate, this results in a shift of frequency  $\Delta f$  proportional to  $\Delta \hat{m}$ . The shift of frequency is proportional to the added of mass, and the initial frequency  $f_0$  is proportional to the total mass of the sensor

$$\frac{\Delta f}{f_0} = - \frac{\Delta \hat{m}}{\rho_q \cdot A \cdot t_q} \quad . \quad (17)$$

$\rho_q$  is the density of the quartz and  $A$  is the top area of the plate. By introducing the Sauerbrey constant,  $C = \frac{\rho_q d}{f_0}$ , which is characteristic for the specific sensor crystal used, and an area mass  $\Delta m = \Delta \hat{m} / A$ , Sauerbrey succeeded in relating the frequency shift in Hz directly to the difference in mass per area

$$\Delta m = -C \cdot \Delta f \quad . \quad (18)$$

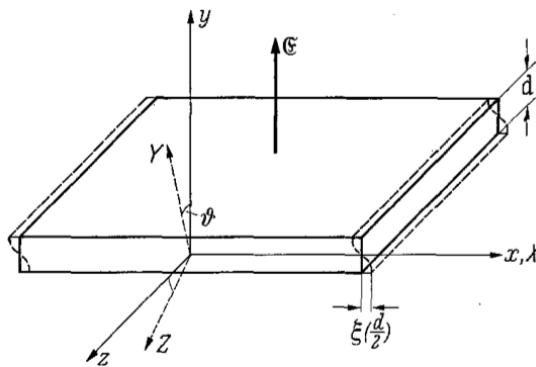
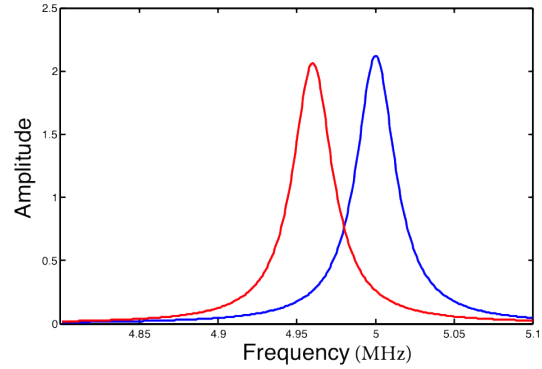


Fig. 1. Ideale Dickenschersungsschwingung einer Quarzplatte. (y Plattennormale, x- und z-Achse liegen in der Plattenebene; X polare Achse, Z optische Achse des Quarzkristalls.) Die für Dickenschersungsschwingungen geeigneten Platten sind um die X-Achse aus der XZ-Ebene herausgedreht; AT-Schnitt:  $\phi = 35^\circ$ ; BT-Schnitt:  $\phi = -49^\circ$ . Das anregende elektrische Feld liegt parallel zur y-Achse



(a) Shear-thickness oscillation of AT-cut quartz. (b) Frequency shift upon mass loading.

Figure 8 – (a) Illustration of the shear-thickness oscillation. Graphic taken from the original publication of Sauerbrey [103]. (b) Illustration of the frequency shift upon mass loading.

The shear thickness oscillation of the AT-cut  $\alpha$ -quartz and the shift of resonance frequency upon mass loading are shown in figure 8.

### Dissipation and contact with liquid

Apart from the frequency, the dissipation is a parameter of the quartz crystal resonance that contains valuable information on the viscoelastic coupling of the resonance to its environment. The dissipation  $D$  is the ratio of the energy dissipated into the environment to the energy stored in the oscillation of the sensor. It relates to the half width at half maximum  $\Gamma$  of the resonance and to the  $Q$ -factor of the resonance by  $D = 1/Q = \Gamma \cdot 2 / f_0$ . Instead of measuring the width of the resonance directly, it is more precise to switch off the driving of the crystal and measure the decay time  $\tau$  of its amplitude. The dissipation is then given by  $D = \frac{1}{\pi f_0 \tau}$ , as illustrated in figure 9.

Kanazawa and Gordon performed fundamental studies on QCM crystals that were in contact with liquid on one side. The Sauerbrey equation holds for gaseous and liquid environments when mass loading with thin rigid films. However, in liquid, the density and the viscosity of the liquid itself have a significant influence on the resonance frequency, corresponding to drag on the sensor surface and to the evanescent shear wave that decays into the liquid. This can be described as proposed by Kanazawa and Gordon [54, 55]

$$\Delta f = f_0^{3/2} \sqrt{\frac{\eta \rho}{\pi \mu_q \rho_q}} \quad (19)$$

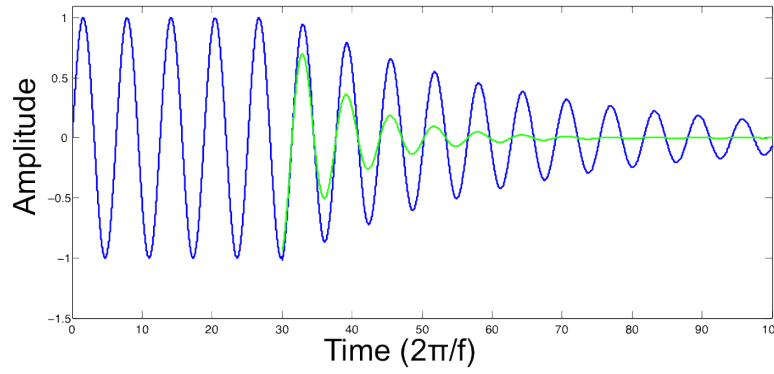


Figure 9 – In the QCM-D machine, the dissipation is measured by switching off the driving of the oscillation and measuring the decay time of the amplitude of the oscillation.

Where  $\eta$  and  $\rho$  are the viscosity and the density of the liquid and  $\mu_q$  is the shear modulus of the quartz. The dissipation strongly depends on the viscosity and the density of the liquid via [110]

$$\Delta D = \frac{1}{t_q \rho_q} \sqrt{\frac{\eta \rho}{\pi f_0}} \quad . \quad (20)$$

Note that the dissipation does not change when adding a thin rigid mass to the surface.



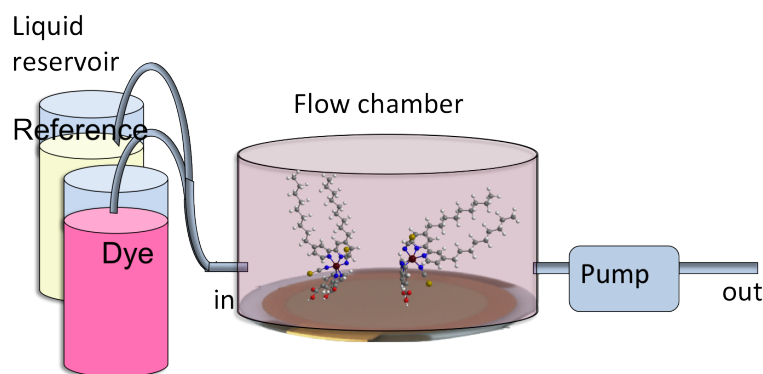


Figure 10 – Illustration of the QCM-D setup. Quartz crystal microbalance with dissipation technique integrated in a liquid flow cell, using a reference liquid and a sample liquid.

### QCM-D measurement technique

In a quartz crystal microbalance with dissipation monitoring, a conventional quartz sensor is mounted in a flow cell as illustrated in figure 10. The sensor can be rinsed with different liquids, for example with a reference liquid or a dye solution.

The sensor is made of AT-cut  $\alpha$ -quartz that is coated with gold electrodes on both sides. When applying a modulated voltage between the electrodes, the sensor undergoes shear thickness oscillations. The fundamental resonance frequency is at about 5 MHz. If mass is added onto the crystal, the resonance is shifted to lower frequencies. If the mass is small, and the attached layer is thin compared to the crystal, the resulting shift of resonance frequency is proportional to the mass uptake and given by the Sauerbrey equation from reference [103]

$$\Delta m = -C \cdot \Delta f \quad , \quad (21)$$

as described above.  $C = \frac{f_0}{\rho_q d}$  is the Sauerbrey constant constant which has a value of approximately  $C = 17.5 \frac{\text{ng}}{\text{cm}^2}$  for the fundamental resonance of our sensors. Measuring both, frequency and dissipation, gives information on the adsorbed mass and on the viscosity and density of the overlying bulk liquid.

In order to account for the signal caused by the overlying bulk liquid, it is essential that the solvent in the beginning and the end of the measurement is the same. This is illustrated in figure 11, which presents the typical kind of data that will be shown throughout the thesis. Part (a) shows a case in which the frequency shift depends only on the change of mass, and the viscosity and density of the overlying bulk liquid are kept almost constant throughout the measurement. The dissipation does not change significantly. Figure 11 (b) shows a case were no mass is attached to the surface, and the observed shifts of frequency and dissipation are solely caused by a change of viscosity and density of the overlying bulk liquid. Figure 11 (c) shows the adsorption of a species from a solvent that is not the same as the reference solvent.

In the latter case, only the final frequency shift will deliver a correct value for the adsorbed Sauerbrey area mass.

It can be sensible to use a reference solvent other than the solvent mixture employed for adsorbing the dye molecule. For example, after staining the mesoporous TiO<sub>2</sub> photoanode of a dye sensitized solar cell in a dye solution in a mixture of MeCN:tBuOH (1:1)<sub>vol</sub>, the electrode is subsequently rinsed in pure MeCN in order to remove excess dye in the pores without desorbing any dye from the TiO<sub>2</sub> surface.

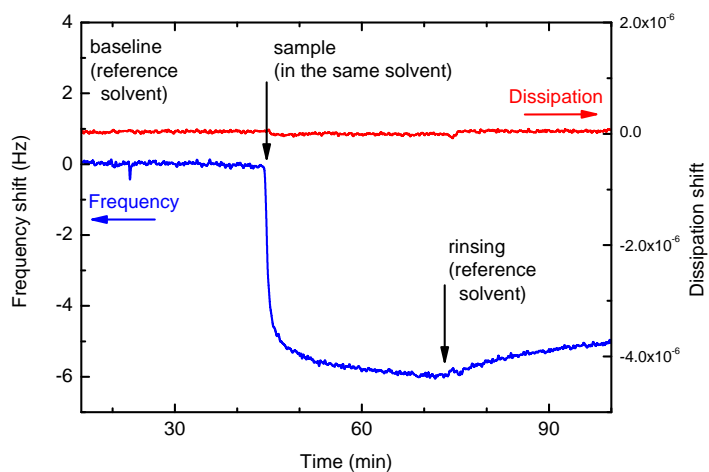
Furthermore, the shift of frequency and dissipation can be used to characterize viscoelastic films that are adsorbed on the surface. Those films are usually soft and relatively thick, for example polymer brushes or surfaces functionalized with pharmaceutically relevant molecules. The analytical and technical approach for their analysis was pushed forward by Rodhal and Kasemo [99, 98], and the viscoelastic modelling of the data is usually done on the basis of a Voight viscoelastic model. The Voight model corresponds to the mechanics of a parallel spring and dashpot and is explained in this context in references [23, 118], including an analytical approach. For a comprehensive review on the modelling of QCM-D data using electrical equivalence circuits, also see the tutorial of Johannsmann [50].

The instrument used in this thesis is a QCM-D of the type E4 by Q-Sense, the company that spun off from the work of Rodhal *et al.*[98]. It can measure 4 parallel flow modules with a relative sensitivity 0.3 Hz, that is 5 ng/cm<sup>2</sup> when assuming a thin rigid film. The standard sensors are the model QSX-301 provided by Q-sense. They consist of an AT-cut alpha-quartz in the shape of a disc of 14 mm diameter and 0.3 mm thickness. The top and bottom of the sensor are coated with a 100 nm thick gold electrode.

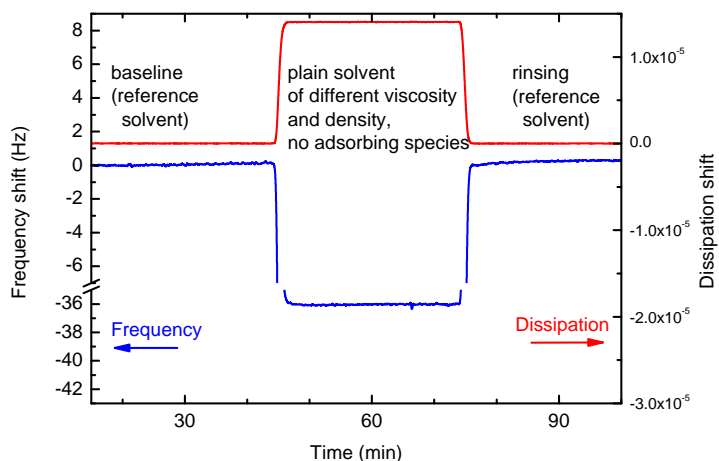
Beyond the fundamental frequency, higher harmonics can be measured as well as their dissipation. Our instrument records all odd harmonics until the 13th overtone, corresponding to resonance frequencies of 5 MHz, 15 MHz, 25MHz, . . . , 65 MHz. Different overtones have different sensitivity profiles[26]. The sensitivity profile of higher harmonics is located closer to the surface in vertical direction, but extends laterally further away from the centre of the sensor. Higher overtones are in general less sensitive to random perturbation or noise.

If using the Sauerbrey equation, the fundamental frequency  $f_0$  needs to be replaced by the frequency of the higher overtone. This is often approximated by multiplication of  $f_0$  with the overtone number  $n$ , or, for the sake of plotting different overtones together, by scaling the shift of frequency and dissipation by the overtone number, i.e. displaying  $\Delta f/n$  and  $\Delta D/n$ .

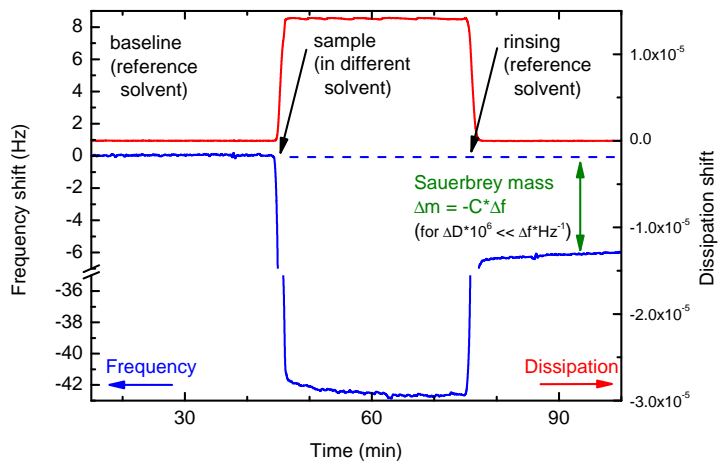
In most of the measurements on flat films displayed in this report, a thin, rigid layer of adsorbate is detected, which is indicated by the fact that the dissipation goes back to its initial zero value upon rinsing with the reference, and all different frequency overtones converge to the same, final value without splitting up. Hence, we only display one stable overtone, usually the 5th (25 MHz) or the 7th (35 MHz), and scale it by the overtone number. In those cases, the Sauerbrey equation 21 is applied in order to obtain the adsorbed area mass.



(a) Adsorbed mass only.



(b) Change of overlying bulk viscosity and density only.



(c) Adsorption of a rigid mass and change of overlying bulk viscosity and density.

Figure 11 – Illustration of QCM-D signals for typical situations encountered throughout this thesis. Scaled shifts of frequency and dissipation on the 7th overtone (35 MHz).

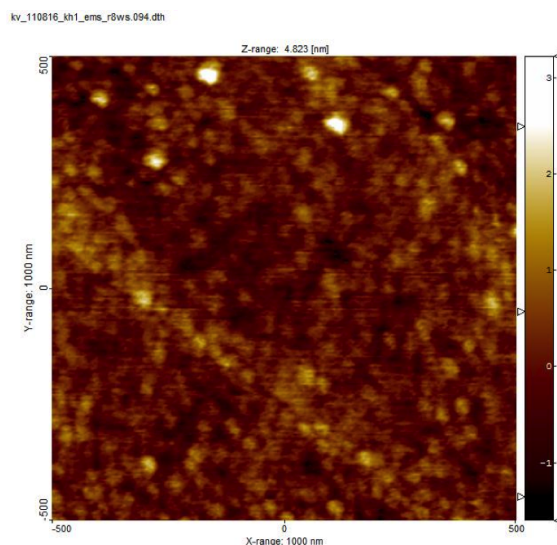


Figure 12 – AFM micrograph of a TiO<sub>2</sub> film deposited by atomic layer deposition. The lateral size of the scan is 1 μm, and the colour-coded height scale stretches over 4 nm of height difference. The image was taken by K. Voitchovsky in liquid environment (EiPS).

### Sensor preparation

The standard sensor supplied by Q-Sense, QSX-301, has a 100 nm thick gold electrode on the top side. On top of the electrode a flat compact TiO<sub>2</sub> film was deposited by atomic layer deposition (ALD) from a tetrakis(dimethylamido)titanium(IV) precursor, usually of 60 nm thickness. Subsequently the film is annealed for 5 hours at 420°C to form the anatase phase. The films were never annealed at 500°C, as usually done for DSC applications, because quartz undergoes a phase transition from  $\alpha$ - to  $\beta$ -quartz at 574°C. Recent AFM images reveal that we can obtain ideally flat surfaces with a roughness below 2 nm by depositing TiO<sub>2</sub> by ALD, see figure 12 which shows a TiO<sub>2</sub> ALD layer on a Si wafer. However, roughness on a sensor crystal is often dominated by the underlying sputtered gold electrode, that has small height differences of 10-20 nm over a length of 500 nm. The X-ray diffraction spectrum (XRD) of a flat, compact TiO<sub>2</sub> film prepared this way is displayed in figure 13. Apart from the amorphous background and the peaks related to the  $\alpha$ -quartz and the gold, there are some anatase peaks detected, but no indications for the rutile phase. If another procedure is applied, especially for porous films, this will be described in the introduction of the according chapter.

After each use, sensors are cleaned according to an appropriate protocol in order to ensure dye removal and a pristine surface similar to that in the fabrication of a DSC device. After staining with dye, the usual cleaning protocol was a 5 min rinse in 0.1 M tetrabutylammonium hydroxide in *N,N*-dimethylformamide (DMF), subsequent rinsing in H<sub>2</sub>O, EtOH, H<sub>2</sub>O, UV-ozone treatment, H<sub>2</sub>O and UV-ozone treatment for 10 min in each. The sensor surface was blown with dry, filtered air before and after each UV-ozone treatment and stored in a clean box after the procedure.

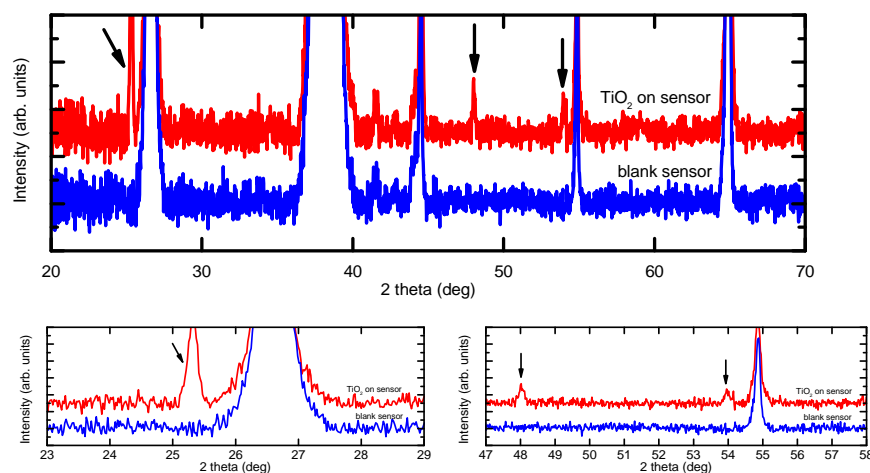


Figure 13 – XRD scan of a QCM-D sensor with an annealed, flat compact  $\text{TiO}_2$  film (red) and a blank QCM-D sensor (blue). The arrows indicate three  $\text{TiO}_2$  anatase peaks at values of  $2\theta$  of  $25.3^\circ$ ,  $48.1^\circ$ ,  $54.0^\circ$ , see jcpds card 00-021-1272. The blank QCM-D sensor consists of an  $\alpha$ -quartz disk, coated with a chromium adhesion layer and a 100 nm thick sputtered gold electrode. Quartz accounts for the large peaks at  $26.6^\circ$  and  $54.9^\circ$ , meanwhile the large peaks at  $38.2^\circ$ ,  $44.5^\circ$  and  $64.9^\circ$  are related to the gold and chromium electrode.

Prior to re-use, the sensors were again subjected to a UV-ozone treatment for 15 min and heated to  $420^\circ\text{C}$  for 30 min (30 min ramping time) in order to remove excess water from the hydrophilic  $\text{TiO}_2$  surface. The sensor was then swiftly transferred into the QCM-D measurement module, and the module was filled with the reference liquid.

Perovskite films were removed by prolonged rinsing in DMF and water at  $95^\circ\text{C}$ . The above cleaning procedure has varied slightly throughout the course of the thesis.

Occasionally, specific overtones of a sensor would show a starkly different response than others. This often indicated a degradation of the sensor, towards the end of its lifetime. However, towards the end of this thesis it was realized that there is an inherent problem with heating the standard QSX-301 sensor to temperatures of  $420^\circ\text{C}$ . Heating to high temperatures resulted in the gold film starting to de-wet the quartz crystal, forming domains of the size of tens of micrometers, either exposing or covering the quartz. This was visible to the bare eye as a haze, and evident in the optical microscope. Interestingly, this phenomena occurred regardless of whether the gold electrode was covered under a 60 nm thick ALD-layer of  $\text{TiO}_2$  or not. Despite the de-wetting of the gold, the overlying  $\text{TiO}_2$  layer was still flat over large areas of the sensor (as confirmed by AFM), and QCM-D operation was still possible, though with larger irregularities. The de-wetting of the gold underneath the  $\text{TiO}_2$  was further confirmed by EDX-mapping in SEM images. The de-wetting does usually not occur when using sensors of the QSX-338 series that employ an adhesion layer of Ti between the quartz and the gold, instead of the usual Cr adhesion layer for the QSX-301 series.



# 1 The adsorption of ruthenium complex Z907 on flat, compact TiO<sub>2</sub> by QCM-D

*The content of the first part of this chapter has been published in the journal PCCP in 2012 [42].*

In this chapter, the QCM-D signal upon Z907 dye adsorption on flat, compact TiO<sub>2</sub> films is explained, and concentration-dependent measurements are shown, which are used to obtain an adsorption isotherm. We confirm the presence of adsorbed Z907 by complementary measurements, and measure the adsorption and desorption kinetics in an approximate manner.

For a first model study on the adsorption of dyes on flat, compact TiO<sub>2</sub> by QCM-D, the ruthenium dye Z907 was chosen. The ruthenium complex Z907 is a well-investigated pigment for dye-sensitized solar cells that is known for its relatively good performance, and in particular for its long-term stability [124, 122, 138]. It does perform very well with non-volatile electrolytes, which is essential for applications outside the laboratory [124]. Compared to other ruthenium complexes like N3, N719 or the black dye, Z907 shows little aggregation [84, 85, 46, 122]. The structures of the above-mentioned ruthenium-based dyes are displayed figures 1.1 and 1.2. Figure 1.1 shows the structure of the Z907Na, the widely-used Z907 salt for making Z907 dye solutions. The dye can bind to the TiO<sub>2</sub> surface via its two carboxylate groups, and its exact binding mode will depend on surface protonation, similar to that of other ruthenium complexes with multiple carboxylate anchoring groups [105]. The most likely binding mode for Z907 will be a mixed bidentate/monodentate mode or a double bidentate, see also the introduction and chapter 3. The long alkyl chains of the Z907 dye were designed to protect the TiO<sub>2</sub> surface and the binding groups from water in the electrolyte, and thereby enhance long-term stability. Z907 shows less aggregation when adsorbed on the surface than N719 or N3 ruthenium dyes without coadsorbates, which could also be related to the alkyl chains in that dimerization of molecules is less favoured on the hydrophilic TiO<sub>2</sub>. Z907 shows furthermore a good performance with cobalt-based electrolytes, which implies that the alkyl chains effectively block access of the fast, one-electron redox shuttle from the TiO<sub>2</sub> surface.

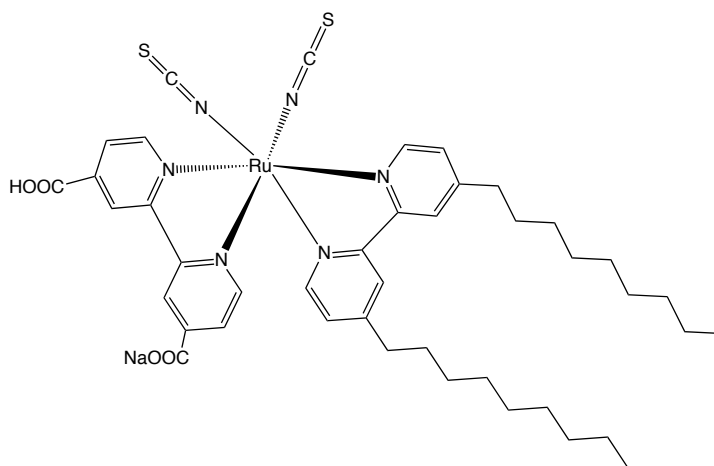


Figure 1.1 – Structure of the Z907 ruthenium complex, its molecular weight is 892 g mol<sup>-1</sup>.

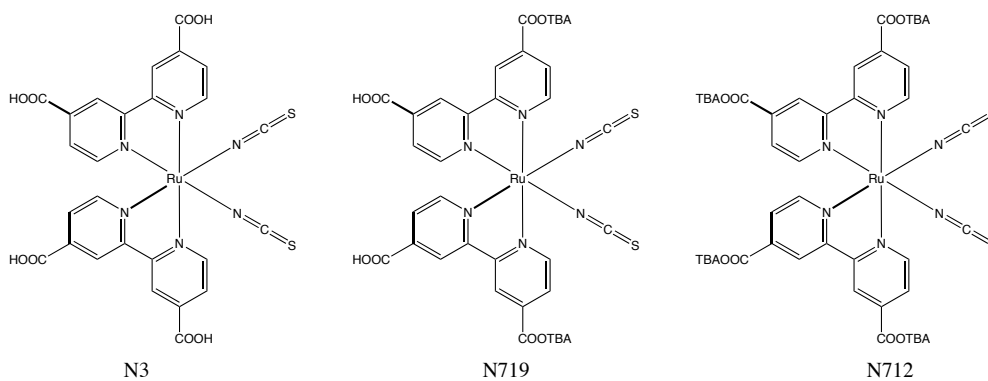


Figure 1.2 – Structure of the N3, N719 and N712 ruthenium complexes. Their degree of protonation is varied by substitution with a tetrabutylammonium cation.

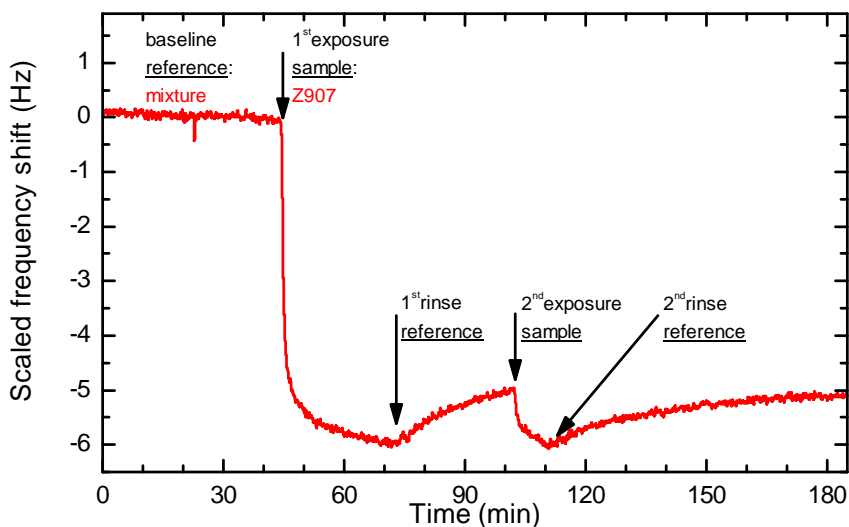


### 1.1 Z907 adsorption on flat, compact TiO<sub>2</sub> by QCM-D

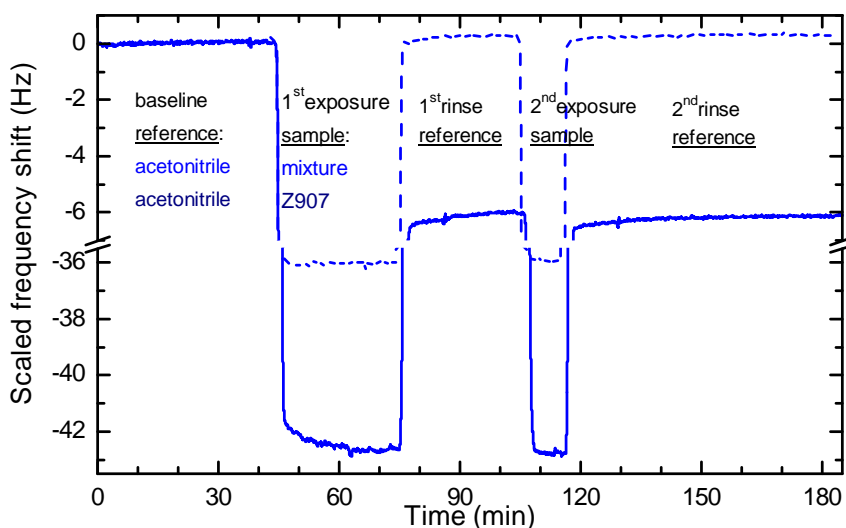
#### 1.1.1 Principle Z907 dye adsorption and solvent baseline

An exemplary measurement of Z907 dye uptake on flat, compact TiO<sub>2</sub> is shown in figure 1.3. The red curve in figure 1.3 (a) shows the most simple case of dye uptake against a reference solution of *tert*-butanol:acetonitrile (tBuOH:MeCN) (1:1)<sub>vol</sub> mixture, which is the same solvent as used for the dye (55 μM Z907 in tBuOH:MeCN mixture). In this configuration, frequency shift relates to mass uptake only, not to viscosity change, since the influence of the latter is constant throughout the measurement. During the first 3 min of the 30 min exposure, the frequency decreases rapidly followed by a much slower shift, indicating at least two different adsorption phases. Upon rinsing with the reference for 30 min, there is 15-20% desorption of the total uptake, shown by an increase in frequency shift. A second exposure results in a fast uptake of an amount similar to what was desorbed in the preceding rinsing period. The final (2nd) rinsing results in qualitatively the same behaviour as for the first one, apart from slower desorption upon rinsing attaining a slightly lower plateau. The latter corresponds to a small additional mass uptake during the second exposure that is likely due to a re-arrangement within the self-assembled monolayer during the first rinsing, leading to a densification of the dye monolayer upon the second exposure. However, this additional mass uptake is very small and indicates that there is no formation of multilayers upon repetitive exposure.

It can be sensible to use a reference solvent other than the solvent mixture employed for adsorbing the dye molecule. For example, after staining the mesoporous TiO<sub>2</sub> photoanode of a dye sensitized solar cell in a dye solution in a mixture of MeCN:tBuOH (1:1)<sub>vol</sub>, the electrode is subsequently rinsed in pure MeCN in order to remove excess dye in the pores without desorbing any dye from the TiO<sub>2</sub> surface. However, in the QCM-D measurement, the different densities and viscosities of the bulk solvents will lead to additional frequency shift when changing between different solvents, see also figure 11 in the introduction. The according experiment shown in figure 1.3 (b) employed plain MeCN as a reference solvent and tBuOH:MeCN (1:1)<sub>vol</sub> mixture for the dye solution. The rationale for this choice is that MeCN is commonly used for rinsing TiO<sub>2</sub> films after dye loading during the preparation of DSCs, reducing dye desorption due to the lower solubility of Z907 in pure MeCN than in the tBuOH:MeCN mixture. The dashed blue line in figure 1.3 (b) shows a blank measurement of tBuOH:MeCN mix against a MeCN reference. Here, the frequency shift relates almost exclusively to bulk viscosity, and upon rinsing with MeCN, the frequency shift returns to zero within an error of 0.2 Hz. The solid red line in figure 1.3 (b) shows an exposure to a 44 μM Z907 solution (in tBuOH:MeCN (1:1)<sub>vol</sub> mixture) against a MeCN reference.



(a) Z907 in MeCN:tBuOH (1:1)<sub>vol</sub> against MeCN:tBuOH (1:1)<sub>vol</sub> baseline.



(b) Z907 in MeCN:tBuOH (1:1)<sub>vol</sub> and blank MeCN:tBuOH (1:1)<sub>vol</sub> against pure MeCN baseline.

Figure 1.3 – Frequency shift versus time upon two subsequent Z907Na dye exposures against different reference solvents as a baseline, and blank measurement on a flat TiO<sub>2</sub> film. (a) 55  $\mu$ M Z907 in tBuOH : MeCN (1:1)<sub>vol</sub> against a tBuOH:MeCN (1:1)<sub>vol</sub> reference (red line). (b) 44  $\mu$ M Z907 in tBuOH:MeCN (1:1)<sub>vol</sub> against a plain MeCN reference (solid blue line). The dashed line in figure (b) also shows the viscosity-related shift of the solvent mixture compared to pure MeCN. All data are scaled QCM-D frequency shifts of the 7th overtone (35 MHz).

## 1.1. Z907 adsorption on flat, compact TiO<sub>2</sub> by QCM-D

---

When switching from a MeCN reference solution to a Z907 dye solution (figure 1.3), the dye will attach to the surface with both of its carboxylate groups, replacing two MeCN molecules [113, 83]. The rest of the TiO<sub>2</sub> underneath the dye will remain covered with solvent molecules [104]. The observed frequency shift of  $-42$  Hz during exposure is due to dye adsorption and a simultaneous bulk viscosity change. After 20 min of exposure, the shift has reached a plateau at  $-43$  Hz, indicating that equilibrium has been reached. During rinsing with the MeCN reference the frequency shifts rapidly back to  $-6$  Hz due to the change of viscosity of the solvent, but little desorption is observed. After the second exposure, desorption is even less pronounced and occurs over a longer time period. The final frequency shift ( $-6.2$  Hz) is 5% larger than the shift after the first exposure ( $-5.9$  Hz), indicating a small additional mass uptake, as was also observed in figure 1.3. This is ascribed again to a molecular re-arrangement within the self-assembled monolayer during the first rinsing and a densification of the dye molecule film upon the second exposure. More importantly, the change upon a second dye exposure is not substantial and indicates, that there is no formation of multilayers of Z907 dye molecules on the surface.

In order to illustrate the choice of the 7th overtone and the validity of the Sauerbrey equation, figure 1.4 shows a typical QCM-D measurement displaying scaled shifts of frequency and dissipation for the 5th to 13th overtone (25 MHz to 65 MHz). The experiment is a double exposure to  $44 \mu\text{M}$  Z907 dye in MeCN:tBuOH (1:1)<sub>vol</sub> mixture against a plain MeCN reference that is used for rinsing. First, we note that the dissipation goes back to zero upon rinsing. This shows that the adsorbed dye forms a thin, rigid film and that the Sauerbrey equation can be used to calculate its area mass. The general spreading of different overtones during the two exposures is due to the different viscosity of the overlying bulk liquid ( $\eta_{\text{MeCN}} = 0.343 \text{ mPa s}$  and  $\rho_{\text{MeCN}} = 0.786 \text{ g cm}^{-3}$ , whereas the viscosity of tert-butanol  $\eta_{\text{tBuOH}}$  is not well defined, because experimental conditions coincide with its melting point  $T_{\text{mp}} = 25.8^\circ \text{ C}$  and  $\rho_{\text{tBuOH}} = 0.789 \text{ g cm}^{-3}$ ). Considering the frequency shifts, almost all of them converge to the same final value upon rinsing. Small deviations of this behaviour can be due to imperfections of the acoustic properties of the TiO<sub>2</sub> film or of the sensor itself, which is the case with the 9th overtone in this example. Lower overtones (1st, 3rd and 5th) are more sensitive to external noise. The oscillations on the 5th overtone in this measurement were caused by an air bubble inside the chamber during the first exposure.

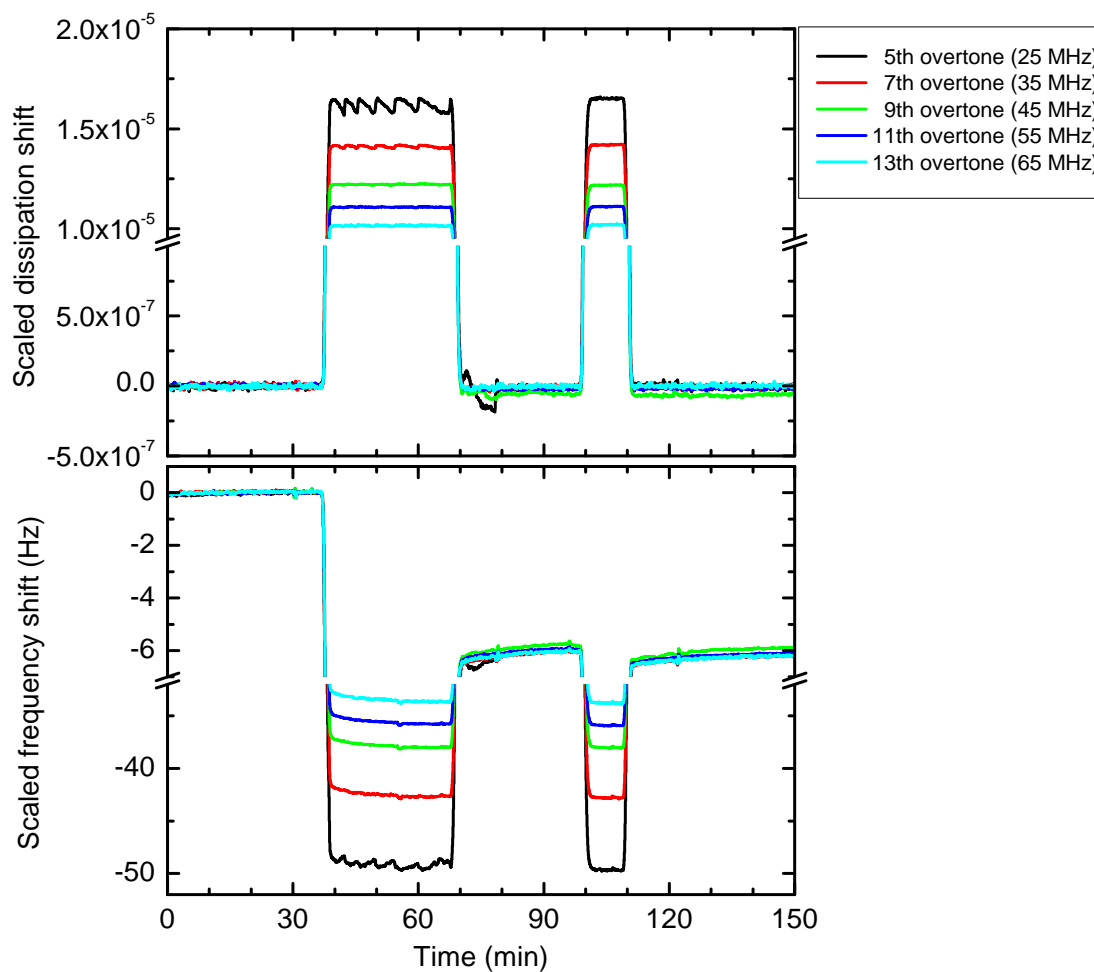


Figure 1.4 – Shift of dissipation and frequency of different overtones during a double exposure to 44  $\mu\text{M}$  Z907 in MeCN:tBuOH (1:1)<sub>vol</sub> mix against a plain MeCN reference. The spreading during dye exposure is due to the different viscosity of the overlying bulk liquid. Upon rinsing, dissipation shift goes back to zero, and all frequency shifts converge to the same final value. The 7th overtone (35 MHz) is representative for the behaviour of the other overtones.

### 1.1.2 Z907 adsorption isotherm

Figure 1.5 (a) shows measurements for different Z907 dye concentrations. It displays frequency shift versus time for a flat TiO<sub>2</sub> film for two subsequent exposures of 30 min and 10 min to Z907 dye solution of concentrations from 0.0 μM to 65.0 μM in a tBuOH:MeCN (1:1)<sub>vol</sub> mixture, using plain MeCN as a reference. There is an increase of absolute final frequency shift with increasing concentration, as well as an increase of the adsorption rate (slope) during the first exposure.

Figure 1.5 (b) shows the absolute frequency shift  $\Delta f_{\text{eq}}$  after 60 min of rinsing with the reference solvent MeCN as a function of the concentration of the dye solution. Red squares represent the same data as shown in the figure 1.5 (a), while blue squares are from an analogous dataset obtained for two subsequent 10 min exposures (measurement not shown). The red curve is a fit with a Langmuir isotherm of the form

$$\Delta f_{\text{eq}} = \frac{\Delta f_{\text{max}} \cdot K_{\text{eq,Z907}} \cdot c_{\text{Z907}}}{1 + K_{\text{eq,Z907}} \cdot c_{\text{Z907}}} \quad , \quad (1.1)$$

$\Delta f_{\text{max}}$  is the scaled final frequency shift for full coverage with a monolayer,  $K_{\text{eq,Z907}}$  is the equilibrium adsorption constant, and  $c_{\text{Z907}}$  is the Z907 equilibrium dye concentration in MeCN:tBuOH (1:1)<sub>vol</sub>. While the Langmuir equation describes the presented data well, the validity of the specific assumptions underlying this model for the present case may be questioned. However, we still pursue this analysis in order to compare with literature data. Fitting the points in the concentration range from 0.0 μM to 65.0 μM gives an equilibrium adsorption constant of

$$K_{\text{eq,Z907}} = 5.1 \pm 0.3 \cdot 10^6 M^{-1} \quad , \quad (1.2)$$

and an absolute value for frequency shift for a monolayer

$$\Delta f_{\text{max}} = 5.9 \pm 0.3 \text{ Hz} \quad . \quad (1.3)$$

Using the Sauerbrey equation, the frequency shift for a monolayer  $\Delta f_{\text{max}}$  corresponds to an area mass of 103 ng cm<sup>-2</sup>, yielding a number concentration of Z907 on the surface of  $1.27 \cdot 10^{-10}$  mol cm<sup>-2</sup>. This estimate assumes a flat surface, and an effective molecular weight of  $MW_{\text{Z907Na}} = 892$  g mol<sup>-1</sup> and  $MW_{\text{MeCN}} = 41$  g mol<sup>-1</sup> for MeCN, in that one adsorbed Z907Na molecule replaces only one surface-associated MeCN molecule. At full monolayer coverage this in turn corresponds to a footprint area of 1.31 nm<sup>2</sup> per Z907 molecule.

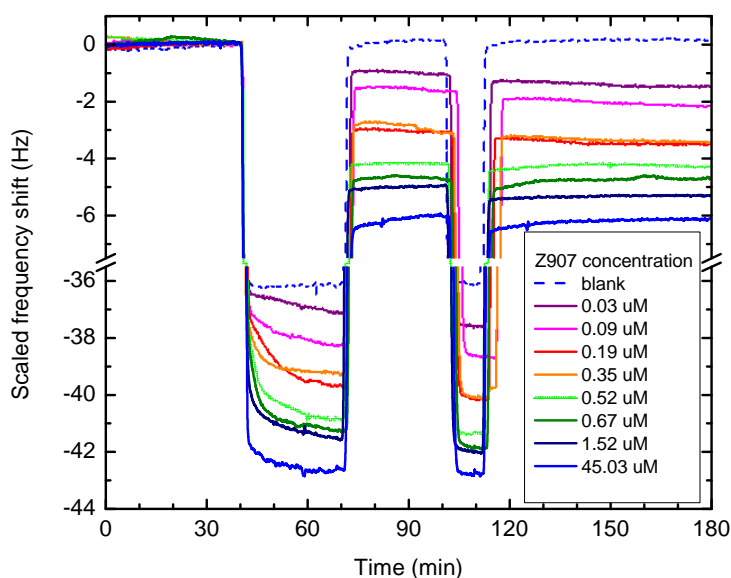
In order to confirm that the frequency shift is truly caused by the dye itself, the Z907 dye was desorbed from the TiO<sub>2</sub> surface after the QCM-D measurement using a solution of tetra-

## **Chapter 1. The adsorption of ruthenium complex Z907 on flat, compact TiO<sub>2</sub> by QCM-D**

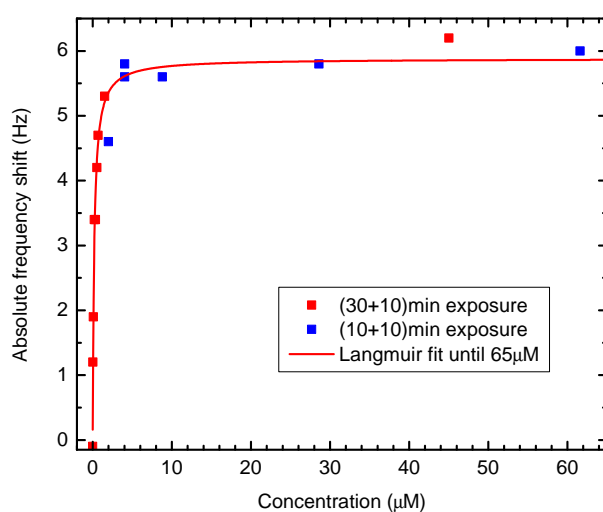
---

butylammonium hydroxide in dimethylformamide. The dye concentration was quantified by comparing its fluorescence signal against a reference solution, leading to a projected area of 1.26 nm<sup>2</sup> per molecule, which is in excellent agreement with the value derived from the QCM-D experiments. These values are also close to the area of 1.6 nm<sup>2</sup> determined for the N719 dye [107], whose structure is similar to that of Z907. However, the signal on the according fluorescence measurement was very low due to the small quantity and the relatively low fluorescence yield of the Z907 ruthenium complex and bears a significant error. We will discuss different complementary measurements in the next subsection.

## 1.1. Z907 adsorption on flat, compact TiO<sub>2</sub> by QCM-D



(a) Various concentrations of Z907 in MeCN:tBuOH (1:1)<sub>vol</sub> against a MeCN baseline.



(b) Isotherm for adsorption of Z907 from MeCN:tBuOH (1:1)<sub>vol</sub> and a Langmuir fit to the data on display.

Figure 1.5 – Adsorption of ruthenium dye Z907 on flat, compact TiO<sub>2</sub> against a pure MeCN baseline. Scaled QCM-D frequency shift of the 7th overtone (35 MHz). Part (a) shows the time-resolved QCM-D frequency shift of each measurement with concentrations ranging from 0 μM to 45 μM. Figure (b) shows the final, absolute frequency shift of different measurements as a function of equilibrium dye concentration in the staining solution. A second data set, based on two staining cycles of 10 min each is included. The red line is a Langmuir fit of the entire data.

### 1.1.3 Confirmation of QCM-D results by complementary techniques

In this section, I present a confirmation of the adsorbed dye molecules on the flat, compact TiO<sub>2</sub> by spectroscopic ellipsometry. These ex-situ measurements are of interest, because there is no literature data related to it, and ellipsometry provides a method to not only monitor the absorption spectrum of the adsorbed dye, but also its optical density. The ellipsometry measurement presented here was performed out by K. Zhao and R. Li in the frame of a collaboration with A. Amassian at the King Abdullah University of Science and Technology (KAUST). An introduction to spectroscopic ellipsometry can be found in reference [115].

Measurements were carried out on a silicon substrate that had been coated with approximately 70 nm flat, compact TiO<sub>2</sub> by atomic layer deposition. The substrate was stained for 30 min +10 min in a 50  $\mu$ M solution of Z907 in MeCN:tBuOH (1:1)<sub>vol</sub> mix and rinsed in pure MeCN, in analogy to the QCM-D experiments.

First, a sample without dye was measured in order to retrieve an optical model of the substrate, including the silicon wafer, the native SiO<sub>x</sub> oxide, and the 70 nm TiO<sub>2</sub> layer. Then, the sample with the dye was measured, and an optical model of the layer stack was fit to the data. This layer stack used the previously determined optical model of the substrate as a fixed input, and only adapted the real and imaginary part  $n$  and  $k$  of the refractive index of a 1 nm thick film in order to fit the data.

The fit to the ellipsometric data values  $\Psi$  and  $\Delta$  is shown in figure 1.6 (a). The resulting free fit of the real and imaginary part  $n$  and  $k$  of the refractive index of the outermost layer are displayed in figure 1.6 (b).

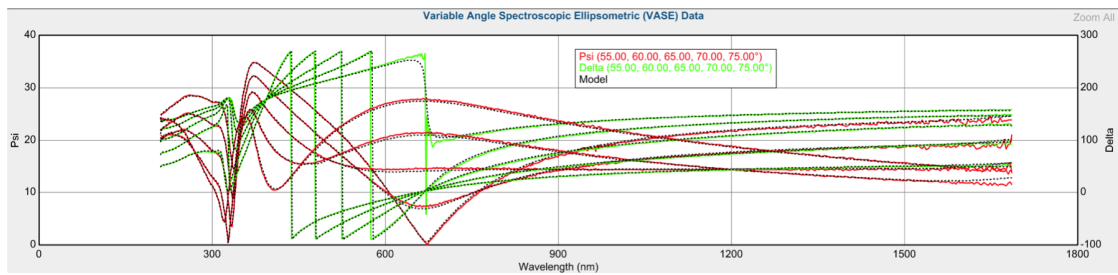
The imaginary part of the refractive index  $k$  describes the exponential attenuation of the electric field by the Lambert-Beer law. It relates to absorption coefficient  $\alpha$  used for describing the attenuation of light intensity by Lambert Beer in chemistry by  $\alpha = 4\pi k/\lambda$ . The observed dispersion of  $k$  matches very well the absorption spectrum of the ruthenium dye Z907, and can be taken as an indication for the dye on the surface.

The measurement allows further for the extraction of the real part of the refractive index  $n$ , which may be important for other optical techniques, for example in applications in indirect nanoplasmonic sensing.

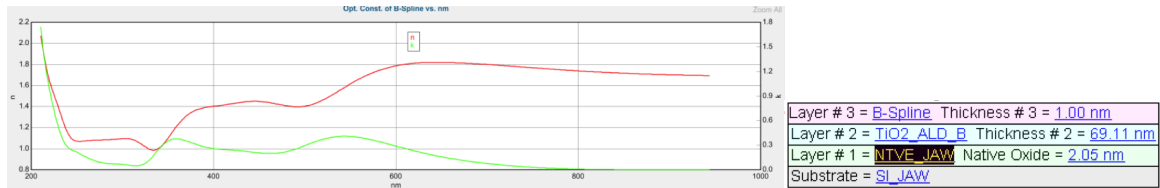
In the end of the previous section I have already mentioned that the amount of Z907 dye adsorbed on the flat, compact TiO<sub>2</sub> film on the QCM-D sensor has been confirmed by fluorescence emission spectroscopy in an approximate manner. The general adsorption kinetics of Z907 on flat, compact TiO<sub>2</sub> has been investigated by indirect nanoplasmonic sensing (INPS) as a complementary, optical technique by Gusak et al. [35]. In chapter 3, I will present direct microscopic confirmation of a monolayer of adsorbed dye molecules by atomic force microscopy in liquid phase.



### 1.1. Z907 adsorption on flat, compact TiO<sub>2</sub> by QCM-D



(a) Data of  $\Psi$  and  $\Delta$  from spectroscopic ellipsometry, and a fit of the optical model.



(b) Resulting  $n$  and  $k$  for the free fit of a dye layer of 1 nm thickness.

(c) Layer stack.

Figure 1.6 – Spectroscopic ellipsometry measurement of Z907 dye adsorbed on flat, compact TiO<sub>2</sub>. The optical model for the substrate (100 Si), layer #1 (native SiO<sub>x</sub>) and layer #2 (TiO<sub>2</sub>) has been taken from a previous blank measurement (not shown). Only the optical constants of the 1 nm thick layer #3 (dye layer) have been determined in a free fit in order match the measured data. Provided by R. Li and K. Zhao.

## **1.2 Kinetics of Z907 dye adsorption and desorption**

This section is a rudimentary discussion of the kinetics of Z907 adsorption and desorption as monitored by QCM-D, that have been carried out in the wake of my first publication [42]. One exemplary measurement is analysed in detail and provides us with two preliminary findings: first, the very high equilibrium adsorption constant extracted from the Langmuir fit in section 1.1.2 is in the same order of magnitude as the one we obtain from adsorption and desorption rate constants from the kinetic measurements. Second, the kinetics of adsorption and desorption strongly suggest that part of the dye is bound more strongly than the rest of it. These findings have recently found strong confirmation in a study using kinetics at different Z907 concentrations by Gusak et al. [37], using a simplified version of a single Langmuir adsorption.

### **1.2.1 Notations: adsorption and desorption rates for the Langmuir equation**

This section is just to point out the notations, following those used by Masel [74].  $r_{ad}$  is the rate of adsorption,  $r_d$  is the rate of desorption which are given by

$$r_{ad} = k_{ad} \cdot c \cdot [S] \quad (1.4)$$

$$r_d = k_d \cdot [A_{ad}] \quad (1.5)$$

where  $c$  is the concentration of the adsorbate over the surface,  $[S]$  is the concentration of bare sites,  $[A_{ad}]$  is the surface concentration of adsorbed molecules and  $k_{ad}$  and  $k_d$  are the adsorption and desorption rate constants respectively. At equilibrium adsorption and desorption rates are the same so that  $r_{ad} = r_d$  yields

$$\frac{[A_{ad}]}{c[S]} = \frac{k_{ad}}{k_d} =: K_{eq}^A \quad (1.6)$$

$K_{eq}^A$  is the Langmuir equilibrium adsorption constant. Considering only one single adsorbate species, the total concentration of sites is  $[S_0] = [S] + [A_{ad}]$ . When defining the coverage  $\theta = \frac{[A_{ad}]}{S_0}$  we yield the Langmuir adsorption isotherm

$$\theta_{equilibrium} = \frac{K_{eq}^A \cdot c}{1 + K_{eq}^A \cdot c} \quad (1.7)$$

### 1.2.2 Desorption dynamics

We describe three different desorption mechanisms that are then used to fit the desorption of a Z907 layer that is exposed to a tBuOH:MeCN mixed solvent and extract desorption rate constants.

For a simple Langmuir-type system, the desorption rate is given by equation 1.5 and can be expressed in terms of coverage as

$$\frac{d\theta}{dt} = k_d\theta \quad . \quad (1.8)$$

This differential equation is solved by

$$\theta = e^{-k_d(t-t_0)} \quad , \quad (1.9)$$

where  $t$  is the time and  $t_0$  is the start of the desorption process from full coverage. For the curve fitting, we express the solution in terms of frequency shift  $\Delta f$  with  $\theta = \frac{\Delta f}{\Delta f_{\text{start}}}$ , where  $\Delta f_{\text{start}}$  is the frequency shift at  $t_0$  which should be close to full coverage

$$\Delta f = \Delta f_{\text{start}} e^{-k_d(t-t_0)} \quad . \quad (1.10)$$

The data may also be described by an irreversible adsorption with an additional Langmuir type adsorption. Hence, the desorption would be described by

$$\Delta f = \Delta f_{\text{irreversible}} + (\Delta f_{\text{start}} - \Delta f_{\text{irreversible}}) e^{-k_d(t-t_0)} \quad . \quad (1.11)$$

However, for very long time scales, it would be reasonable to assume full desorption since the dye is well soluble in the surrounding tBuOH:MeCN solvent mixture. Therefore we will also employ a double Langmuir-type model to account for strongly adsorbed molecules with a low desorption rate constant  $k_{\text{ad, strong}}$  and weakly adsorbed molecules with a higher desorption rate constant  $k_{\text{ad, weak}}$ . The observed frequency shift will be given by

$$\Delta f = \Delta f_{\text{start, strong}} e^{-k_{\text{ad, strong}}(t-t_0)} + \Delta f_{\text{start, weak}} e^{-k_{\text{ad, weak}}(t-t_0)} \quad . \quad (1.12)$$

The numerical fit of the desorption dynamics is shown in figure 1.7. The data is a 30 min plus 10 min exposure to Z907 (55  $\mu\text{M}$ ) against a tBuOH:MeCN baseline, which has already been displayed in figure 1.3. At the end of the 1st exposure, a plateau is reached that is already close to saturation coverage. The subsequent desorption during the 1st rinse is fitted by using the three models described above. The simple Langmuir model (orange line, equation 1.10)

## Chapter 1. The adsorption of ruthenium complex Z907 on flat, compact TiO<sub>2</sub> by QCM-D

---

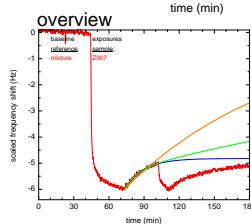
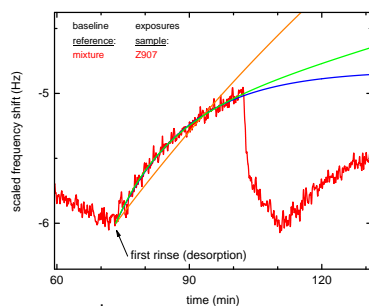
gives a very poor fit. The irreversible plus Langmuir model (blue line, equation 1.11) and the double-Langmuir model (green line, equation 1.12) both are in good agreement with the data. Fitting of the desorption after the second exposure gives the same outcome for the quality of the fit comparing the different models. During the second exposure there is a small additional frequency shift, so amounts of strongly (or irreversibly) bound and weakly bound molecules will have changed whereas their respective desorption rate constants should be the same as during the first exposure. However, for best fit, the respective adsorption rate constants were changed. When fixing these rate constants to the values obtained from the first desorption fit, the fit quality of the irreversible plus Langmuir fit becomes slightly worse than the quality of the double-Langmuir fit (not shown).

Desorption rate constants from the 1st desorption are for the simple Langmuir model (orange, poor fit, equation 1.10)  $k_d = 1.25 \cdot 10^{-4} \text{ s}^{-1}$  and for the double-Langmuir model (green, equation 1.12)  $k_{d,\text{strong}} = 3.7 \cdot 10^{-5} \text{ s}^{-1}$ ,  $k_{d,\text{weak}} = 1.51 \cdot 10^{-3} \text{ s}^{-1}$ .

## 1.2. Kinetics of Z907 dye adsorption and desorption

### fit of desorption during 1st rinse

set initial shift of 6 Hz at 73.3 min (4400 s) as fixed parameters;  
set final frequency shift to 0 Hz (t-> infinity) for Langmuir-type fit



(orange) simple Langmuir

$kd = 1.25 \times 10^{-4} \text{ s}^{-1}$ ; very poor fit

Model		LangmuirDesorptionHH (User)	
Equation	$y_{\text{end}} + (y_{\text{full}} - y_{\text{end}}) \exp(-kd \cdot (t-t_0))$		
Reduced Chi-Sqr	0.0085		
Adj. R-Square	0.84821		
	Value	Standard Error	
Books_S	y_end	0	0
	y_full	-6	0
	kd	1.25312E-4	1.72428E-7
	t0	4400	0

(blue) simple first order

$kd = 1.03 \times 10^{-3} \text{ s}^{-1}$ ;  $\Delta f_{\text{final}} = 4.8 \text{ Hz}$

Model		LangmuirDesorptionHH (User)		ALLOW FOR FINAL NON-ZERO FREQUENCY SHIFT	
Equation	$y_{\text{end}} + (y_{\text{full}} - y_{\text{end}}) \exp(-kd \cdot (t-t_0))$				
Reduced Chi-Sqr	0.0012				
Adj. R-Square	0.97803				
	Value	Standard Error			
Books_S	y_end	-4.8213	0.00253		
	y_full	-6	0		
	kd	0.00103	4.07143E-6		
	t0	4400	0		

(green) double Langmuir

$kd_{\text{weak}} = 1.51 \times 10^{-3} \text{ s}^{-1}$ ;  
 $kd_{\text{strong}} = 3.7 \times 10^{-5} \text{ s}^{-1}$ ;

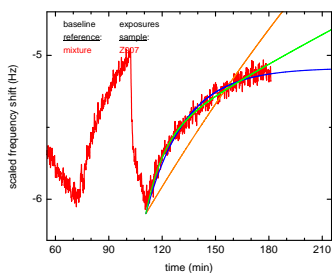
0.7 Hz in weakly bound state;

significant parameter interdependence

Model		Double_LangmuirDesorptionHH (User)	
Equation	$y_{\text{weak}} \exp(-kd_{\text{weak}} \cdot (t-t_0)) + (y_{\text{full}} - y_{\text{weak}}) \exp(-kd_{\text{strong}} \cdot (t-t_0))$		
Reduced Chi-Sqr	0.00113		
Adj. R-Square	0.97855		
	Value	Standard Error	
Books_S	y_full	-6	0
	y_weak	-0.72191	0.02022
	kd_weak	0.00151	3.49921E-5
	kd_strong	3.69506E-5	1.79187E-6
	t0	4400	0

### Fit of desorption during 2nd rinse

set initial shift of 6.1 Hz at 73.3 min (6650 s) as fixed parameters;  
set final frequency shift to 0 Hz (t-> infinity) for Langmuir-type fit



(orange) simple Langmuir

$kd = 5.7 \times 10^{-5} \text{ s}^{-1}$ ; very poor fit

(blue) simple first order

$kd = 7.6 \times 10^{-4} \text{ s}^{-1}$ ;  $\Delta f_{\text{final}} = -5.1 \text{ Hz}$

parameter interdependence

Model		LangmuirDesorptionHH (User)	
Equation	$y_{\text{end}} + (y_{\text{full}} - y_{\text{end}}) \exp(-kd \cdot (t-t_0))$		
Reduced Chi-Sqr	0.02427		
Adj. R-Square	0.39559		
	Value	Standard Error	
Books_S	y_end	0	0
	y_full	-6.1	0
	kd	5.67994E-5	8.06182E-8
	t0	6650	0

Model		LangmuirDesorptionHH (User)	
Equation	$y_{\text{end}} + (y_{\text{full}} - y_{\text{end}}) \exp(-kd \cdot (t-t_0))$		
Reduced Chi-Sqr	0.0019		
Adj. R-Square	0.9527		
	Value	Standard Error	
Books_S	y_end	-5.08766	8.52936E-4
	y_full	-6.1	0
	kd	7.62816E-4	1.69913E-6
	t0	6650	0

(green) double Langmuir

$kd_{\text{weak}} = 1.67 \times 10^{-3} \text{ s}^{-1}$ ;  
 $kd_{\text{strong}} = 2.3 \times 10^{-5} \text{ s}^{-1}$ ;

0.5 Hz in weakly bound state;

significant parameter interdependence

Model		Double_LangmuirDesorptionHH (User)	
Equation	$y_{\text{weak}} \exp(-kd_{\text{weak}} \cdot (t-t_0)) + (y_{\text{full}} - y_{\text{weak}}) \exp(-kd_{\text{strong}} \cdot (t-t_0))$		
Reduced Chi-Sqr	0.0013		
Adj. R-Square	0.96776		
	Value	Standard Error	
Books_S	y_full	-6.1	0
	y_weak	-0.53261	0.00196
	kd_weak	0.00167	1.02623E-5
	kd_strong	2.29756E-5	1.10928E-7
	t0	6650	0

Figure 1.7 – Numerical fit of the desorption dynamics of a Z907 layer when rinsing with tBuOH:MeCN solvent mix, using three different desorption models. See figure for details. The simple Langmuir model (orange line) gives a very poor fit. The irreversible plus Langmuir model (blue line) and the double-Langmuir model (green line) both are in good agreement with the data.

### 1.2.3 Adsorption dynamics

During adsorption of one adsorbate onto a virgin surface, the net adsorption rate will be given by  $r_{\text{net}} = r_{\text{ad}} - r_{\text{d}}$ , expressed in terms of coverage by

$$\frac{d\theta}{dt} = k_{\text{ad}} \cdot c - (k_{\text{ad}} \cdot c + k_{\text{d}})\theta \quad . \quad (1.13)$$

The solution for Langmuir adsorption is

$$\theta = \frac{1}{1 + \frac{k_{\text{d}}}{k_{\text{ad}} \cdot c}} \cdot \left(1 - e^{-(k_{\text{ad}} \cdot c + k_{\text{d}}) \cdot (t - t_0)}\right) \quad (1.14)$$

or in terms of frequency

$$\Delta f = \Delta f_{\text{full}} \cdot \frac{1}{1 + \frac{k_{\text{d}}}{k_{\text{ad}} \cdot c}} \cdot \left(1 - e^{-(k_{\text{ad}} \cdot c + k_{\text{d}}) \cdot (t - t_0)}\right) \quad . \quad (1.15)$$

Where  $\Delta f_{\text{full}}$  would be the maximum possible shift for a full monolayer. For a double-Langmuir model, we use a more empirical equation

$$\begin{aligned} \Delta f = & \Delta f_{\text{strong}} \cdot \left(1 - e^{-(k_{\text{ad, strong}} \cdot c + k_{\text{d, strong}}) \cdot (t - t_0)}\right) \\ & + \Delta f_{\text{weak}} \cdot \left(1 - e^{-(k_{\text{ad, weak}} \cdot c + k_{\text{d, weak}}) \cdot (t - t_0)}\right) \quad . \end{aligned} \quad (1.16)$$

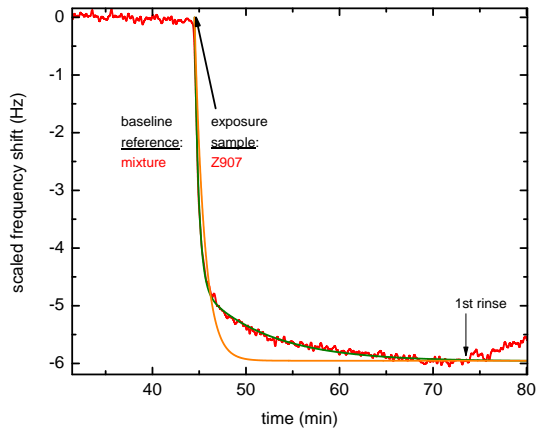
The use of  $\Delta f_{\text{strong}}$  and  $\Delta f_{\text{weak}}$  as fit parameters allows to account for the fact that we do not know details on the binding mechanism or the adsorption sites.

Figure 1.8 shows adsorption dynamics of Z907 (55  $\mu\text{M}$ ) against a tBuOH:MeCN baseline. Pre-adsorbed tBuOH molecules do have an influence on the adsorption dynamics and should lead to smaller adsorption rates than on a pristine surface and could change the ratio between strongly and weakly adsorbed molecules. For the numerical fit, the desorption rate constants obtained from the first rinse in the previous section are used as fixed parameters.

Using the simple Langmuir model (orange line, equation 1.15) gives a poor fit and an adsorption rate constant of  $k_{\text{ad}} = 209 \text{ s}^{-1} \text{ M}^{-1}$ , leading to an equilibrium adsorption rate constant of  $K_{\text{eq}}^{\text{ad}} = \frac{k_{\text{ad}}}{k_{\text{d}}} = 1.7 \cdot 10^6 \text{ M}^{-1}$ . The double-Langmuir model (green line, equation 1.16) gives a good fit with adsorption rate constants of  $k_{\text{ad, strong}} = 703 \text{ s}^{-1} \text{ M}^{-1}$  and  $k_{\text{ad, weak}} = 15 \text{ s}^{-1} \text{ M}^{-1}$ , which leads to an equilibrium adsorption rate constant of  $K_{\text{eq}}^{\text{ad}} = \frac{k_{\text{ad, strong}}}{k_{\text{d, strong}}} + \frac{k_{\text{ad, weak}}}{k_{\text{d, weak}}} = 1.9 \cdot 10^7 \text{ M}^{-1}$ .

## 1.2. Kinetics of Z907 dye adsorption and desorption

Dynamics of first adsorption against (tBuOH:MeCN) baseline



setting desorption rate constant to fixed values  
previously found by desorption dynamics;  
set adsorption onset fix to 2670 s

simple Langmuir adsorption dynamics

very poor fit; set  $k_d = 1.25 \times 10^{-4} \text{ s}^{-1}$  fixed;

find  $k_{ad} = 2.9 \times 10^2 \text{ s}^{-1} \text{ mol}^{-1}$

Langmuir_Adsorption_Dynamics (User)			
Model	Langmuir_Adsorption_Dynamics (User)		
Equation	$y_{full}(1+k_d/(k_{ad}c))^{1-\exp(-(k_{ad}c+k_d)(t-t_0))}$		
Reduced Chi-Sqr	0.10908		
Adj. R-Square	0.54584		
	Value	Standard Error	
F(M2)	t0	2670	0
	k <sub>d</sub>	1.25E-4	0
	k <sub>ad</sub>	290	1.68655
	c	5.5E-5	0
	y <sub>full</sub>	-6	0.00341

double Langmuir adsorption dynamics,

allowing for different adsorption site availabilities.

set  $k_{d, \text{strong}} = 3.7 \times 10^{-5} \text{ s}^{-1}$ ;  $k_{d, \text{weak}} = 1.51 \times 10^{-3} \text{ s}^{-1}$  fixed;

find  $k_{ad, \text{strong}} = 703 \text{ s}^{-1} \text{ mol}^{-1}$ ;  $k_{ad, \text{weak}} = 15 \text{ s}^{-1} \text{ mol}^{-1}$

different_Sites_possible_Double_Langmuir_Ad_Dyn (User)			
Model	different_Sites_possible_Double_Langmuir_Ad_Dyn (User)		
Equation	$A1^{1-(1-\exp(-(t-t_0)/(k_{ad1}c+k_{d1})))} + A2^{1-(1-\exp(-(t-t_0)/(k_{ad2}c+k_{d2}))}$		
Reduced Chi-Sqr	0.00209		
Adj. R-Square	0.9914		
	Value	Standard Error	
F(M2)	k <sub>ad1</sub>	702.91001	1.53841
	k <sub>ad2</sub>	14.65016	0.18476
	t0	2670	0
	A1	-4.62284	0.00329
	c	5.5E-5	0
		k <sub>d1</sub>	3.7E-5
	k <sub>d2</sub>	0.00151	0
	A2	-1.34091	0.00277

Figure 1.8 – Adsorption dynamics upon a Z907 (55  $\mu\text{M}$ ) exposure against a tBuOH:MeCN baseline. Numerical fit with a simple Langmuir adsorption model (orange line, poor fit) and a double-Langmuir model (green line, good fit).

### 1.3 Conclusion

This QCM-D study on the adsorption of Z907 first of all demonstrates the capability of the technique to study dye adsorption in-situ on a flat TiO<sub>2</sub> film as a model system. For the given solvents and molecules, it is possible to detect sub-monolayer quantities, and even resolve the approximate kinetics of adsorption and desorption.

The Z907 isotherm clearly shows, that the coverage approaches a saturation value at concentrations as low as 10  $\mu\text{M}$  in MeCN:tBuOH (1:1)<sub>vol</sub> mixture. This strongly suggests the formation of a Z907 monolayer. We will confirm the presence of a monolayer by direct observation by in-situ atomic force microscopy in chapter 3. The presence of the dye on the surface is further confirmed ex-situ by desorption of the dye and subsequent fluorescence emission spectroscopy, as well as by spectroscopic ellipsometry on the sensitized TiO<sub>2</sub> film.

Interestingly, we see a slightly lower mass uptake at very high Z907 dye concentrations of 300  $\mu\text{M}$ . This is probably due to the deposition of loosely attached dye aggregates and their subsequent removal during rinsing. Although dye concentrations of 300  $\mu\text{M}$  are usually used for staining mesoporous TiO<sub>2</sub> photoanodes, the observed dye aggregates are too large to penetrate the pores of the mesoporous film. Experimental studies by indirect nanoplasmonic sensing (INPS) [36] and other techniques [92] suggest that the staining of the film proceeds via the gradual progression of a diffusion front through the mesoporous film. This implies that most part of the mesoporous TiO<sub>2</sub> film is first exposed to a moderately low Z907 dye concentration. Therefore moderately low concentrations of Z907 are the most sensible way of investigating the adsorption on a flat, compact TiO<sub>2</sub> film as a model system.

In the second part of the chapter, I discuss three different models to fit the dynamics of the adsorption and the desorption process of Z907 dye on TiO<sub>2</sub>: a simple Langmuir model, a model of irreversible adsorption plus Langmuir adsorption, and a double-Langmuir model allowing strongly adsorbed and weakly adsorbed molecules. The simple Langmuir model shows a very poor agreement with the adsorption data, meanwhile the other two models are in good agreement with the data.

Both Langmuir models are used to directly estimate adsorption and desorption rate constants. The simple Langmuir model gives an adsorption rate constant of  $k_{\text{ad}} = 209 \text{ s}^{-1} \text{ M}^{-1}$ , and a desorption rate constant  $k_{\text{d}} = 1.25 \cdot 10^{-4} \text{ s}^{-1}$ . This would correspond to an equilibrium adsorption constant of  $K_{\text{eq}}^{\text{ad}} = \frac{k_{\text{ad}}}{k_{\text{d}}} = 1.7 \cdot 10^6 \text{ M}^{-1}$ . The double-Langmuir model gives an equilibrium adsorption constant of  $K_{\text{eq}}^{\text{ad}} \approx \frac{k_{\text{ad, strong}}}{k_{\text{d, strong}}} = \frac{703 \text{ s}^{-1} \text{ M}^{-1}}{3.7 \cdot 10^{-5} \text{ s}^{-1}} = 1.9 \cdot 10^7 \text{ M}^{-1}$  for Z907 when starting from a tBuOH:MeCN mixture. The latter value is almost four times as high as the value obtained by the Langmuir fit to the adsorption isotherm  $K_{\text{eq}}^{\text{ad}} = 5.1 \cdot 10^6 \text{ M}^{-1}$  presented in the previous section 1.1 and reference [42].

For comparison, Gusak et al. [37] estimated an adsorption rate constant of  $k_{\text{ad}} = 1384 \text{ s}^{-1} \text{ M}^{-1}$  and a desorption rate constant of  $k_{\text{d}} = 3.2 \cdot 10^{-4} \text{ s}^{-1}$ , based on a simplified Langmuir adsorption model. Gusak et al. estimate an equilibrium adsorption constant of  $K_{\text{eq}}^{\text{ad}} = 4.3 \cdot 10^6 \text{ M}^{-1}$  from the kinetic measurement, but  $K_{\text{eq}}^{\text{ad}} = 1.6 \cdot 10^6 \text{ M}^{-1}$  when fitting a Langmuir adsorption isotherm to their concentration dependent measurement at equilibrium [37].



A Langmuir analysis of the Z907 adsorption isotherm yields a saturation value which corresponds to a number density of 0.76 molecules per  $\text{nm}^2$  at full monolayer coverage. The isotherm furthermore gives an equilibrium adsorption constant of  $K_{\text{eq,Z907}} = 5.1 \cdot 10^6 \text{M}^{-1}$ , which is much two orders of magnitude higher than literature values for ruthenium dyes which were obtained on mesoporous films [30, 32]. This high equilibrium adsorption constant was confirmed by adsorption and desorption rate constants from the kinetics of dye uptake, and it corresponds well to more recent investigations by Gusak et al., studying dye uptake on flat  $\text{TiO}_2$  films. My measurements on adsorption and desorption kinetics further indicate, that a single Langmuir adsorption mechanism is too simplistic to describe the dye adsorption.

I think that the lower equilibrium adsorption constant on mesoporous films is due to the fact that dye molecules occasionally desorb from the  $\text{TiO}_2$  and thereby can create a high local dye concentration in the solution inside the pores of the film. This in turn inhibits diffusion of dye molecules from the overlying bulk solution into the mesoporous film if the concentration in the bulk solution is too low. The inhibition will depend on the absolute internal surface area that is already covered with dye, thus the absolute film thickness, and pore size. After an initial, fast staining of the bare  $\text{TiO}_2$  in the upper part of a thick mesoporous film, further infiltration can be inhibited significantly.

This difference between flat and mesoporous films also highlights the importance of studying flat metal oxide films as a model system in order to clearly separate the diffusion process inside the mesoporous film from the actual adsorption process.

The findings that a single Langmuir adsorption process does describe the data only in an approximate way, and that repetitive staining and rinsing cycles slightly increase the dye uptake, points to reorganization phenomena within the molecular film. The latter may have implications for the staining process of dye sensitized solar cells, and repetitive staining and rinsing cycles may allow to reduce the overall staining time significantly, which is important for industrial processing.

Most of results presented in this chapter could have equally been carried out using optical techniques. In the next section, we will extend the measurements to a system of dye and coadsorbates, where the coadsorbate is not directly accessible by optical techniques, so we can make use of the unique advantage of the QCM-D technique, that enables us to track mass changes with a sub-monolayer resolution on a flat metal oxide film.

In order to gain a better understanding of the morphology of the adsorbed film, direct microscopic studies are indispensable. In chapter 3, I show the results of a collaboration with K. Voitchovski and F. Stellacci who performed atomic force microscopy in liquid phase, which provides for complementary, qualitative in-situ information. High-resolution imaging resolve changes in the film morphology at different mass coverage of the surface, and the measurements confirm the presence of a dye monolayer at full coverage.



## 2 Coadsorption of chenodeoxycholic acid and various types of donor – $\pi$ -bridge – acceptor dyes

*The content of this chapter has partially been published in the journal PCCP in 2012 [42] and in the SPIE proceedings in 2013 [44].*

### 2.1 Introduction to coadsorbates in dye-sensitized solar cells

All of the recent high-efficiency, dye sensitized cells based on liquid electrolyte do use chenodeoxycholic acid as a coadsorbate, and it is of particular advantage in those that deploy organic dyes in conjunction with a one-electron redox shuttle, e.g. cobalt-based electrolytes. For many organic dyes, chenodeoxycholic acid does in particular improve the photovoltage and the fill factor of the device when compared to the same dye without coadsorbates [58, 90, 133]. However, the mechanism in which it does so is not well understood, and cheno has proven notoriously difficult to detect when coadsorbed with the dye.

Chenodeoxycholic acid will be referred to as cheno throughout this chapter.

Coadsorbates are molecular agents that adsorb with the dye in the molecular film on the TiO<sub>2</sub> surface. Classic examples are decylphosphonic acid (DPA) [123], dioneohexyl *bis* (3,3-dimethylbutyl) phosphinic acid (DINHOP) [121]. Both of them bond strongly to the TiO<sub>2</sub> surface, and they act as molecular insulators. Although they improve the photovoltage of a dye sensitized solar cell, overall performance is often unchanged because they reduce the amount of dye on the TiO<sub>2</sub> significantly and they replace dye molecules, probably due to their stronger binding to the TiO<sub>2</sub>. Cetrimonium bromide (CTAB), a cationic surfactant, has been used for the same purpose, leading to modest improvements in photocurrent and photovoltage [131]. Chenodeoxycholic acid is a bile acid that was first extracted from goose liver, hence the name, and its structure is on display in figure 2.1. Cheno is known to act as a chelating agent in solution, and thus prevents aggregation of molecules in solution. Recent computational studies by Kusama and Sayama [64] suggests that this is also the case for the black dye when in solution with cheno.

Coadsorbates fulfil their role as a molecular insulator by that they hinder the access of the electrolyte to the TiO<sub>2</sub> surface, and thereby block a major recombination pathway. In the

## Chapter 2. Coadsorption of chenodeoxycholic acid and various types of donor – $\pi$ -bridge – acceptor dyes

---

case of DPA, DINHOP and CTAB, this blocking function can obviously be related to their hydrophobic alkyl chains. Cheno, however, does not have any alkyl chains, but still effectively blocks access of the redox couple to the surface when coadsorbed with the dye.

Detection and quantification of coadsorbates in the adsorbed molecular layer is difficult, because many important coadsorbates only absorb light in the UV, and their FTIR fingerprints overlap with those of the dye. Especially chenodeoxycholic acid (cheno) has proven notoriously difficult to quantify when adsorbed on  $\text{TiO}_2$ . Marinando et al. [72] did a study to deduce the molecular arrangement of a triphenylamine dye and different coadsorbates on the surface, using photoelectron spectroscopy. They had great success for DPA and DINHOP, but their data for cheno proved difficult to interpret due to the missing elemental contrast.

Although it is evident from previous experiments that cheno does reduce the amount of dye adsorbed on the  $\text{TiO}_2$  surface, it has never been measured how much cheno is actually adsorbed in the molecular film on the surface.

I developed a method to quantify the ratio between cheno and dye molecules when coadsorbed on the  $\text{TiO}_2$ , using a combination of QCM-D and subsequent fluorescence spectroscopy. The strength of the QCM-D technique lies in measuring mass uptake of both, dye and coadsorbate, on a flat  $\text{TiO}_2$ . Subsequently, the dye is desorbed from the QCM-D sensor and quantified by an optical measurement of an adequate sensitivity, for example fluorescence emission spectroscopy.

I demonstrate this method using the example of the coadsorption of the triphenylamine dye Y123 with chenodeoxycholic acid, and then apply it to porphyrin dye YD2-o-C8, ullazine dye JD21 and diketopyrrolopyrrole dye DPP17. This will illustrate that the effect of cheno depends on its interaction with the dye. The structures of all compounds are displayed in figure 2.1.

## 2.2 Chenodeoxycholic acid and triphenylamine dye Y123

### 2.2.1 Experimental procedure

**QCM-D measurements** QCM-D measurements were performed on flat, compact  $\text{TiO}_2$  films that were deposited by atomic layer deposition, in the same way as described in the introduction and the previous chapter 1.1.

**Fluorescence emission spectroscopy** In order to quantify the amount of dye on the sensor after the QCM-D measurement, a complementary, optical measurement was made by fluorescence emission spectroscopy. Therefore, the stained sensor was removed from the QCM-D chamber after the QCM-D measurement, then rinsed with MeCN to remove possible contaminations from the o-ring, and subsequently immersed in a known quantity of 0.1 M tetrabutylammonium hydroxide (TBAOH) in *N,N*-dimethylformamide (DMF) for 10 min in order to desorb the dye from the  $\text{TiO}_2$  surface.

## 2.2. Chenodeoxycholic acid and triphenylamine dye Y123

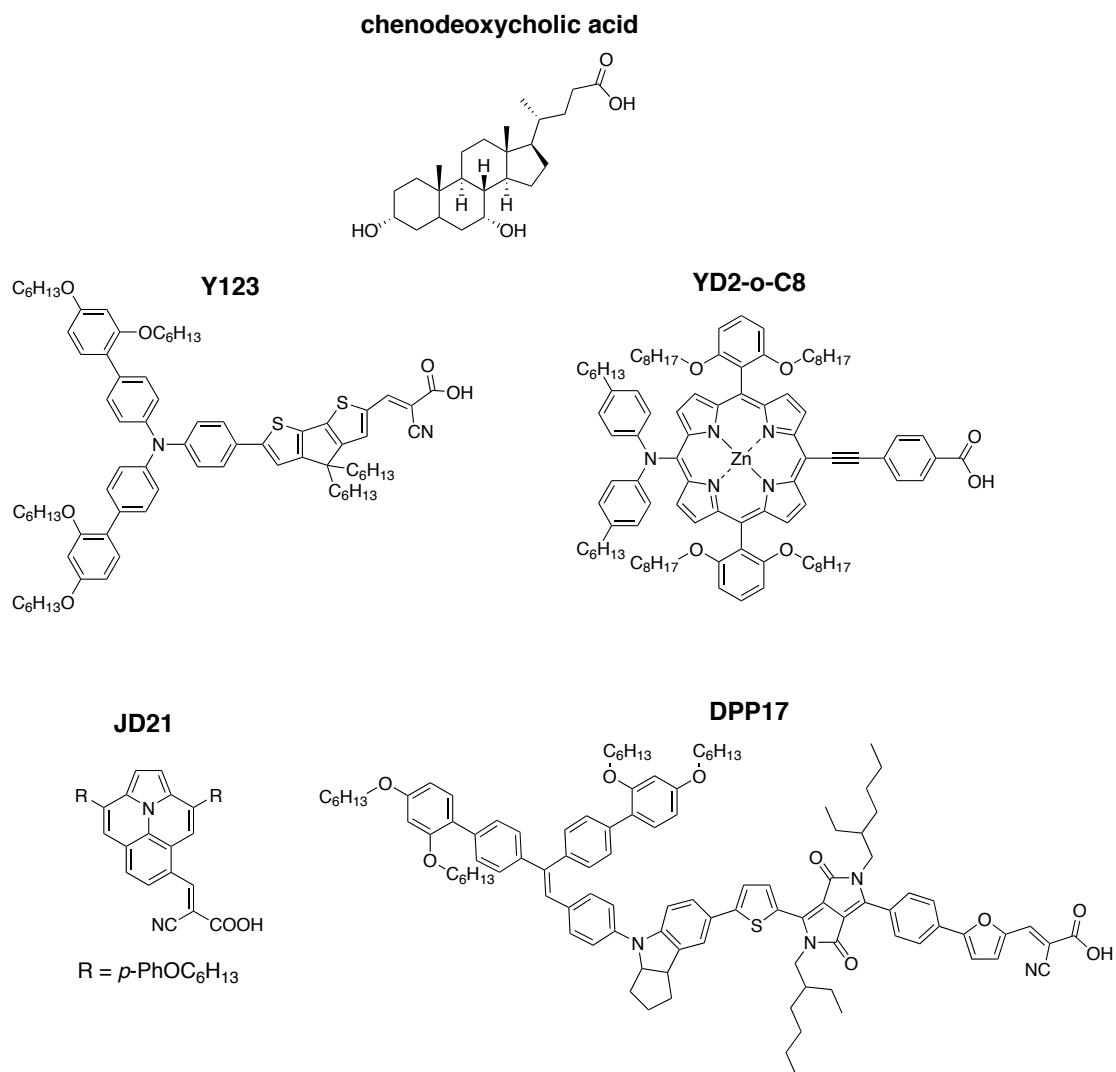


Figure 2.1 – Structures of the different compounds investigated in this chapter: coadsorbate chenodeoxycholic acid, triphenylamine dye Y123, porphyrin dye YD2-o-C8, ullazine dye JD21 and diketopyrrolopyrrole dye DPP17.

## Chapter 2. Coadsorption of chenodeoxycholic acid and various types of donor – $\pi$ -bridge – acceptor dyes

---

Steady state fluorescence measurements were carried out using a Horiba Jobin Yvon Fluorolog-3 spectrofluorometer. To ensure comparability, all measurements were carried out using a constant slit width for excitation and emission, corresponding to a spectral width of 5 nm. The displayed fluorescence emission intensity is the spectrally corrected emission in counts per second (CPS) divided by the excitation intensity in ( $\mu A$ ). However, measurements in different chapters of this thesis are not freely comparable with each other due to the occasional maintenance of the machine or a change of the sample holder. I recommend carrying out future experiments using an integrating sphere.

The excitation wavelength was chosen close to the long-wavelength absorption maximum of the basic form of the dye. Special care was taken to carry out the measurement quickly after the staining in the QCM-D, while exposing the sample to minimal ambient light. Unless otherwise mentioned, the fluorescence signals after the exposure to pure dye and after the exposure to dye+cheno were compared directly to each other. The blank was usually negligible against the measured emission intensities. It should be noted that the wavelength of the absorption maximum as well as the according extinction coefficient of the presented dyes strongly depend on the pH of the solution and on the solvent itself [19]. Although cheno may have an effect on the absorption spectrum of the dye, either by dissolving aggregates or by changing the pH of the solution, this effect is probably negligible in the fluorescence measurements presented here. This is supported by the fact, that the emission spectrum in the presented examples is the same with and without cheno, except for its intensity. This makes sense, since the excess of TBAOH in solution will dominate the pH, and shall furthermore dissolve possible dye aggregates efficiently.

### 2.2.2 Cheno and triphenylamine dye Y123

The organic triphenylamine dye Y123 is a leading example for a donor- $\pi$ -bridge-acceptor (D- $\pi$ -A) dye. It shows very good performance when used with a cobalt-based electrolyte, and it is renowned for its extremely high photovoltage of more than 1.0 V [116, 136]. It is the next evolutionary step from the traditional D35 triphenylamine dye that was previously used in conjunction with the cobalt-based redox shuttle [31]. Y123 has a very high extinction coefficient of  $52000 \text{ mol}^{-1} \text{ cm}^{-1}$  (at 532 nm in THF [133]), but it should be noted that the peak of the absorbance as well as the extinction coefficient itself depend strongly on the pH and the optical density of the surrounding medium.

Figure 2.2 (a) shows QCM-D frequency shifts for adsorption of the organic D- $\pi$ -A dye Y123 only (green line) and for coadsorption of Y123+cheno (red line), as well as the signal from cheno only (dashed blue line). The reference solvent was pure acetonitrile, and the solvent for dye and coadsorbate was a mixture of *tert*-butanol (tBuOH) and acetonitrile (MeCN) in a (1:1)<sub>vol</sub> mixture. Concentrations were chosen in analogy to staining recipes for high-efficiency photovoltaic devices, with the Y123 dye concentration of 0.1 mM and a cheno concentration of 5.0 mM [136, 133].

## 2.2. Chenodeoxycholic acid and triphenylamine dye Y123

For the exposure of TiO<sub>2</sub> to Y123, green line in figure 2.2, a fast adsorption onto the surface is observed, followed by a quasi-linear frequency shift with a slope of approximately  $-3 \text{ Hz h}^{-1}$  during exposure to the dye solution. Upon rinsing, a slight desorption and a final frequency shift of approximately  $-12.7 \text{ Hz}$  is measured after a second exposure and final rinsing. This final frequency shift corresponds to a mass uptake of  $222 \text{ ng cm}^{-2}$ . Assuming a flat substrate and an effective molecular weight of  $MW_{\text{Y123}} - MW_{\text{MeCN}} = 1196 \text{ g mol}^{-1}$ , a coverage of  $1.86 \cdot 10^{-10} \text{ mol cm}^{-2}$  is calculated. This corresponds a number density of  $1.1 \text{ molecules per nm}^2$ . The dashed blue line is the QCM-D measurement during exposure to a solution of  $5 \text{ mM}$  cheno in tBuOH:MeCN solution, without any dye in solution. This measurement is important in that it shows that chenodeoxycholic acid itself can permanently adsorb on the TiO<sub>2</sub> surface. During exposure, a moderate linear frequency shift of about  $-1 \text{ Hz h}^{-1}$  is observed, but the value upon rinsing with the reference solution is constant and yields a final frequency shift of  $-3.5 \text{ Hz}$ . Using an effective molecular weight of  $MW_{\text{cheno}} - MW_{\text{MeCN}} = 352 \text{ g mol}^{-1}$  we obtain a coverage of  $1.74 \cdot 10^{-10} \text{ mol cm}^{-2}$ .

The red line in figure 2.2 shows the coadsorption of  $0.1 \text{ mM}$  Y123 and  $5 \text{ mM}$  cheno. During exposure to Y123+cheno (red line), we observe a shift with a steep linear slope of approximately  $-12 \text{ Hz h}^{-1}$ . Upon rinsing with the reference solution, considerable desorption from the film can be observed, but the frequency shift seems to approach a constant final value. The second exposure shows a similar trend with a measured absolute frequency shift of  $-15.0 \text{ Hz}$  after rinsing for  $80 \text{ min}$ .

Interestingly, the pronounced negative linear slopes observed during exposure are mirrored by linear increases in dissipation (figure 2.3), indicating the build-up of a viscous multilayer. However, mass loss during rinsing is found to be of the same magnitude as the linear mass uptake during exposure. This desorption is accompanied by an analogous decrease of dissipation, reaching its initial zero-value after  $80 \text{ min}$  of rinsing ( $\Delta D = 0.4 \cdot 10^{-6}$  for Y123 and  $\Delta D = 0.7 \cdot 10^{-6}$  for Y123+cheno). Thus, we can confidently assume that we have a thin rigid film and use the Sauerbrey equation to quantify the mass uptake.

The final QCM-D frequency shift after the adsorption of Y123 dye was  $-12.7 \text{ Hz}$ , and after coadsorption of Y123+cheno the final frequency shift was  $-15.0 \text{ Hz}$ , as shown in figure 2.2 (a). For further analysis, Y123 and Y123+cheno were desorbed from the sensors after the QCM-D measurement, and their fluorescence emission intensities were compared, as shown in figure 2.2 (b). For the Y123+cheno sample, fluorescence is decreased by  $24\%$  compared to the sample that had Y123 only adsorbed. Thus, it can be inferred that cheno reduces the Y123 surface concentration by the same percentage. Since both, Y123 and cheno can bind to the surface via one carboxylic acid, it is plausible if coadsorption results in a decrease in dye uptake, and this has been observed in numerous examples [72]. The decrease of fluorescence emission intensity can be taken into account for interpreting the QCM-D frequency shift that represents mass uptake. The QCM-D frequency shift for the pure Y123 measurement is  $-12.7 \text{ Hz}$ ; for coadsorption of Y123+cheno, the dye loading is  $24\%$  lower, according to the fluorescence measurement, which would correspond to a frequency shift of only  $-9.7 \text{ Hz}$  for Y123. This means that of the  $-15.0 \text{ Hz}$  shift measured for Y123+cheno, only  $-9.7 \text{ Hz}$  can be

## Chapter 2. Coadsorption of chenodeoxycholic acid and various types of donor – $\pi$ -bridge – acceptor dyes

---

attributed to Y123, and -5.3 Hz to cheno. Assuming a thin rigid film on a flat surface, this gives a coverage of  $1.42 \cdot 10^{-10}$  mol cm<sup>-2</sup> for Y123 and  $2.63 \cdot 10^{-10}$  mol cm<sup>-2</sup> for cheno, corresponding to a molar ratio of 1:1.7 for Y123 to cheno when both are coadsorbed at the surface.

For clarity, and because it is used as a method throughout this chapter, I explain the above calculus for combining QCM-D and fluorescence intensity explicitly. It is only applicable as long as the dye shows fluorescence at the given excitation wavelength and cheno does not. Further, the Sauerbrey equation needs to hold for the adsorbed layer, so that frequency shift and massuptake are proportional to each other.

The Fluorescence intensity is proportional to the amount of dye that has been in the film. The QCM-D measurement of the dye only  $\Delta f_{\text{dye only}} = -12.7$  Hz is directly proportional to the corresponding fluorescence intensity  $I_{\text{dye only}}$ . The fluorescence intensity after coadsorption  $I_{\text{dye cheno}}$  is decreased by 24%

$$\frac{I_{\text{dye cheno}}}{I_{\text{dye only}}} = 0.76 \quad . \quad (2.1)$$

Thus the dye in the case of coadsorption can only account for a frequency shift of

$$\Delta f_{\text{dye fraction}} = \frac{I_{\text{dye cheno}}}{I_{\text{dye only}}} \cdot \Delta f_{\text{dye only}} = 0.76 \cdot (-12.7 \text{ Hz}) = -9.7 \text{ Hz} \quad , \quad (2.2)$$

and the rest of the frequency shift in the case of coadsorption is attributed to cheno in the adsorbed film:

$$\Delta f_{\text{cheno fraction}} = \Delta f_{\text{dye cheno}} - \Delta f_{\text{dye fraction}} = -15.0 \text{ Hz} - (-9.7 \text{ Hz}) = 5.3 \text{ Hz} \quad . \quad (2.3)$$





## Chapter 2. Coadsorption of chenodeoxycholic acid and various types of donor – $\pi$ -bridge – acceptor dyes

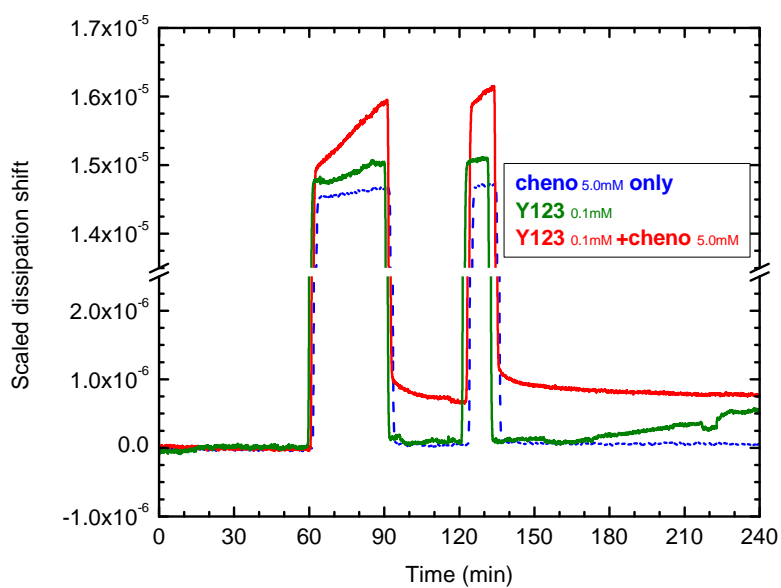


Figure 2.3 – QCM-D scaled dissipation shift upon the adsorption of organic D- $\pi$ -A dye Y123 (0.1 mM) with or without coadsorbate chenodeoxycholic acid (5.0 mM) in tBuOH:MeCN (1:1)<sub>vol</sub> against a MeCN reference.

## 2.3 Coadsorption with porphyrin dye YD2-o-C8, ullazine dye JD21, and diketopyrrolopyrrole dye DPP17

The above principle of measuring the entire mass of the adsorbed film by QCM-D, and subsequently quantifying the amount of dye by fluorescence emission spectroscopy can be applied to any dye that is used with the coadsorbate chenodeoxycholic acid. Here, I present measurements of coadsorption of cheno and dyes that are representative for one type of molecular structure each: the porphyrin dye YD2-o-C8, the ullazine dye JD21, and the diketopyrrolopyrrole dye DPP17. Each of these dyes has been tailored for a different purpose.

The zinc-porphyrin dye YD2-o-C8 is a typical porphyrin dye that was developed to have a broad absorption spectrum and deliver a high photocurrent whilst working with a cobalt-based electrolyte. Coadsorption with the above-mentioned triphenylamine dye Y123 allows to produce record-efficiency solar cells of up to 12.3% efficiency [133]. The ullazine dye JD21 is a fully organic, non-toxic dye of low molecular weight, which provides a viable alternative to ruthenium complexes as sensitizers in iodide-based dye sensitised solar cells. The diketopyrrolopyrrole dye DPP17 is renowned for its aesthetic blue colour, its very high extinction coefficient, and it delivers a good photovoltaic performance.

### 2.3.1 Cheno and porphyrin dye YD2-o-C8

The zinc-porphyrin dye YD2-o-C8 is a typical porphyrin dye for dye-sensitized solar cells. Porphyrin dyes are particularly inspiring, not only because of their broad absorption spectrum, but because of the fact, that their most prevalent natural occurring variant is the manganese-porphyrin chlorophyll, which is the light-absorbing molecule in natural photosynthesis.

In its broad absorption spectrum, YD2-o-C8 has a maximum extinction coefficient in the visible spectrum at 532 nm of  $31200 \text{ mol}^{-1} \text{ cm}^{-1}$  in  $\text{CH}_2\text{Cl}_2$ . However, YD2-o-C8 based devices shown a dip in their ICPE spectrum around 550 nm, and co-sensitisation with the previously discussed triphenylamine dye Y123 leads to efficient light harvesting over the entire visible spectrum, and record-efficiencies of up to 12.3% have been achieved when using a Co(II/III)tris(bipyridyl)-based electrolyte [133]. The porphyrin dye YD2-o-C8 is usually employed with the coadsorbate cheno, and this holds also true for its successor porphyrin dye SM315 that enabled 13% power conversion efficiency [76]. The latter delivers a higher IPCE without any dip over the entire visible spectrum, and does thus not require co-sensitization with a second dye. The structure of YD2-o-C8 is shown in the insert in figure 2.4 (b).

Figure 2.4 (a) shows QCM-D measurements of adsorption of YD2-o-C8 and coadsorption of YD2-o-C8 with cheno on a flat, compact  $\text{TiO}_2$  film. The reference solvent is a mixture of EtOH:THF (4:1)<sub>vol</sub>, and the dye is equally dissolved in a mixture of EtOH:THF, although with a slightly lower fraction of THF due to partial evaporation of the solvent during storage of the dye solution. The nominal concentrations were 0.3 mM YD2-o-C8 and 5.0 mM chenodeoxycholic acid [131].

## Chapter 2. Coadsorption of chenodeoxycholic acid and various types of donor – $\pi$ -bridge – acceptor dyes

---

Figure 2.4 (b) shows the fluorescence emission intensity of the YD2-o-C8 dye that was desorbed from the QCM-D sensor after the measurement in a basic solution of 0.1 M TBAOH in DME.

The final frequency shift (after 60 min rinsing) for YD2-o-C8 ( $MW_{\text{YD2-o-C8}} = 1518 \text{ g mol}^{-1}$ ) only is 3.0 Hz. This gives a Sauerbrey mass of  $52 \text{ ng cm}^{-2}$ , and corresponds to a molar coverage of  $3.43 \cdot 10^{-11} \text{ mol cm}^{-2}$  or 0.2 molecules per  $\text{nm}^2$  under the given conditions.

For coadsorption with cheno, the amount of dye (by fluorescence) decreases to 75% of the initial value. Thus, in the case of coadsorption, only 2.3 Hz of the 4.1 Hz overall shift can be attributed to the dye, whereas 1.8 Hz are attributed to cheno ( $m_{\text{w,cheno}}=393 \text{ g mol}^{-1}$ ). Considering the molecular weight of the adsorbed species and assuming validity of the Sauerbrey relation, we obtain a molar ratio of 1:3 for YD2-o-C8 to cheno when coadsorbed on the surface.

Care needs to be taken when comparing the above results to other experiments. The concentration of the dye and the ratio in the solvent mixture was rather approximate, since it was based on a previously used dye solution because of the scarcity of the pigment at the time of experiment. The concentration is however the same in the solution with and without cheno, so internal comparability is given.

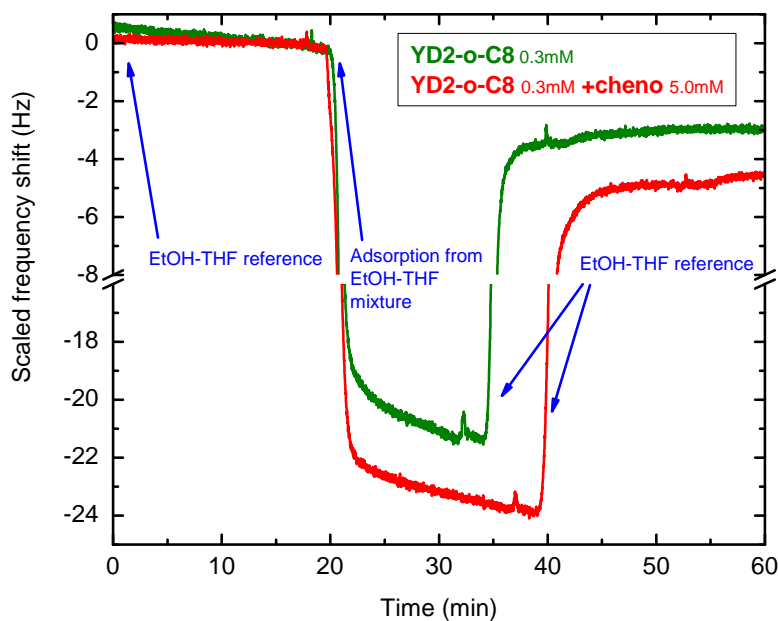
Furthermore, the above measurement employed a mixture of EtOH and THF as a reference. In THF containing solvent mixtures, we regularly observe large linear drifts of the QCM-D signal, which are presumably related to swelling of sealing component by THF, e.g. the o-ring. Moreover, the THF containing solvent mixture may desorb part of the dye during the final rinsing and thereby lead to underestimating the amount of dye adsorbed.

### 2.3.2 Cheno and ullazine dye JD21

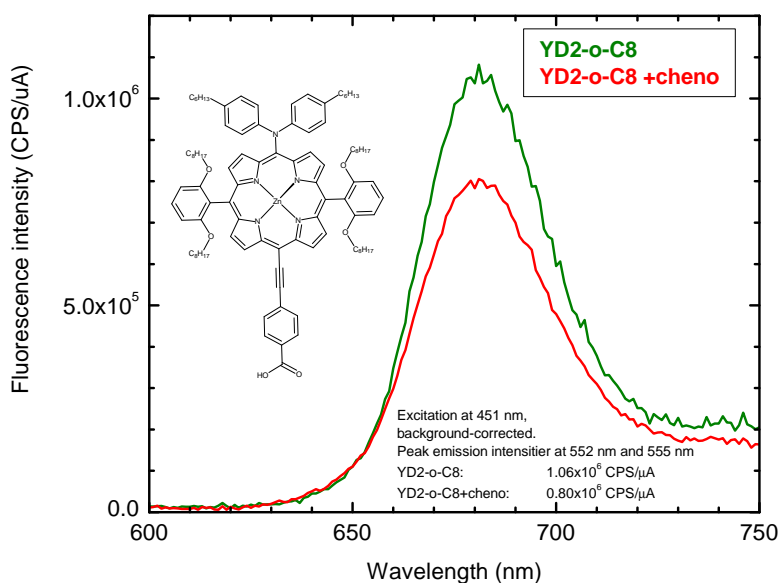
The ullazine dye JD21 was synthesised by Jared Delcamp [19, 24] with the aim of creating a fully organic, non-toxic dye of low molecular weight, with a reasonably good performance. Its structure is shown in the insert in figure 2.5 (b). The ullazine dyes of the JD-series perform well in both, iodide-based and cobalt-based electrolytes, and they offer an important alternative to dyes based on a ruthenium complex. JD21 has an extinction coefficient of  $28000 \text{ mol}^{-1} \text{ cm}^{-1}$  at 582 nm in THF. Although JD21 is often used with the coadsorbate cheno, the influence of cheno on device performance is not as pronounced as with other dyes. Cheno alone without the dye does adsorb on  $\text{TiO}_2$  from the EtOH-THF mixture at 0.4 mM concentration and remains on the surface during subsequent rinsing with EtOH (data not shown).

Figure 2.5 shows the QCM-D frequency shift (a) and fluorescence emission intensity (b) for the ullazine dye JD21 and cheno. Pure EtOH is used as a reference for the QCM-D experiment, and a (4:1)<sub>vol</sub> mixture of EtOH and THF is employed for sensitization with 0.2 mM JD21 and 0.4 mM cheno. The positive frequency shift upon exposure is related to the lower viscosity of the mixture than of pure EtOH. Note that the linear decrease of frequency during exposure is caused not only by the adsorption of species onto the surface, but also by the swelling of the o-ring material around the QCM-D sensor, which leads to strain and may result in a frequency shift. After rinsing with EtOH for 45 min (final value not shown), the staining with

### 2.3. Coadsorption with porphyrin dye YD2-o-C8, ullazine dye JD21, and diketopyrrolopyrrole dye DPP17



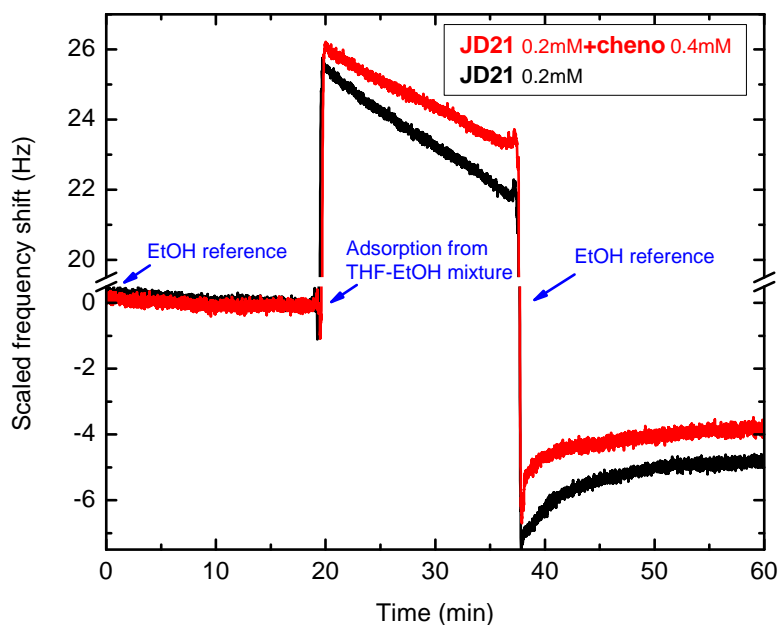
(a) QCM-D frequency shift.



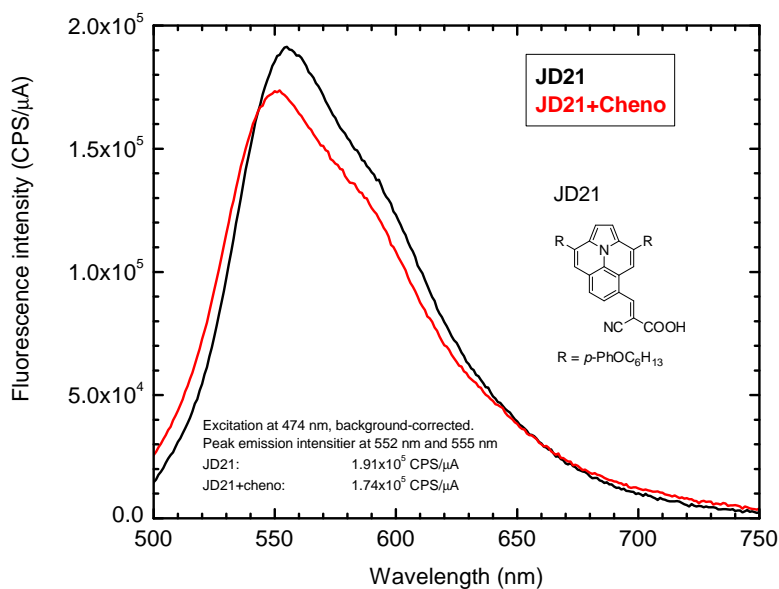
(b) Fluorescence emission intensity.

Figure 2.4 – (a) QCM-D frequency shift after 15 min and 20 min exposure for adsorption of pure YD2-o-C8 and for coadsorption of YD2-o-C8 with cheno, respectively. Porphyrin dye YD2-o-C8 (0.3 mM) with or without coadsorbate chenodeoxycholic acid (5.0 mM) in EtOH-THF (4:1)<sub>vol</sub> against a reference of EtOH-THF (4:1)<sub>vol</sub>. (b) Fluorescence emission intensity after desorbing the dye from the QCM-D sensor.

**Chapter 2. Coadsorption of chenodeoxycholic acid and various types of donor –  $\pi$ -bridge – acceptor dyes**



(a) QCM-D frequency shift.



(b) Fluorescence emission intensity.

Figure 2.5 – (a) QCM-D frequency shift after 15 min exposure. Adsorption of ullazine dye JD21 (0.2 mM) with or without coadsorbate chenodeoxycholic acid (0.4 mM) in EtOH:THF (4:1)<sub>vol</sub> against an EtOH reference. (b) Fluorescence emission intensity after desorbing the dye from the QCM-D sensor.

### 2.3. Coadsorption with porphyrin dye YD2-o-C8, ullazine dye JD21, and diketopyrrolopyrrole dye DPP17

JD21 only produces a frequency shift of  $-4.4$  Hz, and JD21+cheno leads to a frequency shift of  $-3.7$  Hz. Assuming this frequency shift is mainly due to mass uptake, the mass uptake in the case of JD21+cheno is only 85% of the mass uptake in the case of plain JD21. Desorption of the dye from the sensor after the QCM-D experiment, and quantification by fluorescence (figure 2.5 (b)) reveal that the dye in the case of JD21+Cheno has diminished to 90% of the value for adsorption of JD21 only. In the current setting, the relative error of each, the QCM-D and the fluorescence measurement, is approximately 5%. The data in figure 2.5 therefore indicates that upon exposure to 0.2 mM JD21 +0.4 mM cheno, no cheno is permanently adsorbed on the TiO<sub>2</sub> surface, but dye only. Furthermore, the amount of dye on the flat film is reduced by 10 to 15 percent when compared to adsorption from a solution of JD21 without cheno. The latter suggests a better solubility of the dye in the solvent mixture containing cheno than in the solvent mixture without cheno. The fact that the cosensitization with cheno and JD21 still gives better photovoltaic performance than the sensitization with JD21 only may thus be related to the chelating effect of cheno, which is known to prevent dye aggregation on the TiO<sub>2</sub> surface and in solution.

JD21 produces a frequency shift of  $-4.4$  Hz and has a molecular weight of  $m_{wJD21} = 638 \text{ g mol}^{-1}$ . The frequency shift gives a Sauerbrey mass of  $77 \text{ ng cm}^{-2}$  and corresponds to a molar coverage of  $1.21 \cdot 10^{-10} \text{ mol cm}^{-2}$  or 0.73 molecules per  $\text{nm}^2$  under the given conditions.

The finding that no cheno remains adsorbed in the molecular film on the surface is not necessarily a result of competitive adsorption alone. The next example of the dye DPP17 uses large concentrations of cheno and low dye concentrations, but we still find a result very similar to the one for JD21.

Again, the above measurements need to be interpreted with care, because JD21 has a tendency to aggregate if the EtOH content in the solvent mixture of EtOH:THF (4:1)<sub>vol</sub> increases. The aggregation will change the dye loading of the film. An increase in EtOH content can for example occur by evaporation of THF which has a lower vapor pressure than EtOH. Furthermore, there are indications that in the current concentration range, dye loading of the film changes strongly with the concentration of the dye in solution, i.e. the current concentration is considerably lower than the concentration at which a Langmuir-saturation is reached, see chapter 4.2.1.

#### 2.3.3 Cheno and diketopyrrolopyrrole dye DPP17

The diketopyrrolopyrrole dye DPP17 is renowned for its aesthetic blue colour, in conjunction with its relatively good performance, delivering energy conversion efficiencies of up to 10% [137]. It has a very high extinction coefficient of  $69000 \text{ mol}^{-1} \text{ cm}^{-1}$  at 602 nm in CH<sub>2</sub>Cl<sub>2</sub>. The structure of DPP17 is shown in the insert in figure 2.6 (b). The dye DPP17 has a tendency to aggregate in its standard staining solvent mixture of EtOH:THF (4:1)<sub>vol</sub>, and for high performance devices, high concentrations of chenodeoxycholic acid as a coadsorbate are used in order to suppress aggregation and to achieve good device performance.

## Chapter 2. Coadsorption of chenodeoxycholic acid and various types of donor – $\pi$ -bridge – acceptor dyes

---

Figure 2.6 (a) shows QCM-D measurements of adsorption of DPP17 and coadsorption of DPP17 with cheno on a flat, compact TiO<sub>2</sub> film. The dye is dissolved in a solvent mixture of EtOH:THF (4:1)<sub>vol</sub>, and the reference solvent is pure EtOH. The difference in bulk viscosity between the dye solvent and the reference solvent produces a positive shift in frequency upon exposure to the dye solution. The nominal concentrations were 0.025 mM DPP17 and 2.5 mM chenodeoxycholic acid.

Figure 2.6 (b) shows the fluorescence emission intensity of the DPP17 dye that was desorbed from the QCM-D sensor after the measurement in a basic solution of 0.1 M TBAOH in DMF.

The final frequency shift (after 30 min rinsing) for DPP17 only is –9.3 Hz. This corresponds to a Sauerbrey mass of 163 ng cm<sup>-2</sup>, and corresponds to ( $m_{\text{DPP17}} = 1644 \text{ g mol}^{-1}$ ) a molar coverage of  $0.99 \cdot 10^{-10} \text{ mol cm}^{-2}$  or 0.60 molecules per nm<sup>2</sup> under the given conditions. For coadsorption with cheno, the amount of dye (absorbance) decreases to 85% of the initial value, and the frequency shift is –7.5 Hz which is 80% of the initial frequency shift (–9.3 Hz for DPP17 only). Thus the mass uptake measured by QCM-D, and the dye uptake measured by fluorescence do match within an error margin of 5%.

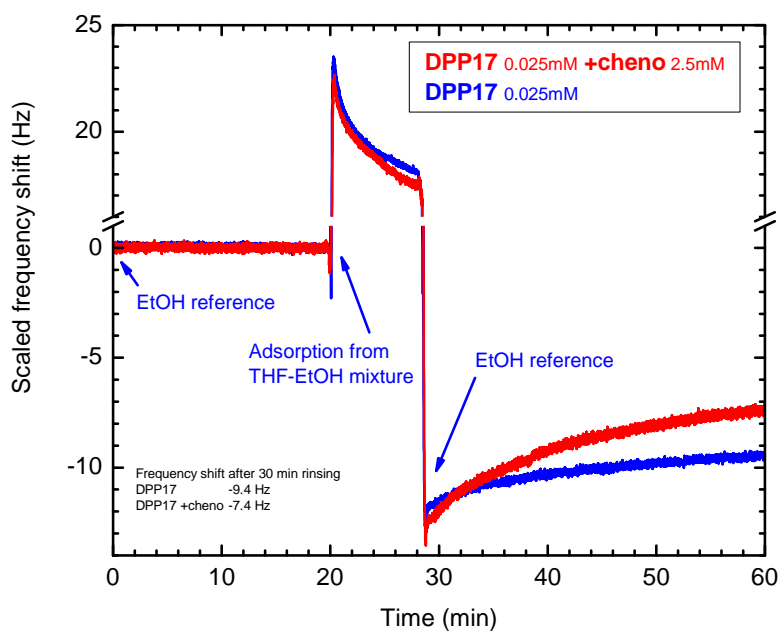
Under the current conditions, we have no indication for cheno being permanently adsorbed on the surface. However, the presence of cheno does reduce the amount of dye adsorbed on the TiO<sub>2</sub> surface.

The amount of dye was not measured by fluorescence spectroscopy after desorption from the QCM-D sensor, because the strong base TBAOH of the desorbing solution leads to fragmentation of the dye, presumably attacking the indole group. The resulting fragment had a fluorescence yield that was too low for detection of a desorbed monolayer. Thus, control samples were fabricated using 2.4  $\mu\text{m}$  thick mesoporous TiO<sub>2</sub> films that were stained in the corresponding solutions for 10 hours. The dye was subsequently desorbed using 0.1 M TBAOH in DMF, and the amount of resulting dye fragments was quantified by absorbance spectroscopy.

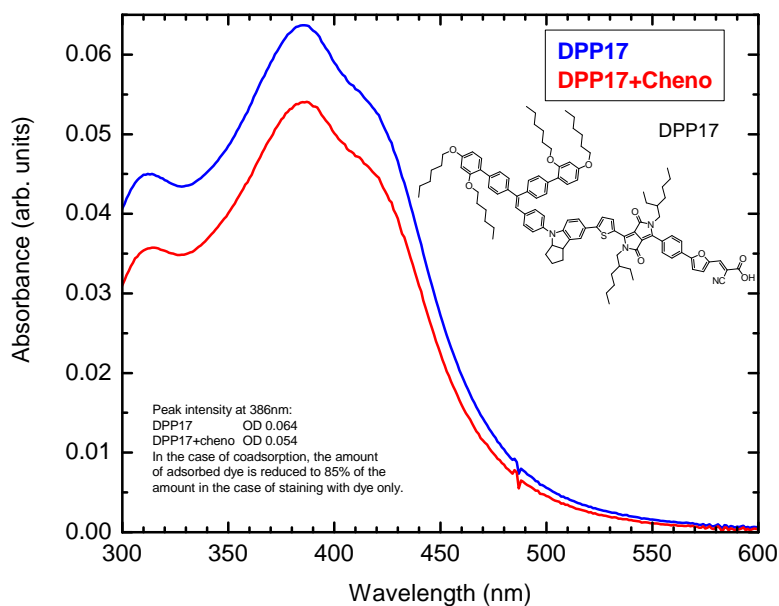
Cheno does not remain adsorbed in the molecular film, but reduces the amount of DPP17 dye on the surface, whilst still improving device performance significantly. These three factors indicate that in the case of DPP17, cheno plays a major role in preventing aggregation of the dye molecules on the surface.



### 2.3. Coadsorption with porphyrin dye YD2-o-C8, ullazine dye JD21, and diketopyrrolopyrrole dye DPP17



(a) QCM-D frequency shift.



(b) Absorbance of desorbed dye solution.

Figure 2.6 – (a) QCM-D frequency shift after 10 min exposure. Adsorption of diketopyrrolopyrrole dye DPP17 (0.025 mM) with or without co-adsorbate chenodeoxycholic acid (2.5 mM) in EtOH:THF (4:1)<sub>vol</sub> against an EtOH reference. (b) Absorbance after desorbing the dye from a set of control samples of 2.4  $\mu\text{m}$  thick mesoporous  $\text{TiO}_2$ . The strongly basic desorbing solution (0.1 M TBAOH in DMF) has apparently fragmented the dye molecule.

## **2.4 Conclusion**

The mechanism by which cheno affects device performance is different for different dyes. If cheno is coadsorbed with triphenylamine dye Y123 or porphyrin dye YD2-o-C8, cheno remains in the adsorbed molecular layer on the surface. In the case of coadsorption with ullazine dye JD21 or with diketopyrrolopyrrole dye DPP17, the above measurements suggest that there is no cheno remaining in the adsorbed molecular layer. The latter measurements correspond largely to the observation that Hayase et al. [46] have made for the coadsorption of chenodeoxycholic acid and the black dye ruthenium complex. All of the measurements show a decrease of dye uptake upon coadsorption with chenodeoxycholic acid, and this corresponds well to general experimental observation [72], that cheno does decrease the dye uptake, but improves device performance in most cases.

In those cases where cheno stays adsorbed in the molecular layer at the surface, it will effectively block access of the redox shuttle to the TiO<sub>2</sub> surface and thereby suppress this recombination pathway. Thus, cheno will increase the photovoltage and decrease the dark current of the device.

In all cases in that cheno works as a chelating agent that prevents aggregation in solution, it will help fast and homogenous infiltration of the mesoporous TiO<sub>2</sub> film. Preventing dye aggregation on the surface, it will improve injection of electrons and regeneration of the dye, and thereby cheno will improve the fill factor and the photocurrent of the device. Dye regeneration is not only improved by the better accessibility of oxidized dye molecules in the monolayer for the electrolyte, but also because aggregates can block pores and thereby hinder diffusion of bulky redox mediators like the Co<sup>II/III</sup> shuttle to part of the mesoporous network.

The findings indicate that the role of chenodeoxycholic acid is dominated mainly by the interaction between the dye and cheno, and only to a lesser extent by the interaction between cheno and the TiO<sub>2</sub> surface. Although we have shown (figure 2.2 (a)) that cheno by itself does permanently adsorb on the TiO<sub>2</sub> surface, it would be in competition with adsorption of the dye in the case of coadsorption. We have not measured the equilibrium adsorption constants for cheno and dye in the relevant solvent mixture, but we can assume that the equilibrium adsorption constant of cheno is much lower than that of the dye, because it has a higher solubility than the dye in the solvent mixture.

As a bile acid, cheno is generally known for its function as a chelating agent, and thereby can prevent aggregation of large molecules, in particular fatty acids, in solution and on the surface. This would in turn increase the solubility of the dye in solution, and thereby facilitate its desorption from the surface.

In the case where cheno stays coadsorbed with the dye (Y123 or YD2-o-c8) on the surface, the QCM-D data for Y123+cheno indicates a continuous built-up of a viscous layer on the surface during exposure to the dye-cheno solution. In the case of dye and cheno, most of the viscous layer is desorbed during subsequent rinsing, until only a thin layer remains permanently adsorbed. Nevertheless, the adsorption behaviour during continuous exposure to dye-cheno solution suggests that the dye and the chenodeoxycholic acid form a molecular adsorbed layer,

in which cheno is not necessarily directly bound to the TiO<sub>2</sub> surface, but associated with the dye molecule, for example by H-bonding.

For future experiments, the drift in the solvent mixture is a major technical issue that needs to be resolved for reliable measurements. Then, interesting topics can be addressed, i.e. adsorption isotherms of both, dye and cheno in order to address a possible competitive adsorption. Moreover, it is important to consider that the above measurements have been carried out against a pure solvent baseline. The presence of an electrolyte should have a strong influence on the possible H-bonding between the dye and cheno. Furthermore, the above interpretations assume that the adsorbed molecular film is laterally homogeneous. This should be verified by direct microscopic techniques.

The presented measurements are of preliminary nature and need further confirmation. However, they illustrate that the role of cheno depends on its specific interaction with the dye molecule, and that it can remain in the molecular layer adsorbed on the TiO<sub>2</sub> surface.



# 3 Microscopic characterization of amphiphilic ruthenium complexes adsorbed on anatase titanium dioxide

*This work is based on a collaboration with Kislou Votchkovskiy<sup>1</sup> in the SUNMIL of Francesco Stellacci, EPFL, and Negar A. Ashari in the Laboratory of Computational Biochemistry and Chemistry of Ursula Röthlisberger, EPFL. The content is based on an advanced manuscript that will soon be submitted for publication [60].*

## 3.1 Introduction to direct microscopic investigation of molecular adsorbate layers

Amphiphilic sensitizers are central to the function of dye-sensitized solar cells. It is known that the cell's performance depends on the molecular arrangement and the density of the dye at its surface, but a molecular-level picture of the cell-electrolyte interface is still lacking. Here, we present sub-nanometer in-situ atomic force microscopy images of the Z907 dye at the surface of TiO<sub>2</sub> in a relevant liquid. Our results reveal changes in the conformation and the lateral arrangement of the dye molecules, depending on their average packing density on the surface. Complementary quantitative measurements on the ensemble of the film are obtained by a quartz-crystal microbalance with dissipation technique. An atomistic picture of the dye coverage-dependent packing, the effectiveness of the hydrophobic alkyl chains as blocking layer and the solvent accessibility is obtained from molecular dynamics simulations.

Beyond light harvesting, the molecular dye film has also a secondary function: it must act as an electronic barrier that prevents the electron photoinjected in the semiconductor to recombine with the oxidized form of the redox mediator present in the electrolyte. For typical dye molecules, this is ensured by hydrophobic alkyl chains that hinder the redox-mediator from accessing the semiconductor surface, and prevent lateral aggregation of dye molecules. The anchoring groups of the dye, usually carboxylic acids, are hydrophilic, which gives the dye an amphiphilic character and behaviour often similar to anionic surfactants. The DSC macroscopic efficiency is known to depend on both the molecular arrangement of the ad-

---

<sup>1</sup>New affiliation of K. V. since September 2013: Lecturer at the University of Durham, United Kingdom.

### **Chapter 3. Microscopic characterization of amphiphilic ruthenium complexes adsorbed on anatase titanium dioxide**

---

sorbed dye layer and the contacting electrolyte (ref). This is generally true for most surfaces functionalized with self-assembled monolayers, which requires linking in-situ molecular-level details with macroscopic observations in order to derive a full understanding[63].

Practically, gaining in-situ information about the molecular arrangement of SAM often proves challenging. Fourier transform infrared spectroscopy [33, 105] was successfully used to observe the binding of dye molecules to the surface DSCs. The average orientation of adsorbed molecules relative to the surface could be derived from combined near-edge x-ray absorption fine structure spectroscopy (NEXAFS) and photoelectron spectroscopy (PES) [135, 72, 97]. However, the irregular mesoporous titania surface prevents averaging techniques from capturing local molecular details. Scanning probe techniques can in principle overcome this difficulty and provide direct, local information about the adsorbed layer. Scanning tunnelling microscopy studies in ultra-high vacuum achieved the first sub-molecular resolution images of the dye layer, but the measurements were conducted far from the functional conditions of a DSC [102]. Recently, C. Kley et al. have achieved impressive resolution for imaging and spectroscopy of adsorbed N3 dye molecules on the (101) anatase surface [61]. Ex-situ atomic force microscopy (AFM) results indicated the existence of large dye aggregates on the flat TiO<sub>2</sub> substrate [73] for standard device preparation procedure, but molecular resolution was not achieved.

Recently developments in the field of AFM have made it possible to achieve sub-nanometer mapping of soft and hard surfaces in solution [119] paving the way for in-situ local observations of a functional DSC's surface.

Here we report in situ molecular-level AFM images of adsorbed dye molecules at the surface of mesoporous and flat TiO<sub>2</sub> surface in a device-relevant liquid. We used the amphiphilic ruthenium complex Z907 dye (insert in figure 3.2) due to its wide-spread use in DSCs [138], its good performance in long-term stability tests [124], and the fact that it is less prone to aggregation than other dyes. The AFM study is conducted with the sample fully immersed either in ethyl-isopropyl sulfone (EiPS), or acetonitrile (MeCN), both solvents being used for sensitization of TiO<sub>2</sub> surfaces in functional DSCs. We show that under normal conditions, the dye forms a single monolayer over the surface. The molecular conformation of the dye depends on the density coverage with domains of different molecular conformation able to coexist [63, 119] within the adsorbed sub-monolayer. The AFM results are complemented with measurements conducted using the quartz crystal microbalance with dissipation technique (QCM-D) [99, 98, 42] so as to assess the average quantity of adsorbed molecules on the substrate with respect to coverage saturation. The experimental AFM and QCM-D results are confirmed by molecular dynamics (MD) simulations of dyes adsorbed on the (101) facet of anatase TiO<sub>2</sub> immersed in acetonitrile solvent. The simulations provide atomic-level insight into the density-dependent change in the arrangement of the adsorbed Z907 molecules.

#### **3.1.1 Experimental and computational methods**

**AFM** The AFM data were acquired on a commercial Multimode Nanoscope IIIa (Digital Instruments, now Bruker, Santa Barbara, USA) operated in amplitude-modulation. The

### 3.1. Introduction to direct microscopic investigation of molecular adsorbate layers

---

sample and the scanning tip were fully immersed into the imaging liquid (ethyl iso-propyl sulfone (EiPS), or acetonitrile (MeCN)). Before each experiment, the liquid cell was thoroughly washed in isopropanol and ultrapure water and subsequently dried with nitrogen. We used standard silicon nitride cantilevers (Olympus RC800 PSA, Olympus, Tokyo) with a nominal stiffness of  $k_n = 0.76 \text{ N m}^{-1}$ . In each experiment the cantilever was driven acoustically with the liquid cell, close to its resonance frequency. Typical imaging amplitudes  $A$  were kept between 0.5 nm and 1.5 nm with the setpoint ratio  $A/A_0$  as large as possible ( $A_0$  is the free vibration amplitude in liquid). When operated in these conditions, the AFM probes mostly the solvation layers of the liquid at the surface of the sample [63, 119] and sub-nanometre resolution images can be routinely achieved. The phase images, acquired simultaneously to the topography, provide information about the local affinity of the liquid to the solid and can be used to calculate the local solid-liquid work of adhesion [63].

**Computational methods** Classical molecular dynamics (MD) simulations were performed for different dye coverage and various packing modes and orientations. The  $\text{TiO}_2$  surface was described by the Bandura Kubicki [5] force field, whereas for the Z907 dye a force field was developed following the AMBER protocol [16]. Classical point charges were derived using the RESP [6] procedure except for the carboxylic anchoring groups, whose charges were chosen in such a way as to reproduce the experimental adsorption energy [112]. The force field was validated via full ab initio simulations of a single dye in vacuum. A united atom OPLS force field was employed for acetonitrile [53].

Experimental and computational studies have suggested different binding modes for Z907 and similar dyes [33, 93, 34, 95]. Initial tests showed that the different binding modes (dissociative, bidentate, or monodentate) hardly affect the space occupied by each dye and hence have little influence on the overall packing geometries. For all studies presented here, we thus have adopted a single, non-dissociative bidentate binding mode (figure 3.6). Initial models of the system composed of two layers of anatase  $\text{TiO}_2$   $108 \times 113 \text{ \AA}^2$  for low and medium coverages and  $54 \times 56 \text{ \AA}^2$  for high coverage) were constructed using Materials Studio [Accelrys Software Inc., Discovery Studio Modeling Environment, Release 4.0, San Diego: Accelrys Software Inc., 2013]. Molecular dynamics simulations were performed with the Amber12 package [13] using the PMEMD module. Production runs of about 20 ns in the NVE ensemble were sampled after initial minimization and 5 ns of equilibration in canonical ensemble using the Nose-Hoover thermostat at room temperature 300 K.

**Sample preparation**  $\text{TiO}_2$  samples for AFM measurements were based on a (100) silicon wafer substrate coated with titanium dioxide by atomic layer deposition from a tetrakis(dimethylamino)titanium (TDMAT) precursor as described previously [114]. The  $\text{TiO}_2$  film of 67 nm thickness was annealed at  $420^\circ\text{C}$  and had a surface roughness of 2.0 nm on a  $4 \mu\text{m}$  AFM frame. X-ray diffraction on the film showed evidence of anatase crystallites but no rutile phase, see general introduction in chapter . The Z907 pigment was dissolved on a 1:1 volumetric mixture of tert-butanol and acetonitrile, and a solution of  $50.0 \mu\text{M}$  concentration was

### Chapter 3. Microscopic characterization of amphiphilic ruthenium complexes adsorbed on anatase titanium dioxide

---

quantified by an absorption measurement using the published [138] extinction coefficient of  $12200 \text{ M}^{-1} \text{ cm}^{-1}$ ; lower concentrations were obtained by dilution.

Prior to staining, the AFM substrates were exposed to UV-ozone for 10 min and heated for 30 min at  $420^\circ\text{C}$  to remove organic residuals and excess water from the  $\text{TiO}_2$  surface. After cooling down to  $70^\circ\text{C}$  they were immersed into the dye solution for 30 min, rinsed in tBuOH:MeCN mixture, immersed in MeCN for 30 min, stained again for 10 min, rinsed in tBuOH:MeCN mixture and MeCN, and subsequently stored in MeCN in the dark.

Samples destined for AFM measurements were usually transferred to EiPS as an imaging liquid. EiPS is a main constituent in non-volatile high-voltage electrolytes that are used in industrial applications of dye sensitized solar cells [129, 14]. EiPS was chosen for its relevance in DSC applications and for its low vapour pressure (compared to MeCN) making it is easier to reach stable imaging conditions at high resolution. Aside from experimental considerations, no differences could be seen in the images obtained in MeCN and EiPS, see figure 3.5.

## 3.2 Local probe by non-contact atomic force microscopy in liquid phase

Figure 3.1 presents a high-resolution image of the sensitized, mesoporous  $\text{TiO}_2$  photoanode of a DSC in a functionally relevant liquid. The measurement, conducted with AFM in EiPS, provides a unique insight into the sub-nanometer details of the device surface and indicates some structure in the dye layer. The dye molecules appear to be arranged along some preferential directions (arrows in the inset) although no long-range order is visible. These result should however be taken cautiously due to the high surface curvature of mesoporous  $\text{TiO}_2$  which renders AFM imaging challenging due to tip-convolution effects. An additional difficulty arise from the fact that dye molecules tend to accumulate primarily in holes and surface groves at intermediate coverage, making a study of the dye molecular arrangement as a function of surface coverage difficult.

To overcome these difficulties, we have used flat  $\text{TiO}_2$  substrates throughout this study. The substrates, obtained by atomic layer deposition, present a sufficiently low roughness on the nanoscale to avoid ambiguous interpretation of the AFM results. For each sample, the actual surface coverage is determined by QCM-D so as to ensure that the local AFM observations reflect global surface properties. The adsorption behaviour of the same Z907- $\text{TiO}_2$  system has previously been studied by using a QCM-D [42], see also chapter 1.1. Figure 3.2 shows the adsorption isotherm for Z907 on flat  $\text{TiO}_2$  films. The figure uses previously published data [42] as a reference for comparison with the current measurements. The isotherm follows a Langmuir-type behaviour (red line), indicating a saturation value of  $103 \text{ ng cm}^{-1}$  area mass uptake over the concentration range on display. This corresponds to  $0.76 \text{ molecules nm}^{-2}$ , or a molecular footprint of  $1.31 \text{ nm}^2$  per molecule when assuming a flat surface. We define this saturation value as 100 % mass coverage, which should correspond to a densely packed monolayer of Z907. For staining the AFM samples, dye concentrations were chosen such that a mass coverage of approximately 30 %, 60 % or 100 % was obtained, green data crosses in



### 3.2. Local probe by non-contact atomic force microscopy in liquid phase

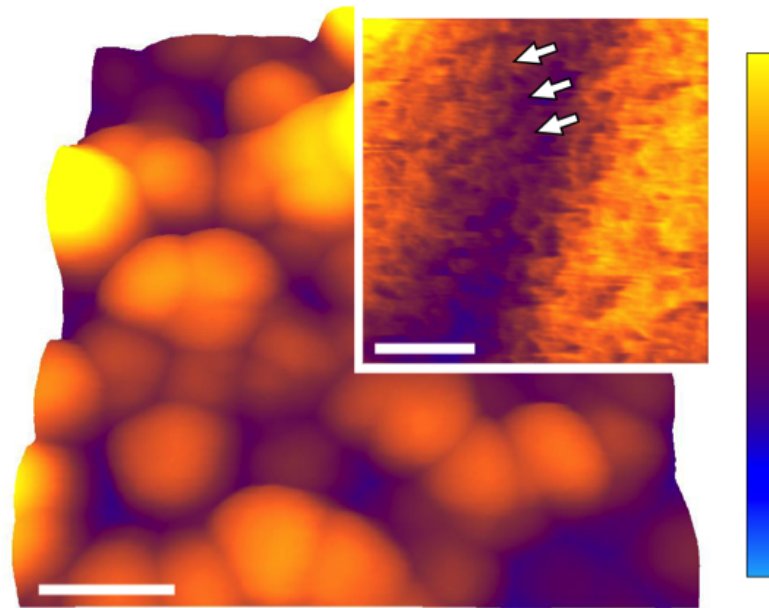


Figure 3.1 – High-resolution AFM image of the surface of a DSC in EiPS solvent. The surface is composed of mesoporous TiO<sub>2</sub> stained with the Z907 ruthenium dye. The TiO<sub>2</sub> nanoparticles are clearly visible in the main image. The inset shows molecular detail of the dye arrangement at the edge of a nanoparticle with some ordering visible (arrows). The scale bars are 40 nm (main image) and 3 nm (inset). The colour scale is 70 nm (main image) and 6 nm (inset).

### Chapter 3. Microscopic characterization of amphiphilic ruthenium complexes adsorbed on anatase titanium dioxide

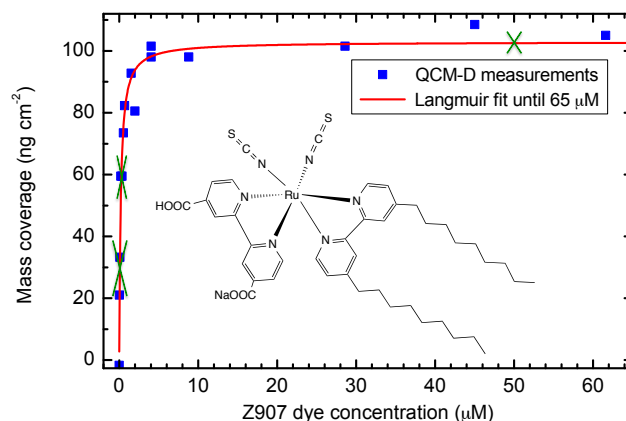


Figure 3.2 – QCM-D area mass uptake over concentration of sensitizing dye solution with fit of a Langmuir isotherm. Blue points are from previous experiments [20]. Green crosses are the dye solutions used for staining the AFM samples. The insert shows the structure of the Z907 ruthenium dye.

figure 3.2.

A representative AFM topographic image of the flat TiO<sub>2</sub> surface after sensitization with dye molecules (50 μM staining solution, 30 % mass coverage) is shown in figure 3.3 a. The image shows large protrusions (20-30 nm wide, and approximately 2 nm high) that are related to the roughness of the TiO<sub>2</sub> substrate. Details of the dye molecules are already visible, appearing as a sub-nanometer, mostly homogeneous roughness on the surface. This is confirmed in higher magnification images of the sample where the dye film appears as homogenous sponge-like structure (inset in figure 3.3 a). Using harsh imaging conditions, it is possible to mechanically remove dye molecules in selected regions by scratching. The scratched region, which corresponds to the TiO<sub>2</sub> substrate, appears darker in the phase image (purple arrow in figure 3.3 b-c). This phase contrast indicates a higher affinity [63, 119] of the solvent for the TiO<sub>2</sub> than for the dye, and could be consistently used throughout this study to identify dye-covered (light) and uncovered (dark) regions. At 30 % mass coverage, the dye layer exhibits dark spots in the phase, suggesting that uniform gaps exist between the adsorbed Z907 molecules. These gaps give the apparent sponge-like appearance to the dye layer topography. The thickness of the dye film is difficult to evaluate directly from figure 3.3 a due to the roughness of the substrate. It is however possible to use the exposed TiO<sub>2</sub> region as a reference. A line profile taken at the edge of the dye layer indicates a thickness of approximately 0.6 nm (figure 3.3 d). This value is a lower estimate of the real thickness due to the mechanical perturbation induced by the AFM tip on the dye molecules during the imaging process.

A closer look at figure 3.3 a reveals occasional variations in height of the dye layer over flat substrate regions (blue arrows). These regions hint to local variations of the Z907 molecular arrangement of the on the substrate surface which could be related to the density of dye

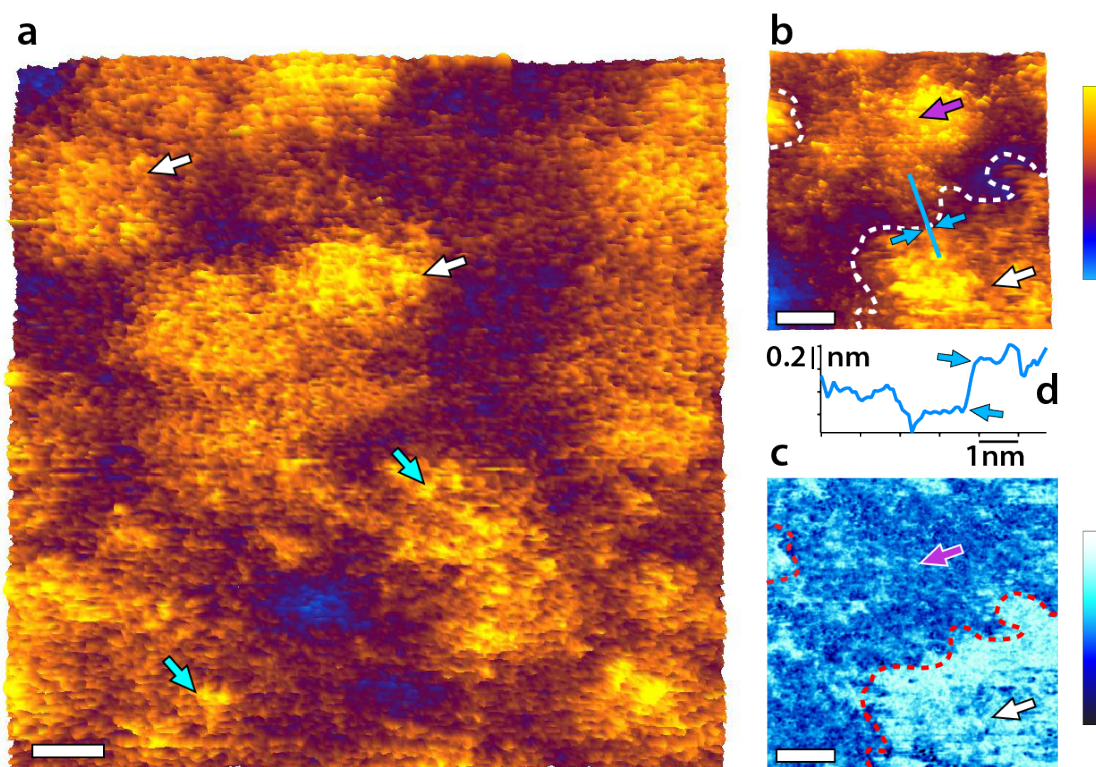


Figure 3.3 – AFM micrographs of a  $\text{TiO}_2$  surface covered with Z907 ruthenium dye (30 % mass coverage). (a) A low magnification (100 nm) topographic image shows almost uniform coverage by the dye apart for a few higher dye domains (blue arrows). The approximately 20 nm wide protrusions (white arrows) are related to the substrate roughness. Higher resolution topographic (b) and phase (d) images of the surface reveal a sponge-like structure of the dye layer (white arrow). Small domains of the  $\text{TiO}_2$  substrate are occasionally exposed (grey arrow) inducing a sharp phase contrast. The substrate can also be exposed by scratching with the AFM tip (d-f) revealing a approximately 0.6 nm dye layer thickness. The topographic images are always represented with an orange-blue color scale and the phase images in blue-black throughout the paper. The scale bars are 10 nm (a) and 3 nm (b,c). The colour bars are 3 nm (a,b) and  $15^\circ$  (c).

### Chapter 3. Microscopic characterization of amphiphilic ruthenium complexes adsorbed on anatase titanium dioxide

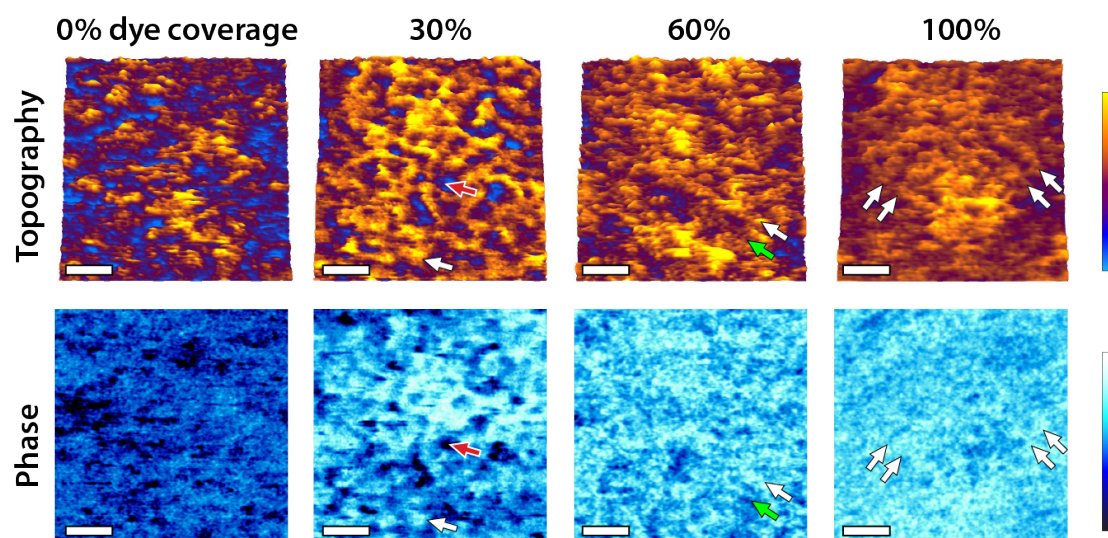


Figure 3.4 – High-resolution AFM images of the dye layer at 0 %, 30 %, 60 % and 100 % mass coverage obtained in similar imaging conditions. At 0 % the substrate appears rough and noisy due to short-range tip-sample attractive interactions. At 30 %, the dye molecules (white arrow) assemble in a soft sponge-like disordered structure that can easily be disrupted by the AFM tip. Multiples holes are visible in the layer (red arrow) and appear darker in the phase. At 60 %, the layer is partially ordered with the apparition of rows (white arrow) and less ordered lower regions (green arrow). At 100 % the surface is fully covered, it appears smooth and only dye rows are visible (white arrows). The scale bar is 2 nm and the colour scales are 1nm (topography) and 15° in all images.

molecules. In order to examine this effect in a systematic manner, we acquired high-resolution AFM images of the dye layer at different mass coverages, as determined by QCM-D. Representative AFM images are presented in figure 3.4 for 0 %, 30 %, 60 % and 100 % mass coverage. A clear trend is visible in both the topography and the phase with the increase of dye coverage. The bare substrate (0 %) appears relatively rough, the image is noisy and provides little phase contrast. At 30 % mass coverage, 1-3 nm wide dye features are visible in both topography and the phase, and form a soft sponge-like layer probably templated by the atomic structure of the TiO<sub>2</sub> substrate. From the phase image, the holes (red arrow) can be attributed to the substrate while the top of the layer is due to dye molecules and appears already more regular and smoother than raw substrate (white arrow). At 60 % mass coverage, the layer is more ordered and appears in an intermediate situation with the dye molecules forming both rows (white arrow) and lower, less ordered regions (green arrow). The fully covered surface appears smooth with little height variations. The whole surface is covered in row-like domains, which are not necessarily aligned (arrows). The phase image becomes consistently brighter as the surface coverage increases, indicating the substrate is fully covered at 100 % mass coverage. Interestingly, the dye molecules always spread over all the space available and never form isolated islands. At 10 % mass coverage, the spreading of the dye molecules prevented non-destructive imaging (not shown).

### 3.2. Local probe by non-contact atomic force microscopy in liquid phase

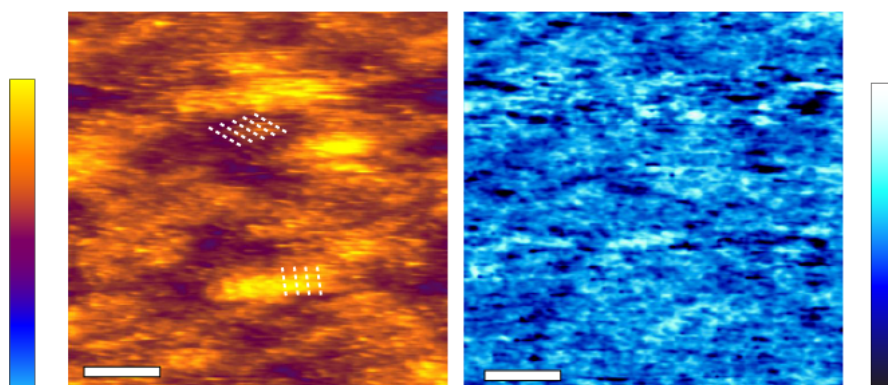


Figure 3.5 – High-resolution AFM image of the Z907 dye layer in acetonitrile. Molecular rows are also visible (indicated with dashed line). Imaging in EiPS was generally preferred for practical reason: the high vapour pressure of acetonitrile favour evaporation and thermal drift in the images. The scale bar is 10 nm. The colour scales are 3 nm (topography) and 15° (phase).

The AFM results suggest a change in the molecular arrangement of the dye molecules on the surface as the dye coverage increases. The coexistence of two height levels at intermediate coverage supports this explanation. The formation of dye rows at higher coverage (also visible in MeCN, see figure 3.5) is consistent with the observations on the mesoporous TiO<sub>2</sub> (figure 3.1) and coincide with an increased layer thickness, suggesting that the Z907 molecules sit with their alkyl chains extended away from the substrate surface when arranged in rows. This interpretation would also explain the increased surface density of dye at higher coverage, especially given the fact that the dye molecules spread over the whole available TiO<sub>2</sub> at all coverage conditions.

### **3.3 Classical molecular mechanics simulations by computing an ensemble of dye molecules adsorbed on anatase titanium dioxide**

To further explore possible conformations of the molecular film on the  $\text{TiO}_2$  surface, N. A. Ashari in the Group of Prof. U. Röthlisberger at EPFL performed molecular dynamics (MD) simulations at different dye densities. 100 % mass coverage was simulated using a density of  $0.76 \text{ molecules nm}^{-2}$  as obtained from QCM-D measurements. The dye molecules were arranged on a crystalline anatase (101)  $\text{TiO}_2$  slab with two layers. Possible binding locations were identified based on geometric arguments: using an approximate distance between the two carboxylate groups of a bipyridine moiety of ca.  $7 \text{ \AA}$  as a gauge, we tried to find adsorbing sites on the substrate with the same distance. Five possible locations were identified (see figure 3.6). The same locations were confirmed by random adsorption simulations where dyes initially located at  $10\text{-}15 \text{ \AA}$  distance from the surface in vacuum were allowed to adsorb randomly during the first nanosecond of the simulation. The random binding sites corresponded to the 5 modes identified using geometrical considerations (figure 3.6). For each binding location, a regular system of 25 dyes adsorbed on the oxide surface was constructed. After minimization, the lowest energy configuration (mode 1 in table 3.1) was chosen for conducting further simulations to study the effect of coverage density on packing.

In order to validate the process, we performed annealing simulation up to 600 K on all 5 systems. As expected, dyes located in the energetically most stable mode 1 arrangement remained at their binding sites, whereas other configurations went through several transitions between different modes, (for configurations with modes 5, 2, and 4) and occasionally detached from the surface (in the case of mode 3). An additional parameter that strongly influences the energetics of the packing is the orientation of the dye. For instance mode 1 (the most stable one), normally pointing the sulfur atoms towards the  $[10\bar{1}]$  direction, can lose its stability by rotating towards the reverse direction and pointing the sulfur atoms backwards, see figure 3.7.

### 3.3. Classical molecular mechanics simulations by computing an ensemble of dye molecules adsorbed on anatase titanium dioxide

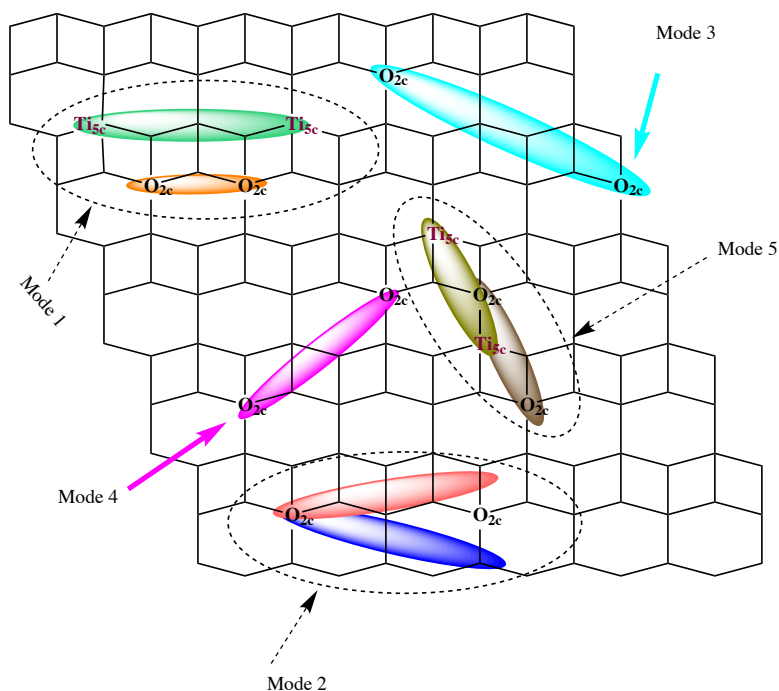


Figure 3.6 – Five possible location modes suitable for anchoring the carboxylate groups of the bipyridine moiety. The Z907 dye always occupies roughly the same (dotted) area in modes 1, 2 and 5, regardless of the selected binding mode inside the ellipse. For mode 1, Z907 in its fully protonated structure can make hydrogen bonds with two 2-fold oxygens ( $O_{2c}$ ). In its deprotonated state, the bipyridine moiety can make bonds to 5-coordinated Ti ( $Ti_{5c}$ ), either way occupying the same space shown in dots. The same holds for mode 5. For mode 2, the bipyridine can be in the salmon-colored ellipse or the blue one, either way making hydrogen bonds to the same two ridge oxygens indicated.

Table 3.1 – Relative energetics for different dye location modes with respect to the most stable mode 1, averaged for a system composed of 25 dyes.

Adsorption mode	Relative energetics ( $\text{kcal mol}^{-1}$ )
Mode 5	48.68
Mode 2	30.76
Mode 3	25.64
Mode 4	15.40
Mode 1	0

### Chapter 3. Microscopic characterization of amphiphilic ruthenium complexes adsorbed on anatase titanium dioxide

---

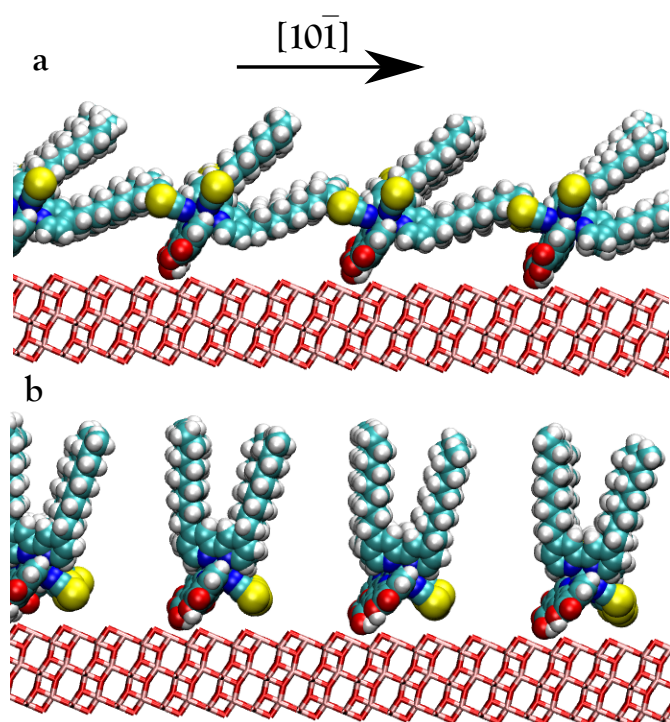


Figure 3.7 – Orientation with respect to the crystal lattice of packing mode 1. (a) Sulfur atoms (shown in yellow color) pointing along the ridge oxygens. This orientation is energetically more favorable. (b) Sulfur atoms pointing along the  $[10\bar{1}]$  direction. This orientation is not energetically favorable.



### 3.3. Classical molecular mechanics simulations by computing an ensemble of dye molecules adsorbed on anatase titanium dioxide

In order to visualize the effect of dye coverage on the conformation of the dye layer, we computed a thermally averaged topographic picture of the system comprising 25 dye molecules after 20 ns of simulation (figure 3.8), comparing 33 % mass coverage ( $0.23 \text{ molecules nm}^{-2}$ ), 66 % ( $0.51 \text{ molecules nm}^{-2}$ ) and 100 % mass coverage ( $0.76 \text{ molecules nm}^{-2}$ ). In order to change the mass coverage in the computations, the size of the  $\text{TiO}_2$  slab was adjusted appropriately while the number of dye molecules was kept constant. At lower densities, the lipophilic alkyl chains (mostly one of the chains) are extended to reach the alkyl chains of neighbouring dyes (figure 3.8). This leads to a configuration where the dyes are packed closer to the surface, i.e. average layer distance of ca.  $8.65 \text{ \AA}$  with an average tilting angle of  $38.66^\circ \pm 10^\circ$  of the alkyl chains with respect to the titanium oxide surface. Figure 3.8 shows that for the 100 % dye coverage the atomic density profile along the  $z$  direction has a shoulder around  $13 \text{ \AA}$  and the probability to find dye atoms (mostly from the alkyl chains) in this range ( $13\text{-}25 \text{ \AA}$ ) is higher than the one of the 33 % mass coverage system (bottom graph in figure 3.8). At higher densities (66 % and 100 %), the alkyl chains of different dyes get entangled and the dyes explore higher heights and stand more upright with an average dye-layer thickness of approximately  $9.00 \text{ \AA}$  and  $10.15 \text{ \AA}$  respectively and an average tilting angle of  $42^\circ$ ,  $55^\circ$  and  $77^\circ \pm 3$  respectively. As the experimental results in this AFM study and in other STM studies [34] suggest, the  $\text{TiO}_2$  surface templates the dye arrangement via the binding mode, and the packing is less driven by dye-dye interactions in terms of energy. AFM nanographs at 60 % mass coverage suggest the possible coexistence of distinct domains of dye molecules with the alkyl chains either pointing away from the surface, or stretched out along the surface. To address this question, we conducted MD calculations at 60 % mass coverage with the dye molecules ( $0.46 \text{ molecules nm}^{-2}$ ) distributed in a homogenous manner (figure 3.9 a,b), versus an arrangement in a non-homogenous manner (figure 3.9 c,d), trying to find the key element imposing the arrangement. Non-homogenous systems where we have some dyes in domains and some regularly distributed patches are higher in energy ( $\Delta = 10.48 \text{ kcal mol}^{-1}$ ). However, in this work only four different distributions were tested, and the inhomogeneous distributions tend to be strongly entropy favoured but not necessarily energetically preferred.

Beyond the conformation of the alkyl chains with respect to the surface, MD simulations at nominal 100 % dye coverage indicate that the binding mode of the molecules close to maximum coverage can change. In the areas with a densely packed arrangement, dyes encumber each other forcing their neighbours to take positions, which are not energetically preferred (in terms of adsorption modes). Figure 3.10 (a) shows a configuration with 100 % surface coverage. Figure 3.10 (b) is the top view of the same system showing the bipyridine moieties while the upper parts of the dyes are not shown to facilitate tracking of location mode transitions. In figure 3.10 (b), dyes in black circles, under the pressure of neighbouring dyes, are forced to switch their location modes to 3 and 4, which are not energetically preferred, and they may get detached from the surface as the dye shown in pink color.

### Chapter 3. Microscopic characterization of amphiphilic ruthenium complexes adsorbed on anatase titanium dioxide

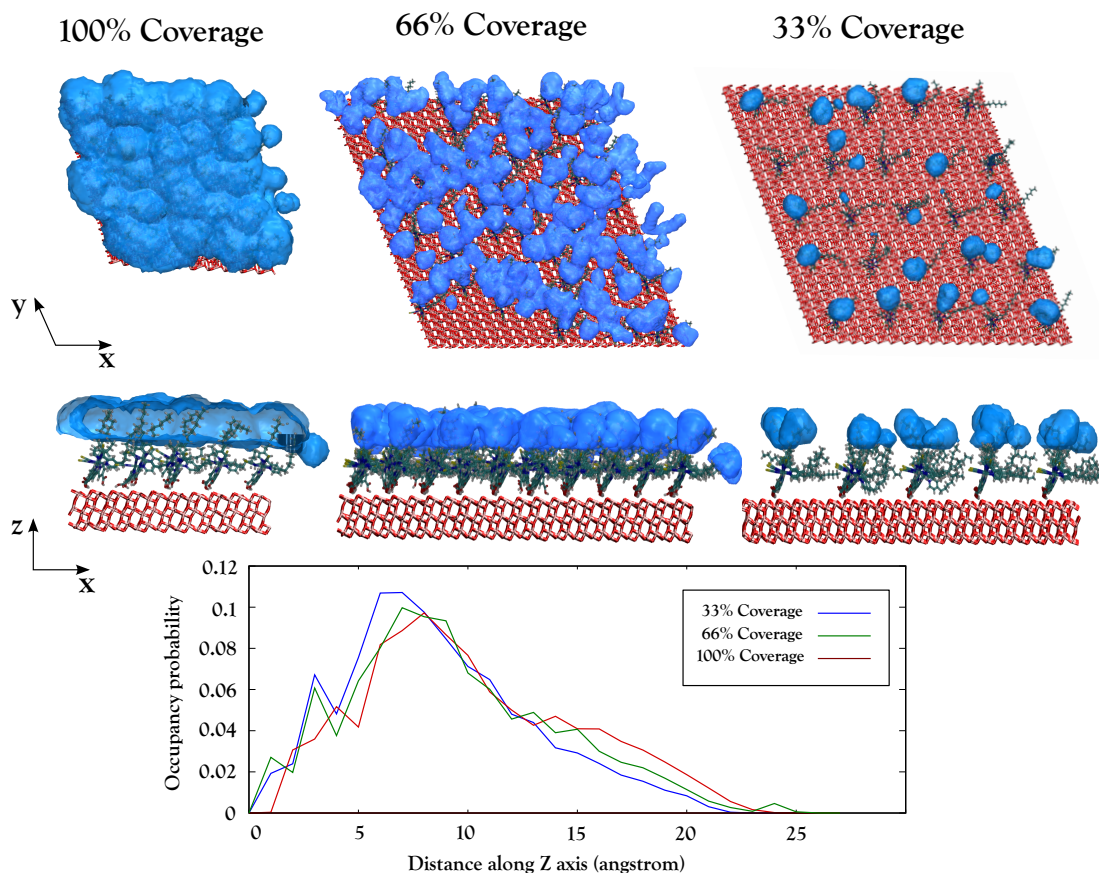


Figure 3.8 – Upper part: Map of the weighted atomic density at 13-25 Å distance from the surface for the low, medium, and high dye coverages. The weights are the occupancy of the selected atoms. The map is done by replacing each dye atom with a normalized gaussian distribution of width (standard deviation) equal to its atomic radius. The gaussian distribution for each atom is then weighted using its occupancy. The various gaussians are then additively distributed on a grid (iceblue color). The isosurface value is 0.0003. Lower part: The probability of finding dye atoms along the z-axis (normal to the surface) for 20 ns of MD simulation in NVE ensemble. At 100 % coverage, dye molecules stand more upward and their presence, mainly alkyl chains, in 13-25 Å distance from the oxide surface is much more prevalent than in the case of 33 % mass coverage. The peak corresponds to the bipyridine units and cyano groups that complex the ruthenium in the octahedral center of the dye. For 33 % mass coverage, the peak is higher and closer to the surface, which implies the additional presence of alkyl chains (mostly one of them) in the vicinity of the surface.

### 3.3. Classical molecular mechanics simulations by computing an ensemble of dye molecules adsorbed on anatase titanium dioxide

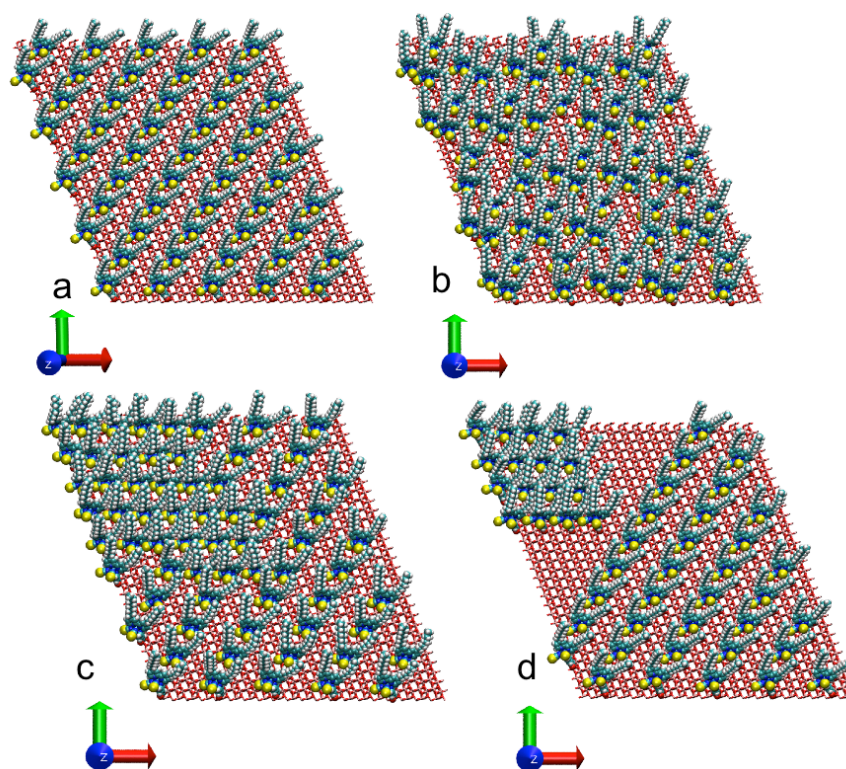


Figure 3.9 – Four different dye distributions at 60 % coverage. (a) and (b) are homogenous cubic and hexagonal lattice packing, respectively. (c) and (d) are half-domain-half-regular distributions for hexagonal and cubic lattice packing, respectively.

### Chapter 3. Microscopic characterization of amphiphilic ruthenium complexes adsorbed on anatase titanium dioxide

---

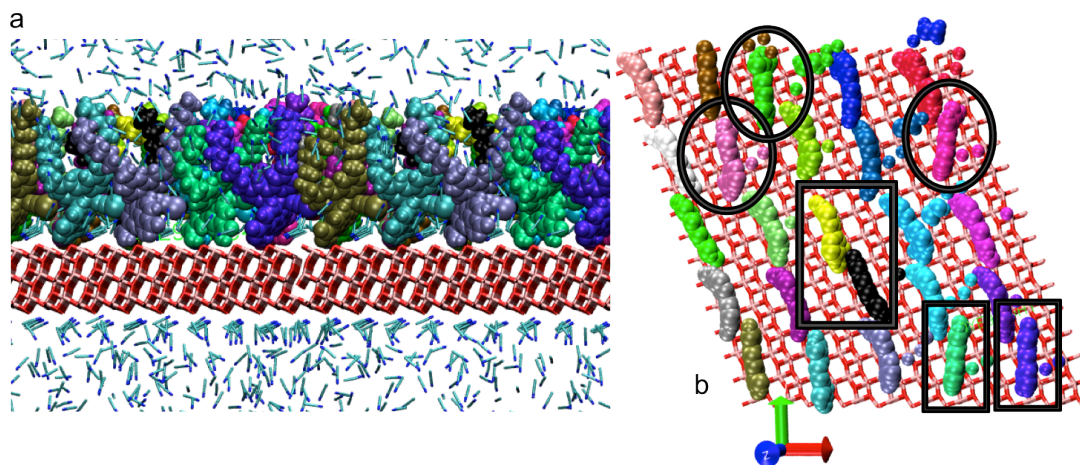


Figure 3.10 – (a) Showing the 100 % coverage system, each dye is depicted in different color for better clarity. (b) Top view of the same system, only showing the bottom part of the dye ( $z < \text{constant}$ ) which mainly shows the bipyridine stand with some parts that occasionally during the simulation get close to the surface (lower than  $z < \text{constant}$ ). Three dyes in black circles have changed modes to modes 3, 4, and 4 from left to right respectively. Four dyes in black rectangles remain in mode 1 with slight tilting.

### 3.4 Conclusion

Results from AFM measurements and MD computations both indicate that the amphiphilic Z907 dye homogeneously covers most of the TiO<sub>2</sub> surface already at 33 % mass coverage by stretching out its alky chains along the TiO<sub>2</sub> surface. For 100 % mass coverage, experiment and simulation show that the molecules form a densely packed monolayer, with the alkyl chains adapting an upright conformation. This microscopic observation confirms the common understanding that alky chains can shield the TiO<sub>2</sub> surface in applications like dye sensitized solar cells and it elucidates the way in which they do.

The observation of two different types of conformation of the dye molecule matches well with previous findings on anisotropic dye molecules by combined NEXAFS and PES studies, and our measurement offers an independent confirmation by a direct and complementary AFM observation in an actually relevant liquid environment [97, 40]. The existence of two adsorbed conformations is reminiscent of the well-known "flat lying" and "standing" molecular configurations of alkanethiols SAMs on gold [106]. The analogy with the present case is nonetheless not obvious given the important differences in the type of bond formed between the dye and the substrate.

Our measurements also provide high-resolution lateral information, i.e. conformity and homogeneity of the film at high mass coverage. Considering the amphiphilic nature of the Z907 molecule, our findings could remain valid for surfactant adsorption at low concentration. In the particular case of dye sensitized solar cells, the staining of mesoporous TiO<sub>2</sub> is carried out at high Z907 dye concentration (250  $\mu$ M). However, it is known that it takes several hours for the dye to reach the bottom of a mesoporous film [92, 37], and even longer to fully saturate the dye uptake in the mesoporous film. This indicates that during the staining process, all of the different conformations and different degrees of mass coverage are present in part of the mesoporous TiO<sub>2</sub> film. This implies that the results derived by QCM-D and AFM on flat model systems provide meaningful insights that are relevant to the mesoporous system. Additionally, the existence of molecular rows could be observed on both the flat and the mesoporous substrate by AFM in EiPS and MeCN, supporting the generality of our findings. The observation of two different conformations is in fact further supported by the two-step adsorption kinetics that are often observed in DSCs [42, 37].

In this study we have combined high-resolution AFM, QCM-D and MD simulations to elucidate the molecular arrangement of the Z907 dye molecules at the surface of TiO<sub>2</sub> in a functionally relevant liquid. Our results detail the formation of the dye monolayer, showing several molecular conformations on the surface at different dye concentration. Since the AFM and computational studies were conducted independently, and both based on the coverage previously measured by QCM-D, the AFM results can be seen as a confirmation of the computational results. If this is confirmed further, it implies that the computational models do describe the microscopic molecular conformation correctly, and it may be applied to predict the behaviour of other systems.

Future work will address molecular films that consist of functional molecules coadsorbed

### **Chapter 3. Microscopic characterization of amphiphilic ruthenium complexes adsorbed on anatase titanium dioxide**

---

with chelating agents such as bile acids, e.g. porphyrin sensitizers and cheno deoxycholic acid, where the nature of interaction and the arrangement of dye and coadsorbate within the sensitizing film still wait to be unveiled.

## 4 QCM-D with mesoporous titanium dioxide films

### 4.1 Introduction mesoporous films and QCM-D

#### 4.1.1 General

Mesoporous films are employed in dye sensitised solar cells because they act as a scaffold with a very large internal surface area. The adjective *mesoporous* implies a pore size in the range between 2 nm and 50 nm [100]. In the case of interconnected pores, the entire internal surface of the mesoporous film will be accessible to solvents as well as to most of the common solvated dye molecules.

The loading with dye molecules is proportional to the available surface area, as has been observed in optical studies. In general, the surface area can be quantified by Brunauer-Emmett-Teller (BET) nitrogen adsorption-desorption measurements, and the increase in surface area compared to the flat film can be conveniently described by the roughness factor  $r$  of the film with

$$r = \frac{\text{accessible surface area}}{\text{projected area}} \quad (4.1)$$

On a flat film, the roughness factor is  $r = 1$ . For a standard mesoporous film of 10  $\mu\text{m}$  thickness, 20 nm particle size, 24 nm pore size and 58 % porosity, the roughness factor is approximately  $r = 1110$ .

This high and accessible surface area makes mesoporous films and their loading with guest molecules interesting for sensing applications such as when a mesoporous film is attached to a QCM-D sensor. The high surface area will increase the relative sensitivity, enabling to detect more subtle changes in mass per covered area than on a flat film. In the (hypothetical) case of an adsorption process in vacuum, relative sensitivity will be increased by the roughness factor  $r$  of the film.

In the more realistic case of adsorption from a solvent, the presence of a gaseous or liquid phase inside the mesoporous film and its replacement by the adsorbing molecules have to be taken into account. Upon immersion, a significant amount of solvent will be trapped inside the mesoporous film, adding to its wet mass. Adsorption of molecules will replace some of the solvent molecules close to the surface, and the measured frequency shift will be proportional to the difference in density multiplied by the replaced volume, similar to an archimedic measurement:

$$\Delta f \propto (\rho_{\text{adsorbate}} - \rho_{\text{solvent}}) \cdot V_{\text{ads}} \quad , \quad (4.2)$$

with  $V_{\text{ads}}$  being the total volume of the adsorbed molecules, which is equal to the number of adsorbed molecules multiplied by their molecular volume.

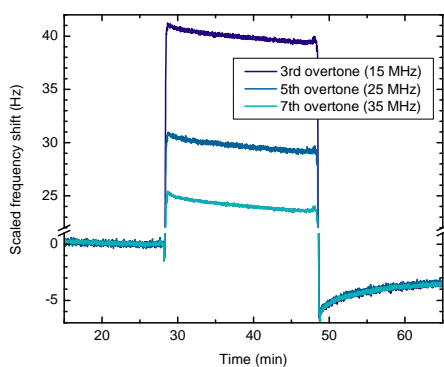
On the interface between the mesoporous film and the overlying bulk solvent, the solvent is not necessarily trapped. Due to the rough interface, the film may experience an increased drag when compared to a flat film[51], leading to additional changes in frequency and dissipation, which depend on viscosity and density of the bulk liquid. Furthermore, the mesoporous film itself can have a certain viscoelastic behaviour, due to its finite shear modulus, which may be important for interpreting measurements on very thick mesoporous films. A shear motion of a mesoporous film enclosing a solvent would imply that liquid is flowing backward and forward inside the film while the sensor undergoes oscillation, similar to a sponge subjected to shear motion. In order to illustrate the different behaviour on mesoporous films, figure 4.1 shows shifts of frequency and dissipation of the first three overtones of a flat, compact TiO<sub>2</sub> film (a), a 200 nm thin mesoporous film (b), and a 10  $\mu\text{m}$  thick mesoporous TiO<sub>2</sub> film (c).

The frequency shift on flat, compact TiO<sub>2</sub> (a) attains a plateau at a value around  $-12$  Hz after 30 s of exposure to JD21. Upon rinsing for 10 min in plain EtOH, the final frequency shift is  $-4$  Hz, which is in reasonable agreement with the expectations for a dense monolayer of this molecule. On the 200 nm thin mesoporous TiO<sub>2</sub> film (b), the behaviour is qualitatively similar to the flat TiO<sub>2</sub>, in that we see a final negative shift of frequency, and in that all overtones converge to a similar value. The quantitative value however, is different, with a frequency shift  $-36$  Hz after 10 min of rinsing. The higher surface area of the mesoporous film results in a higher dye uptake per projected area. The increase in surface area compared to the flat film is described by the roughness factor mentioned above, which is approximately  $r = 22$  for the 200 nm thin mesoporous film. However, the frequency shift, or the mass change, only changed by a factor of 9, from  $-4$  Hz to  $-36$  Hz. This reflects the fact, that the measured mass difference is only due to the replacement of solvent molecules inside the pores by adsorbed dye molecules, as will be shown in chapter 4.2.1 and 4.2.2.

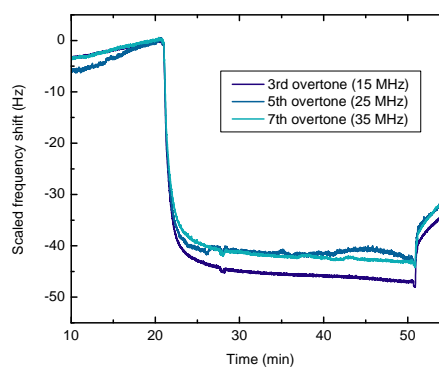
On the 10  $\mu\text{m}$  thick mesoporous TiO<sub>2</sub> film (c), only the 1st overtone behaves qualitatively as the previous two examples, attaining a final frequency shift of  $-1800$  Hz. However, the 3rd and the 5th overtone exhibit a peculiar behaviour in shifting towards positive frequency during dye exposure, with the 5th overtone attaining a frequency shift of  $+5000$  Hz after 10 min of



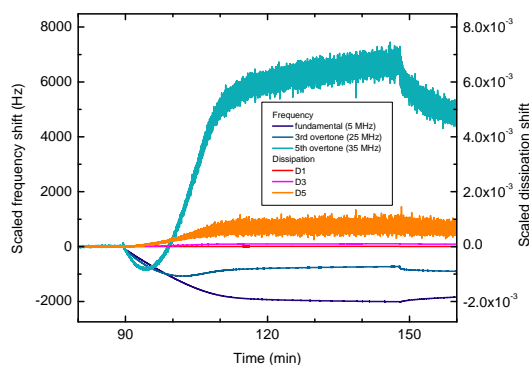
## 4.1. Introduction mesoporous films and QCM-D



(a) On flat, compact TiO<sub>2</sub>.



(b) On 200 nm thin, mesoporous TiO<sub>2</sub>.



(c) On 10  $\mu\text{m}$  thick, mesoporous TiO<sub>2</sub>.

Figure 4.1 – Adsorption of ullazine dye JD21 from an ethanol-THF mixture (4:1)<sub>vol</sub> on (a) flat, compact TiO<sub>2</sub> against plain ethanol as a reference solvent, on (b) 200 nm thin mesoporous and (c) 10  $\mu\text{m}$  thick mesoporous TiO<sub>2</sub> film, the latter two against ethanol-THF mixture (4:1)<sub>vol</sub> as a reference solvent.

rinsing. Furthermore, there is a permanent and large shift of dissipation.

We separate this chapter in one part dedicated to the dye adsorption in thin mesoporous films, and a second part for the discussion on the adsorption in mesoporous films of a thickness greater than 2  $\mu\text{m}$  and their the viscoelastic properties.

### 4.1.2 Sample preparation and characterisation

**TiO<sub>2</sub> nanoparticle synthesis and preparation of the paste.** The synthesis of the TiO<sub>2</sub> nanoparticles, the preparation of the paste, and its deposition by screen-printing are described in [49]. The 20 nm sized colloidal particles are synthesised by hydrolysis from a titanium iso-propoxide precursor that is modified with acetic acid. The paste is made by addition of ethyl cellulose as a filler material and terpineol to an ethanolic solution of the nanoparticles. The particle size of 20 nm was confirmed by transmission electron microscopy and by dynamic light scattering. Its pore size and porosity were determined by BET measurements on large amounts of thick screen-printed films, that had been scrapped off the supporting glass substrate. The characteristics of the paste are: 20 nm particle diameter, 25 nm pore size and 68 % porosity. This paste was used for all films except for the 10  $\mu\text{m}$  thick mesoporous TiO<sub>2</sub>. The paste for the 10  $\mu\text{m}$  thick mesoporous TiO<sub>2</sub> film was purchased from Dyesol Inc. (paste 18-NRT, batch 380). An analysis in our lab by Comte *et al.* gives the characteristics of 20 nm particle diameter, 24 nm pore size and 68 % porosity. After TiCl<sub>4</sub> post-treatment, the porosity decreases from 68% to 58 % .

**Compact TiO<sub>2</sub> underlayer.** Prior to deposition of the mesoporous TiO<sub>2</sub> film, the sensor is cleaned and covered with an underlayer of thin, compact TiO<sub>2</sub> of approximately 20 nm thickness. This underlayer improves mechanical adhesion of the overlying mesoporous TiO<sub>2</sub> film, and prevents direct interaction between the gold electrode of the sensor and the solvent or dye molecules. Here, the underlayer was deposited by atomic layer deposition (ALD) from a tetrakis (dimethylamino)titanium precursor at 150°C as described in [114] with subsequent annealing for 3 hours at 420°C. The ALD-TiO<sub>2</sub> underlayer was applied to all samples except for the one with a 10  $\mu\text{m}$  thick mesoporous TiO<sub>2</sub> film. For the 10  $\mu\text{m}$  thick mesoporous TiO<sub>2</sub> film, the underlayer was applied by spray-pyrolysis of an ethanolic solution of di-iso-propoxy titanium-bis(acetylacetonate) with an added amount of acetylacetonate, using oxygen as a carrier gas for the aerosol [77, 56, 109], and heating the substrate at 420°C during deposition.

**Deposition of mesoporous film.** The deposition of mesoporous TiO<sub>2</sub> films of 2  $\mu\text{m}$  and 10  $\mu\text{m}$  thickness was made by screen-printing (90T and 45T mesh, Estal Mono, Schweiz. Seidengazefabrik, AG, Thal), kept in a clean box for 3 min allowing the paste to relax in order to reduce the surface irregularity and then dried for 6 min at 125°C in order to evaporate the solvent. For the 10  $\mu\text{m}$  thick film, the procedure was carried out twice.

For the deposition of thin mesoporous TiO<sub>2</sub> films, here of 60 nm, 80 nm, 100 nm, and 200 nm thickness, a diluted paste was deposited by spin-casting. Usually, 40  $\mu\text{l}$  of diluted paste were deposited on the substrate, accelerated by 3000  $\text{RPM}/\text{s}$  to a final speed of 6000 RPM for a duration of 30 s. Pastes were diluted by addition of a mixture of ethanol and terpineol in order to obtain the desired thickness. Typical dilutions for obtaining a thickness of a few hundred nm were (1:4) by weight of original paste to solvent mixture. The ratio of ethanol to terpineol was mostly

(1:1)<sub>vol</sub>, although the terpineol fraction was increased for very thin films in order to achieve a laterally homogenous TiO<sub>2</sub> film.

After deposition, the TiO<sub>2</sub> paste was gradually heated under an airflow to 420°C with hold times of 5 min at 325°C and 375°C, at 420°C the temperature was kept for 35 min in order to decompose the ethyl cellulose filler material and sinter the TiO<sub>2</sub> nanoparticles with the aim of creating necking connections.

**TiCl<sub>4</sub> post-treatment.** Finally, a TiCl<sub>4</sub> post-treatment was applied by a chemical bath deposition in 40 mM aqueous TiCl<sub>4</sub> solution for 30 min at 70°C. The films were subsequently rinsed in water and ethanol, and sintered for 30 min at 420°C. This treatment does create a thin layer of pristine anatase on the nanocrystalline TiO<sub>2</sub>, and thereby encapsulates possible impurities left from the degradation of the filler material ethyl cellulose. The treatment further improves the necking between the TiO<sub>2</sub> nanoparticles, and thereby improves mechanical connectivity and electrical conductivity. As a result of the TiCl<sub>4</sub> post-treatment, the pore size decreases slightly from 20 nm to 18 nm, and the porosity decreases from 68 % to 58 % [49], but the roughness factor increases from 116 to 138 per  $\mu\text{m}$  film thickness.

**Measurement of film thickness.** The thickness of the 2  $\mu\text{m}$  and 10  $\mu\text{m}$  thick mesoporous TiO<sub>2</sub> film was measured using a surface profiler (Alpha step, Tencor Instruments). The thickness of the mesoporous TiO<sub>2</sub> films between 60 nm and 200 nm thickness were measured by AFM (Veeco CP-II) on a control sample of silicon, coated with a flat ALD-TiO<sub>2</sub> underlayer.

**Fluorescence emission.** Steady state fluorescence measurements were carried out using a Horiba Jobin Yvon Fluorolog-3 spectrofluorometer. To ensure comparability, all measurements were carried out using a constant slit width for excitation and emission, corresponding to a spectral width of 5 nm. The displayed fluorescence emission intensity is the spectrally corrected emission in counts per second (CPS) divided by the excitation intensity in ( $\mu\text{A}$ ). However, measurements in different chapters of this thesis are not freely comparable with each other because of the occasional maintenance of the machine or a change of the sample holder. I recommend carrying out future experiments using an integrating sphere.

Unless mentioned otherwise, the dye was desorbed from the sensor in 3.4 ml of 0.1 mM tetrabutylammonium hydroxide (TBAOH) in *N,N*-dimethylformamide (DMF) after being removed from the QCM-D measurement chamber. Since the amount of added desorbing solution was constant for all samples in this chapter, no scaling with respect to volume was performed for comparing the fluorescence measurements within this chapter.

## 4.2 Dye loading of thin mesoporous TiO<sub>2</sub> films of 60 nm to 200 nm thickness

We show exemplary measurements of dye loading of mesoporous films between 60 nm and 200 nm thickness in the first subsection 4.2.1, and we observe by fluorescence, that the dye loading increases with surface area as expected. The QCM-D frequency shift, also increases proportional to film thickness but the proportionality factor is not the surface area alone, but a factor that is related to the volume of the dye monolayer with respect to the entire pore volume. The mesoporous film holds liquid trapped inside its pores, and the mass difference in QCM-D is only due to the replacement of solvent molecules by dye molecules in a small volume of the adsorbed layer of dye molecules at the TiO<sub>2</sub>-solvent interface, similar to an archimedic measurement.

In the second subsection we demonstrate a quantitative measurement of the liquid trapped inside the pores of a 200 nm thin mesoporous TiO<sub>2</sub> film.

### 4.2.1 QCM-D on thin mesoporous TiO<sub>2</sub> and fluorescence spectroscopy

The ullazine dye JD21 was chosen for a first series of measurements mainly for two reasons: its low molecular weight would allow for rapid infiltration of mesoporous films, and its high fluorescence yield would allow for quantification of very small amounts of dye after desorption from flat, compact substrates.

However, this choice of dye turned out to be challenging because of several issues related to the mixture of tetrahydrofuran (THF) and ethanol that it is dissolved in. The most noteworthy challenges are the general drift of QCM-D signals in THF-containing solvent mixtures, and the tendency of the dye to coagulate when the ethanol fraction in the solvent mixture is increased. The presented measurements are of preliminary nature and quantitative values should be interpreted with care.

Figure 4.2 serves as an introduction and shows the QCM-D signal and the fluorescence emission intensity of JD21 after desorption for a flat, compact TiO<sub>2</sub> film. The final frequency shift is  $-4$  Hz, and the peak fluorescence intensity is  $1.91 \cdot 10^5$  CPS  $\mu\text{A}^{-1}$ . The concentration of the staining solution is approximately 0.11 mM in ethanol-THF (4:1)<sub>vol</sub>, and the QCM-D measurement is made against a reference of ethanol.

QCM-D and fluorescence measurements of 80 nm and 200 nm thick films are displayed in figure 4.3, using a 0.17 mM dye solution against a reference of ethanol-THF (4:1)<sub>vol</sub>. Using a mixture of ethanol and THF as a reference helps to prevent coagulation of the dye upon solvent exchange. However, the mixture also redissolves the dye from the TiO<sub>2</sub> surface, and the ratio between ethanol and THF will change because of their different vapour pressures. Frequency shifts after 10 min rinsing time were  $-16$  Hz and  $-30$  Hz, and the fluorescence

## 4.2. Dye loading of thin mesoporous TiO<sub>2</sub> films of 60 nm to 200 nm thickness

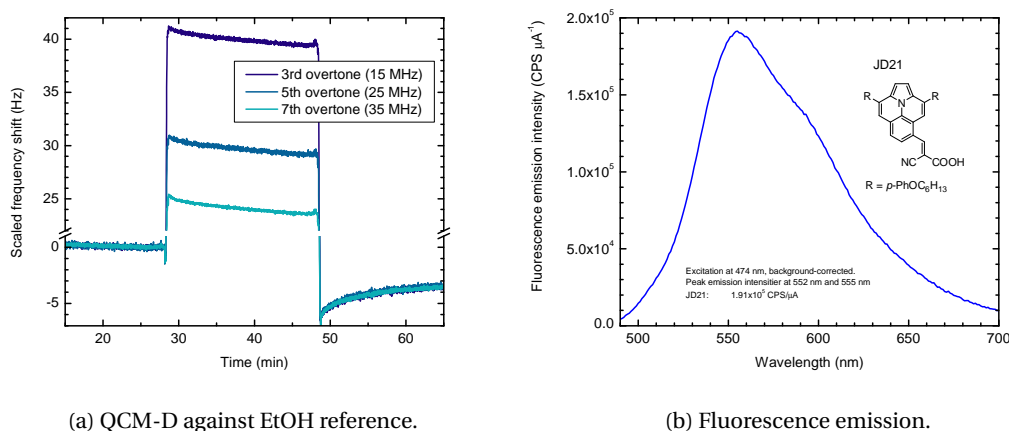


Figure 4.2 – Adsorption of ullazine dye JD21 on flat, compact TiO<sub>2</sub>. Note that the reference solvent for the QCM-D measurement is ethanol, which results in an apparent up-shift in frequency during exposure to the dye solution. This is due to the lower density and viscosity of the dye solution based on a (4:1)<sub>vol</sub> mixture of ethanol and THF. In all other measurements presented in this chapter, a (4:1)<sub>vol</sub> mixture of ethanol and THF is used as a reference.

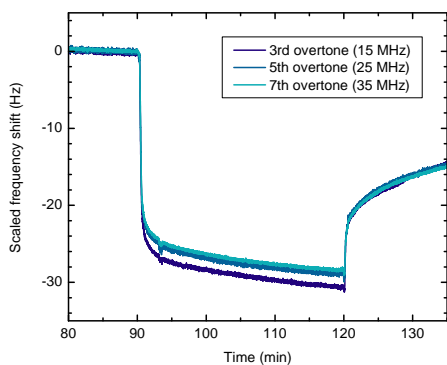
emission intensities were  $1.17 \cdot 10^7 \text{ CPS } \mu\text{A}^{-1}$  and  $2.294 \cdot 10^7 \text{ CPS } \mu\text{A}^{-1}$  for the 80 nm and for the 200 nm thick mesoporous TiO<sub>2</sub> film, respectively.

Figure 4.4 displays QCM-D and fluorescence measurements on mesoporous films of 60 nm, 100 nm and 200 nm thickness that were conducted in the same manner as for figure 4.3, but with a lower dye concentration of 0.14 mM, and some visible coagulation in the staining solution. For the 60 nm thick film, we record a frequency shift of  $-9 \text{ Hz}$  and a fluorescence emission intensity  $0.543 \cdot 10^7 \text{ CPS } \mu\text{A}^{-1}$ ; for 100 nm mesoporous film, we obtain values of  $-13 \text{ Hz}$  and  $0.970 \cdot 10^7 \text{ CPS } \mu\text{A}^{-1}$ ; for 200 nm mesoporous film, we measure a frequency shift of  $-23 \text{ Hz}$  and a fluorescence emission intensity of  $1.734 \cdot 10^7 \text{ CPS } \mu\text{A}^{-1}$ .

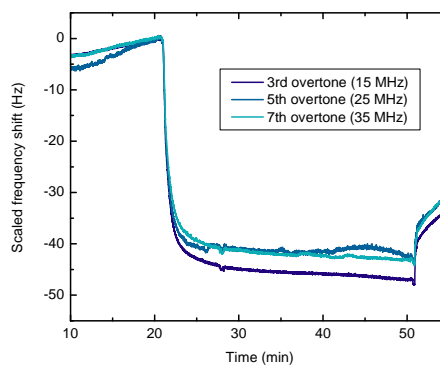
Comparing the measurements on the same 200 nm mesoporous film with solution (i) in figure 4.3 and solution (ii) in figure 4.4, it is clear that the amount of adsorbed dye has decreased, which can be related to the lower concentration of JD21 as well as to coagulation in the aged and recycled dye solution. However, we can use the two measurements on the 200 nm mesoporous film, in order to relate all measurements with solutions (i) and (ii) in a sensible and approximate manner.

The QCM-D frequency shift on the 200 nm mesoporous film in solution (i) is  $-32 \text{ Hz}$  after 10 min of rinsing, whereas it is  $-23 \text{ Hz}$  for solution (ii), a factor of 0.72 lower. The fluorescent emission is  $2.294 \cdot 10^7 \text{ CPS } \mu\text{A}^{-1}$  from solution (i) and  $1.734 \cdot 10^7 \text{ CPS } \mu\text{A}^{-1}$  from solution (ii), a factor of 0.76 lower. In order to allow for a rough comparison, we can estimate that the dye uptake from solution (ii) is by a mean factor of 0.74 lower than from solution (i). Table 4.1 summarises the QCM-D frequency shifts and fluorescence emission intensities of the measurements from solution (i) in figure 4.3, scaled by a factor of 0.74, and those from solution (ii)

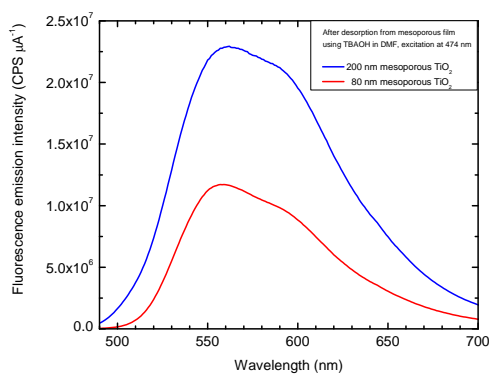
## Chapter 4. QCM-D with mesoporous titanium dioxide films



(a) 80 nm mesoporous TiO<sub>2</sub>.



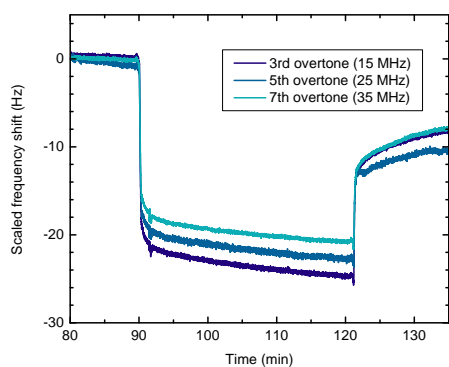
(b) 200 nm mesoporous TiO<sub>2</sub> with fresh dye solution (i).



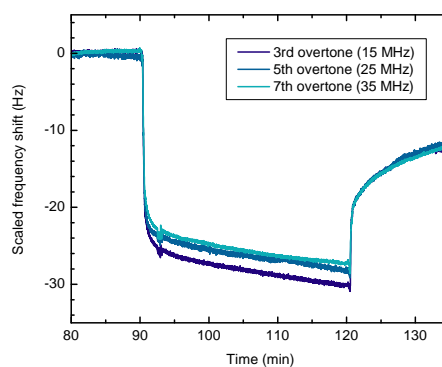
(c) From 200 nm and 80 nm mesoporous TiO<sub>2</sub>, JD21 solution (i).

Figure 4.3 – Adsorption of ullazine dye JD21 from solution (i) on 80 nm and 200 nm thin mesoporous TiO<sub>2</sub> film. Frequency shift by QCM-D (a), (b) against a reference of (4:1)<sub>vol</sub> mixture of ethanol and THF. Part (c) shows the fluorescence emission spectroscopy after desorption of the dye from the QCM-D sensor, excitation at 474 nm.

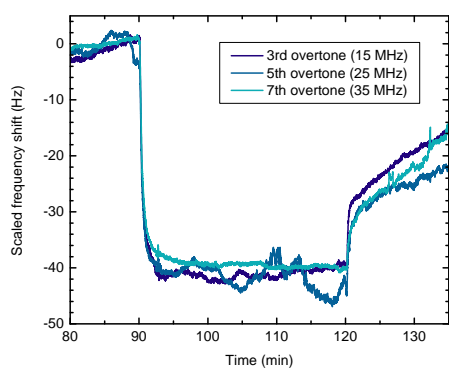
## 4.2. Dye loading of thin mesoporous TiO<sub>2</sub> films of 60 nm to 200 nm thickness



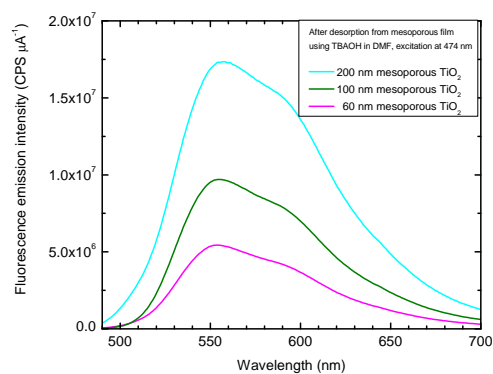
(a) On 60 nm mesoporous TiO<sub>2</sub>.



(b) 100 nm mesoporous TiO<sub>2</sub>.



(c) On 200 nm mesoporous TiO<sub>2</sub> with degrading sensor



(d) From 200 nm, 100 nm and 60 nm mesoporous TiO<sub>2</sub>, quality and an aged dye solution (ii). JD21 solution (ii).

Figure 4.4 – Adsorption of ullazine dye JD21 from solution (ii) on thin mesoporous TiO<sub>2</sub> film. Frequency shift by QCM-D (a), (b), (c) against a reference of (4:1)<sub>vol</sub> mixture of ethanol and THF Part (d) shows fluorescence emission spectroscopy after desorption from the sensors, excitation at 474 nm.

## Chapter 4. QCM-D with mesoporous titanium dioxide films

Table 4.1 – Summarising QCM-D frequency shift on mesoporous films and fluorescence emission intensity from desorbed JD21 dye. Mean frequency shift on the 5th overtone after 10 min of rinsing. Marked values\* have been scaled by a factor of 0.74, all measurements are displayed in figures 4.2, 4.3 and 4.4 and .

Film thickness (nm)	Estimated surface area (cm <sup>2</sup> )	Frequency shift (Hz)	Fluorescence intensity (CPS $\mu\text{A}^{-1}$ )
flat	1.0	-4	$1.91 \cdot 10^5$
60	7.8	-9	$0.54 \cdot 10^7$
80*	10.1	-12*	$0.87 \cdot 10^7$ *
100	12.4	-13	$0.97 \cdot 10^7$
200*	23.8	-22*	$1.70 \cdot 10^7$ *
200	23.8	-23	$1.73 \cdot 10^7$

in figure 4.4, as well as those from the flat film in figure 4.2.

We note that the fluorescence emission intensity on the flat film of  $0.2 \cdot 10^6$  CPS  $\mu\text{A}^{-1}$  is lower than the value of  $0.5 \cdot 10^6$  CPS  $\mu\text{A}^{-1}$  obtained by the interpolation from all measurements. This is probably due to two sources of error. First, as we have seen in chapter 2, the error on fluorescence emission intensity measurements of the ullazine dye JD21 desorbed from flat films is relatively large. Since the dye desorbs readily in its staining mixture of ethanol and THF (4:1)<sub>vol</sub>, small technical irregularities in the handling of the desorption from the QCM-D sensor can easily lead to partial desorption of the dye before the sensor is transferred to the actual desorbing solution. This would lead to an underestimation of the amount of dye from the flat film. The mesoporous film however, is less prone to small experimental irregularities and it could possibly even contain small aggregations of dye molecules inside its pores. The desorbed amount would hence overestimate the amount of dye actually bond to the TiO<sub>2</sub> surface. Nevertheless, both values of fluorescence emission intensity on the flat film, the measured  $0.2 \cdot 10^6$  CPS  $\mu\text{A}^{-1}$  and the value of  $0.5 \cdot 10^6$  CPS  $\mu\text{A}^{-1}$  that is obtained by the interpolation from all measurements, are of the same order of magnitude.

The adjusted values listed in table 4.1 have been plotted over the surface area which has been estimated from the AFM thickness and the BET measurement, which predict an increase by a factor of 11.1 per 100 nm mesoporous film, see the beginning of this section 4.1.2. A linear fit has been made on the QCM-D frequency shift and on the fluorescence emission intensity. Extrapolation to zero surface area reveals that the fluorescence emission intensity, hence the dye uptake, correlates directly with the surface area, as expected. Extrapolation on the QCM-D frequency shift, however, shows a clear offset against the origin, indicating that the QCM-D shift does correlate with dye uptake, but not in the same way on mesoporous films as on flat films.

It is well known that QCM-D measures the wet weight of an adsorbed film [120], including associated solvent. In our case, we actually measure also the solvent trapped inside the pores



## 4.2. Dye loading of thin mesoporous TiO<sub>2</sub> films of 60 nm to 200 nm thickness

of the mesoporous film, which we discuss in detail in the next subsection 4.2.2. In the case of molecular adsorption on the internal surface of the TiO<sub>2</sub> film, we therefore only measure the frequency shift (or mass difference) due to the replacement of solvent molecules by dye molecules in a small volume of the adsorbed layer close to the TiO<sub>2</sub> surface, similar to an archimedic measurement:

$$\Delta f \propto \underbrace{\Delta m_{\text{monolayer,flat}}}_{\propto \Delta f_{\text{mono}} \approx -4 \text{ Hz}} + \underbrace{(\rho_{\text{adsorbate}} - \rho_{\text{solvent}}) \cdot V_{\text{ads}}}_{=\Delta m_{\text{inside pores}}}, \quad (4.3)$$

$\Delta m_{\text{monolayer,flat}}$  is the mass difference associated with a monolayer, as measured on a flat film, and  $V_{\text{ads}}$  is the total volume of the adsorbed molecules inside the mesoporous film, which is equal to the number of adsorbed molecules multiplied by the molecular volume. In order to deduct the adsorbed mass directly from this equation, we need additional information, for example the volume  $V_{\text{ads}}$  of the adsorbed molecular layer inside the pores.

We can in principle measure this volume by the method demonstrated in the next subsection 4.2.2, measuring the volume of the pores before and after dye adsorption :

$$V_{\text{ads}} = V_{\text{pore,before}} - V_{\text{pore,after}}, \quad (4.4)$$

and thereby calculate the amount of adsorbed molecules.

As mentioned in the beginning of this chapter, the measurements are affected by a number of errors. The solvent mixture of ethanol and THF often causes a linear drift, even when using purified solvents. This drift is probably related to the swelling of the Kalrez sealing by THF. Furthermore, the vapour pressure of THF is lower than that of ethanol, leading to changes in ratio and hence in density and viscosity over time. Coagulation of the JD21 dye was observed when increasing the ethanol content in the solvent mixture, or when contaminating the dye solution with acetonitrile. We used different dye concentrations during the measurements, which did significantly affect dye uptake. Before future experiments on this dye, an adsorption isotherm should be recorded in an appropriate solvent.

In this subsection, we have shown exemplary measurements of dye uptake on thin, mesoporous TiO<sub>2</sub> films by QCM-D and subsequent fluorescence emission spectroscopy. The fluorescence emission intensity quantifies the dye uptake directly and, and corresponds to the increase in surface area when comparing mesoporous films to flat films. The QCM-D frequency shift in contrast, which measures the change in mass, does not describe well the increased dye uptake when comparing flat and mesoporous films, but it still scales with with film thickness when comparing mesoporous films with each other, excluding the result on flat films. The results suggest that the measured mass difference is only due to the replacement of solvent molecules inside the pores by adsorbed dye molecules. In the next section 4.2.2 we

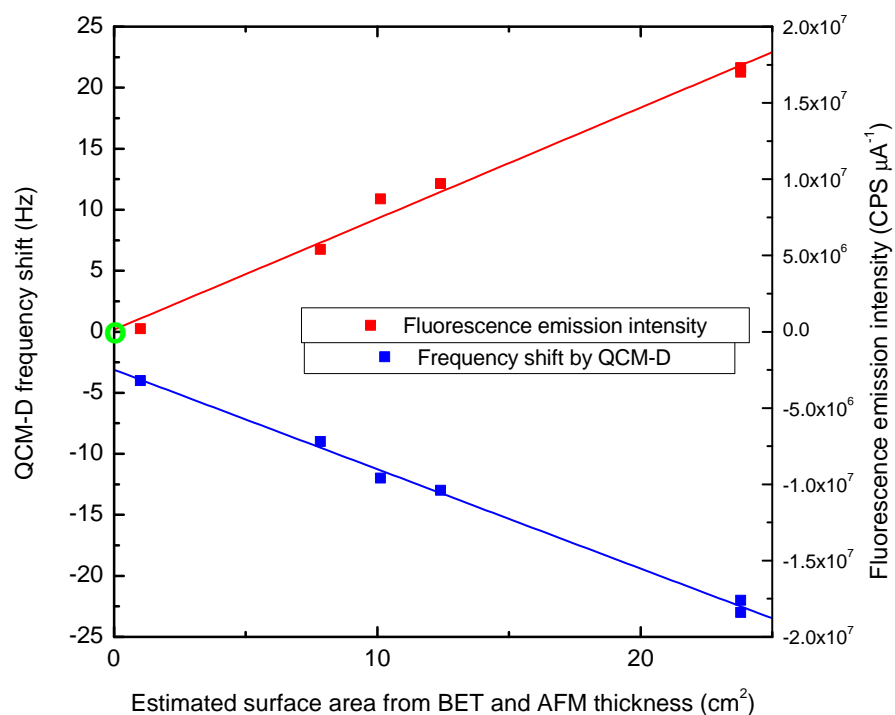


Figure 4.5 – Adjusted frequency shift by QCM-D and fluorescence emission intensity over estimated surface area, based on BET measurements and AFM-film thickness, as listed in table 4.1. The line is a linear fit of each data set. Note that the fit on the QCM-D data (blue) does miss the origin clearly. The origin is marked in green.

#### **4.2. Dye loading of thin mesoporous TiO<sub>2</sub> films of 60 nm to 200 nm thickness**

---

will clearly see that we indeed measure changes of the entire mass of the mesoporous film, including the liquid enclosed within.

### 4.2.2 Liquid volume trapped inside thin mesoporous TiO<sub>2</sub> by QCM-D

The measurements of dye from thin mesoporous TiO<sub>2</sub> film in section 4.2.1 have shown that the mass difference in QCM-D is mostly due to the replacement of solvent molecules in a small volume of the adsorbed layer  $V_{\text{ads}}$  close to the TiO<sub>2</sub> surface.

In order to assess the actual amount of solvent trapped inside the mesoporous TiO<sub>2</sub> film, mainly given by the solvent-accessible pore volume  $V_{\text{pores,liq}}$ , we performed QCM-D measurements using solvents of different densities and compared these to a flat film. Figure 4.6 shows shifts of frequency and dissipation on the 5th overtone (25 MHz) on a 200 nm thick mesoporous TiO<sub>2</sub> film and on a flat gold film. Acetonitrile is used as a baseline, the solvents are isopropanol, chlorobenzene and water. The difference of frequency shift between flat and mesoporous films mainly corresponds to the mass difference of liquid trapped inside the pores, moving along with the mesoporous film.

The QCM-D signals in figure 4.6 show rapid transitions between constant values when switching from one solvent to another, and they go back to their initial value when exposed to the reference acetonitrile. This indicates that the solvent exchange inside the 200 nm mesoporous TiO<sub>2</sub> happens on the same timescale as the solvent exchange in the flow chamber. It furthermore confirms that the solvent exchange is complete, and that there is almost no adsorption or desorption of contaminations from and to the solvent.

The only exception is the exposure to chlorobenzene, where a gradual decrease in frequency and an increase in dissipation are observed on both, flat and mesoporous films. This points to a contamination and a deposition of material from the chlorobenzene solvent to the TiO<sub>2</sub> surface. However, this shift seems to be reversible upon subsequent rinsing with acetonitrile and water. Furthermore, the measurement on the gold sensor (fig. 4.6 (a)) shows a small positive linear drift in frequency throughout the measurement, which is likely related to effects other than desorption from the surface.

The measurement on the flat gold film (fig. 4.6 (a)) serves as a reference in order to correct for effects from the overlying bulk liquid, where changes of density and viscosity effect the frequency and dissipation as described by Kanazawa and Gordon [55, 54, 110]:

$$\Delta f = f_0^{3/2} \sqrt{\frac{\eta \rho}{\pi \mu_q \rho_q}} \quad \text{and} \quad \Delta D = \frac{1}{t_q \rho_q} \sqrt{\frac{\eta \rho}{\pi f_0}} \quad . \quad (4.5)$$

$\eta$  and  $\rho$  are the viscosity and the density of the liquid, and  $\mu_q$  and  $t_q$  are the shear modulus and the transversal sound velocity of the AT-cut quartz.

The QCM-D signals on the 200 nm mesoporous TiO<sub>2</sub> film in figure 4.6 (b) should mainly depend on three factors: (i) the relative mass change due to the different densities of the solvents trapped inside the pores. This should influence the frequency only, and not the dissipation,

## 4.2. Dye loading of thin mesoporous TiO<sub>2</sub> films of 60 nm to 200 nm thickness

assuming a rigid mesoporous network. (ii) A possible drag due to turbulences on the rough interface between the mesoporous film and the bulk liquid, similar to the observation by Johannsmann et al. [51].(iii) The density and viscosity of the overlying bulk liquid will have the same effect as on a flat sensor.

The shifts of frequency and dissipation on the 5th overtone upon exposure to solvents of different density and viscosity, relative to acetonitrile as a reference, were extracted from the QCM-D measurement in figure 4.6 and are compiled in table 4.2. Values have been corrected for linear drift or contamination from the chlorobenzene solvent.

In order to correct the shifts on the mesoporous film for effects from the simple coupling to the overlying bulk liquid (iii), the shifts recorded on the flat sensor have been subtracted, and the differences  $\delta f$  and  $\delta D$  are displayed in the last two columns of the table:

$$\delta f = \Delta f_{\text{mesoporous}} - \Delta f_{\text{flat}} \quad \text{and} \quad \delta D = \Delta D_{\text{mesoporous}} - \Delta D_{\text{flat}} \quad . \quad (4.6)$$

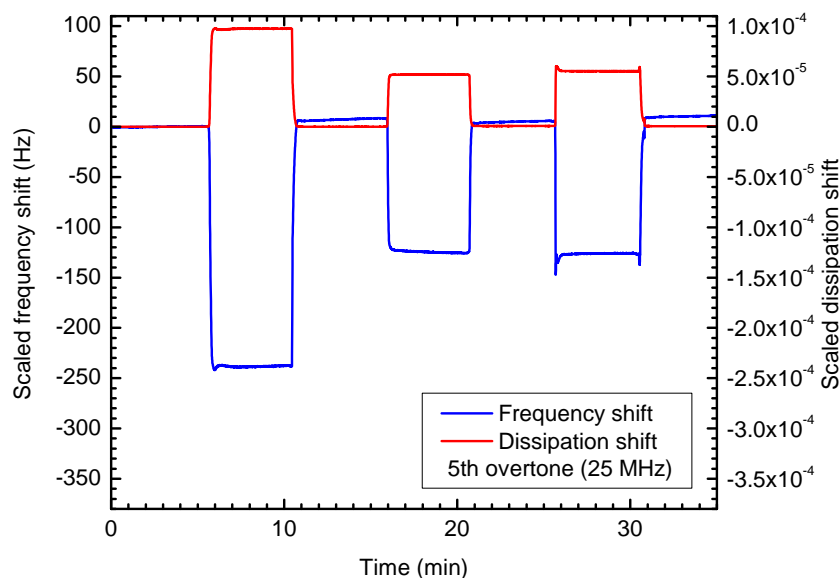
The first surprising result is, that the dissipation shift is the same on the flat and the porous film  $\delta D = 0$  in each solvent. This indicates that the turbulent drag (ii) on the interface between the mesoporous film and the overlying bulk liquid is very similar to the one on the flat surface. This could be related to the small amplitude of the oscillation relative to the size of the protrusions. According to Edvardsson [27, 26] the lateral amplitude of the oscillation of the fundamental resonance is about 3 nm, and significantly less for higher overtones. This is small compared to the size of 20 nm of the TiO<sub>2</sub> nanoparticles that constitute the mesoporous film. The remaining overtones deliver approximately the same values as overtone five displayed in figure 4.6. The differences of shifts of frequency and dissipation on flat compact TiO<sub>2</sub> and mesoporous TiO<sub>2</sub> upon exposure to solvents are summarised in table 4.4.

Consequently, the difference in frequency shift  $\delta f$  should be primarily related to the change in mass (i) given by the difference in volumetric density  $\delta\rho$  relative to acetonitrile, described by the Sauerbrey equation:

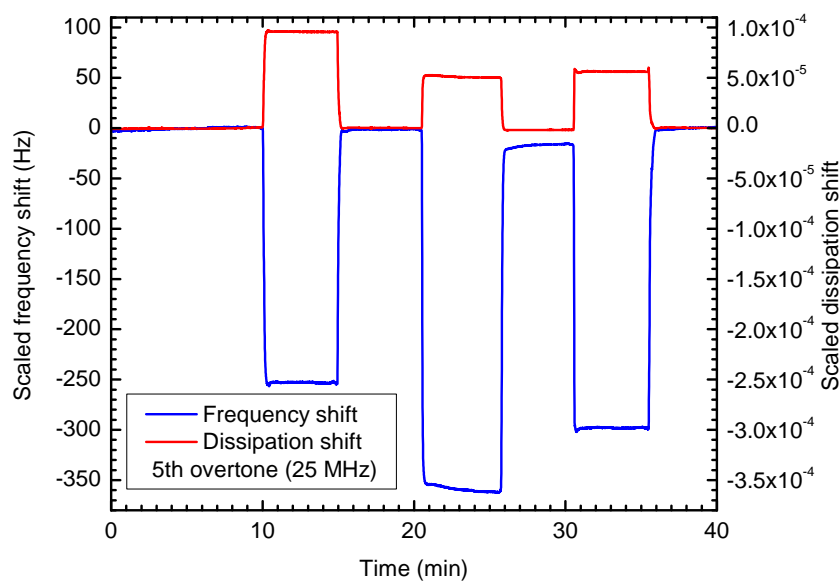
$$-C \cdot \delta f = \delta m = V_{\text{pores,liq}} \cdot \underbrace{(\rho_{\text{solvent}} - \rho_{\text{acetonitrile}})}_{\delta\rho_{\text{solvent}}} \quad , \quad (4.7)$$

with the Sauerbrey constant  $C = \frac{f_0}{\rho_a v_a} \approx 17.5 \text{ ng cm}^{-2} \text{ Hz}^{-1}$ . Note that  $\delta m$  and  $V_{\text{pores,liq}}$  are mass and volume *per area*.

The literature values for density and viscosity of the solvents used in this experiment are taken from the *Handbook of Chemistry and Physics* [45] and are mentioned in table 4.2. Table 4.3



(a) On flat Au surface.



(b) On 200 nm mesoporous TiO<sub>2</sub>.

Figure 4.6 – QCM-D signal for plain solvents of different viscosity and density on a flat gold sensor as a reference, and on a 200 nm thick mesoporous TiO<sub>2</sub> film. Acetonitrile is used as a reference solvent, the different solvents are isopropanol, chlorobenzene and water. The difference in frequency shift between the two measurements mainly corresponds to the mass difference of the liquid trapped inside the pores, moving along with the mesoporous film. See table 4.2 .

#### 4.2. Dye loading of thin mesoporous TiO<sub>2</sub> films of 60 nm to 200 nm thickness

Table 4.2 – Shifts of frequency and dissipation on flat compact TiO<sub>2</sub> and mesoporous TiO<sub>2</sub> upon exposure to solvents of different density and viscosity, relative to a acetonitrile as a reference, taken from the measurement displayed in figure 4.6. The density of acetonitrile is  $\rho = 0.785 \text{ g cm}^{-3}$ , and its viscosity is  $\eta = 0.369 \text{ mPa s}$  [45]. The last two columns show the differences  $\delta f$  and  $\delta D$  between the shifts on flat and mesoporous films. The difference in frequency shift  $\delta f$  provides an Archimedic measure for the liquid trapped inside the mesoporous film, whereas  $\delta D \approx 0$  indicates that the turbulence on the interface with the bulk liquid is similar for the porous and the flat film.

	200 nm meso-porous TiO <sub>2</sub>		Flat, compact TiO <sub>2</sub>		Difference between mesoporous and flat film	
	$\Delta f_5 \text{ Hz}$	$\Delta D_5 (10^{-6})$	$\Delta f_5 \text{ (Hz)}$	$\Delta D_5 (10^{-6})$	$\delta f_5 \text{ (Hz)}$	$\delta D_5 (10^{-6})$
2-propanol $\rho = 0.781 \text{ g cm}^{-3}$ $\eta = 2.040 \text{ mPa s}$	-240	+97	-255	+96	-15	-1
chloro-benzene $\rho = 1.106 \text{ g cm}^{-3}$ $\eta = 0.753 \text{ mPa s}$	-132	+52	-351	+52	-219	0
water $\rho = 0.997 \text{ g cm}^{-3}$ $\eta = 0.890 \text{ mPa s}$	-137	+55	-297	+55	-160	0

Table 4.3 – Density difference  $\delta\rho_{\text{solvent}} = \rho_{\text{solvent}} - \rho_{\text{acetonitrile}}$  to acetonitrile  $\rho_{\text{acetonitrile}} = 0.785 \text{ g cm}^{-3}$  at 25°C [45], and the difference in frequency shift  $\delta f$  between flat and mesoporous films. The difference in frequency shift  $\delta f$  provides a measure for the mass of liquid trapped inside the mesoporous film.

	Density difference $\delta\rho_{\text{solvent}}$ in $\text{g cm}^{-3}$	Frequency difference between mesoporous and flat film $\delta f$ in Hz
2-propanol	-0.004	-15
chlorobenzene	+0.321	-219
water	+0.212	-160

shows the difference in density relative to acetonitrile, and difference in frequency shift  $\delta f$ . Surprisingly, the frequency shift for isopropanol is negative ( $-15 \text{ Hz}$ ), although its density is slightly lower than that of acetonitrile (relative  $-0.5 \%$ ), which would imply a positive frequency shift. I suspect that this is due to a contamination of the isopropanol solvent, and we discuss this at the end of this section. Assuming that the largest values of frequency difference  $\delta f$  bear the smallest relative error, the measurements on chlorobenzene and water can be used to estimate the area volume  $V_{\text{pores,liq}}$  of trapped liquid:

$$V_{\text{pores,liq}} = \frac{-C \cdot \delta f}{\delta \rho_{\text{solvent}}} \quad . \quad (4.8)$$

For chlorobenzene against acetonitrile, an area volume of  $V_{\text{pores,MeCN-C}_6\text{H}_5\text{Cl}} = 1.19 \cdot 10^{-5} \text{ cm}^3/\text{cm}^2$  is obtained, and for water the value is  $V_{\text{pores,MeCN-H}_2\text{O}} = 1.32 \cdot 10^{-5} \text{ cm}^3/\text{cm}^2$ . The deviation of the lower value from the upper one is 9 %, and their mean value for the area volume is

$$V_{\text{pores,liq}} = 1.26 \cdot 10^{-5} \frac{\text{cm}^3}{\text{cm}^2} \quad . \quad (4.9)$$

In order to briefly evaluate whether this value makes sense, I consider the previously determined porosity  $p_{\text{BET}}$  and the film thickness  $d_{\text{AFM}}$  in order to estimate the expected volume per area

$$V_{\text{pores,expected}} = p_{\text{BET}} \cdot d_{\text{AFM}} \cdot \frac{\text{cm}^2}{\text{cm}^2} \quad . \quad (4.10)$$

The porosity has been estimated from BET measurements on amassed screen-printed mesoporous  $\text{TiO}_2$  films *with  $\text{TiCl}_4$  post-treatment* to be  $p_{\text{BET}} = 0.58$  . The film thickness  $d_{\text{AFM}} = 200 \text{ nm}$  has been measured by AFM on a mesoporous  $\text{TiO}_2$  film deposited on a silicon control substrate by the same process as on the QCM-D sensor. Equation 4.10 yields an expected area volume of

$$V_{\text{pores,expected}} = 0.58 \cdot 200 \text{ nm} \frac{\text{cm}^2}{\text{cm}^2} = 1.16 \cdot 10^{-5} \frac{\text{cm}^3}{\text{cm}^2} \quad . \quad (4.11)$$

This expected value is 8 % smaller than the value obtained by QCM-D, which is a rather good agreement.

I present a brief and mostly qualitative discussion of the sources of error in this exemplary measurement. For the comparison to the expected area volume above, we note that also the BET and the AFM measurement bear a certain error, and they have been performed on different physical samples. The error on this AFM measurement was approximately 10 % and



## 4.2. Dye loading of thin mesoporous TiO<sub>2</sub> films of 60 nm to 200 nm thickness

Table 4.4 – Differences of shifts of frequency and dissipation on flat compact TiO<sub>2</sub> and mesoporous TiO<sub>2</sub> upon exposure to solvents of different density and viscosity, relative to a acetonitrile as a reference, taken from the measurement partially displayed in figure 4.6. The density of acetonitrile is  $\rho = 0.785 \text{ g cm}^{-3}$ , and its viscosity is  $\eta = 0.369 \text{ mPa s}$  [45]. The deviation of the values on the fundamental resonance in water (grey) correlate with a gas bubble trapped inside the flow cell. The 3rd, 7th and 13th overtone exhibited a general irregular behaviour and were excluded from evaluation.

	All $\delta f_n$ in Hz, all $\delta D_n$ in ( $10^{-6}$ )							
	$\delta f_1$	$\delta D_1$	$\delta f_5$	$\delta D_5$	$\delta f_9$	$\delta D_9$	$\delta f_{11}$	$\delta D_{11}$
2-propanol $\rho = 0.781 \text{ g cm}^{-3}$	-10	+3	-15	-1	-5	-2	-16	-5
chlorobenzene $\rho = 1.106 \text{ g cm}^{-3}$	-233	-2	-219	0	-221	+2	-223	0
water $\rho = 0.997 \text{ g cm}^{-3}$	-188	+22	-160	0	-159	1	-160	+1

some of this uncertainty is caused by the TiO<sub>2</sub> particle size of 20 nm.

The sources of error of the QCM-D measurements are various: in the case of exposure to chlorobenzene, we observe the deposition of a contamination, whereas we observe its dissolution upon exposure to water. The frequency shift for each of these measurements has an uncertainty of  $\pm 10$  Hz on the mesoporous film and of  $\pm 2$  Hz on the flat film. On the flat film, we furthermore observed a small, positive linear drift.

The values of volumetric density of all solvents are literature values at 25°C [45], which was the nominal temperature of the QCM-D platform at all times. However, the density of the solvents used in this experiment has not been measured in our laboratory. Solvents have not been purified prior to the measurement. It is therefore possible, that some of them contain impurities or stabilisers, which may have an impact on density. Isopropanol is the only solvent that had been stored over molecular sieve, and we speculate that suspended nanoparticles could have been present in the solvent.

Furthermore, the density and viscosity are given as bulk liquid properties. The interaction with the TiO<sub>2</sub> surface will induce ordering of the liquid at the surface and might thereby change the local density for each solvent in a different way.

### 4.3 Mesoporous films of more than 2 $\mu\text{m}$ thickness

On mesoporous  $\text{TiO}_2$  films of several micrometer thickness, the frequency shift upon dye loading does show some unexpected behaviour at overtones higher than the fundamental resonance. This is well illustrated by figure 4.1 (c) and figure 4.10 in the introduction of this chapter, where the 1st resonance shows a shift to lower values, as expected, but the 3rd and especially the 5th overtone show an upshift in frequency with increased dye loading. With the aim of understanding these phenomena in particular, and the viscoelastic response of mesoporous films in general, we present selected, preliminary QCM-D measurements made in air after each step of the fabrication process of mesoporous films.

#### 4.3.1 QCM-D throughout the deposition of mesoporous $\text{TiO}_2$ films

For a simple introduction, figure 4.7 (a) shows the scaled difference of resonance frequency for different overtones measured on mesoporous  $\text{TiO}_2$  films between 60 nm and 200 nm thickness, comparing the frequency of the pristine sensor to that with the final,  $\text{TiCl}_4$ -treated mesoporous film in air. In almost all experiments, all overtones attain the same scaled frequency shift. For 60 nm film thickness, the scaled shift is approximately -1500 Hz, for 80 nm it is -1900 Hz, and for 100 nm film thickness it is -2200 Hz on all overtones. For the 200 nm thick film, there is a shift of -2800 Hz on the 3rd and 5th overtone, whereas the remaining overtones exhibit a more irregular behaviour, ranging from -3200 Hz on the fundamental resonance to  $+10^6$  Hz for overtones 7 to 11.

The added mass should be proportional to film thickness, and the frequency shift is expected to shift proportional to the mass. This holds true only in an approximate manner, and it is worth noting that the frequency shift per film thickness slightly decreases for higher film thickness.

The scaled dissipation shift is small and irregular on all samples, mostly scattered between  $-3 \cdot 10^{-6}$  to  $2 \cdot 10^{-6}$ . This dissipation shift is relatively small, and lies within the error of measurement, especially since sensor crystals are unmounted and re-mounted for the  $\text{TiO}_2$  film deposition between the measurements.

Figure 4.8 shows QCM-D data taken on a sensor after each step in the deposition procedure of a 2  $\mu\text{m}$  thick mesoporous film for different overtones: on the pristine sensor, after spray-pyrolysis of  $\text{TiO}_2$  and annealing, after screen-printing and sintering of the 2  $\mu\text{m}$  thick mesoporous film, and after  $\text{TiCl}_4$  post-treatment and sintering; each of them relative to the pristine sensor. The scaled frequency shift (fig. 4.8 (a)) due to the spray-pyrolysis underlayer is approximately a constant  $-680$  Hz on each overtone, and small compared to the shift caused by deposition of the mesoporous film, which are in the range of several  $10^4$  Hz.

The screen-printing and sintering of the 2  $\mu\text{m}$  thick mesoporous film does produce scaled frequency shifts from  $-3 \cdot 10^4$  Hz on the 3rd overtone to  $-5 \cdot 10^4$  Hz on the 7th overtone, showing

### 4.3. Mesoporous films of more than 2 $\mu\text{m}$ thickness

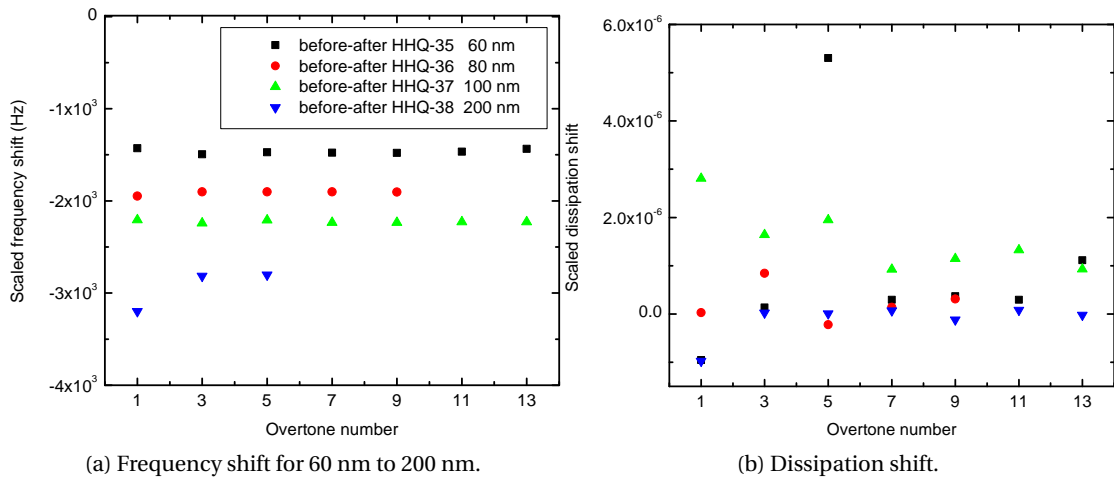


Figure 4.7 – (a) Scaled difference of resonance frequency over the different overtones on mesoporous TiO<sub>2</sub> films of 60 nm to 200 nm thickness, comparing the frequency of the pristine sensor to that with the final, TiCl<sub>4</sub>-treated mesoporous film. Part (b) Shows the according difference of dissipation over the different overtones.

a strong negative dispersion with overtone frequency. The 1st overtone shows an irregular behaviour which we will not elaborate on. Overtones beyond the 7th could not be detected. On overtones 3 to 7, the scaled dissipation does increase steeply from  $0.2 \cdot 10^{-5}$  to  $2.0 \cdot 10^{-5}$ . We want to point out that values of dissipation larger than  $5 \cdot 10^{-5}$  in air correspond an almost complete attenuation the QCM-D signal compared to the high noise in air. Consequently, overtones with a very high dissipation cannot be detected any more.

Upon TiCl<sub>4</sub> treatment and sintering, we observe a stiffening of the film as we would expect, since the the interconnectivity of the particles does improve. Relative to the pristine sensor, the scaled frequency shift shows a regular behaviour, with values between  $-4 \cdot 10^4$  Hz on the fundamental resonance and  $-6 \cdot 10^4$  Hz on the 13th overtone. We are again able to detect all overtones, and we remark that dissipation has almost returned to its initial low values around  $2 \cdot 10^{-6}$ .

Figure 4.9 shows QCM-D data of a sensor after each step of the deposition of a 10  $\mu\text{m}$  thick mesoporous TiO<sub>2</sub> film over the different overtones, similar to the way it was carried out for the 2  $\mu\text{m}$  thick mesoporous film in figure 4.8. The underlayer and the mesoporous TiO<sub>2</sub> have slightly different details, but the behaviour on overtones 1 to 3 during the fabrication of the 10  $\mu\text{m}$  thick mesoporous film is qualitatively the same as on the 2  $\mu\text{m}$  thick mesoporous film. At intermediate overtone frequencies, the dissipation seems to exceed  $4.0 \cdot 10^{-5}$ , and those overtones cannot be detected. At higher overtone frequency though, dissipation goes back to lower values, and a positive frequency shift is observed. We will discuss this particular behaviour of higher overtones at the end of the chapter.

## Chapter 4. QCM-D with mesoporous titanium dioxide films

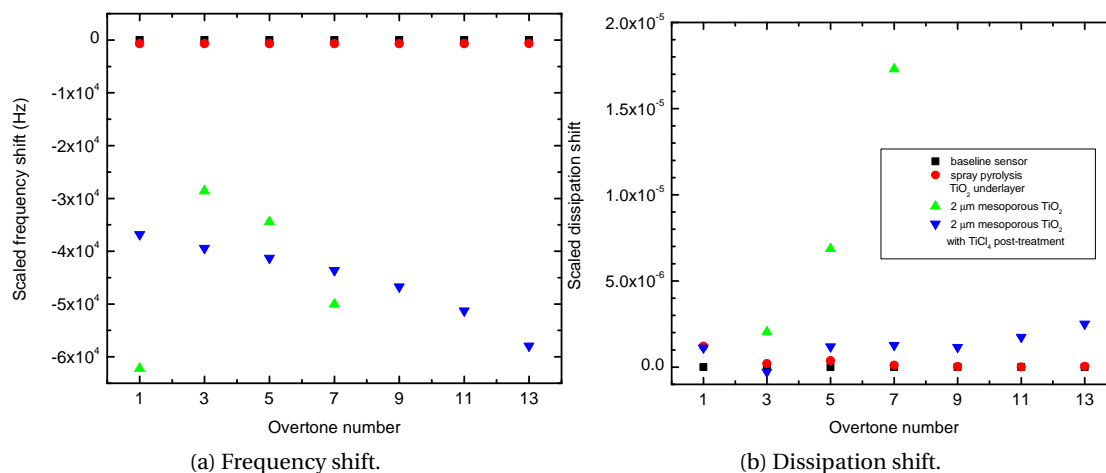


Figure 4.8 – (a) Scaled difference of resonance frequency over the different overtones after each fabrication step of a 2 μm mesoporous TiO<sub>2</sub> film, relative to the frequency of the pristine sensor. Part (b) Shows the according difference of dissipation over the different overtones.

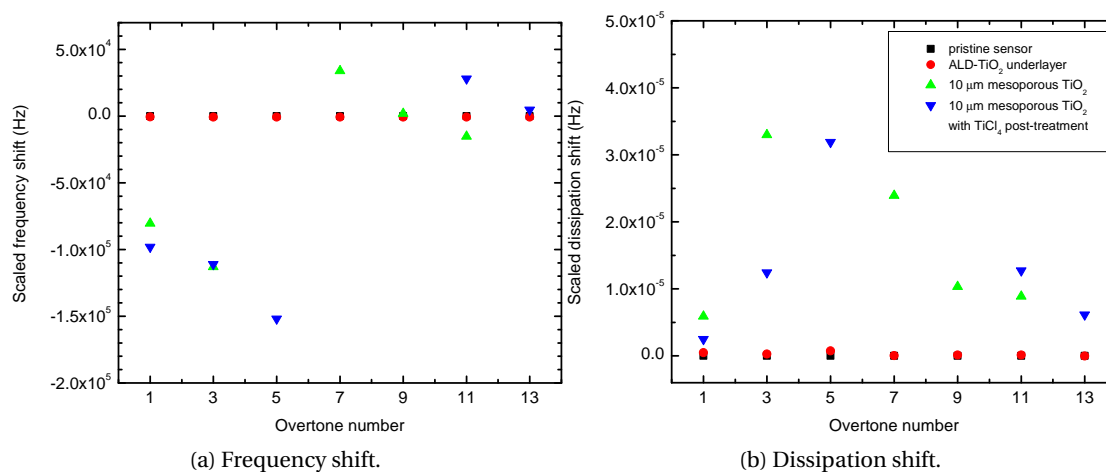


Figure 4.9 – (a) Scaled difference of resonance frequency over the different overtones after each fabrication step of a 10 μm mesoporous TiO<sub>2</sub> film, relative to the frequency of the pristine sensor. Part (b) Shows the according difference of dissipation over the different overtones.

#### 4.3.2 QCM-D during dye adsorption on 10 $\mu\text{m}$ thick mesoporous $\text{TiO}_2$

To explain the frequency shifts observed upon dye loading of mesoporous films, we first discuss the behaviour of the overtones 1, 3 and 5 of the 10  $\mu\text{m}$  thick mesoporous film, see figure 4.10. The QCM-D characterisation of the film during fabrication is displayed in figure 4.9, and the response of overtones 1, 3 and 5 to dye loading with ullazine dye JD21 from ethanol-THF solution is displayed in figure 4.10 (the same as in figure 4.1 (c)). In the ethanol-THF (4:1)<sub>vol</sub> reference solution, the higher overtones of the sensor could not be detected.

The fundamental resonance shows qualitatively the same behaviour as we would expect for a flat film, but with a larger frequency shift due to higher mass uptake inside the mesoporous film, attaining  $-2000$  Hz during dye exposure, and  $-1800$  Hz after 10 min of rinsing. Meanwhile, the dissipation behaves similar as on a flat film since dye solvent and reference solvent are the same in this case. At higher overtone frequency (3rd and 5th) however, we observe an immediate and initially linear upshift in dissipation until a plateau is reached, indicating that dye adsorption has reached an equilibrium. Note that this plateau is reached for all overtone on both, frequency and dissipation at the same time. This plateau is at a value of  $1.0 \cdot 10^{-4}$  for the 3rd overtone and at  $7.0 \cdot 10^{-4}$  for the 5th overtone, the latter showing considerable noise. The frequency meanwhile, on the 3rd overtone decreases to lower values of  $-1100$  Hz and then shifts upwards to its plateau at  $-800$  Hz. The frequency of the 5th overtone decreases to about  $-800$  Hz in the first 5 min and then rises steeply to reach its quasi-plateau at  $+6000$  Hz. Upon rinsing, the dissipation on the 3rd and 5th overtone slightly decreases, and so does their frequency.

It is rather unusual that frequency increases when the mass of the adsorbed film increases. However, this can be explained by evaluating the dissipation, which corresponds to the damping of the oscillation. If dissipation attains very high values, like the 5th overtone does in our example with  $7.0 \cdot 10^{-4}$  in liquid, this implies that the oscillation is greatly suppressed, and suggests that detection of the resonance reaches its limit for a given driving amplitude. This is also confirmed by the high noise level on the QCM-D signals of the 5th overtone during and after dye exposure. The reason for this damping will be discussed separately at the end of this section. For the moment we simply observe that there is a significant damping on the higher overtone, which we can detect by the dissipation.

Since the damping is almost strong enough to completely suppress the resonance, it will have an influence on the sensing length of the resonance, to such extent that the resonance may not sense the entire mesoporous film any more, but only a part of it. As damping (dissipation) increases, the sensing length retreats into the mesoporous film. This causes the frequency to shift upwards to positive values, since only the mass of the mesoporous film within its sensing length is detected.

This explains the behaviour of the 3rd and the 5th overtone in figure 4.10 upon dye loading of the 10  $\mu\text{m}$  thick mesoporous  $\text{TiO}_2$  film.

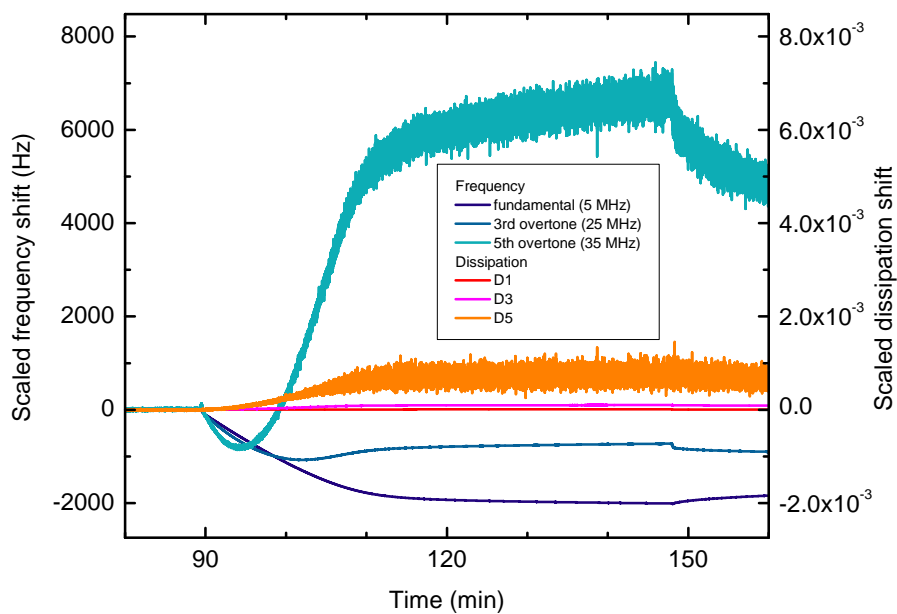


Figure 4.10 – Scaled QCM-D shifts of frequency (blue) and dissipation (red) of overtones 1,3 and 5 upon loading of a 10  $\mu\text{m}$  thick mesoporous  $\text{TiO}_2$  film with ullazine dye JD21 from a 0.2 mM solution in ethanol-THF (4:1)<sub>vol</sub> against a ethanol-THF (4:1)<sub>vol</sub> reference solution.

### 4.3. Mesoporous films of more than 2 $\mu\text{m}$ thickness

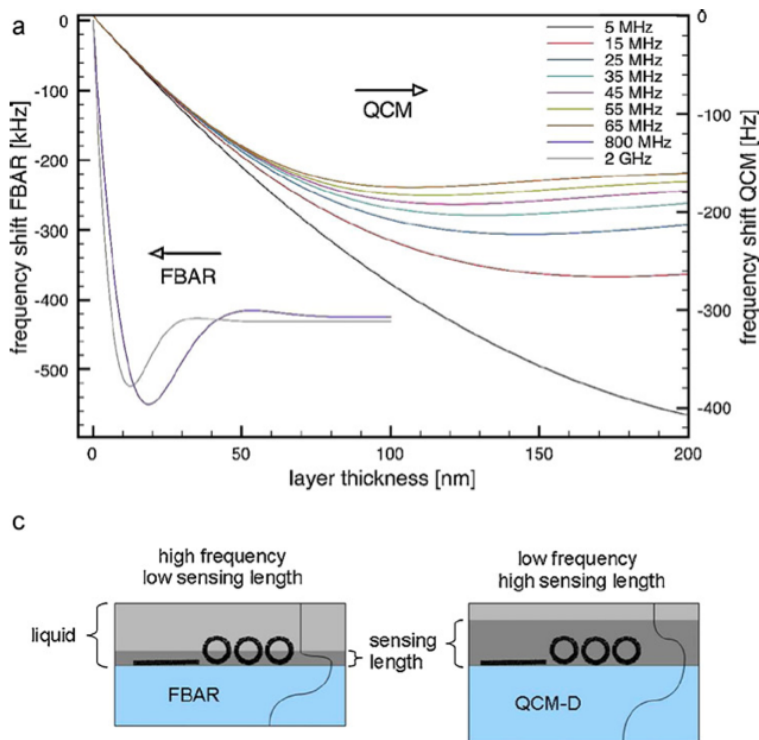


Figure 4.11 – Illustration of the sensing length for different frequencies. Calculation of the frequency shift for GHz-frequency FBAR sensors and MHz-frequency QCM-D sensors by Nirschl et al. [86] for the loading with a viscoelastic film (a). The lower part shows a schematic drawing sensing length for different frequencies (b). Figure taken from Nirschl et al. [86]

Similar upshifts of frequency due to changes in sensing length have been calculated by Nirschl et al. when comparing FBAR devices operating in the GHz range to QCM-D operating in the MHz range. To illustrate the idea, the according excerpt from the publication is displayed in figure 4.11.

### 4.3.3 Resonant coupling to a 10 $\mu\text{m}$ thick mesoporous $\text{TiO}_2$ film

An increase of dissipation and a damping of the oscillation is often related to the coupling of the QCM-D sensor to a viscous film or a viscous liquid. However, this is not the case for the mesoporous  $\text{TiO}_2$  film. As we have seen from films with thickness below 200 nm, they behave like rigid films.

We recall the surprising observation from figure 4.9 that in air, the scaled dissipation shift of the mesoporous film relative to the pristine sensor, seems to approach a maximum at medium overtone frequencies, and goes back to lower values for higher overtone frequencies. Simultaneously, the scaled frequency decreases with increasing overtone frequency, but after the dissipation passed its maximum, the scaled frequency shift jumps to a positive value higher than the initial frequency, and decreases again slightly.

This peculiar behaviour has a flagrant similarity with a particular phenomena in semiconductor optics: the coupling between electromagnetic radiation and phonon modes of a dielectric material. Two well-known interactions of this kind are the Reststrahlen band and the phonon-polariton as described in semiconductor textbooks [134].

For illustration of this analogy, an example of the Reststrahlen band for THz radiation in GaAs is displayed in figure 4.12. It describes the complete reflection of electromagnetic radiation in a certain frequency range due to its coupling to optical phonon modes in a dielectric bulk material. Figure 4.12 contains the expression for the dielectric function  $\epsilon(\omega)$  which describes the propagation of transversal electromagnetic waves in a dielectric medium, here with the coupling to transversal and longitudinal optical phonons. The right part of the same figure 4.12 shows plots of the real part and the imaginary part of the dielectric function. What catches the eye is the way in that the real part  $-\text{Re}(\epsilon(\omega))$  resembles the scaled frequency shift we observed for depositing the 10  $\mu\text{m}$  mesoporous  $\text{TiO}_2$  film as a function of driving frequency, see figure 4.9 and 4.14. Furthermore, the imaginary part  $\text{Im}(\epsilon(\omega))$ , which corresponds to the absorption of electromagnetic radiation, resembles very much to the peak of the scaled dissipation shift as a function of driving frequency.

Keep in mind that dissipation shifts larger than  $5 \cdot 10^{-5}$  correspond to a damping of the resonance below the noise level *in air*. We can therefore not detect any of the quartz crystal overtones in the vicinity of the resonance  $\omega_T$  of the mesoporous  $\text{TiO}_2$  film.

Although the idea may seem far-fetched, it was this analogy that made me consider the possibility of a coupling of the QCM-D driving frequency to an acoustic resonance frequency of the 10  $\mu\text{m}$  mesoporous  $\text{TiO}_2$  film.

In principle, we should be able to observe a similar behaviour for the interaction between transversal acoustic waves and the acoustic phonon modes in the mesoporous  $\text{TiO}_2$ . We note that the term "phonon" is not correct in this context, because it refers to a quantised lattice vibration in a crystal which is described as a quasi-particle. However, in the most general sense, the interaction is described as a coupling between harmonic oscillators, i.e. the coupling between the quartz crystal microbalance and an eigenfrequency of the attached mesoporous film.



### 4.3. Mesoporous films of more than 2 μm thickness

- mit **Dämpfung**  $\gamma$  (Zerfall optisches Phonon über anharmonische WW):

$$\varepsilon(\omega) = \varepsilon_{\infty} \left[ 1 + \frac{\omega_L^2 - \omega_T^2}{\omega_T^2 - \omega^2 - i\gamma\omega} \right]$$

- Beispiel GaAs:  
 $\varepsilon_{\infty} = 11.0$ ,  $\gamma = 7.2 \times 10^{10} \text{ s}^{-1}$ ,  
 $\omega_T = 8.06 \text{ THz}$ ,  $\omega_L = 8.76 \text{ THz}$

- spektrale Reflektivität  $R(\omega)$ :

$$R(\omega) = \frac{|\sqrt{\varepsilon(\omega)} - 1|}{|\sqrt{\varepsilon(\omega)} + 1|}$$

- nahezu perfekte Reflexion zwischen  $\omega_L$  und  $\omega_T$   
 → "Reststrahlenbande"

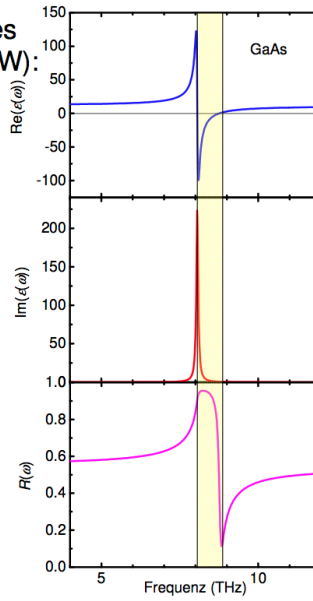


Figure 4.12 – The interaction between transversal electromagnetic waves and optical phonons in a dielectric material leads to a band of perfect reflectance the reststrahlenbande, in which the electromagnetic wave cannot penetrate the material. Here: THz radiation on GaAs. Taken from the course on semiconductor physics of Prof. A. Leitenstorfer [67].

In the context of QCM measurements, this has actually been described in 1985 by Dybwad [25] for the coupling of an attached sphere to a resonator plate. More recently, this description has also been adapted for separated, attached microspheres on a QCM sensor in liquid environment by Johannsmann *et al.* [96]. In our case of the attached mesoporous films, the situation may be slightly different, because we probably observe coupling to vibrational modes of the entire matrix and not of individual particles. However, we can still keep the same formal description as in [96]. In order to keep the notation consistent with existing literature, we here use the half bandwidth at half maximum  $\Gamma$  of the resonance instead of the dissipation  $D$ , which relate to each other by  $\Gamma = \frac{D \cdot f}{2}$ . The coupled-resonance model describes the shift of the complex resonance frequency  $\Delta f^* = \Delta f + i\Delta\Gamma$  by

$$\begin{aligned} \frac{\Delta f + i\Delta\Gamma}{f_F} &= \frac{N_S m_S \omega}{\pi Z_q} \cdot \frac{(\omega_S^2 + i\omega\gamma)}{(\omega^2 - \omega_S^2 - i\omega\gamma)} \\ &= \frac{-N_S m_S \omega}{\pi Z_q} \cdot \frac{1}{\left(1 - \frac{\omega^2}{\omega_S^2 + i\omega\gamma}\right)} \end{aligned} \quad (4.12)$$

$f_F$  is the unloaded resonance frequency,  $N_S$  and  $m_S$  are the number density per area and mass of the attached individual spheres and  $\omega_S$  is their resonance frequency.  $Z_q$  is the acoustic impedance of the quartz crystal, and  $\gamma$  describes the damping by decay through anharmonic interaction. In our case of an attached mesoporous film of several  $\mu\text{m}$  thickness, the expression

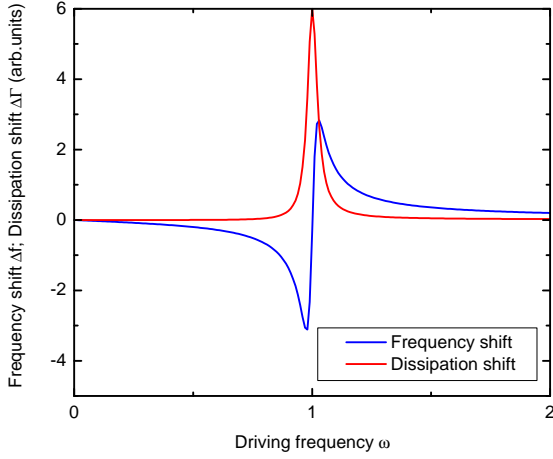


Figure 4.13 – Illustration of  $\delta f$  and  $\delta D$  as a function of driving frequency  $\omega$  when coupling to a resonance at  $\omega_T = 1$ . This is a calculation based on equation 4.14, using  $\frac{-d \cdot \rho_{\text{film}}}{\pi Z_q} = 0.3$ ,  $\omega_T = 1$  and  $\gamma = 0.05$ .

becomes

$$\frac{\Delta f + i\Delta\Gamma}{f_F} = \frac{d \cdot \rho_{\text{film}} \cdot \omega}{\pi Z_q} \cdot \frac{(\omega_T^2 + i\omega\gamma)}{(\omega^2 - \omega_T^2 - i\omega\gamma)} \quad (4.13)$$

The area mass of the film is given by the product of its thickness  $d$  and its overall density  $\rho_{\text{film}}$ . The vibrational mode of the film to which we couple has the frequency  $\omega_T$ , and we suspect that the coupling happens primarily to transversal waves since we drive the crystal in shear motion. Figure 4.13 displays an exemplary plot of the real and imaginary part of equation 4.13. By expanding equation 4.13 with  $\frac{(\omega^2 - \omega_T^2) + i\omega\gamma}{(\omega^2 - \omega_T^2 - i\omega\gamma)}$ , we can separate real and imaginary part more clearly:

$$\begin{aligned} \frac{\Delta f + i\Delta\Gamma}{f_F} = & \frac{d \cdot \rho_{\text{film}} \cdot \omega}{\pi Z_q} \cdot \frac{(\omega_T^2 - \gamma^2) \cdot \omega^2 - \omega_T^4}{(\omega^2 - \omega_T^2)^2 + \gamma^2 \omega^2} \\ & + i \cdot \frac{d \cdot \rho_{\text{film}}}{\pi Z_q} \cdot \frac{\gamma \cdot \omega^4}{(\omega^2 - \omega_T^2)^2 + \gamma^2 \omega^2} \end{aligned} \quad (4.14)$$

For small  $\gamma$ , the shift of frequency and dissipation diverge in a singularity for driving frequencies close to the vibrational mode of the attached film at  $\omega \approx \omega_T$ . Note that equation 4.13 shows that the sign of the frequency shift  $\delta f$  is changing when the singularity is crossed. For driving frequencies  $\omega < \omega_T$ , an increase in mass will lead to a decrease of frequency, meanwhile for driving frequencies  $\omega > \omega_T$ , an increase in mass will lead to an increase in frequency. For driving frequencies  $\omega \ll \omega_T$ , equation 4.14 actually becomes the Sauerbrey equation, and the

loading can be described as an inertial loading, see reference [96] and references therein. For driving frequencies  $\omega \gg \omega_T$  the loading is sometimes called elastic loading.

In order to illustrate the validity of the above expression for our measured data, I have performed a manual fit of an equation similar to 4.14 to the QCM-D shift of frequency and dissipation measured on different overtone frequencies upon deposition of the mesoporous film. The manual fit to the QCM-D data is displayed in figure 4.14.

Equation 4.14 needs to be adapted to be fit to the QCM-D data. First, all above QCM-D data is in *scaled* frequency shift  $\Delta f/n$  and scaled dissipation shift  $\Delta D/n$ , with the overtone number  $n$ . The frequency of each resonance  $f_F$  in equation 4.13 and 4.14 relates to the overtone number  $n$  and the fundamental resonance frequency  $f_0 \approx 4.95 \cdot 10^6$  Hz by  $f_F = n \cdot f_0$ . Thus, the real part of equation 4.14 describes the scaled frequency shift and can be written as

$$\Delta f/n = f_0 \cdot \frac{d \cdot \rho_{\text{film}} \cdot \omega}{\pi Z_q} \cdot \frac{(\omega_T^2 - \gamma^2) \cdot \omega^2 - \omega_T^4}{(\omega^2 - \omega_T^2)^2 + \gamma^2 \omega^2} + y_0 \quad (4.15)$$

I introduced a vertical offset  $y_0$  to the frequency shift, because the mesoporous  $\text{TiO}_2$  film is in rigid contact with the QCM-D sensor, and will thus always lead to an inertial loading which is similar to the Sauerbrey loading. Equation 4.14 is a simplified description and by itself is only valid for a resonator attached by a point contact to a QCM crystal.

The imaginary part of equation 4.14 gives the scaled dissipation shift, using the relation  $\Delta D = 2\Gamma/f_F$

$$\Delta D/n = \frac{2f_0}{\omega} \cdot \frac{d \cdot \rho_{\text{film}}}{\pi Z_q} \cdot \frac{\gamma \cdot \omega^4}{(\omega^2 - \omega_T^2)^2 + \gamma^2 \omega^2} \quad (4.16)$$

In the last equation I used a continuous expression for the overtone number,  $n = \omega/f_0$ .

In figure 4.14 (a), I have performed a manual fit of equation 4.15 to the frequency shift measured on different overtone frequencies upon deposition of the mesoporous film, as well as a simultaneous, manual fit of equation 4.16 to the shift of dissipation (b). Using the impedance of AT-cut quartz  $Z_q = 8.8 \cdot 10^6 \text{ kg m}^{-2} \text{ s}^{-1}$ , the density of dry mesoporous (58% porosity) anatase  $\rho = 0.42 \cdot 3.9 \cdot 10^3 \text{ kg m}^{-3} = 1.64 \cdot 10^3 \text{ kg m}^{-3}$  and thickness  $d = 10.0 \cdot 10^{-3} \text{ m}$  of the film, we can estimate the frequency of the vibrational mode in the mesoporous  $\text{TiO}_2$  film without  $\text{TiCl}_4$  post-treatment as  $\omega_T \approx 22 \text{ MHz}$  with an anharmonic damping factor of  $\gamma \approx 0.13 \cdot 10^6 \text{ s}^{-1}$ . For the mesoporous  $\text{TiO}_2$  film with  $\text{TiCl}_4$  post-treatment, the respective values are  $\omega_T \approx 35 \text{ MHz}$  and  $\gamma \approx 0.12 \cdot 10^6 \text{ s}^{-1}$ . The vertical offset of the frequency shift was  $y_0 = -44.6 \cdot 10^3 \text{ Hz}$  for the untreated mesoporous  $\text{TiO}_2$  film and  $y_0 = -58.2 \cdot 10^3 \text{ Hz}$  for the  $10 \mu\text{m}$  mesoporous  $\text{TiO}_2$  film with  $\text{TiCl}_4$  treatment.

Keep in mind that dissipation shifts larger than  $5 \cdot 10^{-5}$  correspond to a damping of the resonance below the noise level *in air*. We can therefore not detect any of the quartz crystal

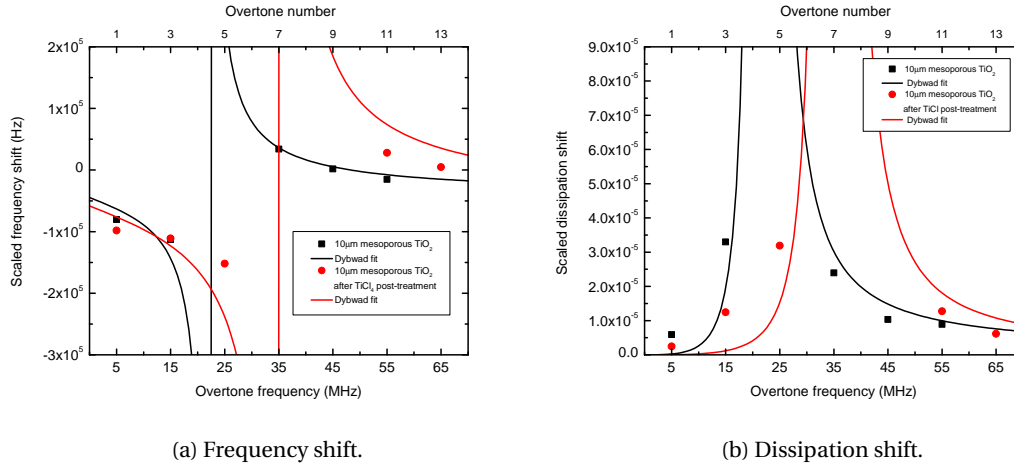


Figure 4.14 – Scaled QCM-D signal for different overtones on 10 μm thick mesoporous TiO<sub>2</sub>. Squares represent the measured shift of frequency and dissipation before and after deposition of the mesoporous film; the lines are fitted curves based on equations 4.15 and 4.16. TiCl<sub>4</sub> treatment of the mesoporous TiO<sub>2</sub> film improves interconnectivity between the nanoparticles and thereby leads to a stiffening of the film, resulting in higher resonance frequencies.

overtones in the vicinity of the resonance  $\omega_T$  of the mesoporous TiO<sub>2</sub> film.

The characteristic dispersion of frequency and dissipation shown in figure 4.14, clearly indicates the coupling to a resonance of the mesoporous TiO<sub>2</sub> film. However, the large offset suggests that equation 4.14 is only a simplified description of the system and the negative offset points to an additional contribution from inertial loading. This makes sense, since our film is rigidly attached to the QCM-D sensor. For a more realistic description, the acoustic impedance matching between the materials has to be taken into account, which would lead to an additional scaling factor.

Although the fitting needs a lot of further improvement, it does describe our data quite well. The only adjustable parameters were the resonance frequency  $\omega_T$  of the mesoporous TiO<sub>2</sub> film, the anharmonic damping factor  $\gamma$  and the frequency offset  $y_0$ ; all other values were taken from literature.

The nature of this resonance of the mesoporous TiO<sub>2</sub> film is accessible by considering the way it is excited and by its dependence on film thickness. The excitation by the shear waves of the QCM-D suggests efficient coupling to transversal acoustic waves. I speculate that the eigenfrequency is simply given by the thickness  $d$  of the mesoporous TiO<sub>2</sub> film and its transversal sound velocity  $v_T$ , similar to the resonance frequency of the quartz crystal itself. The fundamental eigenfrequency  $\omega_T$  of the mesoporous TiO<sub>2</sub> film should relate to the transversal sound velocity and the film thickness by

$$\omega_T = \frac{v_T}{2 \cdot d} \quad . \quad (4.17)$$

### 4.3. Mesoporous films of more than 2 $\mu\text{m}$ thickness

---

For the measured resonance frequency of 35 MHz of the  $\text{TiCl}_4$  post-treated mesoporous  $\text{TiO}_2$  film of 10  $\mu\text{m}$  thickness, this would give a transversal sound velocity of

$$v_T = 2 \cdot d \cdot \omega_T = 700 \text{ m s}^{-1} \quad . \quad (4.18)$$

This sound velocity is about one fifth of the literature value for single-crystalline anatase  $\text{TiO}_2$ ,  $v_T(\text{TiO}_2, \text{anatase, averaged}) = 3560 \text{ m s}^{-1}$  [17]. Note that the eigenfrequency shifts to higher frequency as the film stiffens with  $\text{TiCl}_4$  treatment, and that stiffening produces an increase in sound velocity.

Although equations 4.15 and 4.16 only describe the QCM-D data in a simplified manner, we can gain qualitative understanding of the measurements on mesoporous films. The fact that the resonance of the film with  $\text{TiCl}_4$  post-treatment is of a higher frequency than that of the untreated film corresponds well to the fact that the  $\text{TiCl}_4$  treatment does improve particle connectivity by necking, which in turn should lead to a stiffening of the film and to higher sound velocity. At the same time, the  $\text{TiCl}_4$  treatment adds a small amount of mass, which is visible as a downshift of frequency at the low overtones.

We can now explain the measurements of dye uptake on the 10  $\mu\text{m}$  thick mesoporous  $\text{TiO}_2$ , which we presented earlier in this section. We recall that we measured a dissipation shift to very high values upon loading with dye, and I concluded that the amplitude was damped so much that only part of the mesoporous film was sensed. Equations 4.15 and 4.16 show how the increase in mass, or in this case density of the mesoporous film, leads to a linear increase in dissipation, i.e. a damping of the oscillation.

## 4.4 Conclusion

This chapter contained exemplary measurements and explanations in order to understand and interpret the QCM-D signals that are recorded on mesoporous TiO<sub>2</sub> films. The findings are summarised below. The first paragraph concerns thin mesoporous films of up to 200 nm thickness, which show regular inertial loading and which allow for an archimedic measure of molecules adsorbed inside the mesoporous matrix. The second paragraph explains the particularities of thick mesoporous TiO<sub>2</sub> films of 2 μm thickness and more, which show a coupling of the quartz crystal driving frequency to an eigenmode of the mesoporous TiO<sub>2</sub> film. Our findings can be the basis for a future, systematic study in order to obtain a set of methods to create standard sensing applications employing mesoporous films in general.

**QCM-D and fluorescence on thin mesoporous TiO<sub>2</sub> films** The QCM-D measurement in section 4.2.2 clearly shows that almost the entire liquid inside thin mesoporous TiO<sub>2</sub> films is trapped and adds to its measured area mass. We can therefore confirm the indications from the previous section 4.2.1, that the adsorption of molecules inside the mesoporous film replace solvent molecules, and lead to a QCM-D signal that corresponds to an archimedic measure of the mass of the adsorbed molecules:

$$\Delta f \propto \Delta m_{\text{monolayer,flat}} + \underbrace{(\rho_{\text{adsorbate}} - \rho_{\text{solvent}}) \cdot V_{\text{ads}}}_{\Delta m_{\text{inside pores}}} . \quad (4.19)$$

With the exemplary measurement in section 4.2.2 we have further demonstrated a method to determine the volume inside the pores directly by QCM-D, which could be applied in order to measure the total volume of the adsorbed molecules  $V_{\text{ads}}$  inside the mesoporous film. The sensitivity can be enhanced by choosing a solvent of low density. Mesoporous films will be particularly useful when employed on QCM-D sensors in gas phase rather than liquid phase.

Further measurements should be carried out in order to confirm the presented example, with the aim of reducing the error margin. This requires the use of pure solvents, and an independent measurement of their density.

In principle, these measurements allow for a very precise measurement of the density of an unknown liquid by using only a very small quantity, if the area volume  $V_{\text{pores,liq}}$  has been determined accurately. The technical resolution of the QCM-D can attain 0.3 Hz on flat film [26]. On the 200 nm mesoporous film in the example above, a difference in frequency shift  $\delta f$  of 1 Hz would correspond to difference in density of 0.0014 g/cm<sup>3</sup>. The total sample volume would be determined by the specifications of the QCM-D flow chamber. In this way, measuring the density could equally be used to measure the concentration of a known solvated species that does not adsorb on the surface.

For high-precision measurements, the constituting material of the mesoporous film should be chosen with care, because differences in liquid-solid-adhesion-energy might eventually influence the QCM-D signal. Surface-associated solvent molecules are known to form a structured layer in the vicinity of the surface, which will have an influence on the density [104, 119].

The internal surface area, the trapped volume and their ratio to the interface with the overlying bulk liquid can all be changed in a systematic way by changing porosity, particle size and thickness of the mesoporous film. The chemistry of the constituting material can be modified in various ways, in particular by atomic layer deposition.

It will be of further help to characterise the thickness and porosity of the mesoporous film directly on the sensor by ellipsometry [65].

**Viscoelastic response of mesoporous films of 2  $\mu\text{m}$  thickness and more** The characteristic dispersion of frequency and dissipation shown in figure 4.14, clearly indicates the coupling to a resonance of the mesoporous  $\text{TiO}_2$  film. In a simple case, such coupling to an attached resonator can be described by an equation of the form

$$\frac{\Delta f + i\Delta\Gamma}{f_F} = \frac{d \cdot \rho_{\text{film}} \cdot \omega}{\pi Z_q} \cdot \frac{(\omega_T^2 + i\omega\gamma)}{(\omega^2 - \omega_T^2 - i\omega\gamma)} \quad (4.20)$$

This equation describes our data qualitatively well if we add a negative offset for the frequency shift. This equation is a simplified description of the system. The necessity of a negative frequency offset implies an additional inertial loading. Furthermore, the acoustic impedance matching between the materials should be taken into account.

Nevertheless, we can gain qualitative understanding of the measurements on mesoporous films. The fact that the resonance of the film with  $\text{TiCl}_4$  post-treatment is of a higher frequency than that of the untreated film corresponds well to the fact that the  $\text{TiCl}_4$  treatment does improve particle connectivity by necking, which in turn should lead to a stiffening of the film and to higher sound velocity. At the same time, the  $\text{TiCl}_4$  treatment adds a small amount of mass, which is visible as a downshift of frequency at the low overtones.

We can furthermore explain the measurements of dye uptake on the 2  $\mu\text{m}$  and 10  $\mu\text{m}$  thick mesoporous  $\text{TiO}_2$ . Equation 4.14 shows how the increase in mass, or in this case density of the mesoporous film, leads to an linear increase in dissipation, i.e. a damping of the oscillation. The amplitude seems to be attenuated to such extend, that only part of the mesoporous film is within the sensing length once the dye loading is completed. Since the sensing length is retreating into the film during dye loading, this can lead to an upshift of frequency upon mass loading on overtones with high dissipation.

The presented measurements are of preliminary nature, and further measurements for different film thickness of mesoporous films of good quality are needed.

#### **Chapter 4. QCM-D with mesoporous titanium dioxide films**

---

However, since we are aware that we couple to the eigenfrequencies of the mesoporous film, we can adjust them accordingly. Strong coupling to eigenmodes is often not desired. This can be avoided by pushing can be avoided by either limiting the thickness of the film, or by enhancing its stiffness, the latter offering interesting applications of scaffolds other than colloidal films.

For sensing applications there are the same points of interest as for thin mesoporous films, especially for applications in the gas phase.



# 5 Conversion of thin lead iodide films to perovskites by exposure to methylammonium iodide

*This chapter is based on a recent QCM-D study on the conversion and back-conversion between  $\text{PbI}_2$  and  $\text{CH}_3\text{NH}_3\text{PbI}_3$  perovskite. It is supplemented by ICP-MS, SEM and XRD measurements that were conducted by Michaël Bensimon, CEL group, EPFL, as well as Nicolas Tétreault and Norman Pellet at the LPI, EPFL. Its content will form the basis of a publication that is in preparation [43].*

## 5.1 Introduction to perovskites in photovoltaic devices

I present a study of the conversion reaction of a  $\text{PbI}_2$  film to  $\text{CH}_3\text{NH}_3\text{PbI}_3$  perovskite by exposure to solution of  $\text{CH}_3\text{NH}_3\text{I}$  in isopropanol in general, and its reversibility in particular. Many scientists were not aware that the above conversion reaction is reversible. The back-conversion is release of methylammonium iodide from the perovskite film into selective solvents and the crystallization of  $\text{PbI}_2$  on the substrate.

I focus on the conversion reaction of films deposited on flat compact titania films. Quantitative data is drawn from relative mass changes measured in-situ by a quartz-crystal microbalance with dissipation technique. Elemental analysis is carried out by inductive-coupling plasma mass spectrometry (ICP-MS) of the outflowing solvent from the QCM-D chamber, and morphological changes are monitored by SEM imaging. Changes in crystal structure are confirmed by XRD.

### 5.1.1 General introduction

Historically, perovskites refer to the crystalline structure of calcium titanate  $\text{CaTiO}_3$ , which was discovered by Gustav Rose and named after the Russian mineralogist Lev Perovski [127]. The name has since been given to any compound that crystallises in a similar way as  $\text{CaTiO}_3$ , and has a structure of  $\text{ABX}_3$  for 3-dimensional perovskites or  $\text{A}_2\text{BX}_4$  for 2-dimensional perovskites. Usually A designates a large cation, B a smaller cation, and X is an anion, usually an oxygen or a halide. Details are explained in the next section 5.1.2.

## Chapter 5. Conversion of thin lead iodide films to perovskites by exposure to methylammonium iodide

---

A variety of perovskite materials have attracted interest because of their exceptional properties, which are often the result of mixed elemental composition and structural distortions with respect to the archaic structure of  $\text{CaTiO}_3$ . Examples include  $\text{SrTiO}_3$  as an intrinsic quantum paraelectric material [82], mixed-valance perovskite manganites that show colossal magneto resistance [52], and high-temperature super conductors like  $\text{YBa}_2\text{Cu}_3\text{O}_{7-x}$  [8]. The latter was discovered by Bednorz and Müller at *IBM Rueschlikon* in 1986 and earned them the Noble Prize in physics only one year later.

Hybrid organic-inorganic perovskites employ an organic cation, and they were first studied by Weber et al. in the 1970s, and more intensely in the 1990s by Mitzi and co-workers at *IBM Watson Research Centre* [125, 79]. In contrast to the above-mentioned traditional perovskites that usually require high temperatures or pressures for processing, hybrid organic-inorganic perovskites are mostly solution-processable close to room temperature. Many compositions lead to the formation of 2-dimensional perovskites  $\text{A}_2\text{BX}_4$ , which result in a layered structure and do in principle impose no limitations on the size of the organic cation A. Changing the cation allows for tuning of many of the material properties, mainly a metal to semiconductor transition, but the 2-dimensional structure imposes a strong anisotropy which is not necessarily desired. There is a limited number of 3-dimensional hybrid organic-inorganic perovskites  $\text{ABX}_3$ , and recently, attention has been drawn to a class of perovskites that employs a methylammonium anion A, a group-IV metal,  $\text{B}=\text{Pb}$  or  $\text{Sn}$ , and a halide  $\text{X}=\text{I}$ ,  $\text{Br}$  or  $\text{Cl}$ .

The application of hybrid organic-inorganic methylammonium metal halide perovskites in photovoltaic cells has gained significant importance over the last two years, mainly due to the surge in published power conversion efficiency from 3.8% in 2009 up to 17.9 % certified efficiency in 2014 [62, 47, 59, 66, 28, 12, 101, 88]. The concept of using a perovskite material in the device architecture of a solid-state dye sensitized solar cell can be seen as a result of the search for inorganic absorber materials other than quantum dots or  $\text{Sb}_2\text{S}_3$ , which can fulfil a similar function as a molecular absorber in a dye sensitized solar cell. Methylammonium lead iodide has proven the most successful material yet, and size estimations of the constituting lattice by Mashiyama et al. as well as by Mitzi et al. suggest that it forms more stable crystals than other methylammonium lead halides [78, 75]. Methylammonium tin halide perovskites are less stable than their lead counterparts due to the facile oxidation of  $\text{Sn}^{2+}$  to  $\text{Sn}^{4+}$ .

One route to high-efficiency devices employs a sequential deposition of a  $\text{PbI}_2$  film that is subsequently converted to  $\text{CH}_3\text{NH}_3\text{PbI}_3$  perovskite by incorporation of methylammonium iodide ( $\text{CH}_3\text{NH}_3\text{I}$  or MAI) from solution. This route, which often gives better morphological control over the resulting film than a one-step deposition of the perovskite, was first successfully demonstrated on a mesoporous titania film by Burschka *et al.* [12], attaining

record efficiencies of 15 %. More recently, the sequential deposition has been adapted to the conversion of  $\text{PbI}_2$  films on compact titania and zinc oxide films, which are solution-processed at low temperatures and yield power conversion efficiencies of 13.7 % and 15.7 %, respectively [132, 69].

The following introduction on perovskites and their conversion is based on the recent PhD thesis of Julian Burschka [10].

### 5.1.2 Perovskite structure

Historically, perovskites refer to the crystalline structure of calcium titanate  $\text{CaTiO}_3$ , which was discovered by Gustav Rose and named after the Russian mineralogist Lev Perovski [127]. The name has since been given to any compound that crystallises in a similar way to  $\text{CaTiO}_3$ , and has a structure of  $\text{ABX}_3$  for 3-dimensional perovskites or  $\text{A}_2\text{BX}_4$  for 2-dimensional perovskites. Usually A designates a large cation, B is a smaller cation, and X is an anion, usually an oxygen or a halogen atom.

Figure 5.1 illustrates the crystal structure of the ideal perovskite. The ideal  $\text{ABX}_3$  compound crystallises in a cubic unit cell with the larger cation A in its centre, and the smaller cation B located at the corners. The smaller cation B is octahedrally coordinated to the anions X that lie at the centre of the edges of the cubic unit cell. In inorganic-organic hybrid perovskites, there is often a competition between the 3-dimensional perovskite structure  $\text{ABX}_3$ , and the 2-dimensional perovskite structure  $\text{A}_2\text{BX}_4$  because of the size difference between the organic cation A and the inorganic cation B. The 2-dimensional perovskite consists of corner-sharing  $\text{BX}_6$  octahedra that are separated by a double layer of organic cations A. This layered structure does in principle impose no limitations on the size of the organic cation A, and the resulting tunability of the material has been investigated in detail by Mitzi et al. in the 1990s at the *IBM Watson Research Centre*.

The synthesis of phase-pure organic-inorganic hybrid perovskites can be difficult, and methylammonium is one of the few organic cations that readily crystallises in a 3-dimensional perovskite structure when used in a lead-halide or tin-halide compound. Methylammonium tin halide perovskites are less stable than their lead counterparts because of the facile oxidation of  $\text{Sn}^{2+}$  to  $\text{Sn}^{4+}$ . Regarding the different methylammonium lead-halide perovskites, the iodide compound  $\text{CH}_3\text{NH}_3\text{PbI}_3$  has attracted the most interest for photovoltaic applications due to its low bandgap and good stability.

## Chapter 5. Conversion of thin lead iodide films to perovskites by exposure to methylammonium iodide

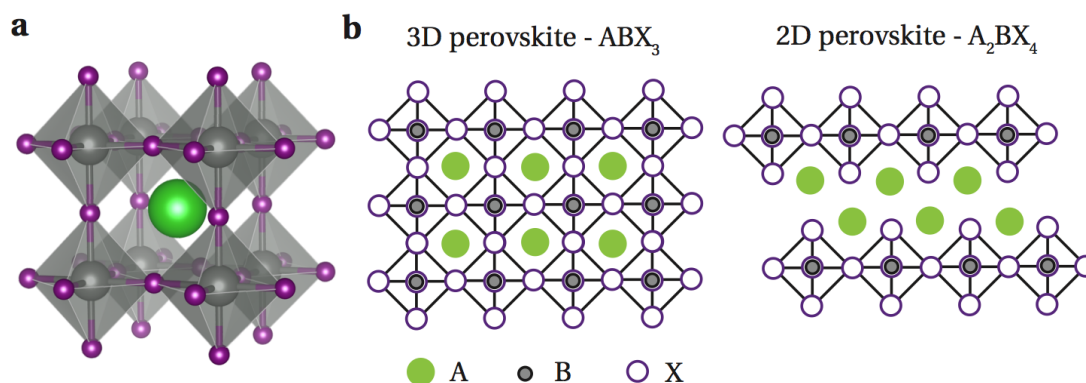


Figure 5.1 – A perspective view of the perovskite  $ABX_3$  crystal structure is shown in part (a). Projected views of the 3-dimensional  $ABX_3$  perovskite and the 2-dimensional  $A_2BX_4$  perovskite crystal structure are given in (b). With permission from Burschka [10].

### 5.1.3 Methylammonium lead iodide perovskites for photovoltaic applications and their synthesis by conversion from lead-iodide salt

For photovoltaic applications, methylammonium lead iodide ( $CH_3NH_3PbI_3$ ) is the perovskite compound that has attracted the most attention. This is due to its low band gap, its high stability, and its good solubility in polar solvents for processing. The direct bandgap of  $CH_3NH_3PbI_3$  is 1.54 eV which corresponds to an absorption onset at approximately 800 nm. In a typical solar cell configuration, the perovskite absorber is in contact with a  $TiO_2$  on one side, which can act as an electron-selective contact and as an n-type conductor. The other side of the perovskite is contacted with a hole transport material that also acts as a hole-selective contact, usually spiro-MeOTAD (2,2',7,7'-tetrakis(*N,N*-di-*para*-methoxyphenyl-amine)-9-9'-spirobifluorene). Figure 5.2 shows the a simplified energy diagram for this configuration with the relevant energy levels against vacuum. The valence band of the  $CH_3NH_3PbI_3$  was measured to be  $-5.4$  eV against vacuum by ultraviolet photoelectron spectroscopy [59]. Considering the optical bandgap of 1.54 eV, the valence band lies around  $-3.9$  eV against vacuum. If we use the published value of  $-4.0$  eV for the  $TiO_2$  conduction band, and of  $-5.1$  eV for the valence band of spiro-MeOTAD, we obtain an offset of 0.1 eV between the conduction bands of the perovskite and the  $TiO_2$ , and 0.3 eV between the valence band of the perovskite and the spiro-MeOTAD. The valence band and conduction band of the  $CH_3NH_3PbI_3$  perovskite are formed only by the orbitals of Pb and I, whereas the organic cation has no direct contribution. The organic anion however influences the structure of the perovskite crystal and thereby indirectly influences the overlap between the orbitals of Pb and I and thus the optoelectronic properties of the material.

The crystal phase of  $CH_3NH_3PbI_3$  depends on temperature, and three different phases have been observed [4]. The ideal cubic perovskite phase prevails at temperatures above  $54^\circ C$ , and allows for rapid reorientation of the methylammonium cation that can occupy 24 different disordered states [57]. Between  $54^\circ C$  and  $-112^\circ C$ , the  $PbI_2$  octahedra undergo a tilting around

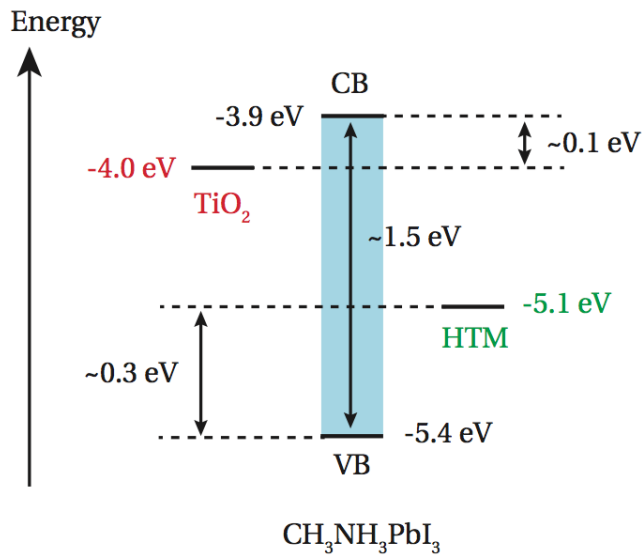


Figure 5.2 – Simplified energy diagram, illustrating the conduction and valence band of the perovskite as well as the conduction band of  $\text{TiO}_2$  and the valence band of the hole transport material spiro-MeOTAD. All energy levels are given in eV against vacuum level. With permission from Burschka [10].

the  $c$ -axis of the crystal and thereby reduce the structure to a tetragonal phase. Limiting the number of disordered states of the methylammonium cation to 8 possibilities. Below  $-112^\circ\text{C}$ , the  $\text{CH}_3\text{NH}_3\text{PbI}_3$  crystallises in an orthorhombic phase, and the alignment of the methylammonium anion is fixed. For the  $\text{CH}_3\text{NH}_3\text{PbI}_3$  material, no 2-dimensional phase of the form  $\text{A}_2\text{BX}_4$  has been observed.

For a single-step deposition methods, the perovskite is usually processed by dissolving two precursors,  $\text{CH}_3\text{NH}_3\text{I}$  and  $\text{PbI}_2$ , in polar organic solvents like  $\gamma$ -butyrolactone or  $N,N$ -dimethylformamide (DMF). The  $\text{CH}_3\text{NH}_3\text{PbI}_3$  perovskite readily crystallises at room temperature upon evaporation of the solvent. However, it can be difficult to control the film morphology or the infiltration of mesoporous films when crystallising the perovskite material directly from solution. In order to achieve a better control of film morphology, Burschka et al. further developed a previously discovered method of sequential deposition [12, 68] in two steps. First, a  $\text{PbI}_2$  film is deposited by spin-casting a concentrated  $\text{PbI}_2$  solution in DMF. In a second step, the  $\text{PbI}_2$  film is exposed to a solution of methylammonium iodide in a solvent that does not dissolve the  $\text{PbI}_2$ , i.e. isopropanol. The process is illustrated in figure 5.3.

In general, two-step-depositions which entail a conversion reaction are often used to template a certain morphology. One example from literature is the conversion of II-V semiconductor nanostructures to III-V materials by ion exchange reactions whilst maintaining the initial nanomorphology [68]. In those examples, the thermodynamic driving force was the difference

## Chapter 5. Conversion of thin lead iodide films to perovskites by exposure to methylammonium iodide

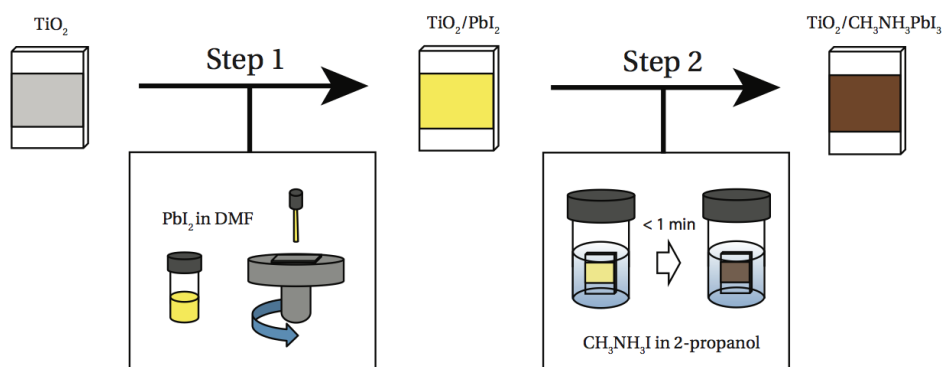


Figure 5.3 – Schematic illustration of the sequential deposition technique in two steps. First, a  $\text{PbI}_2$  film is spin-cast from a solution of DME. Subsequently, the film is immersed in a solution of  $\text{CH}_3\text{NH}_3\text{I}$  in isopropanol for less than one minute. In our experimental work, a pre-wetting with isopropanol has been applied prior to the second step. With permission from [10].

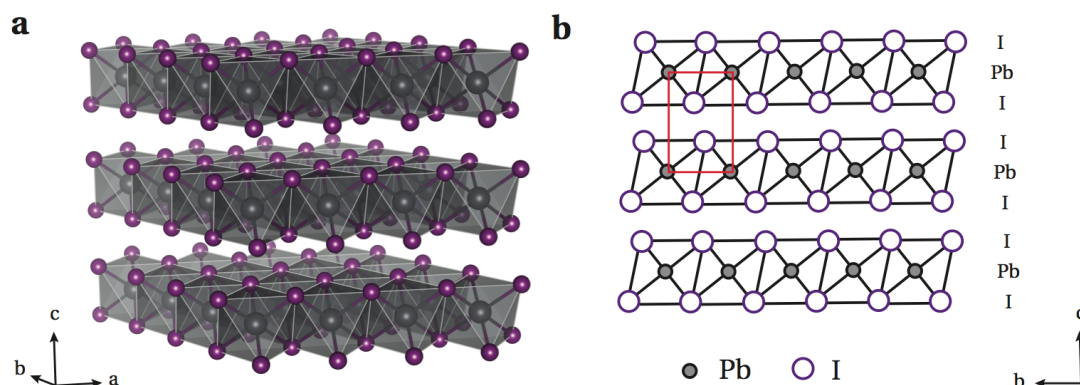


Figure 5.4 – Illustration of the layered  $\text{PbI}_2$  crystal structure in the hexagonal 2H polytype. (a) is a perspective view and (b) shows a projection along the  $a$ -axis. With permission from [10].

in bulk lattice energy between the different compounds.

Here, the starting material  $\text{PbI}_2$  is itself a well-studied semiconductor [29].  $\text{PbI}_2$  crystallises in layers of edge-sharing  $\text{PbI}_6$  octahedra, which lead to strong intralayer bonding in a hexagonal crystal lattice, but only weak interlayer bonding, which allows for the formation of different polytypes for the stacking of layers. Figure 5.4 is an illustration of the crystal structure of  $\text{PbI}_2$  in the most prevalent layer stacking of the 2H polytype.

Concerning the conversion reaction, the weak interlayer bonding seems to allow for rapid intercalation of guest molecules into the  $\text{PbI}_2$  crystal, and this is the reason for the relatively fast conversion reaction from  $\text{PbI}_2$  to the  $\text{CH}_3\text{NH}_3\text{PbI}_3$  perovskite. This conversion results into a two-fold increase of volume per formula, as can be estimated from the lattice parameters for  $\text{PbI}_2$  and  $\text{CH}_3\text{NH}_3\text{PbI}_3$  that are listed in table 5.1. The literature values of the density are  $6.16 \text{ g cm}^{-3}$  for  $\text{PbI}_2$  and  $4.22 \text{ g cm}^{-3}$  for  $\text{CH}_3\text{NH}_3\text{PbI}_3$ .

## 5.1. Introduction to perovskites in photovoltaic devices

Table 5.1 – Comparison of the crystal lattice parameters of  $\text{PbI}_2$  and the tetragonal phase of  $\text{CH}_3\text{NH}_3\text{PbI}_3$ . Adapted from [10], based on literature data [125, 4, 20].

		$\text{PbI}_2^a$	$\text{CH}_3\text{NH}_3\text{PbI}_3^b$
Crystal system		Trigonal	Tetragonal
Space group		P3m1	I4/mcm
Lattice parameters (Å)	$a$	4.558	8.874
	$b$	4.558	8.874
	$c$	6.986	12.67
Formula for unit cell volume		$a^2c \sin(60^\circ)$	$a^2c$
Unit cell volume ( $\text{Å}^3$ )	$V$	125.7	997.9
Formula units per unit cell	$Z$	1	4
Volume per formula unit	$V/Z$	125.7	249.5
Molecular weight ( $\text{g mol}^{-1}$ )	$M$	461.0	620.0
Density <sup>c</sup> ( $\text{g cm}^{-3}$ )	$\rho$	6.090 (6.16)	4.127 (4.22)

### 5.1.4 Sample preparation and characterisation

The sample preparation aimed for producing perovskite films by sequential deposition as illustrated in figure 5.3 in the previous section. I decided to use  $\text{PbI}_2$  and perovskite films on an underlayer of flat, compact  $\text{TiO}_2$  as a model system. The details of  $\text{PbI}_2$  deposition and conversion to the perovskite were adapted from the procedure used by Yella et al. [132].

**Compact  $\text{TiO}_2$  underlayer.** Prior to deposition of the mesoporous  $\text{TiO}_2$  film, the QCM-D sensor or the silicon substrate is cleaned, and an underlayer of thin, compact  $\text{TiO}_2$  of approximately 20 nm thickness is deposited. One method applied was atomic layer deposition (ALD) from a tetrakis (dimethylamino)titanium precursor at  $150^\circ\text{C}$  as described in [114] with subsequent annealing for 3 hours at  $420^\circ\text{C}$ . Alternatively, the underlayer was applied by spray-pyrolysis of an ethanolic solution of di-iso-propoxy titanium-bis(acetylacetonate) with an added amount of acetylacetonate, using oxygen as a carrier gas for the aerosol [77, 56, 109], and heating the substrate at  $420^\circ\text{C}$  during deposition.

**Deposition of the  $\text{PbI}_2$  film.** The  $\text{PbI}_2$  was dissolved in  $N,N$ -dimethylformamide at a concentration of  $600 \text{ mg ml}^{-1}$  by heating the solution to  $120^\circ\text{C}$  under occasional stirring. Subsequently, the solution was cooled down to  $70^\circ\text{C}$ . For deposition of an approximately 200 nm thick  $\text{PbI}_2$  film on a flat, compact  $\text{TiO}_2$  underlayer,  $50 \mu\text{l}$  of solution were applied to the sample by spin-casting at 6000 RPM for 30 s, using an acceleration of  $4500 \text{ RPM s}^{-1}$ , and by repeating this procedure once. The entire preparation was carried out in a dry air box.

**QCM-D measurement of the conversion and back-conversion.** For QCM-D measurements, the sensor with the  $\text{PbI}_2$  film was transferred in a closed sample box with dry silica gel from the drybox to the QCM-D setup, where humidity was kept under 5% for most of the time. After

## Chapter 5. Conversion of thin lead iodide films to perovskites by exposure to methylammonium iodide

---

mounting the sensor, the flow cell was flushed with pure isopropanol and signal acquisition was re-started soon after the filling of the chamber. After approximately 10 min of rinsing with isopropanol, the liquid handling system was switched to the solution of  $8 \text{ mg ml}^{-1}$   $\text{CH}_3\text{NH}_3\text{I}$  in isopropanol, which had been prepared previously in a dry box. In order to achieve a rapid exchange of solvent inside the liquid handling system without creating a concentration gradient, the solvent was flushed in at the maximum pump speed for about 30 s. The maximum pump speed is approximately  $800 \mu\text{l min}^{-1}$ . The same procedure was applied when changing back to pure isopropanol. The usual nominal pump speed during the experiment was  $100 \mu\text{l min}^{-1}$ . The experiment in section 5.2.2 will show that increasing this regular nominal pump speed to  $500 \mu\text{l min}^{-1}$  does not significantly affect the reaction kinetics in our experiment. We can therefore assume that the kinetics monitored here are not limited by depletion of species from or their accumulation in the solvent.

**Humidity control on the QCM-D setup.** The technical details of the QCM-D *E4* machine and the setup of the flow cell have been explained previously in the introduction. In order to keep humidity low, but maintain easy access to the liquid handling system, the QCM-D machine was placed in a plexiglas box that was flushed with large currents of dry air and had a large hatch for manipulations. At 35% ambient humidity in the lab, the humidity inside the box was below 5% when the hatch was closed. Upon opening the hatch for manipulations, the humidity would jump up to 20%, but go back down to 5% within 30 s after closing the hatch.

**Samples for SEM and XRD.** The films for SEM imaging were prepared on Si wafer substrates, that had been coated with a  $\text{TiO}_2$  underlayer just as the QCM-D sensors by ALD or by spray-pyrolysis, and the  $\text{PbI}_2$  film was deposited in the same way as above unless otherwise mentioned. Sample preparation then continued in a dry air box in analogy to those in the QCM-D experiment: pre-wetting in isopropanol for 10 min, approximately 50 s of immersion in  $0.8 \text{ mg ml}^{-1}$   $\text{CH}_3\text{NH}_3\text{I}$  in isopropanol, and rinsing with isopropanol for 5 min. Different samples were taken out of the process at each stage of interest, e.g. after conversion to the perovskite, solvent was removed by spin-coating at 4000 RPM for 30 s and subsequent drying at  $70^\circ\text{C}$  on a hotplate. The samples were stored in dry air for less than 24 hours and transferred to the SEM facility in a closed box filled with dry air and silica gel. After SEM imaging, the same samples were further used for XRD analysis.

It should be noted that on pre-wet samples the conversion is often irregular across large sample surface areas and visible conversion often started from the edge of the sample of from the tweezers holding the sample. The irregularities only equal out after 50 s of  $\text{CH}_3\text{NH}_3\text{I}$  exposure on flat, compact, pre-wet  $\text{TiO}_2$  films.



## 5.2 Overview of the conversion and back-conversion

### 5.2.1 Quantitative overview by QCM-D

A QCM-D measurement of the conversion from  $\text{PbI}_2$  to  $\text{CH}_3\text{NH}_3\text{PbI}_3$  perovskite comes along with the refreshing pleasure of a large and well reproducible signal. Figure 5.5 shows an exemplary measurement, starting from a 200 nm thick  $\text{PbI}_2$  film that is rinsed with plain isopropanol.

During this rinse, which corresponds to a pre-wetting situation, a small but continuous up-drift of approximately +40 Hz in 10 min is observed. This is insignificant compared to the overall mass of the  $\text{PbI}_2$  film, which corresponds to ca. 6600 Hz in frequency shift, and elemental analysis of the outflow suggest that small amounts of iodide are dissolved, but no lead. After  $t = 720$  s in the same figure 5.5, the film is exposed to  $8 \text{ mg ml}^{-1}$   $\text{CH}_3\text{NH}_3\text{I}$  in isopropanol, resulting in a stark drop in frequency by  $-1000$  Hz. This drop corresponds to the incorporation of  $\text{CH}_3\text{NH}_3\text{I}$  into the  $\text{PbI}_2$ , and to the according increase of mass. During the exposure to  $\text{CH}_3\text{NH}_3\text{I}$  for more than 60 s, we observe a small linear decrease in frequency, possibly corresponding to a much slower, continued incorporation of  $\text{CH}_3\text{NH}_3\text{I}$ . The XRD analysis in section 5.2.4 will reveal that we do indeed form the  $\text{CH}_3\text{NH}_3\text{PbI}_3$  perovskite, but that about half of the perovskite remains unconverted after 60 s of  $\text{CH}_3\text{NH}_3\text{I}$  exposure under these particular conditions. Simultaneously to the steep drop in frequency, dissipation shifts up by  $2.0 \cdot 10^{-5}$ , correlating with a change in film morphology, as SEM images in section 5.2.3 will show.

At  $t = 800$  s, we start rinsing again with pure isopropanol until the end of the displayed measurement. Almost instantly, frequency starts to shift upwards in an approximately linear manner until it reaches a sudden plateau at a constant value of  $-70$  Hz after 180 s, close to its initial value. The dissipation goes through a maximum of  $5.0 \cdot 10^{-5}$ , before going back to a value of  $1.8 \cdot 10^{-5}$ . The linear upshift of frequency and the sudden transition to a constant value indicates the dissolution of a species to a certain minimum. XRD measurements in section 5.2.4 and ICP-MS analysis in section 5.2.2 show that this corresponds indeed to the complete dissolution of  $\text{CH}_3\text{NH}_3\text{I}$  and the recrystallisation to the  $\text{PbI}_2$  salt. The particular behaviour of the dissipation correlates again with a change in film morphology as observed by SEM in sections 5.2.3 and 5.4. This shift in dissipation will be addressed along with the effect of  $\text{PbI}_2$  film morphology on QCM-D signals in section 5.2.5.

The conversion and back-conversion reaction, as depicted in figure 5.5, can be repeated several times on the same film, and the  $\text{PbI}_2$  itself can be subsequently dissolved in *N,N*-dimethylformamide (DMF) as demonstrated in figure 5.6. The details of repetitive conversion and back-conversion between  $\text{PbI}_2$  and  $\text{CH}_3\text{NH}_3\text{PbI}_3$  perovskite will be discussed in detail in section 5.3.

Here, we just note that the dissolution of  $\text{PbI}_2$  in DMF, as shown in figure 5.6 from  $t = 3500$  s onwards, leads to an increase in frequency of +6600 Hz when keeping isopropanol as a reference. This allows us to estimate the amount of  $\text{PbI}_2$  in the film and compare it to the amount of  $\text{CH}_3\text{NH}_3\text{I}$  incorporated during conversion to the  $\text{CH}_3\text{NH}_3\text{PbI}_3$  perovskite.

## Chapter 5. Conversion of thin lead iodide films to perovskites by exposure to methylammonium iodide

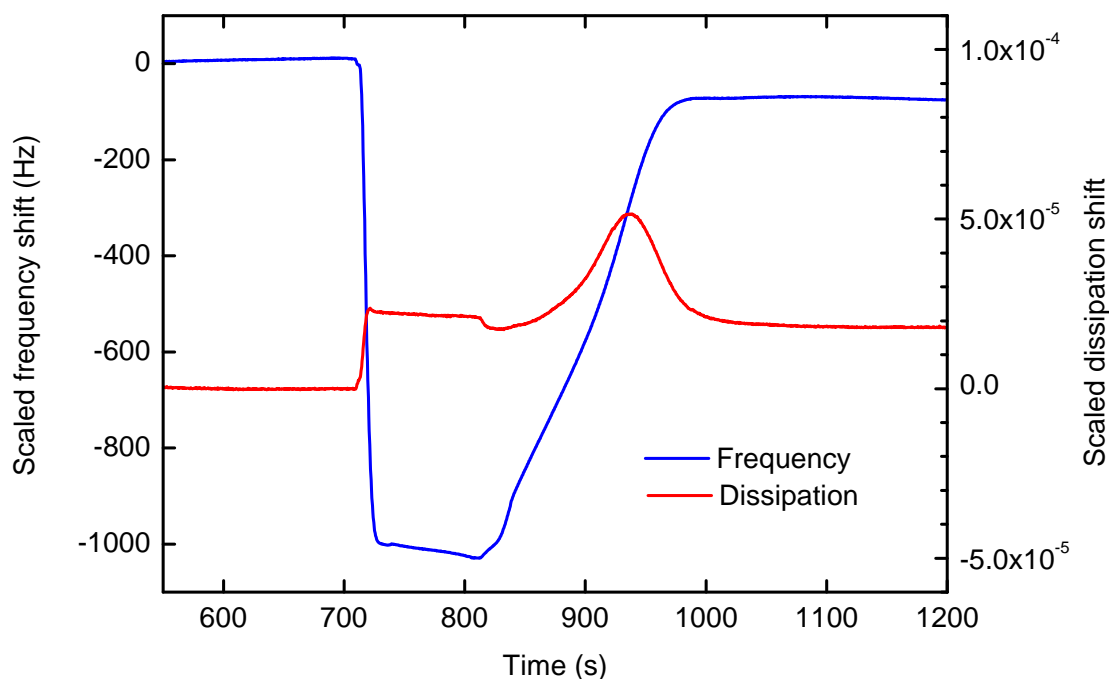


Figure 5.5 – QCM-D signal of the conversion of a  $\text{PbI}_2$  film to  $\text{CH}_3\text{NH}_3\text{PbI}_3$  perovskite by exposure to a  $\text{CH}_3\text{NH}_3\text{I}$  solution in isopropanol, and the subsequent back-conversion by exposure to isopropanol.

In order to make a rough estimate of the amount of incorporated  $\text{CH}_3\text{NH}_3\text{I}$ , we note from the QCM-D measurement in figure 5.5 that the decrease in frequency is approximately  $-1100$  Hz, which corresponds to a change in Sauerbrey mass of  $+19.25 \cdot 10^{-6} \text{ g cm}^{-2}$ . If we consider that the initial  $\text{PbI}_2$  is porous and assume that the  $\text{CH}_3\text{NH}_3\text{PbI}_3$  perovskite is not, then we should account for the amount of isopropanol adding to the wet mass of the initial  $\text{PbI}_2$  film, which will be discussed in detail in section 5.2.5. The amount of trapped isopropanol is  $0.97 \cdot 10^{-6} \text{ g cm}^{-2}$ , and the true mass of the incorporated  $\text{CH}_3\text{NH}_3\text{I}$  should thus be approximately  $20.22 \cdot 10^{-6} \text{ g cm}^{-2}$ . Using the molecular weight of  $\text{mw}_{\text{CH}_3\text{NH}_3\text{I}} = 159 \text{ g mol}^{-1}$ , we obtain an amount of  $0.127 \cdot 10^{-6} \text{ mol cm}^{-2}$  of incorporated  $\text{CH}_3\text{NH}_3\text{I}$  after conversion to the  $\text{CH}_3\text{NH}_3\text{PbI}_3$  perovskite for this type of preparation.

The dissolution of the back-converted  $\text{PbI}_2$  in DMF solvent does result in an increase of frequency by  $+6600$  Hz, which corresponds to a Sauerbrey mass of  $+115.50 \cdot 10^{-6} \text{ g cm}^{-2}$ . The isopropanol trapped inside the porous, back-converted  $\text{PbI}_2$  amounts to an area mass of approximately  $4.63 \cdot 10^{-6} \text{ g cm}^{-2}$ , and thus the dry mass of the  $\text{PbI}_2$  film should be around  $110.87 \cdot 10^{-6} \text{ g cm}^{-2}$ . Assuming that the  $\text{PbI}_2$  is stoichiometric, i.e. neglecting a possible excess of lead, we use the molar mass of  $\text{mw}_{\text{PbI}_2} = 461 \text{ g mol}^{-1}$  and estimate the amount of  $\text{PbI}_2$  in the film is approximately  $0.240 \cdot 10^{-6} \text{ mol cm}^{-2}$ .

The stoichiometry between  $\text{PbI}_2$  and  $\text{CH}_3\text{NH}_3\text{I}$  after conversion to the perovskite is thus approximately  $(2 : 1)_{\text{PbI}_2:\text{CH}_3\text{NH}_3\text{I}}$ , and not (1:1), as would be expected in the case of complete

## 5.2. Overview of the conversion and back-conversion

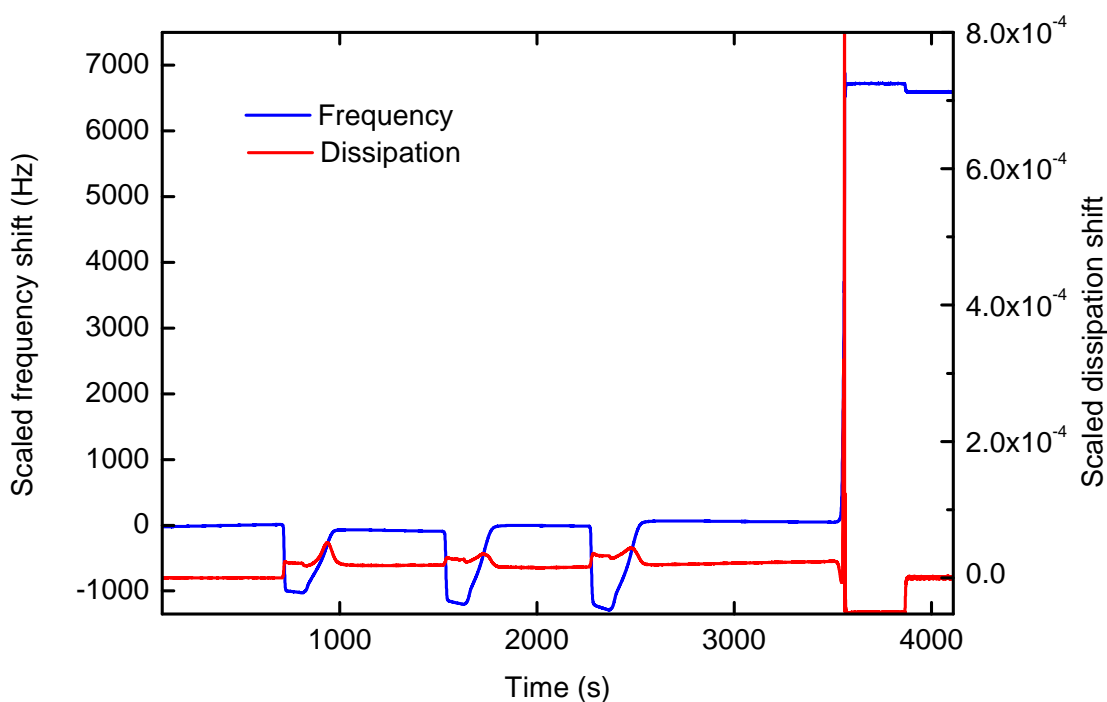


Figure 5.6 – QCM-D signal of the repetitive conversion of a  $\text{PbI}_2$  film to  $\text{CH}_3\text{NH}_3\text{PbI}_3$  perovskite, as well as the final dissolution of the  $\text{PbI}_2$  in DMF. Subsequent rinsing with isopropanol in order to account for effects of the bulk liquid on the QCM-D signal.

conversion. This ratio indicates that only half of the  $\text{PbI}_2$  has been converted to  $\text{CH}_3\text{NH}_3\text{PbI}_3$  during the initial exposure to  $\text{CH}_3\text{NH}_3\text{I}$ . This finding is in very good agreement with XRD data presented in section 5.2.4. The incomplete conversion on the flat, compact  $\text{TiO}_2$  underlayer is in agreement with the general experimental experience, that rapid complete conversion from liquid phase is only achieved for  $\text{PbI}_2$  films that are deposited on either mesoporous or very rough compact metal oxides.

We note that the correction made for the liquid trapped inside the pores is smaller than the variation that we observe between different samples made by the same procedure. Initial  $\text{CH}_3\text{NH}_3\text{I}$  incorporation produces frequency shifts between  $-950$  Hz and  $-1200$  Hz, and  $\text{PbI}_2$  dissolution leads to upshifts between  $+6000$  Hz and  $+7000$  Hz. These variations are probably due to variations in the morphology and thickness of the  $\text{PbI}_2$  film, and we have observed occasional irregularities of the dissolution of  $\text{PbI}_2$  in the DMF solution prior to spin-casting. We have further observed durations of the back-conversion process that range from 150 s to 250 s.

We have carried out the above QCM-D experiment using flat underlayers of  $\text{TiO}_2$  deposited by ALD or by spray pyrolysis, and we have found no systematic difference in the QCM-D signals for the conversion of the  $\text{PbI}_2$  or its re-dissolution.

## Chapter 5. Conversion of thin lead iodide films to perovskites by exposure to methylammonium iodide

---

### 5.2.2 Elemental analysis by ICP-MS

Elemental analysis of the outflowing liquid has been carried out by Dr. Michaël Bensimon, CEL group, EPFL. The measure of lead is very precise ( $\pm 1$  ppb) whereas the measure of iodide bears a large error.

The error on the iodide measure has several reasons. First, there is a certain fluctuation on its detection: when measuring different subsequent blank solutions, we find a variation of  $\pm 30$  ppb. Second, cleaning the measurement chamber after an iodide containing sample is tedious, because the substance leaves a significant memory effect over more than three subsequent measurements. Third, some of the iodide will undergo reactions and produce volatile compounds that will escape from the sample of liquid before it is transferred to the ICP-MS facility.

The QCM-D measurement used for collecting the outflow is shown in figure 5.7. This measurement was performed at a higher nominal pump speed of  $500 \mu\text{l min}^{-1}$  which is five times faster than the usual  $100 \mu\text{l min}^{-1}$ . The increased flow allowed us to avoid intermixing and uncontrolled dilution inside the tubings of the outflow. This was necessary because dissolution processes on the film take place within less than 2 min, and the specific sample had to be taken from the outflow accordingly.

Apart from the advantage in technical handling, this measurement shows that the QCM-D results are approximately the same for  $100 \mu\text{l min}^{-1}$  and  $500 \mu\text{l min}^{-1}$  nominal pump speed. Our conversion and back conversion reactions are therefore not limited by depletion or accumulation of chemical species in the flow chamber, which might influence reaction kinetics at very low flow speeds. The measurement dates from an earlier period, using  $10 \text{ mg ml}^{-1}$   $\text{CH}_3\text{NH}_3\text{I}$  in isopropanol.

In table 5.2 we present the results of the ICP-MS and the approximate concentration in the outflow, collected at a nominal pump speed of  $500 \mu\text{l min}^{-1}$ . The actual ICP-MS measurement was performed on samples diluted with an aqueous solution of 1 % nitric acid, in order to obtain measured concentrations in the range of 5 ppb to 500 ppb where precision of the ICP-MS setup is best.

The outflow during the rinsing of the initial  $\text{PbI}_2$  contained small traces of iodide, nominally 670 ppb, but almost no lead was detected (6 ppb). The outflow during exposure to the  $\text{CH}_3\text{NH}_3\text{I}$  solution has not been measured due to its excessive iodide content. Upon rinsing of the perovskite with pure isopropanol, the outflow during the significant mass loss,  $t = 850$  s to  $t = 1000$  s in the example in figure 5.5, was collected separately from the outflow after the signals had reached a plateau. The solution collected during the mass loss was of a high concentration of iodide, nominally  $2.8 \cdot 10^5$  ppb, but only a very small amount of lead (35 ppb). The outflow during the plateau seemed to contain some iodide, nominally 1220 ppb, and very little lead (23 ppb), which is very similar to the outflow from rinsing the initial  $\text{PbI}_2$  film. When, after prolonged rinsing with isopropanol, the film was dissolved by rinsing with DMF

## 5.2. Overview of the conversion and back-conversion

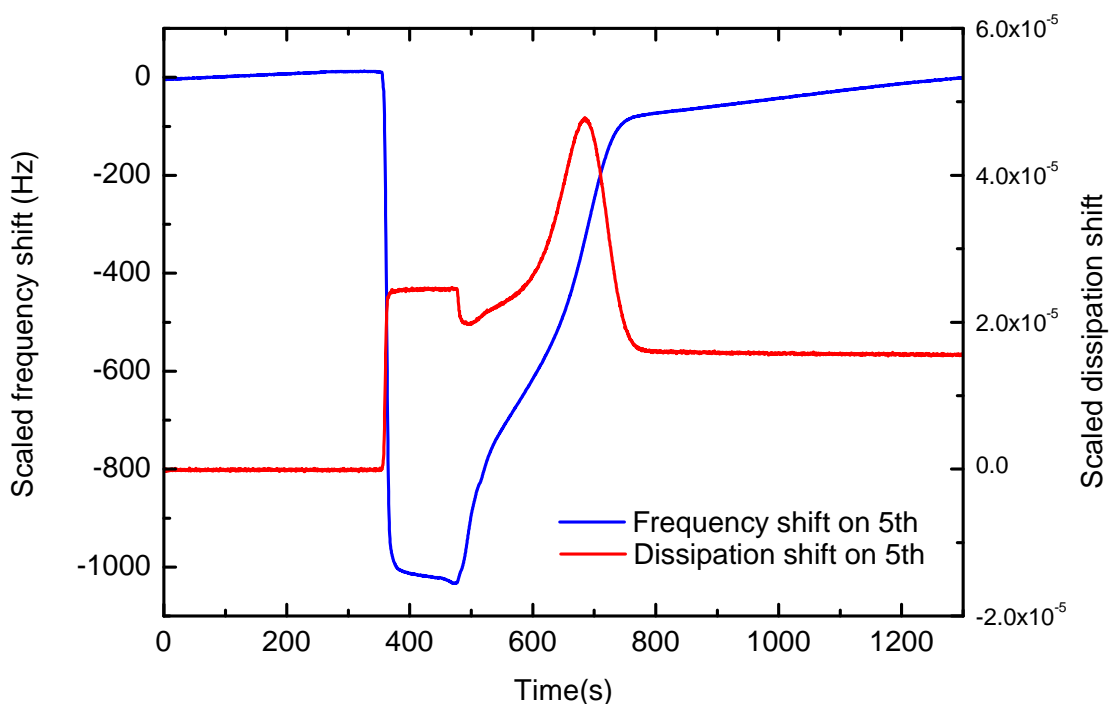


Figure 5.7 – QCM-D signal of the conversion of a  $\text{PbI}_2$  film to  $\text{CH}_3\text{NH}_3\text{PbI}_3$  perovskite by exposure to a  $10 \text{ mg ml}^{-1}$   $\text{CH}_3\text{NH}_3\text{I}$  solution in isopropanol, and the subsequent back-conversion by exposure to isopropanol. The outflow from this measurement was used for elemental analysis by ICP-MS; the nominal pump speed was  $500 \mu\text{l min}^{-1}$ .

Table 5.2 – Concentrations of the outflow during conversion and back-conversion obtained by inductive coupling plasma mass spectrometry (ICP-MS). As explained in the text, the concentration of iodide bears a large error, and numbers are understood as nominal values.

	Measured concentration on diluted sample		Dilution factor	Estimated concentration in outflow	
	c(I)	c(Pb)		c(I)	c(Pb)
Initial rinsing with isopropanol	67 ppb	0.6 ppb	x 10	670 ppb	6 ppb
Mass loss from $t = 500 \text{ s}$ to $t = 750 \text{ s}$	20224 ppb	2.5 ppb	x 14	$2.8 \cdot 10^5$ ppb	35 ppb
Rinsing with isopropanol on the plateau from $t = 850 \text{ s}$	122 ppb	2.3 ppb	x 10	1220 ppb	23 ppb
Final rinsing with DMF	27 ppb	48.5 ppb	> 125	–	–

## Chapter 5. Conversion of thin lead iodide films to perovskites by exposure to methylammonium iodide

---

as depicted in figure 5.6 at  $t = 3600$  s, the outflow contained large amounts of both, lead and iodide, in an approximate ratio (27 ppb : 48 ppb)<sub>I:Pb</sub>, which corresponds to a molar ratio of (1:2)<sub>I:Pb</sub>. This molar ratio is the reciprocal value of what is expected for stoichiometric  $\text{PbI}_2$ . However, the apparent yellow colour of the control sample, and the XRD measurement suggest that the back-converted  $\text{PbI}_2$  is mostly stoichiometric. This is an indication that the ICP-MS technique and the primary preparation lead to an underestimation of the iodide content.

### 5.2.3 Morphology by SEM

The morphology of the films was investigated by scanning electron microscopy by acquiring high-resolution images of the top view and of the cross-section. All images were taken by Dr. Nicolas Tétreault. As described in section 5.1.4, the films for SEM imaging were prepared on Si wafer substrates, that had been coated with approximately 20 nm  $\text{TiO}_2$  by ALD and subsequently annealed for 30 min at  $420^\circ\text{C}$ , so the underlayer was the same as for the QCM-D sensors. The  $\text{PbI}_2$  film was prepared the same way as on the on the QCM-D sensors, according to the procedure used by Yella et al. [132].

The samples were then prepared in a dry air box in analogy to those in the QCM-D experiment: pre-wetting in isopropanol for 5 min to 10 min, approximately 50 s of immersion in  $0.8 \text{ mg ml}^{-1}$   $\text{CH}_3\text{NH}_3\text{I}$  in isopropanol, and rinsing with isopropanol for 5 min. Different samples were taken out of the process at the stage of interest, e.g. after conversion to the perovskite, solvent was removed by spin-coating at 4000 RPM for 30 s and subsequent drying at  $70^\circ\text{C}$  on a hotplate.

Figure 5.8 shows SEM images of the initial  $\text{PbI}_2$  film, after conversion to the  $\text{CH}_3\text{NH}_3\text{PbI}_3$  perovskite, and after back-conversion to  $\text{PbI}_2$ .

The top view of the initial  $\text{PbI}_2$  film in figure 5.8 (a), which had been pre-wet in isopropanol for 10 min, shows a morphology that strongly reminds of morphologies obtained by phase-separation in polymer blends or of phase-separation in organic-inorganic mixtures. The latter may well be a driving force for the morphology we find, since we start from a highly concentrated mixture of  $\text{PbI}_2$  and DMF which is subsequently dried at  $70^\circ\text{C}$ . The typical domain size is between 100 nm and 200 nm, and the flat appearance on the top is a result of the double-spin-coating process. The side view in figure 5.8 (b) confirms the existence of up to 200 nm large pores, and the locally homogenous film thickness of slightly less than 200 nm. Pre-wetting of the  $\text{PbI}_2$  for 10 min did not change the film morphology significantly, compared to a non-wetted  $\text{PbI}_2$  film (image not shown). Pre-wetting for 30 min resulted in very slight changes of film morphology, seemingly having less pronounced edges than in the non-pre-wet film (image not shown).

Figure 5.8 (c) and (d) show the top and cross-sectional view of the film after conversion to the  $\text{CH}_3\text{NH}_3\text{PbI}_3$  perovskite by a 50 s immersion in  $0.8 \text{ mg ml}^{-1}$   $\text{CH}_3\text{NH}_3\text{I}$  in isopropanol. The SEM images show homogeneously distributed crystallites of cubic appearance, which have lateral dimensions of up to 500 nm and extend to a maximum height of about 300 nm from

## 5.2. Overview of the conversion and back-conversion

---

the surface of the TiO<sub>2</sub> underlayer. Although the cubic crystallites form large protrusions, the film does not show any visible pores.

The last set of figures 5.8 (e) and (f) show the PbI<sub>2</sub> film after back-conversion from the perovskite by rinsing for more than 5 min with pure isopropanol. The top view (e) reveals a homogenous distribution of up to 200 nm large platelets of hexagonal shape. Most of these platelets have a thickness of approximately 20 nm, though some of them are up to 80 nm thick. The cross-sectional view (f) suggests that the hexagonal platelets lie on top of a layer of smaller particles of a less regular shape. The overall thickness of the layer on this sample is about 350 nm.

The film morphology of the initial PbI<sub>2</sub> and the CH<sub>3</sub>NH<sub>3</sub>PbI<sub>3</sub> perovskite correspond very well to previously published results [132]. Since the back conversion has never been studied explicitly, the PbI<sub>2</sub> film after back-conversion is noteworthy for its drastic morphology change compared to the initial PbI<sub>2</sub> film. The shape of the particles points to a re-crystallisation process that leads to a larger crystallite size. This will be confirmed by XRD in the next section 5.2.4 and discussed in more detail in sections 5.3 and 5.4.

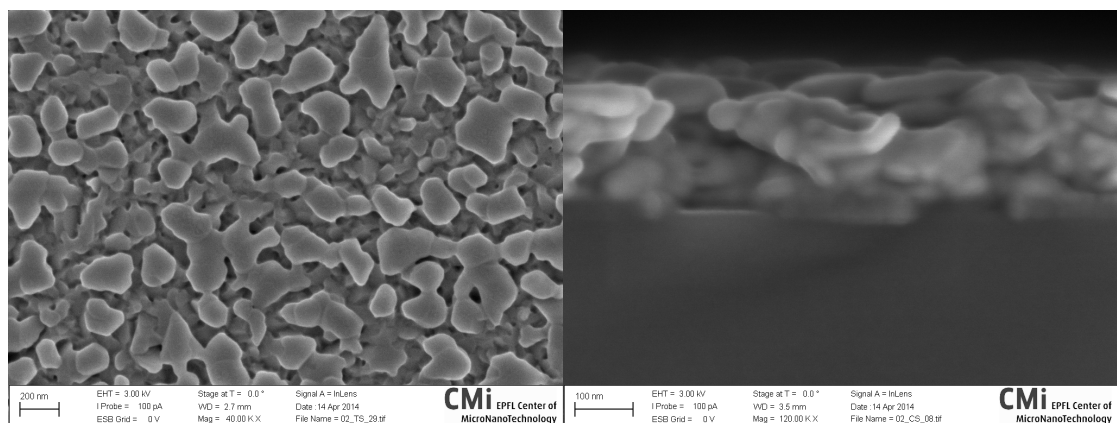
### 5.2.4 Structural analysis by XRD

The same samples that had been used for SEM imaging in the previous section 5.2.3 were subsequently taken for a crystallographic analysis by x-ray diffraction (XRD). These measurements were performed by Norman Pellet. Figure 5.9 shows the spectra of the initial, pre-wet PbI<sub>2</sub>, of the film after (partial) conversion to the CH<sub>3</sub>NH<sub>3</sub>PbI<sub>3</sub> perovskite by 50 s exposure to CH<sub>3</sub>NH<sub>3</sub>I, and of the film after back-conversion to PbI<sub>2</sub> by rinsing with pure isopropanol for more than 5 min. Furthermore, the spectra of a film during back-conversion is shown. In this case, the back-conversion was stopped by starting the drying process of spin-coating and heating after 150 s of rinsing the perovskite film in pure isopropanol. The according SEM picture of the sample is shown in figure 5.15 (a) and b in section 5.4 below.

An overview of the XRD spectra from  $2\theta = 10^\circ$  to  $2\theta = 60^\circ$  is shown in figure 5.9 (a). Figure 5.9 (b) shows a close-up of the PbI<sub>2</sub>-related peak at  $12.7^\circ$  and the CH<sub>3</sub>NH<sub>3</sub>PbI<sub>3</sub> perovskite-related peak at  $14.2^\circ$ , which are exemplary for all PbI<sub>2</sub> and perovskite peaks.

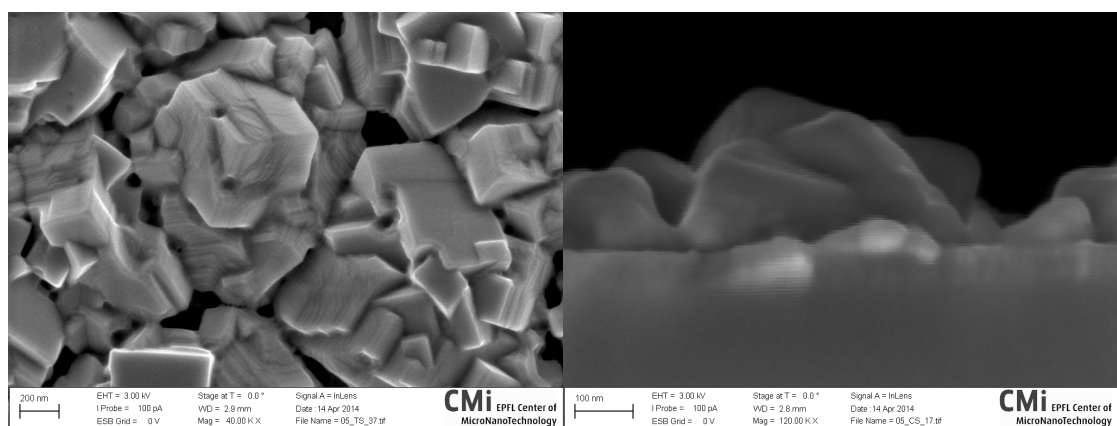
The initial PbI<sub>2</sub> peak at  $12.7^\circ$  has an intensity of 640 counts. After conversion to the perovskite, the PbI<sub>2</sub> peak at  $12.7^\circ$  decreases to half of its intensity (360 counts), indicating that only part of the crystalline PbI<sub>2</sub> material has been converted to the CH<sub>3</sub>NH<sub>3</sub>PbI<sub>3</sub> perovskite, which corresponds to the peak at  $14.2^\circ$ . We note that the perovskite peak is actually split into one lower peak at  $14.1^\circ$ , and a second, slightly higher peak at  $14.2^\circ$ . After 120 s of rinsing the perovskite with isopropanol, the back-conversion is not complete yet, as we know from the QCM-D measurements in the beginning of this chapter 5.2.1. However, the according XRD spectrum shows no more perovskite peaks, but a PbI<sub>2</sub> peak at  $12.7^\circ$ , which is of a higher inten-

## Chapter 5. Conversion of thin lead iodide films to perovskites by exposure to methylammonium iodide



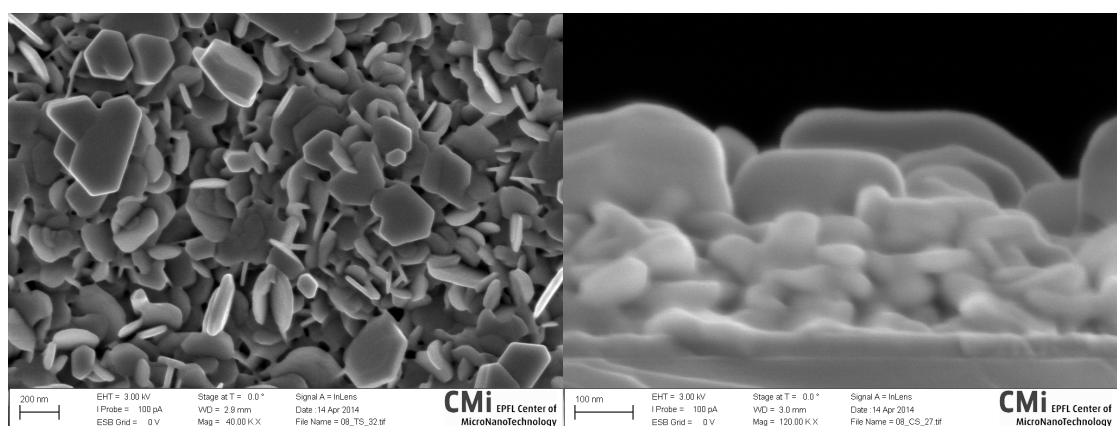
(a)  $\text{PbI}_2$  prior to conversion, top view 40 kX.

(b)  $\text{PbI}_2$  prior to conversion, cross-sectional view 120 kX.



(c)  $\text{CH}_3\text{NH}_3\text{PbI}_3$  after conversion, top view 40 kX.

(d)  $\text{CH}_3\text{NH}_3\text{PbI}_3$  after conversion, cross-sectional view 120 kX.



(e)  $\text{PbI}_2$  after back-conversion, top view 40 kX.

(f)  $\text{PbI}_2$  after back-conversion, cross-sectional view 120 kX.

Figure 5.8 – SEM images of the film morphology at the major steps of initial, pre-wet  $\text{PbI}_2$  (a), (b), after conversion to  $\text{CH}_3\text{NH}_3\text{PbI}_3$  perovskite by exposure to  $\text{CH}_3\text{NH}_3\text{I}$  for 50 s (c), (d), and after back-conversion to  $\text{PbI}_2$  by rinsing with plain isopropanol for 300 s (e), (f).



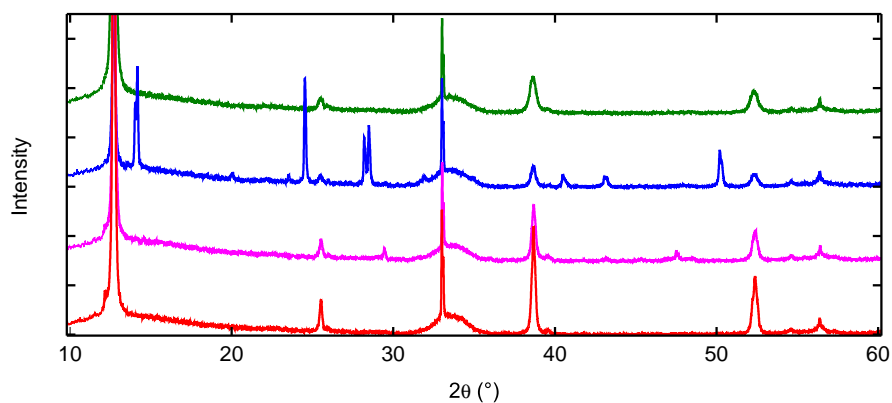
## 5.2. Overview of the conversion and back-conversion

---

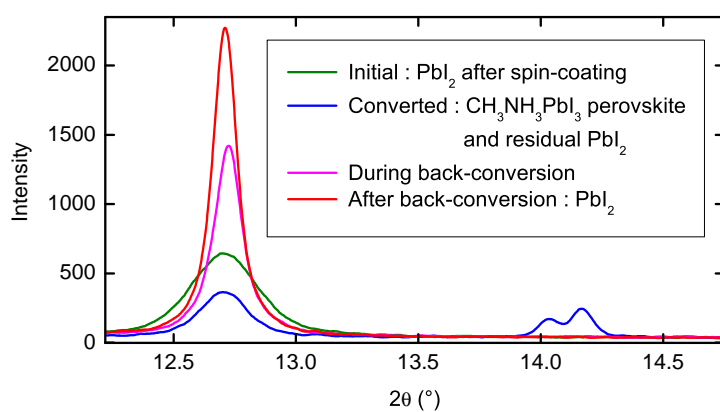
sity (1420 counts) than the peak of the initial  $\text{PbI}_2$ . We note that in the complete spectrum in figure 5.9 (a), this sample shows two low-intensity peaks at diffraction angles of  $29.45^\circ$  and  $47.51^\circ$ . These two peaks do not exist in any of the other samples in this figure, and they indicate that the back-conversion may proceed via a different crystalline phase. After having rinsed the perovskite for more than 5 min with isopropanol and thus completing the back-conversion to  $\text{PbI}_2$ , the  $\text{PbI}_2$  peak at  $12.7^\circ$  has the highest intensity of all peaks (2270 counts), and the most narrow line width.

This XRD measurement gives important information on the crystal structure, and the different species present. The emergence of the perovskite peak upon  $\text{CH}_3\text{NH}_3\text{I}$  exposure, and the decrease of the  $\text{PbI}_2$  peak confirm that we have indeed the desired conversion reaction. The fact that the  $\text{PbI}_2$  peak does not disappear proves that the conversion is incomplete despite the fact that reaction kinetics have reached a quasi-plateau as seen by QCM-D analysis earlier. Upon back-conversion, the perovskite structure seems to disintegrate before the  $\text{CH}_3\text{NH}_3\text{I}$  has actually left the material. However, the details of this back-conversion shall be discussed later in section 5.4. Back-conversion leads to a significant increase in intensity of the  $\text{PbI}_2$  peak and to a narrowing of its width. We refrain from a Scherrer analysis of the peaks at this point because the instrumental broadening needs to be assessed more accurately first. Nevertheless, the narrowing does indicate a significant increase in crystallite size upon back-conversion, and this correlates very well with the morphology observed by SEM in the previous section 5.2.3. We note that the area under the  $\text{PbI}_2$  peak is significantly larger after back-conversion than it was on the initial film. Small variations could be related to inconsistent film thickness between the different samples or to the XRD machine. However, the increase in peak area may be an indication that the initial  $\text{PbI}_2$  film has a rather amorphous character with a very small average crystallite size, which would result into a much lower peak intensity and area than for larger crystallites.

## Chapter 5. Conversion of thin lead iodide films to perovskites by exposure to methylammonium iodide



(a) Complete XRD spectra.



(b) Details of the  $\text{PbI}_2$ -related peak at  $12.7^\circ\text{C}$  and the  $\text{CH}_3\text{NH}_3\text{PbI}_3$  perovskite peak at  $14.2^\circ\text{C}$

Figure 5.9 – XRD spectra of the  $\text{PbI}_2$  film prior to conversion, after conversion to the  $\text{CH}_3\text{NH}_3\text{PbI}_3$  perovskite, during back-conversion, and after completion of the back-conversion to  $\text{PbI}_2$ .

### 5.2.5 Effect of PbI<sub>2</sub> morphology on QCM-D signals

**Frequency shift, trapped liquid and effective porosity** These measurements aim to understand the influence the morphology of the PbI<sub>2</sub> film on the QCM-D frequency shift and dissipation shift. The porous character leads to a certain amount of liquid trapped inside the film, adding to its wet mass and thereby increasing the measured frequency shift. We furthermore observe an influence of the morphology on the dissipation, indicating a significant drag at the interface between the porous film and the overlying bulk liquid.

We have carried out a QCM-D measurement while changing between two solvents of different density and viscosity, similar to the analysis previously shown on thin mesoporous TiO<sub>2</sub> films in chapter 4.2.2. Our choice of solvents was isopropanol ( $\rho = 0.781 \text{ g cm}^{-3}$ ,  $\eta = 2.040 \text{ mPa s}$ ) and chlorobenzene ( $\rho = 1.106 \text{ g cm}^{-3}$ ,  $\eta = 0.753 \text{ mPa s}$ ), since they do not dissolve PbI<sub>2</sub>. The according measurement is shown in figure 5.10: The green line shows the QCM-D response on a flat, compact TiO<sub>2</sub> film as a reference, which corresponds to the changes in bulk viscosity and density of the overlying liquid, and should correspond to the description by Kanazawa and Gordon [55, 54, 110]:

$$\Delta f = f_0^{3/2} \sqrt{\frac{\eta \rho}{\pi \mu_q \varrho_q}} \quad \text{and} \quad \Delta D = \frac{1}{t_q \varrho_q} \sqrt{\frac{\eta \rho}{\pi f_0}} \quad . \quad (5.1)$$

$\eta$  and  $\rho$  are the viscosity and the density of the liquid, and  $\mu_q$  and  $t_q$  are the shear modulus and the transversal sound velocity of the AT-cut quartz.

The black line shows the QCM-D response on the initial PbI<sub>2</sub> film deposited by spin-casting prior to conversion. The red line shows QCM-D shifts of frequency and dissipation on the same PbI<sub>2</sub> film after conversion to the CH<sub>3</sub>NH<sub>3</sub>PbI<sub>3</sub> perovskite and back-conversion to PbI<sub>2</sub>. The data are offset in time and y-value in order to facilitate a direct comparison.

Table 5.3 summarises the shifts of frequency and dissipation upon changing from isopropanol to chlorobenzene displayed in figure 5.10 at offset time  $t = 560 \text{ s}$ . The last two columns show the differences  $\delta f = \Delta f_{\text{PbI}_2} - \Delta f_{\text{flat, TiO}_2}$  and  $\delta D = \Delta D_{\text{PbI}_2} - \Delta D_{\text{flat, TiO}_2}$  relative to the flat film. Remarkably, and in contrast to similar measurements on mesoporous TiO<sub>2</sub> in chapter 4.2.2, we observe a small difference in dissipation shift  $\delta D$  when comparing the dissipation shift on flat film to each of the dissipation shifts on the porous PbI<sub>2</sub>. The difference in dissipation shift is  $\delta D = +3 \cdot 10^{-6}$  for the PbI<sub>2</sub> film prior to conversion, and  $\delta D = +10 \cdot 10^{-6}$  for the PbI<sub>2</sub> film after conversion to the CH<sub>3</sub>NH<sub>3</sub>PbI<sub>3</sub> perovskite and back-conversion to PbI<sub>2</sub>.

However, for a very rough analysis, we will neglect the shift of dissipation and apply the Sauerbrey equation in order to obtain the approximate amount of trapped liquid from the frequency shift. As a rule of thumb, the Sauerbrey equation is still valid if the dissipation shift in  $10^{-6}$  does not exceed 10 % of the value of the frequency shift in Hz. This is the case in the above measurement, and we will discuss the dissipation shift at the end of this section. This rule of thumb, which relates the unit-less dissipation to the frequency shift in Hz, is best

## Chapter 5. Conversion of thin lead iodide films to perovskites by exposure to methylammonium iodide

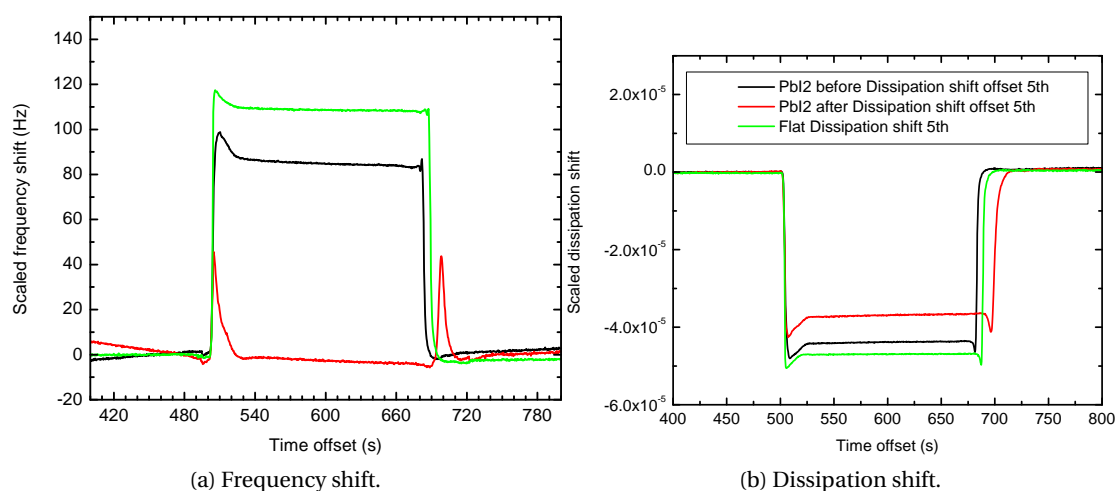


Figure 5.10 – QCM-D data for solvent exchange from isopropanol to chlorobenzene and back to isopropanol. Comparing a  $\text{PbI}_2$  film prior to conversion (black), the same  $\text{PbI}_2$  film after back-conversion (red), and a flat, compact  $\text{TiO}_2$  film as a reference (green).

Table 5.3 – Summarising shifts of frequency and dissipation upon changing from isopropanol to chlorobenzene. Sample surfaces are flat, compact  $\text{TiO}_2$ , porous initial  $\text{PbI}_2$  before conversion, and porous  $\text{PbI}_2$  after back-conversion. Values of  $\Delta f$  and  $\Delta D$  are taken from measurements displayed in figure 5.10 at offset time  $t = 560$  s. The last column shows the differences  $\delta f = \Delta f_{\text{PbI}_2} - \Delta f_{\text{flat, TiO}_2}$  and  $\delta D$  relative to the flat film.

	$\Delta_{\text{flat TiO}_2}$	$\Delta_{\text{PbI}_2, \text{ before}}$	$\Delta_{\text{PbI}_2, \text{ after}}$	$\delta_{\text{PbI}_2, \text{ before}}$	$\delta_{\text{PbI}_2, \text{ after}}$
Frequency shift $\Delta f, \delta f$ in Hz	+109	+86	-1	-23	-110
Dissipation shift $\Delta D, \delta D$	$-47 \cdot 10^{-6}$	$-44 \cdot 10^{-6}$	$-37 \cdot 10^{-6}$	$+3 \cdot 10^{-6}$	$+10 \cdot 10^{-6}$

understood when recalling the introduction or the previous section 4.3.2: QCM-D measures the properties of a resonance. The frequency shift is the shift of the (central) resonance frequency upon mass loading. The dissipation is proportional to the width of the resonance divided by its absolute frequency,  $D = 1/Q = \Gamma \cdot 2/f_0$ , ( $D$ : dissipation,  $Q$ : quality-factor,  $\Gamma$ : full width at half maximum in Hz,  $f_0$ : resonance frequency in Hz). The above rule of thumb expresses that the change in the width of the resonance has to be small compared to the shift of the resonance frequency.

The analysis of the frequency shift in order to obtain the Volume of liquid trapped inside the film  $V_{\text{liq}}$  is the same as in chapter 4.2.2. The difference in frequency shift  $\delta f_{\text{PbI}_2}$  should be primarily related to the change in mass given by the product of the volume of trapped liquid  $V_{\text{liq}}$  and the difference in volumetric density ( $\rho_{\text{chlorobenzene}} - \rho_{\text{isopropanol}}$ ) between chlorobenzene

## 5.2. Overview of the conversion and back-conversion

and isopropanol, described by the Sauerbrey equation:

$$-C \cdot \delta f = \delta m = V_{\text{liq}} \cdot (\rho_{\text{chlorobenzene}} - \rho_{\text{isopropanol}}) \quad , \quad (5.2)$$

with the Sauerbrey constant  $C = \frac{f_0}{\rho_q^2} \approx 17.5 \text{ ng cm}^{-2} \text{ Hz}^{-1}$ . Note that  $\delta m$  and  $V_{\text{liq}}$  are mass and volume *per area*.

Resolving equation 5.2 gives the volume of liquid trapped inside the initial  $\text{PbI}_2$  film prior to conversion, and the volume of liquid trapped inside the  $\text{PbI}_2$  film after one back-conversion:

$$V_{\text{liq}}(\text{PbI}_2, \text{ before}) = 1.24 \cdot 10^{-12} \frac{\text{m}^3}{\text{cm}^2} \quad \text{and} \quad V_{\text{liq}}(\text{PbI}_2, \text{ after}) = 5.92 \cdot 10^{-12} \frac{\text{m}^3}{\text{cm}^2} \quad .$$

On the initial  $\text{PbI}_2$  film, the trapped isopropanol thus accounts for  $V_{\text{liq}}(\text{PbI}_2, \text{ before}) \cdot \rho_{\text{isopropanol}} = 967 \text{ ng cm}^{-2}$  of its wet mass. On the  $\text{PbI}_2$  film after back-conversion and before complete dissolution in DMF, the trapped isopropanol accounts for  $V_{\text{liq}}(\text{PbI}_2, \text{ after}) \cdot \rho_{\text{isopropanol}} = 4626 \text{ ng cm}^{-2}$  of its wet mass. The latter can be used to calculate the dry mass of the adsorbed  $\text{PbI}_2$  by dissolution of the entire film, which gives a measure of its wet mass. We did this in section 5.2.1 and obtained a dry area mass of  $110.92 \cdot 10^{-6} \text{ g cm}^{-2}$  for the  $\text{PbI}_2$  film. Taking into account the density of  $\text{PbI}_2$ ,  $\rho_{\text{PbI}_2} = 6.160 \text{ g cm}^{-3}$  from [70], we can obtain a  $\text{PbI}_2$  volume per area of  $18.01 \cdot 10^{-12} \text{ m}^3 \text{ cm}^{-2}$ . For the  $\text{PbI}_2$  film after one back-conversion from the perovskite, we measured a trapped liquid volume of  $5.92 \cdot 10^{-12} \text{ m}^3 \text{ cm}^{-2}$ , giving an effective porosity of 24.7 %. Prior to conversion, the volume of trapped liquid is approximately  $1.24 \cdot 10^{-12} \text{ m}^3 \text{ cm}^{-2}$ . This leads us to estimating the effective porosity of the initial, spin-cast  $\text{PbI}_2$  film to be only around 6.4 %.

**Dissipation shift and viscoelastic behaviour** Evaluating the difference in dissipation shift observed in the measurement above (figure 5.10) is less straight forward. In order to obtain a general overview, we recall the QCM-D measurement of the conversion from  $\text{PbI}_2$  to the perovskite and its back-conversion, as displayed in figure 5.5.

During conversion to the perovskite, the dissipation went up to approximately  $25 \cdot 10^{-6}$ , including a small contribution from changes in bulk viscosity, which produced  $5 \cdot 10^{-6}$  dissipation shift on a flat, non-reacting control sample (not shown). During back-conversion, dissipation goes through a peak of approximately  $50 \cdot 10^{-6}$ , and finally falls back to a value that is  $18 \cdot 10^{-6}$  higher than on the initial  $\text{PbI}_2$  film. Upon dissolution of the  $\text{PbI}_2$  film, the dissipation goes approximately back to the same value as the initial  $\text{PbI}_2$  film (dissipation shift 0). The SEM picture in sections 5.2.3 show, that the change of dissipation clearly correlates with a change in film morphology.

I speculate that the change in dissipation is due to a change in the way the surface of the film

## Chapter 5. Conversion of thin lead iodide films to perovskites by exposure to methylammonium iodide

---

couples to the overlying bulk liquid. In a simplified picture, the different morphology will produce a different drag in the liquid, which leads to a change in dissipation. This would require to introduce a form factor describing the interface morphology into the equations of Kanazawa and Gordon [55, 54, 110] which describe the coupling to the overlying bulk liquid:

$$\Delta f = f_0^{3/2} \sqrt{\frac{\eta \rho}{\pi \mu_q \rho_q}} \quad \text{and} \quad \Delta D = \frac{1}{t_q \rho_q} \sqrt{\frac{\eta \rho}{\pi f_0}} \quad . \quad (5.3)$$

We do not attempt to provide a quantitative description of this correlation yet, but we can try to exclude other possible sources of a shift in dissipation.

A common reason for an increase in dissipation would be a softening of the adsorbed film. This is not the case since the  $\text{PbI}_2$  film and the perovskite itself are rigid and they should be well interconnected. It would be possible that the attachment of the  $\text{PbI}_2$  film to the  $\text{TiO}_2$  underlayer is weakened upon the first conversion and thereby causes an upshift in dissipation. However, I think this is unlikely because the conversion was incomplete in this experiment, and the SEM pictures in section 5.2.3 indicate that some of the  $\text{PbI}_2$  close to the  $\text{TiO}_2$  substrate does not change its morphology.

Another possible reason for the frequency shift would be turbulent drag due to the flow inside the flow chamber. A turbulent flow can be described by the Reynolds number  $Re$ , which is usually defined as a dimensionless number

$$Re = \frac{\rho \cdot v}{\eta} \cdot \hat{D} \quad . \quad (5.4)$$

$\rho$  and  $\eta$  are the density and the viscosity of the liquid, and  $v$  is a mean velocity of the liquid.  $\hat{D}$  is a form factor of a length unit m, which describes the flow around an object, for example a tube, a sphere, or a rough surface. Below a certain Reynolds number, the flow is laminar, whereas it becomes turbulent above a certain Reynolds number. Increased turbulent flow may lead to increased dissipation in the QCM-D signal as shown by Johannsmann et al. [51]. However, we do not see any significant change in the dissipation when either stopping the flow, or when pumping with a nominal pump speed  $500 \mu\text{l}$  instead of the usual  $100 \mu\text{l}$  as shown in section 5.2.2, which changes the velocity of the liquid  $v$  and thus will influence the turbulent drag.

The quantitative impact of the morphology on QCM-D signals is not understood in detail, and we therefore refrain from further analysis of this phenomena, since its influence on shifts of frequency and dissipation appears to be relatively small compared to the major shifts of frequency due to mass change, which we observe during the conversion and back-conversion reaction.

## 5.3 Repetitive conversion and back-conversion between $\text{CH}_3\text{NH}_3\text{PbI}_3$ and $\text{PbI}_2$

The SEM images and XRD measurements in the previous sections in sections 5.2.3 and 5.2.4 have shown that a cycle of conversion and back-conversion of the  $\text{PbI}_2$  film to and from the perovskite does indeed change its morphology and crystallinity significantly. This conversion and back-conversion can be carried out repetitively, as we have already shown in figure 5.6 in the QCM-D overview in section 5.2.1. Here we present morphology, crystal structure and material composition during repetitive conversion in more detail.

### 5.3.1 Repetitive conversion by QCM-D

Figure 5.11 shows a detailed view of the QCM-D frequency and dissipation shift of three consecutive cycles of conversion and back-conversion, starting from a 200 nm thick  $\text{PbI}_2$  film. Qualitatively, the QCM-D signals of the 1st, 2nd and 3rd cycle resemble each other very much:  $\text{CH}_3\text{NH}_3\text{I}$  exposure causes a pronounced decrease in frequency by roughly 1000 Hz to a quasi-plateau with a negative linear slope, which is reversible upon rinsing with pure isopropanol. The dissipation shift always shows a pronounced peak during back-conversion.

Quantitatively, there are several differences. After the first conversion and back-conversion cycle, the frequency has decreased by  $-70$  Hz, and the dissipation has increased by  $+20$  Hz. After the second and the third cycle, the frequency has shifted up by  $+50$  Hz each time, whereas the dissipation returns to approximately the same value after each cycle. During  $\text{CH}_3\text{NH}_3\text{I}$  exposure, the rapid initial frequency shift is larger with each additional cycle,  $-1000$  Hz for the first exposure,  $-1150$  Hz for the second, and  $-1250$  Hz for the third exposure. At the same time, the linear slope during  $\text{CH}_3\text{NH}_3\text{I}$  exposure becomes steeper: it is approximately  $-40$  Hz  $\text{min}^{-1}$ ,  $-80$  Hz  $\text{min}^{-1}$ , and  $-120$  Hz  $\text{min}^{-1}$  during each exposure.

The frequency shift upon  $\text{CH}_3\text{NH}_3\text{I}$  exposure should mainly correspond to  $\text{CH}_3\text{NH}_3\text{I}$  uptake into the  $\text{PbI}_2$  film and conversion to the  $\text{CH}_3\text{NH}_3\text{PbI}_3$  perovskite. The frequency shift of  $-70$  Hz between the  $\text{PbI}_2$  film before and after the first cycle corresponds mostly to the change of wet mass of the film, since the back-converted  $\text{PbI}_2$  does trap a larger volume of liquid than the initial  $\text{PbI}_2$  film. This has been demonstrated in section 5.2.5. The subsequent increase of frequency by  $+50$  Hz after the second and after the third conversion cycle could have two possible reasons. First, there could be a slight loss of material from part of the  $\text{PbI}_2$  during and after the back-conversion process. The ICP-MS measurement in section 5.2.2 does indeed show a small quantity of Pb and an indication for iodide in the outflow. Second, there could be a further morphological change of the  $\text{PbI}_2$  film that decreases the volume of trapped liquid and thus leads to a loss of wet mass. However, the dissipation shift and the SEM images in the next subsection 5.3.2 indicate that there is only a minor change in morphology of the  $\text{PbI}_2$  film after the second and the third conversion cycle.

## Chapter 5. Conversion of thin lead iodide films to perovskites by exposure to methylammonium iodide

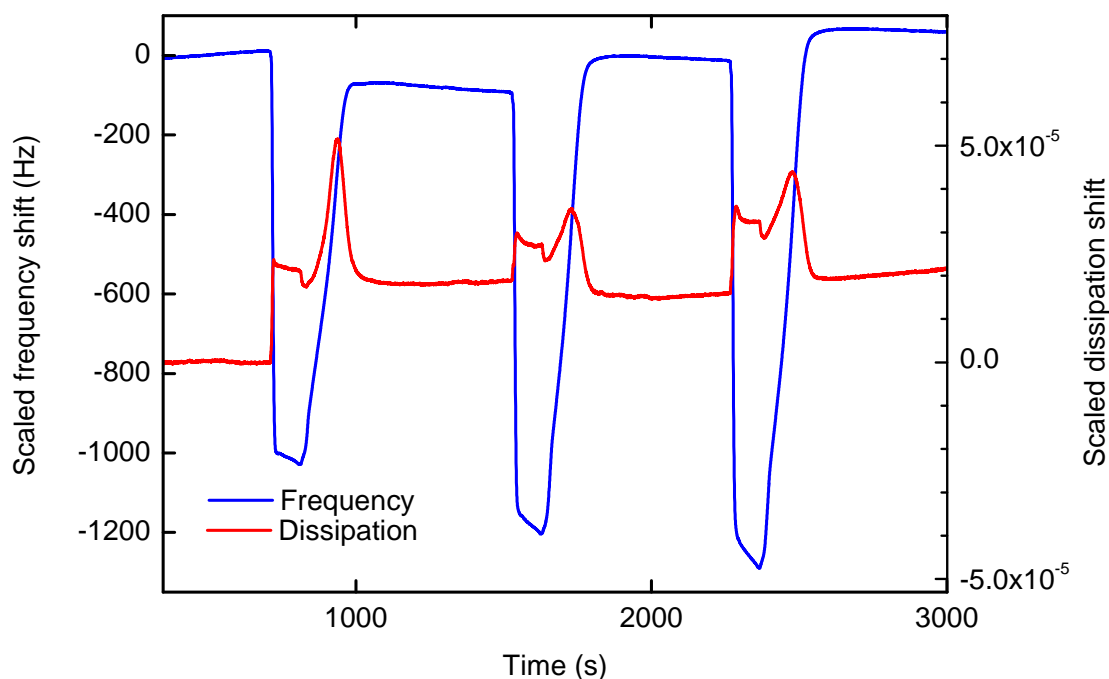


Figure 5.11 – QCM-D signal of the conversion of a  $\text{PbI}_2$  film to  $\text{CH}_3\text{NH}_3\text{PbI}_3$  perovskite by exposure to a  $\text{CH}_3\text{NH}_3\text{I}$  solution in isopropanol, and the subsequent back-conversion by exposure to isopropanol.

Concerning the dissipation shift, the most remarkable feature is that during the first conversion, the dissipation shifts up by  $20 \cdot 10^{-6}$  and then returns approximately to this value after the second and the third cycle of conversion and back-conversion.

As explained in section 5.2.5, the dissipation shift correlates directly with large changes in film morphology, although we cannot explain the correct mechanism yet. Furthermore, there is an influence of the bulk viscosity and density which are slightly higher during the exposure to the  $\text{CH}_3\text{NH}_3\text{I}$  solution than for the pure isopropanol and account for a shift of approximately  $+5 \cdot 10^{-6}$  on a flat film.

### 5.3.2 Repetitive conversion by SEM and XRD

All studies above had been carried out starting from 200 nm thick  $\text{PbI}_2$  films. For the SEM study in this subsection and the following subsection on XRD analysis, 600 nm thick  $\text{PbI}_2$  films have been used, because they illustrate more clearly how the conversion to the perovskite increases progressively with each conversion-back-conversion cycle. These 600 nm  $\text{PbI}_2$  films have been prepared in the same way as the 200 nm thick films, with the only difference of a slightly lower spin-coating speed of 4000 RPM and an incompletely dissolved  $\text{PbI}_2$  solution. Unfortunately, this procedure lead to significant irregularities if the  $\text{PbI}_2$  film thickness across the samples. For the SEM images, a largely homogeneous and representative area of the sam-



### 5.3. Repetitive conversion and back-conversion between $\text{CH}_3\text{NH}_3\text{PbI}_3$ and $\text{PbI}_2$

ple was chosen. The XRD measurements however, provide an average across the entire sample and did not allow for rigorous interpretation of this set of samples. The only trustworthy information that we can extract for now, is that conversion and back-conversion between  $\text{PbI}_2$  and  $\text{CH}_3\text{NH}_3\text{PbI}_3$  perovskite are confirmed by XRD data, and that the conversion to the perovskite is not complete.

All SEM images were made by Dr. Nicolas Tétreault. The thick  $\text{PbI}_2$  films initially have almost the same morphology as the thin ones, as depicted in figure 5.12 (a). After 50 s exposure to  $0.8 \text{ g ml}^{-1}$   $\text{CH}_3\text{NH}_3\text{I}$  in isopropanol, the film has turned completely black to the eye, and the SEM in figure 5.12 (b) shows that a layer of homogeneously distributed cubic crystals of up to 200 nm size has formed in the upper part of the film, whereas the lower part does show a morphology similar to the initial  $\text{PbI}_2$  film. This indicates that the  $\text{CH}_3\text{NH}_3\text{I}$  has not penetrated to the bottom of the  $\text{PbI}_2$  film, in contrast to the morphology that we observed on the SEM pictures of the thin, 200 nm  $\text{PbI}_2$  film in figure 5.8 (a) and (b) in section 5.2.3.

Cross-sectional SEM images of a 600 nm thick  $\text{PbI}_2$  film after 50 s exposure to  $\text{CH}_3\text{NH}_3\text{I}$  and after subsequent rinsing for 5 min with pure isopropanol, as well as two more repetitions of this cycle of conversion and back-conversion are shown in figure 5.13. The image of the film in part (a) is the same as in figure 5.12 (b), and is taken after the first exposure to  $\text{CH}_3\text{NH}_3\text{I}$ . The cubic crystals of up to 200 nm size in the upper part of the film should correspond to perovskite material. The lower part does show a morphology similar to the initial  $\text{PbI}_2$  film and has a thickness of about 500 nm.

Figure 5.13 (b) shows a cross-sectional image of the film after 50 s exposure to  $\text{CH}_3\text{NH}_3\text{I}$  and subsequent rinsing with pure isopropanol for 5 min. On this particular sample, some residuals of the perovskite crystals seem to be still reminiscent on top of the back-converted  $\text{PbI}_2$  film. I think these apparent residuals are an experimental irregularity on this specific sample. The back-converted  $\text{PbI}_2$  film has a different morphology than the initial one, and its morphology is similar to the one observed in the cross-section of the 200 nm thick film which has been shown in figure 5.12 (d), featuring more platelet-like shapes.

A second exposure of the back-convert film to  $\text{CH}_3\text{NH}_3\text{I}$  for 50 s produces a morphology shown in figure 5.13 (c). Compared to the first conversion, perovskite crystals after the second conversion show a significantly larger maximum lateral extension of up to 800 nm. However, the lower part of the film still contains domains of a morphology similar to that of unconverted  $\text{PbI}_2$ . Those domains are visible underneath large perovskite crystals and measure an apparent thickness of up to 300 nm.

Back-converting the film to  $\text{PbI}_2$  for a second time by rinsing for 5 min with pure isopropanol results in the morphology shown in figure 5.13 (d). The morphology seems very similar to the one after the first back-conversion, ignoring the irregularities in figure (b). However, the crystallite platelets seem slightly larger and more homogeneously distributed across the thickness of the film.

Figure 5.13 (e) shows the film morphology after the third repetitive conversion reaction by

## Chapter 5. Conversion of thin lead iodide films to perovskites by exposure to methylammonium iodide

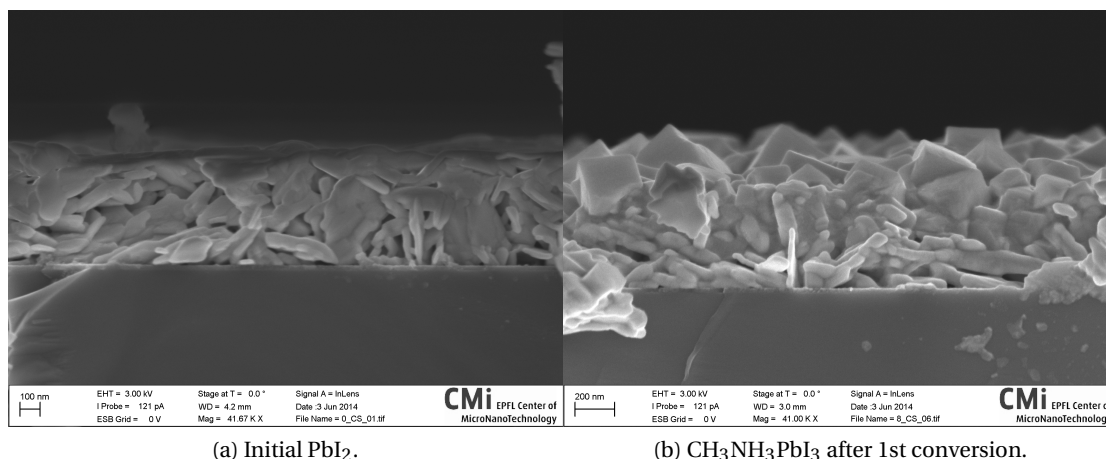


Figure 5.12 – Cross-sectional SEM images of the film morphology of initial pre-wetted, thick  $\text{PbI}_2$  film, and of the  $\text{CH}_3\text{NH}_3\text{PbI}_3$  perovskite after the 1st conversion.

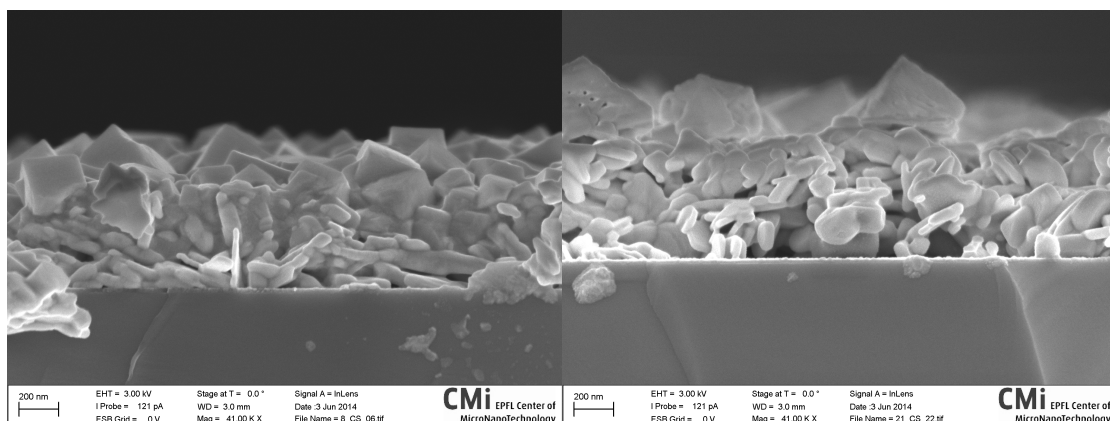
exposure to  $\text{CH}_3\text{NH}_3\text{I}$  for 50 s. In the centre of the image are two large perovskite crystals that have grown into each other and form a crystallite of a size of  $1.8 \mu\text{m}$ . Close to the  $\text{TiO}_2$  surfaces, there are still domains of a morphology similar to that of unconverted  $\text{PbI}_2$  close, but they seem to be less prevalent than during previous conversions, and measure a maximum thickness of 200 nm.

A third back-conversion to  $\text{PbI}_2$  by rinsing with pure isopropanol for 5 min leads to the morphology shown in figure 5.13 (f). The morphological change with respect to the previously back-converted film in figure (d) is small. The crystallite size seems to have increased slightly, and the size distribution is more homogeneous. Furthermore, the spacing between the crystallites seems to have decreased.

Summarising the morphology change upon the first, second and third conversion in figure 5.13 (a), (c) and (e), we can clearly see that the size of the perovskite crystallites increases, and that the amount of unconverted  $\text{PbI}_2$  decreases. The series indicates that the perovskite formation begins from the top of the pre-wet  $\text{PbI}_2$  film. The series shows a dependence of the crystal growth on the details of the morphology and on the crystallinity of the  $\text{PbI}_2$ . Assuming that the conversion has already reached its quasi-plateau after 50 s of  $\text{CH}_3\text{NH}_3\text{I}$  exposure, the images further suggest that a fully formed perovskite layer hinders the access of  $\text{CH}_3\text{NH}_3\text{I}$  to any underlying  $\text{PbI}_2$ , which is thus not converted or only at a much slower rate.

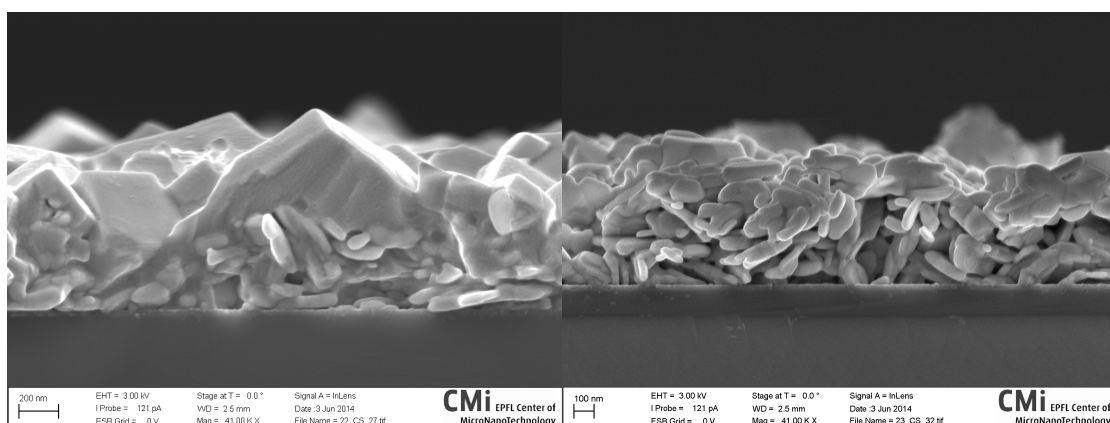
The morphology change of the  $\text{PbI}_2$  film after one, two and three back-conversion cycles in figure 5.13 (b), (d) and (f) is more subtle. However, there seems to exist a trend that the  $\text{PbI}_2$  crystallite size increases slightly, and the size distribution becomes more narrow. Furthermore, the spacing between the crystallites appears to have decreased.

### 5.3. Repetitive conversion and back-conversion between $\text{CH}_3\text{NH}_3\text{PbI}_3$ and $\text{PbI}_2$



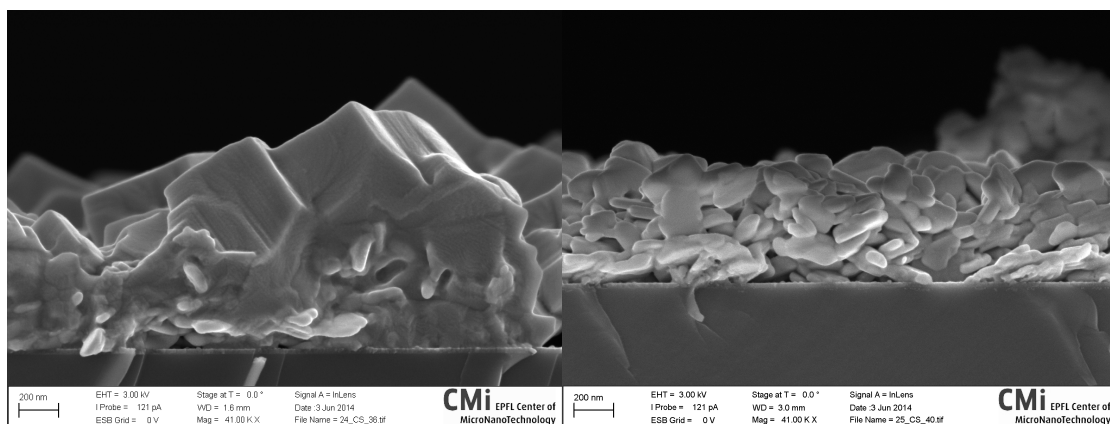
(a)  $\text{CH}_3\text{NH}_3\text{PbI}_3$  after 1st conversion.

(b)  $\text{PbI}_2$  after 1st back-conversion.



(c)  $\text{CH}_3\text{NH}_3\text{PbI}_3$  after 2nd conversion.

(d)  $\text{PbI}_2$  after 2nd back-conversion.



(e)  $\text{CH}_3\text{NH}_3\text{PbI}_3$  after 3rd conversion.

(f)  $\text{PbI}_2$  after 3rd back-conversion.

Figure 5.13 – Cross-sectional SEM images of the film morphology at 41 K x magnification during repetitive conversion and back-conversion between  $\text{CH}_3\text{NH}_3\text{PbI}_3$  perovskite and  $\text{PbI}_2$  having started from the 470 nm thick  $\text{PbI}_2$  film depicted in figure 5.12.

## **5.4 Details of the back-conversion process**

Whereas the conversion process from the  $\text{PbI}_2$  to the  $\text{CH}_3\text{NH}_3\text{PbI}_3$  perovskite has been studied in by various optical techniques, XRD and SEM, the back-conversion has not. We here discuss the limited data that we have collected until now, and we can already offer some insight. The data presented has been collected on a film with an initial  $\text{PbI}_2$  thickness of 200 nm on its first back-conversion, but the results should be of general validity.

The change of film morphology during back-conversion can be well illustrated by high-resolution SEM images. Therefore, a set of samples was prepared with initial  $\text{PbI}_2$  film thickness of 200 nm. The film was pre-wet, converted to the perovskite by 50 s exposure to  $0.8 \text{ mg ml}^{-1}$   $\text{CH}_3\text{NH}_3\text{I}$  in isopropanol, and subsequently rinsed for the desired time in pure isopropanol, i.e. 0 s, 3 s, 10 s, 120 s, 300 s. After rinsing, the film was dried by spinning at 4000 RPM for 30 s and subsequently put on a hotplate at  $70^\circ\text{C}$ . This drying procedure could potentially affect film morphology, but it does avoid contamination, and effects should be limited because the drying process is still significantly faster than the back-conversion process. The rinsing times mentioned above can be understood as a lower limit for the true duration of the back-conversion, and all rinsing times shall have the same offset to the true duration of the back-conversion. We note that this situation does not hold true for the conversion process, where taking a momentary snapshot of the process for ex-situ analysis is more prone to error.

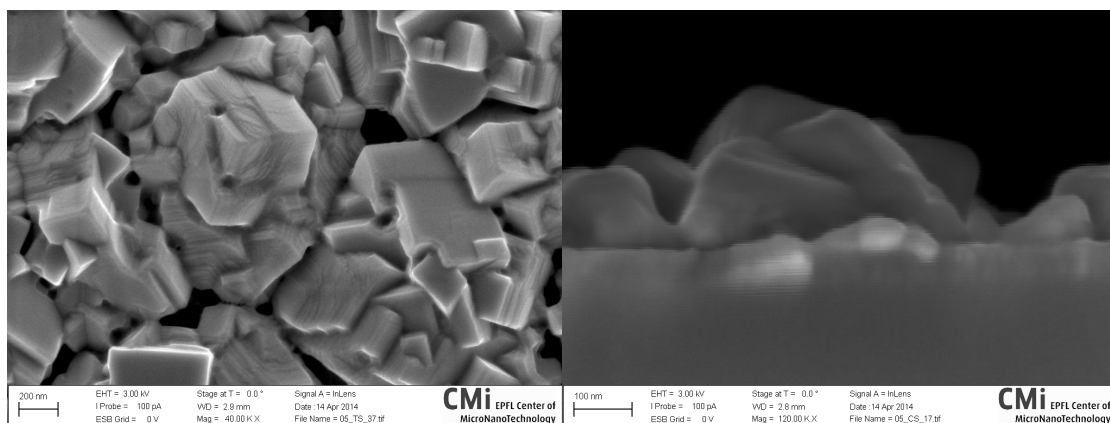
We describe the SEM images of the film morphology after rinsing in pure isopropanol for 0 s and for 3 s are shown in figure 5.14, and after rinsing for 10 s, 120 s, and 300 s are shown in figure 5.15. The image at 0 s in figure 5.14 (a) and (b) shows the perovskite crystals that appear to have a crystalline surface which goes all the way down to the  $\text{TiO}_2$  underlayer.

After 3 s of rinsing, the top view (c) of the film still looks very similar, but the cross-sectional view (d) reveals a different morphology in the bottom 50 nm of the film, below the apparent perovskite crystallites. This bottom layer show a more irregular shapes that resemble slightly to the morphology typical for a  $\text{PbI}_2$  film

Figure 5.15 (a) and (b) show the film morphology after 10 s of rinsing. Whereas the top view in (a) is still very similar to the samples after 0 s and 3 s of rinsing, the cross-sectional view in (b) shows a stark difference in the bottom 100 nm of the film. The morphology of the bottom layer has a great similarity to the morphology observed in  $\text{PbI}_2$  films. A more detailed image of the same sample is shown further down in figure 5.16.

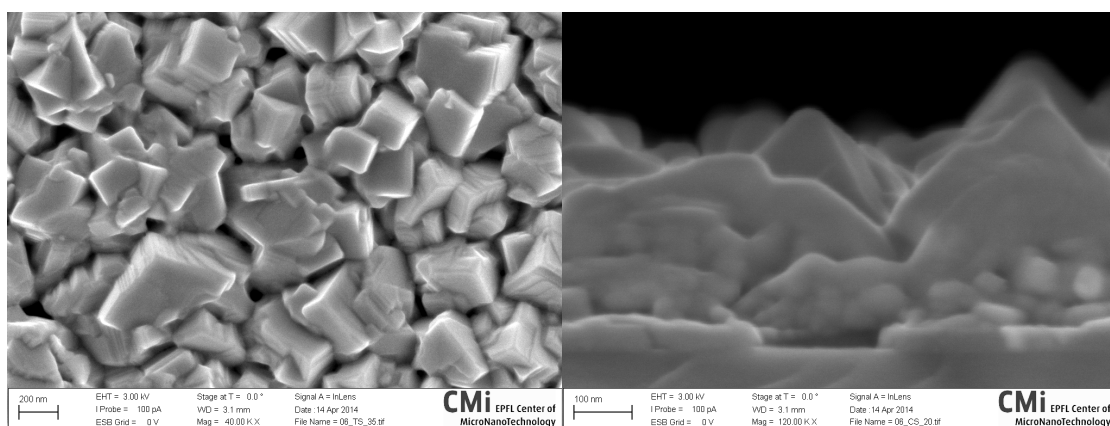
Figure 5.15 (c) and (d) show the film after 120 s of rinsing. The morphology is very different in that no more cubic perovskite crystals are visible. The top view (c) shows platelets of roughly 50 nm to 150 nm size, some of them of hexagonal shape. The cross-sectional view (d) reveals that the large platelets form the top part of the film, whereas the bottom 100 nm of the film consists of the smaller platelets. In the cross-sectional view, these smaller platelets resemble very much to the particles that we have seen in the bottom part of the film during back-conversion in the same figure 5.15 (b) and figure 5.14 (d).

## 5.4. Details of the back-conversion process



(a)  $\text{CH}_3\text{NH}_3\text{PbI}_3$  after conversion, top view 40 kX.

(b)  $\text{CH}_3\text{NH}_3\text{PbI}_3$  after conversion, cross-sectional view 120 kX.



(c)  $\text{CH}_3\text{NH}_3\text{PbI}_3$  after rinsing for 3 s., top view 40 kX.

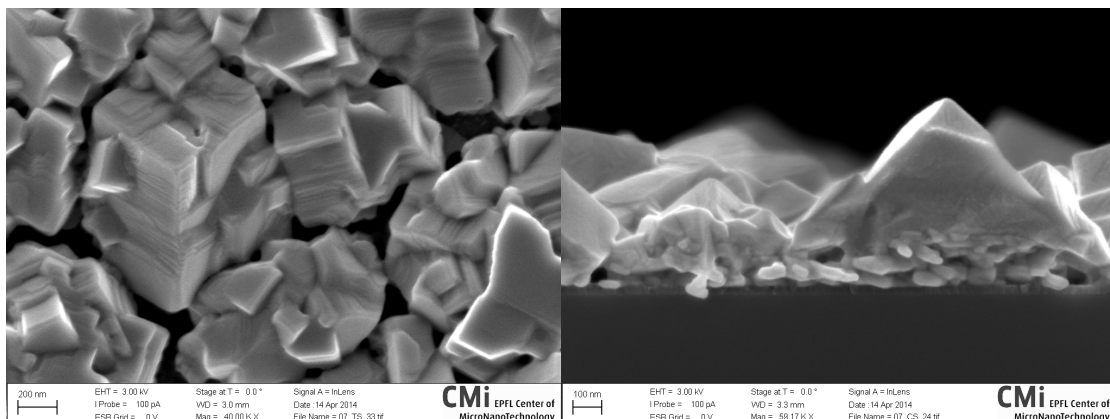
(d)  $\text{CH}_3\text{NH}_3\text{PbI}_3$  after rinsing for 3 s., cross-sectional view 120 kX.

Figure 5.14 – SEM images of the film morphology after conversion from  $\text{PbI}_2$  to the  $\text{CH}_3\text{NH}_3\text{PbI}_3$  perovskite by 40 s exposure to  $\text{CH}_3\text{NH}_3\text{I}$ , without rinsing with (a) and (b). And after 3 s of rinsing with isopropanol, thus initiating the back-conversion (c) and (d).

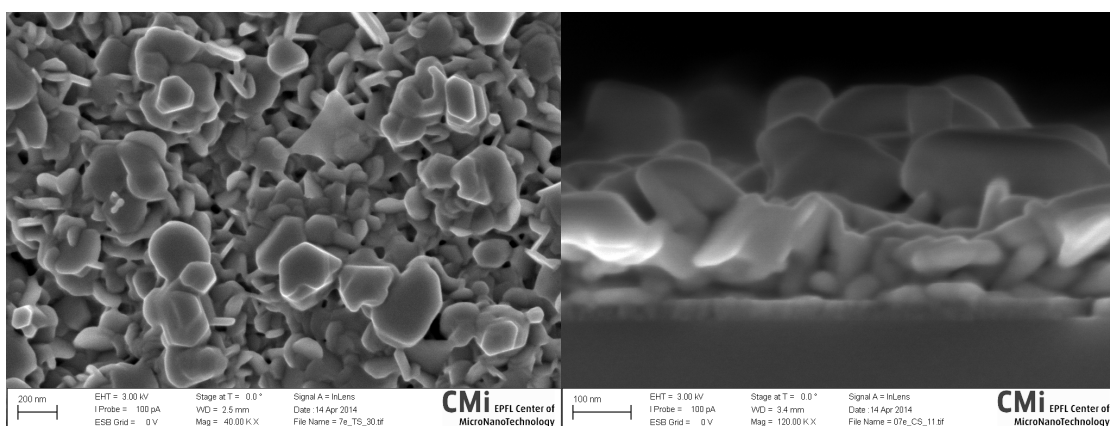
Upon complete back-conversion after 300 s of rinsing, as shown in figure 5.15, the top view (e) shows platelets of roughly 50 nm to 150 nm size, now almost all of them of hexagonal shape. The cross-sectional view (f) appears almost the unchanged compared to the sample rinsed for 120 s shown in part (d) of the same figure.

The series of samples for different rinsing times in figures 5.14 and 5.15 reveals details of the back-conversion process that shall be discussed. Surprisingly, it seems as if back-conversion proceeds from the bottom of the film. This phrasing is slightly misleading. It is however plausible, that the  $\text{PbI}_2$ , which is produced during back-conversion, re-crystallises and that it does preferably re-crystallise on already existing  $\text{PbI}_2$ , and not on top of a perovskite surface exposed to solution.

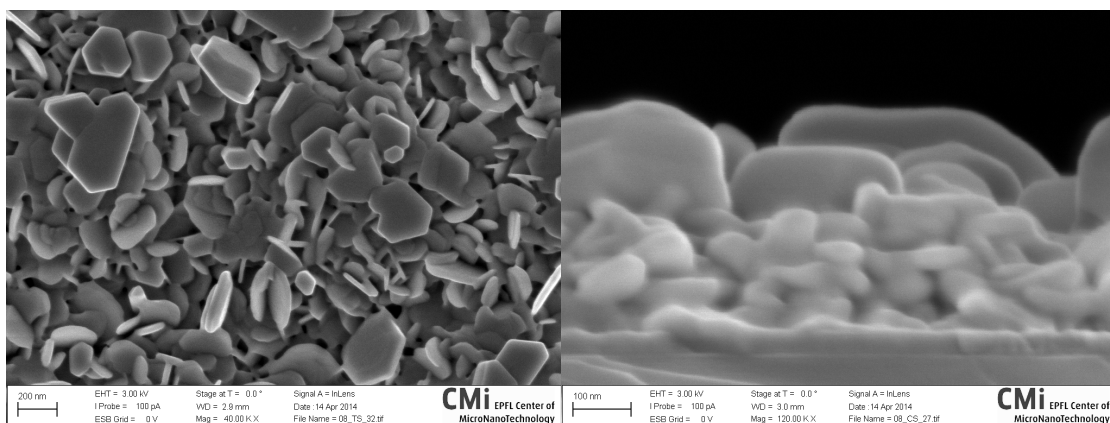
## Chapter 5. Conversion of thin lead iodide films to perovskites by exposure to methylammonium iodide



(a)  $\text{CH}_3\text{NH}_3\text{PbI}_3$  after rinsing for 10 s, top view 40 kX. (b)  $\text{CH}_3\text{NH}_3\text{PbI}_3$  after rinsing for 10 s, cross-sectional view 60 kX.

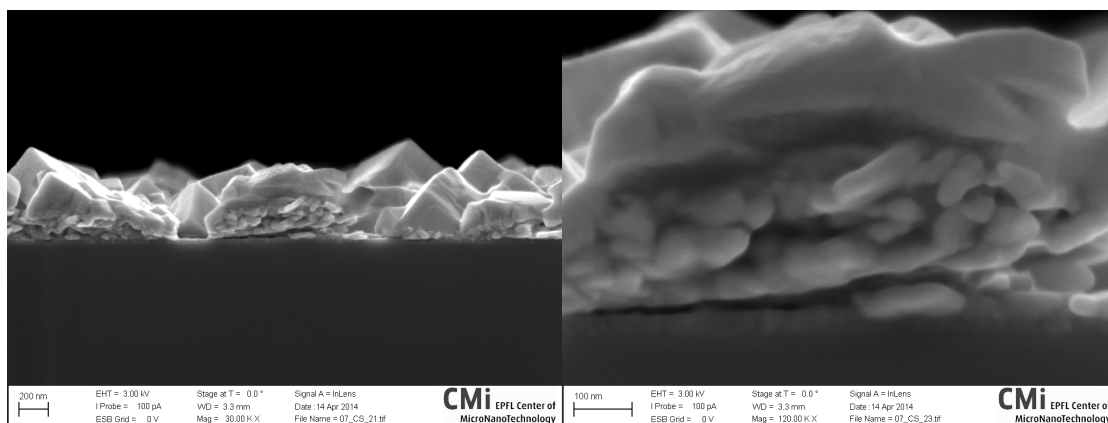


(c)  $\text{CH}_3\text{NH}_3\text{PbI}_3$  after rinsing for 120 s, top view 40 kX. (d)  $\text{CH}_3\text{NH}_3\text{PbI}_3$  after rinsing for 120 s, cross-sectional view 120 kX.



(e)  $\text{PbI}_2$  after back-conversion (5 min rinsing), top view 40 kX. (f)  $\text{PbI}_2$  after back-conversion (5 min rinsing), cross-sectional view 120 kX.

Figure 5.15 – SEM images of the film morphology during the back-conversion from  $\text{CH}_3\text{NH}_3\text{PbI}_3$  perovskite to  $\text{PbI}_2$  by rinsing with isopropanol for 10 s, 120 s and 300 s.



(a) Cross-sectional view, 30k x magnification.

(b) Cross-sectional view, 120k x magnification.

Figure 5.16 – SEM images of details of film morphology after rinsing  $\text{CH}_3\text{NH}_3\text{PbI}_3$  perovskite for 10 s with isopropanol. The sample is the same as in figure 5.15 (a) and (b).

We recall that the initial perovskite film after 0 s of rinsing, figure 5.14 (a), (b), is not completely converted but still contains a small amount of crystalline  $\text{PbI}_2$  as we have seen in an XRD measurement on in figure 5.9, section 5.2.4, on the very same sample. However, the SEM images suggest very plain facets of the perovskite crystallites. This can be seen as an indication that the unconverted  $\text{PbI}_2$  possibly lies buried inside of the apparent crystallite, close to the  $\text{TiO}_2$  underlayer.

After 10 s of rinsing, it becomes evident that some recrystallisation of  $\text{PbI}_2$  has taken place close to the  $\text{TiO}_2$  surface underneath the layer of perovskites. This is well illustrated in the detailed images of the sample in figure 5.16. This interpretation is based on the fact that  $\text{PbI}_2$  crystallites usually have a different morphological shape, hexagonal sheets, than perovskite crystals, which crystallise in a cubic crystal phase that transforms to a tetragonal (pseudo-cubic) phase at room temperature.

We recall that all QCM-D measurements show a pronounced peak in the dissipation shift during back-conversion from the perovskite to the  $\text{PbI}_2$ . It should be possible to use an SEM-study of the morphology change during back-conversion in order to relate morphology and dissipation in a more systematic manner in future.

It should be noted that the sample after 120 s of rinsing in figure 5.15 (c), (d) shows a qualitatively slightly different XRD pattern than the completely back-converted film, although the apparent morphology is very similar. The XRD measurement are displayed in figure 5.9 in section 5.2.4, and the sample after 120 s of rinsing shows two minor peaks at  $2\theta = 29.45^\circ$  and  $2\theta = 47.51^\circ$  which do neither belong to the standard  $\text{PbI}_2$  phase nor to the usual perovskite structure. This indicates that the back-conversion may proceed via an intermediate phase. The QCM-D measurement after 120 s of rinsing still records a continuous mass loss, corre-

## Chapter 5. Conversion of thin lead iodide films to perovskites by exposure to methylammonium iodide

---

sponding to the ongoing dissolution of  $\text{CH}_3\text{NH}_3\text{I}$  from the film. Hence, the according SEM and XRD sample could still contain  $\text{CH}_3\text{NH}_3\text{I}$ , but not in the form of a perovskite. However, this is speculation, since there may be an offset between the rinsing time used for SEM and XRD sample preparation and the true back-conversion time, which is shown in the QCM-D measurement.

### 5.5 Conclusion

The most evident conclusion from the above results is, that the conversion reaction of  $\text{PbI}_2$  to  $\text{CH}_3\text{NH}_3\text{PbI}_3$  perovskite is reversible by dissolution of  $\text{CH}_3\text{NH}_3\text{I}$  from the perovskite. Although this should have been obvious before, the community often cited a general degradation mechanism of the perovskite, and many scientists were not aware of an actually reversible reaction.

The implications are numerous. First, the dissolution of the  $\text{CH}_3\text{NH}_3\text{I}$  from the perovskite in a moderately polar solvent like isopropanol implies that the same should hold true for any polar solvent, including water. Since  $\text{CH}_3\text{NH}_3\text{I}$  is volatile (the solid sublimates under ambient conditions), this suggest one possible decomposition pathway in humid environments. Stronger polar solvents will equally dissolve parts of the  $\text{PbI}_2$ .

In general, the reversibility of the conversion reaction should hold true for any lead-halide perovskite, and should determine its interplay with the respective  $\text{PbX}$  salt and  $\text{CH}_3\text{NH}_3\text{X}$  in solution. This is one reason why experimentalists have failed in producing mixed-halide perovskites by exposing for example a  $\text{PbCl}_2$  salt to a  $\text{CH}_3\text{NH}_3\text{I}$  solution for conversion, the result being a pure  $\text{CH}_3\text{NH}_3\text{PbI}_3$  perovskite without any detectable chloride. This can be explained by the initial formation of a mixed compound, and the subsequent dissolution of  $\text{Cl}^-$  or  $\text{CH}_3\text{NH}_3\text{Cl}$  from the mixed compound, and the simultaneous incorporation of  $\text{I}^-$  or  $\text{CH}_3\text{NH}_3\text{I}$  into the compound, finally leading to a pure  $\text{CH}_3\text{NH}_3\text{PbI}_3$  perovskite. The main thermodynamical driving force in this case will be the difference in concentrations of  $\text{CH}_3\text{NH}_3\text{Cl}$  in solution and in the perovskite lattice. In addition, it is known that that  $\text{CH}_3\text{NH}_3\text{PbI}_3$  perovskite forms a slightly more stable perovskite due to a large unit cell that can accommodate the  $\text{CH}_3\text{NH}_3^+$  cation more easily than the slightly smaller unit cell of the  $\text{CH}_3\text{NH}_3\text{PbCl}_3$  perovskite [75].

The reversibility of the conversion reaction further suggest, that a readily formed perovskite of one halide may possibly be converted directly to the perovskite of another halide, simply by exposing to a  $\text{CH}_3\text{NH}_3\text{X}$  solution of the second halide. This would be closer to an actual ion-exchange reaction without back-conversion to a  $\text{PbX}_2$  salt.

The SEM study in section 5.2.3 has shown that the morphology of the  $\text{PbI}_2$  film can be templated by conversion and back-conversion, resulting in a  $\text{PbI}_2$  film that consists of larger  $\text{PbI}_2$  crystallites. The QCM-D results in section 5.3 further indicate that this does increase the



amount of incorporated  $\text{CH}_3\text{NH}_3\text{I}$ , as well as the size of perovskite crystallites. This templating can be used to change the morphology in a desired way and improve the overall amount of converted material on flat films.

Beyond the back-conversion, the QCM-D measurements also shed some light on the kinetics of the conversion process from  $\text{PbI}_2$  to  $\text{CH}_3\text{NH}_3\text{PbI}_3$ . There clearly is a rapid initial conversion, which occurs in the first 30 s of the exposure to  $\text{CH}_3\text{NH}_3\text{I}$  on a pre-wet sample. This correlates well with optical measurements [12]. However, the QCM-D results suggest that during continued  $\text{CH}_3\text{NH}_3\text{I}$  exposure, there is  $\text{CH}_3\text{NH}_3\text{I}$  incorporated into the film, but at a much slower rate. We recall that the SEM images in sections 5.3 and 5.4 indicate that only the upper part of the film is converted to perovskite crystallites, whereas the bottom part resembles the morphology of  $\text{PbI}_2$  crystallites. This suggests that the perovskite layer, as soon as forming a complete cover, effectively hinders the access of  $\text{CH}_3\text{NH}_3\text{I}$  to the underlying  $\text{PbI}_2$ .

Back-conversion leads to higher crystallinity and a morphology change of the  $\text{PbI}_2$ , and repetitive conversion results in incorporation of more  $\text{CH}_3\text{NH}_3\text{I}$ . A better incorporation could be caused either by the different morphology, or by the improved crystallinity which may allow for better intercalation of  $\text{CH}_3\text{NH}_3\text{I}$  between the stacked layers of a  $\text{PbI}_2$  crystal, which has less grain boundaries than the initial  $\text{PbI}_2$ .



# Bibliography

- [1] Bundesgesetzblatt Jahrgang 2011 Teil I Nr. 43, Ausgegeben zu Bonn am 5. August 2011 Dreizehntes Gesetz zur Änderung des Atomgesetzes Vom 31. Juli 2011. 2011.
- [2] Tables for reference solar spectral irradiances: Direct normal and hemispherical on 37° tilted surface, 2012.
- [3] S. Anderson, E. C. Constable, M. P. Dare-Edwards, J. B. Goodenough, A. Hamnett, K. R. Seddon, and R. D. Wright. Chemical modification of a titanium (IV) oxide electrode to give stable dye sensitisation without a supersensitiser. *Nature*, 280(5723):571–573, Aug. 1979.
- [4] T. Baikie, Y. Fang, J. M. Kadro, M. Schreyer, F. Wei, S. G. Mhaisalkar, M. Graetzel, and T. J. White. Synthesis and crystal chemistry of the hybrid perovskite (CH<sub>3</sub>NH<sub>3</sub>)PbI<sub>3</sub> for solid-state sensitised solar cell applications. *Journal of Materials Chemistry A*, 1(18):5628–5641, 2013.
- [5] A. V. Bandura and J. D. Kubicki. Derivation of Force Field Parameters for TiO<sub>2</sub> - H<sub>2</sub>O Systems from ab Initio Calculations. *The Journal of Physical Chemistry B*, 107(40):11072–11081, Oct. 2003.
- [6] C. I. Bayly, P. Cieplak, W. Cornell, and P. A. Kollman. A well-behaved electrostatic potential based method using charge restraints for deriving atomic charges: the RESP model. *The Journal of Physical Chemistry*, 97(40):10269–10280, Oct. 1993.
- [7] G. Bazzan, J. R. Deneault, T.-S. Kang, B. E. Taylor, and M. F. Durstock. Nanoparticle/Dye Interface Optimization in Dye-Sensitized Solar Cells. *Advanced Functional Materials*, 21(17):3268–3274, July 2011.
- [8] J. G. Bednorz and K. A. Müller. Possible high T<sub>c</sub> superconductivity in the Ba-La-Cu-O system. *Zeitschrift für Physik B - Condensed Matter*, 64(2):189–193, June 1986.
- [9] E. A. Becquerel. Recherches sur les effets de la radiation chimique de la lumière solaire, au moyen des courant électriques. *C.R. Acad. Sci.*, 9:145–149, 1839.
- [10] J. Burschka. *High performance solid-state mesoscopic solar cells*. PhD thesis, École polytechnique fédérale de Lausanne (EPFL), Nov. 2013. no 6006 (2013).

## Bibliography

---

- [11] J. Burschka, A. Dualeh, F. Kessler, E. Baranoff, N.-L. Cevey-Ha, C. Yi, M. K. Nazeeruddin, and M. Grätzel. Tris(2-(1 H-pyrazol-1-yl)pyridine)cobalt(III) as p-Type Dopant for Organic Semiconductors and Its Application in Highly Efficient Solid-State Dye-Sensitized Solar Cells. *Journal of the American Chemical Society*, page 111025100913002, Oct. 2011.
- [12] J. Burschka, N. Pellet, S.-J. Moon, R. Humphry-Baker, P. Gao, M. K. Nazeeruddin, and M. Grätzel. Sequential deposition as a route to high-performance perovskite-sensitized solar cells. *Nature*, 499(7458):316–319, July 2013.
- [13] D. A. Case, T. A. Darden, T. E. Cheatham, and C. L. Simmerling. Amber package, 2012.
- [14] K. Chiba, T. Ueda, Y. Yamaguchi, Y. Oki, F. Saiki, and K. Naoi. Electrolyte Systems for High Withstand Voltage and Durability II. Alkylated Cyclic Carbonates for Electric Double-Layer Capacitors. *Journal of The Electrochemical Society*, 158(12):A1320, 2011.
- [15] I. Concina, E. Frison, A. Braga, S. Silvestrini, M. Maggini, G. Sberveglieri, A. Vomiero, and T. Carofiglio. On-line monitoring and active control of dye uptake in dye-sensitised solar cells. *Chemical Communications*, 2011.
- [16] W. D. Cornell, P. Cieplak, C. I. Bayly, I. R. Gould, K. M. Merz, D. M. Ferguson, D. C. Spellmeyer, T. Fox, J. W. Caldwell, and P. A. Kollman. [AMBER] A Second Generation Force Field for the Simulation of Proteins, Nucleic Acids, and Organic Molecules. *Journal of the American Chemical Society*, (117):5179–5197, 1995.
- [17] C. Dames, B. Poudel, W. Z. Wang, J. Y. Huang, Z. F. Ren, Y. Sun, J. I. Oh, C. Opeil, M. J. Naughton, and G. Chen. Low-dimensional phonon specific heat of titanium dioxide nanotubes. *Applied Physics Letters*, 87(3):031901, 2005.
- [18] B. J. M. de Vries, D. P. van Vuuren, and M. M. Hoogwijk. Renewable energy sources: Their global potential for the first-half of the 21st century at a global level: An integrated approach. *Energy Policy*, 35(4):2590–2610, Apr. 2007.
- [19] J. H. Delcamp, A. Yella, T. W. Holcombe, M. K. Nazeeruddin, and M. Grätzel. The Molecular Engineering of Organic Sensitizers for Solar Cell Applications. *Angewandte Chemie International Edition*, 52(1):376–380, Aug. 2012.
- [20] S. E. Derenzo, M. J. Weber, and M. K. Klintonberg. Temperature dependence of the fast, near-band-edge scintillation from CuI, HgI<sub>2</sub>, PbI<sub>2</sub>, ZnO:Ga and CdS:In. *Nuclear Instruments and Methods in Physics Research Section A: Accelerators, Spectrometers, Detectors and Associated Equipment*, 486(1-2):214–219, June 2002.
- [21] J. Desilvestro, M. Graetzel, L. Kavan, J. Moser, and J. Augustynski. Highly efficient sensitization of titanium dioxide. *Journal of the American Chemical Society*, 107(10):2988–2990, May 1985.
- [22] U. Diebold. ScienceDirect - Surface Science Reports : The surface science of titanium dioxide. *Surface Science Reports*, 2003.

- [23] A. Domack, O. Prucker, J. R uhe, and D. Johannsmann. Swelling of a polymer brush probed with a quartz crystal resonator. *Physical Review E*, 56(1):680–689, July 1997.
- [24] A. Dualeh, R. Humphry-Baker, J. H. Delcamp, M. K. Nazeeruddin, and M. Gr atzel. Solid-State Dye-Sensitized Solar Cells Using a Novel Class of Ullazine Dyes as Sensitizers. *Advanced Energy Materials*, pages n/a–n/a, Nov. 2012.
- [25] G. L. Dybwad. A sensitive new method for the determination of adhesive bonding between a particle and a substrate. *Journal of Applied Physics*, 58(7):2789–2790, 1985.
- [26] M. Edvardsson. *QCM-D: With Focus on Variations in Oscillation Amplitude*. Doktor-savhandlingar vid Chalmers Tekniska H ogskola: Chalmers Tekniska H ogskola. Chalmers University of Technology, 2006.
- [27] M. Edvardsson, M. Rodahl, B. Kasemo, and F. Hook. A Dual-Frequency QCM-D Setup Operating at Elevated Oscillation Amplitudes. *Analytical Chemistry*, 77(15):4918–4926, Aug. 2005.
- [28] L. Etgar, P. Gao, Z. Xue, and P. Qin. Mesoscopic CH<sub>3</sub>NH<sub>3</sub>PbI<sub>3</sub>/TiO<sub>2</sub> Heterojunction Solar Cells. *Journal of the American Chemical Society*, 134:17396–17399, 2012.
- [29] M. Faraday. *Experimental Researches in Electricity*. Everyman’s Library, London, Toronto, New York, 1914 edition, 1839. Compendium of Faraday’s previously published researches, with an introduction by John Tyndall.
- [30] A. Fattori, L. M. Peter, K. L. McCall, N. Robertson, and F. Marken. Adsorption and redox chemistry of cis-RuLL’(SCN)<sub>2</sub> with L=4,4’-dicarboxylic acid-2,2’-bipyridine and L’=4,4’-dinonyl-2,2’-bipyridine (Z907) at FTO and TiO<sub>2</sub> electrode surfaces. *Journal of Solid State Electrochemistry*, 14(10):1929–1936, 2010.
- [31] S. M. Feldt, E. A. Gibson, E. Gabrielsson, L. Sun, G. Boschloo, and A. Hagfeldt. Design of Organic Dyes and Cobalt Polypyridine Redox Mediators for High-Efficiency Dye-Sensitized Solar Cells. *Journal of the American Chemical Society*, 132(46):16714–16724, Nov. 2010.
- [32] A. Fillinger. The Adsorption Behavior of a Ruthenium-Based Sensitizing Dye to Nanocrystalline TiO<sub>2</sub> Coverage Effects on the External and Internal Sensitization Quantum Yields. *Journal of The Electrochemical Society*, 146(12):4559, 1999.
- [33] F. Gao, Y. Wang, D. Shi, J. Zhang, M. Wang, X. Jing, R. Humphry-Baker, P. Wang, S. M. Zakeeruddin, and M. Gr atzel. Enhance the Optical Absorptivity of Nanocrystalline TiO<sub>2</sub> Film with High Molar Extinction Coefficient Ruthenium Sensitizers for High Performance Dye-Sensitized Solar Cells. *Journal of the American Chemical Society*, 130(32):10720–10728, Aug. 2008.
- [34] D. C. Grinter, M. Nicotra, and G. Thornton. Acetic acid adsorption on anatase TiO<sub>2</sub> (101). *The Journal of Physical Chemistry C*, 116(21):11643–11651, 2012.

## Bibliography

---

- [35] V. Gusak, L.-P. Heiniger, M. Graetzel, C. Langhammer, and B. Kasemo. Time-Resolved Indirect Nanoplasmonic Sensing Spectroscopy of Dye Molecule Interactions with Dense and Mesoporous TiO<sub>2</sub> Films. *Nano Letters*, 12(5):2397–2403, May 2012.
- [36] V. Gusak, L.-P. Heiniger, V. P. Zhdanov, M. Grätzel, B. Kasemo, and C. Langhammer. Diffusion and adsorption of dye molecules in mesoporous TiO<sub>2</sub> photoelectrodes studied by indirect nanoplasmonic sensing. *Energy & Environmental Science*, 6(12):3627–3636, 2013.
- [37] V. Gusak, E. Nkurunziza, C. Langhammer, and B. Kasemo. Real-Time Adsorption and Desorption Kinetics of Dye Z907 on a Flat Mimic of Dye-Sensitized Solar Cell TiO<sub>2</sub> Photoelectrodes. *The Journal of Physical Chemistry C*, page 140528095151004, May 2014.
- [38] H. T. H. Gerischer. Dye-sensitized photogalvanic cell. *Ber. Bunsenges. Phys. Chem*, 72:437, 1968.
- [39] A. Hagfeldt, G. Boschloo, L. Sun, L. Kloo, and H. Pettersson. Dye-Sensitized Solar Cells. *Chemical Reviews*, 110(11):6595–6663, Nov. 2010.
- [40] M. Hahlin, E. M. J. Johansson, R. Schölin, H. Siegbahn, and H. Rensmo. Influence of Water on the Electronic and Molecular Surface Structures of Ru-Dyes at Nanostructured TiO<sub>2</sub>. *The Journal of Physical Chemistry C*, page 110526100155008, May 2011.
- [41] J. Halme, P. Vahermaa, K. Miettunen, and P. Lund. Device Physics of Dye Solar Cells. *Advanced Materials*, 22(35):E210–E234, Aug. 2010.
- [42] H. A. Harms, N. Tétreault, V. Gusak, B. Kasemo, and M. Grätzel. In-situ Investigation of Dye Adsorption on TiO<sub>2</sub> Films Using a Quartz Crystal Microbalance with Dissipation Technique. *Physical Chemistry Chemical Physics*, (14):9037–9040, May 2012.
- [43] H. A. Harms, N. Tétreault, N. Pellet, M. Besimon, and M. Grätzel. Mesoscopic photo-systems for light harvesting and conversion: Facile and reversible transformation of metal-halide perovskites. *Faraday Discussions*, submitted, 2014.
- [44] H. A. Harms, N. Tétreault, K. Voitchovsky, F. Stellacci, and M. Grätzel. In-situ investigation of adsorption of dye and coadsorbates on TiO<sub>2</sub> films using QCM-D, fluorescence and AFM techniques. In N. Banerji and C. Silva, editors, *SPIE NanoScience + Engineering*, page 88110C. SPIE, Sept. 2013.
- [45] W. M. Haynes. *Handbook of Chemistry and Physics*. CRC, <http://www.hbcponline.com>, 95th edition, 2014.
- [46] R. Hirota, Y. Ogomi, S. S. Pandey, and S. Hayase. Dye adsorption feature on titania surface and role of dye aggregation inhibitor monitored by quartz crystal microbalance (QCM). In Z. H. Kafafi, C. J. Brabec, and P. A. Lane, editors, *SPIE Organic Photonics + Electronics*, pages 847712–847712–4. SPIE, Sept. 2012.

- [47] J.-H. Im, C.-R. Lee, J.-W. Lee, S.-W. Park, and N.-G. Park. 6.5% efficient perovskite quantum-dot-sensitized solar cell. *Nanoscale*, 3(10):4088–4093, 2011.
- [48] International Energy Agency (IEA). *World Energy Outlook 2012, New Policies Scenario*. OECD / IEA, Paris, 2012.
- [49] S. Ito, T. N. Murakami, P. Comte, P. Liska, C. Gratzel, M. K. Nazeeruddin, and M. Grätzel. Fabrication of thin film dye sensitized solar cells with solar to electric power conversion efficiency over 10%. *Thin solid films*, 516(14):4613–4619, May 2008.
- [50] D. Johannsmann. Modeling of QCM Data. pages 1–64, June 2011.
- [51] D. Johannsmann, I. Reviakine, and R. P. Richter. Dissipation in Films of Adsorbed Nanospheres Studied by Quartz Crystal Microbalance (QCM). *Analytical Chemistry*, 81(19):8167–8176, Oct. 2009.
- [52] G. H. Jonker and J. H. Van Santen. Ferromagnetic compounds of manganese with perovskite structure. *Physica*, 16(3):337–349, Mar. 1950.
- [53] W. L. Jorgensen and J. Tirado-Rives. The OPLS [optimized potentials for liquid simulations] potential functions for proteins, energy minimizations for crystals of cyclic peptides and crambin. *Journal of the American Chemical Society*, 110(6):1657–1666, Mar. 1988.
- [54] K. Kanazawa and J. Gordon. Frequency of a quartz microbalance in contact with liquid. *Analytical Chemistry*, 57(8):1770–1771, 1985.
- [55] K. K. Kanazawa and J. Gordon. Analytica Chimica Acta : The oscillation frequency of a quartz resonator in contact with liquid. *Analytica Chimica Acta*, 1985.
- [56] L. Kavan and M. Grätzel. Highly efficient semiconducting TiO<sub>2</sub> photoelectrodes prepared by aerosol pyrolysis. *Electrochimica acta*, 40(5):643–652, Apr. 1995.
- [57] Y. Kawamura, H. Mashiyama, and K. Hasebe. Structural Study on Cubic–Tetragonal Transition of CH<sub>3</sub>NH<sub>3</sub>PbI<sub>3</sub>. *Journal of the Physical Society of Japan*, 71(7):1694–1697, July 2002.
- [58] A. Kay and M. Graetzel. Artificial photosynthesis. 1. Photosensitization of titania solar cells with chlorophyll derivatives and related natural porphyrins. *The Journal of Physical Chemistry*, 97(23):6272–6277, June 1993.
- [59] H.-S. Kim, C.-R. Lee, J.-H. Im, K.-B. Lee, T. Moehl, A. Marchioro, S.-J. Moon, R. Humphry-Baker, J.-H. Yum, J. E. Moser, M. Grätzel, and N.-G. Park. Lead Iodide Perovskite Sensitized All-Solid-State Submicron Thin Film Mesoscopic Solar Cell with Efficiency Exceeding 9%. *Scientific Reports*, 2:–, Aug. 2012.

## Bibliography

---

- [60] Kislun Voïtchovsky, Hauke A. Harms, Negar Ashari-Astani, Ivano Tavernelli, Basile Curchod, Nicolas Tétreault, Ursula Röthlisberger, Francesco Stellacci and Michael Grätzel. In-situ mapping of the molecular arrangement of amphiphilic molecules at the TiO<sub>2</sub> surface of dye sensitized solar cells. *Manuscript in preparation*, x, 2014.
- [61] C. S. Kley, C. Dette, G. Rinke, C. E. Patrick, J. Čechal, S. J. Jung, M. Baur, M. Dürr, S. Rauschenbach, F. Giustino, S. Stepanow, and K. Kern. Atomic-Scale Observation of Multiconformational Binding and Energy Level Alignment of Ruthenium-Based Photosensitizers on TiO<sub>2</sub>Anatase. *Nano Letters*, 14(2):563–569, Feb. 2014.
- [62] A. Kojima, K. Teshima, Y. Shirai, and T. Miyasaka. Organometal Halide Perovskites as Visible-Light Sensitizers for Photovoltaic Cells. *Journal of the American Chemical Society*, 131(17):6050–6051, May 2009.
- [63] J. J. Kuna, K. Voïtchovsky, C. Singh, H. Jiang, S. Mwenifumbo, P. K. Ghorai, M. M. Stevens, S. C. Glotzer, and F. Stellacci. The effect of nanometre-scale structure on interfacial energy. *Nature Materials*, 8(10):837–842, Sept. 2009.
- [64] H. Kusama and K. Sayama. Theoretical Study on the Intermolecular Interactions of Black Dye Dimers and Black Dye–Deoxycholic Acid Complexes in Dye-Sensitized Solar Cells. *The Journal of Physical Chemistry C*, 116(45):23906–23914, Nov. 2012.
- [65] D. Lee, M. F. Rubner, and R. E. Cohen. All-Nanoparticle Thin-Film Coatings. *Nano Letters*, 6(10):2305–2312, Oct. 2006.
- [66] M. M. Lee, J. Teuscher, T. Miyasaka, T. N. Murakami, and H. J. Snaith. Efficient Hybrid Solar Cells Based on Meso-Superstructured Organometal Halide Perovskites. *Science*, 338(6107):643–647, Nov. 2012.
- [67] A. Leitenstorfer and A. Pashkin. *Vorlesung Halbleiterphysik*. Universität Konstanz, 2011.
- [68] K. Liang, D. B. Mitzi, and M. T. Prikas. Synthesis and Characterization of Organic-Inorganic Perovskite Thin Films Prepared Using a Versatile Two-Step Dipping Technique. *Chemistry of Materials*, 10(1):403–411, Jan. 1998.
- [69] D. Liu and T. L. Kelly. nphoton.2013.342. *Nature Photonics*, 8(2):133–138, Dec. 2013.
- [70] S.-A. C. LLC. Aldrich website, June 2014.
- [71] X. Lu, M. B. McElroy, and J. Kiviluoma. Global potential for wind-generated electricity. *Proceedings of the National Academy of Sciences*, 106(27):10933–10938, July 2009.
- [72] T. Marinado, M. Hahlin, X. Jiang, M. Quintana, E. M. J. Johansson, E. Gabrielsson, S. Plogmaker, D. P. Hagberg, G. Boschloo, S. M. Zakeeruddin, M. Grätzel, H. Siegbahn, L. Sun, A. Hagfeldt, and H. Rensmo. Surface Molecular Quantification and Photoelectrochemical Characterization of Mixed Organic Dye and Coadsorbent Layers on TiO<sub>2</sub> for Dye-Sensitized Solar Cells. *The Journal of Physical Chemistry C*, 114(27):11903–11910, July 2010.



- [73] P. Marquet, G. Andersson, A. Snedden, L. Kloo, and R. Atkin. Molecular Scale Characterization of the Titania - Dye - Solvent Interface in Dye-Sensitized Solar Cells. *Langmuir*, 26(12):9612–9616, June 2010.
- [74] R. I. Masel. *Principles of Adsorption and Reaction on Solid Surfaces*. Wiley, 1996.
- [75] H. Mashiyama, Y. Kurihara, and T. Azetsu. Disordered Cubic Perovskite Structure of  $\text{CH}_3\text{NH}_3\text{PbX}_3$  ( $X=\text{Cl}, \text{Br}, \text{I}$ ). *Journal of the Korean Physical Society*, 32:156–158, Feb. 1998.
- [76] S. Mathew, A. Yella, P. Gao, R. Humphry-Baker, B. F. E. Curchod, N. Ashari Astani, I. Tavernelli, U. Rothlisberger, M. K. Nazeeruddin, and M. Grätzel. Dye-sensitized solar cells with 13% efficiency achieved through the molecular engineering of porphyrin sensitizers. *Nature Chemistry*, 6(3):242–247, Feb. 2014.
- [77] F. Matteocci, G. Mincuzzi, F. Giordano, A. Capasso, E. Artuso, C. Barolo, G. Viscardi, T. M. Brown, A. Reale, and A. Di Carlo. Blocking layer optimisation of poly (3-hexylthiophene) based Solid State Dye Sensitized Solar Cells. *Organic Electronics*, 14(7):1882–1890, 2013.
- [78] D. Mitzi. Organic-Inorganic Perovskites: Structures, Properties and Electronic Devices, oral presentation HOPV conference Lausanne, 2014.
- [79] D. B. Mitzi, C. A. Feild, W. T. A. Harrison, and A. M. Guloy. Conducting tin halides with a layered organic-based perovskite structure. *Nature*, 369(6480):467–469, June 1994.
- [80] J. Moser. Notiz über die verstärkung photoelektrischer ströme durch optische sensibilisierung. *Monatsh. Chem*, 8:373, 1887.
- [81] J. E. Moser. *Photochemistry II*. lecture EPFL, June 2011.
- [82] K. A. Müller and H. Burkard.  $\text{SrTiO}_3$ : An intrinsic quantum paraelectric below 4 K. *Physical Review B*, 19(7):3593–3602, Apr. 1979.
- [83] M. K. Nazeeruddin, R. Humphry-Baker, P. Liska, and M. Grätzel. Investigation of Sensitizer Adsorption and the Influence of Protons on Current and Voltage of a Dye-Sensitized Nanocrystalline  $\text{TiO}_2$  Solar Cell. *The Journal of Physical Chemistry B*, 107(34):8981–8987, Aug. 2003.
- [84] M. K. Nazeeruddin, A. Kay, I. Rodicio, R. Humphry-Baker, E. Mueller, P. Liska, N. Vlachopoulos, and M. Graetzel. Conversion of light to electricity by cis- $\text{X}_2\text{bis}(2,2'$ -bipyridyl-4,4'-dicarboxylate)ruthenium(II) charge-transfer sensitizers ( $X = \text{Cl}^-, \text{Br}^-, \text{I}^-, \text{CN}^-$ , and  $\text{SCN}^-$ ) on nanocrystalline titanium dioxide electrodes. *Journal of the American Chemical Society*, 115(14):6382–6390, July 1993.
- [85] M. K. Nazeeruddin, S. M. Zakeeruddin, R. Humphry-Baker, M. Jirousek, P. Liska, N. Vlachopoulos, V. Shklover, C.-H. Fischer, and M. Grätzel. Acid-base equilibria of (2, 2'-bipyridyl-4, 4'-dicarboxylic acid) ruthenium (II) complexes and the effect of protonation on charge-transfer sensitization of nanocrystalline titania. *Inorganic Chemistry*, 38(26):6298–6305, 1999.

## Bibliography

---

- [86] M. Nirschl, M. Schreiter, and J. Vörös. Comparison of FBAR and QCM-D sensitivity dependence on adlayer thickness and viscosity. *Sensors and Actuators A: Physical*, 165(2):415–421, Feb. 2011.
- [87] NREL. Best research-cell efficiencies, June 2014.
- [88] NREL, Seok et al., Korean Research Institute of Chemical Technology (KRICT). Best research-cell efficiencies, record perovskite cell of 17.9 % power conversion efficiency, June 2014.
- [89] NREL/FS-5400-52006. Reference solar spectral irradiance: Astm g-173, June 2014.
- [90] R. Y. Ogura, S. Nakane, M. Morooka, M. Orihashi, Y. Suzuki, and K. Noda. High-performance dye-sensitized solar cell with a multiple dye system. *Applied Physics Letters*, 94(7):073308, 2009.
- [91] B. O'Regan and M. Grätzel. A low-cost, high-efficiency solar cell based on dye-sensitized colloidal TiO<sub>2</sub> films. *Nature*, 353(6346):737–740, Oct. 1991.
- [92] B. O'Regan, L. Xiaoe, and T. Ghaddar. Dye adsorption, desorption, and distribution in mesoporous TiO<sub>2</sub> films, and its effects on recombination losses in dye sensitized solar cells. *Energy & Environmental Science*, 5(5):7203–7215, 2012.
- [93] M. Pastore and F. D. Angelis. First-Principles Computational Modeling of Fluorescence Resonance Energy Transfer in Co-Sensitized Dye Solar Cells. *The Journal of Physical Chemistry Letters*, 3(16):2146–2153, Aug. 2012.
- [94] M. Planck. Ueber das Gesetz der Energieverteilung im Normalspectrum. *Annalen der physik*, 1901.
- [95] L. E. Polander, A. Yella, B. F. E. Curchod, N. Ashari Astani, J. Teuscher, R. Scopelliti, P. Gao, S. Mathew, J. E. Moser, I. Tavernelli, U. Rothlisberger, M. Grätzel, M. K. Nazeeruddin, and J. Frey. Towards Compatibility between Ruthenium Sensitizers and Cobalt Electrolytes in Dye-Sensitized Solar Cells. *Angewandte Chemie International Edition*, 52(33):8731–8735, July 2013.
- [96] A. Pomorska, D. Shchukin, R. Hammond, M. A. Cooper, G. Grundmeier, and D. Johannsmann. Positive Frequency Shifts Observed Upon Adsorbing Micron-Sized Solid Objects to a Quartz Crystal Microbalance from the Liquid Phase. *Analytical Chemistry*, 82(6):2237–2242, Mar. 2010.
- [97] A. Rienzo, L. C. Mayor, G. Magnano, C. J. Satterley, E. Ataman, J. Schnadt, K. Schulte, and J. N. O'Shea. X-ray absorption and photoemission spectroscopy of zinc protoporphyrin adsorbed on rutile TiO<sub>2</sub>(110) prepared by in situ electrospray deposition. *The Journal of Chemical Physics*, 132(8):084703, 2010.
- [98] M. Rodahl. Frequency and dissipation-factor responses to localized liquid deposits on a QCM electrode. *Sensors and Actuators B: Chemical*, 37(1-2):111–116, Nov. 1996.

- [99] M. Rodahl, F. Hook, A. Krozer, P. Brzezinski, and B. Kasemo. Quartz crystal microbalance setup for frequency and Q-factor measurements in gaseous and liquid environments. *Review of Scientific Instruments*, 66(7):3924–3930, 1995.
- [100] J. Rouquerol, D. Avnir, C. W. Fairbridge, D. H. Everett, J. M. Haynes, N. Pernicone, J. D. F. Ramsay, K. S. W. Sing, and K. K. Unger. Recommendations for the characterization of porous solids (Technical Report). *Pure and Applied Chemistry*, 66(8):1739–1758, 1994.
- [101] S. Ryu, J. H. Noh, N. J. Jeon, Y. C. Kim, W. S. Yang, J. Seo, and S. Il Seok. Voltage output of efficient perovskite solar cells with high open-circuit voltage and fill factor. *Energy & Environmental Science*, pages –, 2014.
- [102] A. Sasahara, K. Fujio, N. Koide, L. Han, and H. Onishi. STM imaging of a model surface of Ru(4,4'-dicarboxy-2,2'-bipyridine)<sub>2</sub>(NCS)<sub>2</sub> dye-sensitized TiO<sub>2</sub> photoelectrodes. *Surface Science*, 604(2):106–110, Jan. 2010.
- [103] G. Sauerbrey. Verwendung von Schwingquarzen zur Wägung dünner Schichten und zur Mikrowägung. *Zeitschrift für Physik*, 155(2):206–222, Apr. 1959.
- [104] F. Schiffmann, J. Hutter, and J. VandeVondele. Atomistic simulations of a solid/liquid interface: a combined force field and first principles approach to the structure and dynamics of acetonitrile near an anatase surface. *Journal of Physics: Condensed Matter*, 20(6):064206, Jan. 2008.
- [105] F. Schiffmann, J. VandeVondele, J. Hutter, R. Wirz, A. Urakawa, and A. Baiker. Protonation-Dependent Binding of Ruthenium Bipyridyl Complexes to the Anatase(101) Surface. *The Journal of Physical Chemistry C*, 114(18):8398–8404, May 2010.
- [106] D. K. Schwartz. MECHANISMS AND KINETICS OF SELF-ASSEMBLED MONOLAYER FORMATION. *Annual Review of Physical Chemistry*, 52:107–137, 2001.
- [107] V. Shklover, Y. Ovchinnikov, L. Braginsky, S. M. Zakeeruddin, and M. Grätzel. Structure of Organic/Inorganic Interface in Assembled Materials Comprising Molecular Components. Crystal Structure of the Sensitizer Bis[(4,4'-carboxy-2,2'-bipyridine)(thiocyanato)]ruthenium(II). *Chemistry of Materials*, 10(9):2533–2541, Sept. 1998.
- [108] W. Shockley and H. J. Queisser. Detailed Balance Limit of Efficiency of p-n Junction Solar Cells. *Journal of Applied Physics*, 32(3):510–519, 1961.
- [109] H. J. Snaith and M. Grätzel. The Role of a “Schottky Barrier” at an Electron-Collection Electrode in Solid-State Dye-Sensitized Solar Cells. *Advanced Materials*, 18(14):1910–1914, July 2006.
- [110] D. Stockbridge. Effects of gas pressure on quartz crystal microbalances. *Vacuum Microbalance Techniques*, 5:147–178, 1966.

## Bibliography

---

- [111] Sunpower corporation. X-series solar panels., 2013.
- [112] M. L. Sushko, A. Y. Gal, and A. L. Shluger. Interaction of Organic Molecules with the TiO<sub>2</sub> (110) Surface: Ab Initio Calculations and Classical Force Fields. *The Journal of Physical Chemistry B*, 110:4853–4862, 2006.
- [113] M. Suzuki and T. Ami. A proposal of epitaxial oxide thin film structures for future oxide electronics. *Materials Science and Engineering: B*, 41(1):166–173, Oct. 1996.
- [114] N. Tétreault, L.-P. Heiniger, M. Stefik, P. L. Labouchère, É. Arsenault, N. K. Nazeeruddin, G. A. Ozin, and M. Grätzel. Atomic Layer Deposition for Novel Dye-Sensitized Solar Cells. In *220th ECS Meeting*, pages 303–314. ECS, 2011.
- [115] H. Tompkins and E. A. Irene. *Handbook of Ellipsometry*. Elsevier, Heidelberg, 1st edition, 2005.
- [116] H. N. Tsao, C. Yi, T. Moehl, J.-H. Yum, S. M. Zakeeruddin, M. K. Nazeeruddin, and M. Grätzel. Cyclopentadithiophene Bridged Donor-Acceptor Dyes Achieve High Power Conversion Efficiencies in Dye-Sensitized Solar Cells Based on the tris-Cobalt Bipyridine Redox Couple. *ChemSusChem*, 4(5):591–594, 2011.
- [117] H. W. Vogel. AgX sensitization. *Ber. Dtsch. Chem. Ges.*, 6:1730, 1873.
- [118] M. Voinova, M. Rodahl, M. Jonson, and B. Kasemo. Viscoelastic Acoustic Response of Layered Polymer Films at Fluid-Solid Interfaces: Continuum Mechanics Approach. *Physica Scripta*, 1999.
- [119] K. Voitchovsky, J. J. Kuna, S. A. Contera, E. Tosatti, and F. Stellacci. Direct mapping of the solid–liquid adhesion energy with subnanometre resolution. *Nature Nanotechnology*, 5(6):401–405, Apr. 2010.
- [120] G. Wang, M. Rodahl, M. Edvardsson, S. Svedhem, G. Ohlsson, F. Hook, and B. Kasemo. A combined reflectometry and quartz crystal microbalance with dissipation setup for surface interaction studies. *Review of Scientific Instruments*, 79(7):075107, July 2008.
- [121] M. Wang, X. Li, H. Lin, P. Pechy, S. M. Zakeeruddin, and M. Grätzel. Passivation of nanocrystalline TiO<sub>2</sub> junctions by surface adsorbed phosphinate amphiphiles enhances the photovoltaic performance of dye sensitized solar cells. *Dalton Transactions*, (45):10015–10020, 2009.
- [122] P. Wang, S. M. Zakeeruddin, I. Exnar, and M. Grätzel. High efficiency dye-sensitized nanocrystalline solar cells based on ionic liquid polymer gel electrolyte. *Chemical Communications*, (24):2972–2973, Nov. 2002.
- [123] P. Wang, S. M. Zakeeruddin, R. Humphry-Baker, J. E. Moser, and M. Grätzel. Molecular-Scale Interface Engineering of TiO<sub>2</sub> Nanocrystals: Improve the Efficiency and Stability of Dye-Sensitized Solar Cells. *Advanced Materials*, 15(24):2101–2104, Dec. 2003.

- [124] P. Wang, S. M. Zakeeruddin, J. E. Moser, M. K. Nazeeruddin, T. Sekiguchi, and M. Grätzel. A stable quasi-solid-state dye-sensitized solar cell with an amphiphilic ruthenium sensitizer and polymer gel electrolyte. *Nature Materials*, 2(6):402–407, May 2003.
- [125] D. Weber.  $\text{CH}_3\text{NH}_3\text{PnX}_3$ , ein Pb(II)-System mit kubischer Perovskitstruktur. *Zeitschrift für Naturforschung B*, 33(B):1443–1445, Aug. 1978.
- [126] S. Wenger. *Strategies to Optimizing Dye-Sensitized Solar Cells: Organic Sensitizers, Tandem Device Structures, and Numerical Device Modeling*. PhD thesis, École polytechnique fédérale de Lausanne (EPFL), Sept. 2010. no 4805 (2010).
- [127] H.-R. Wenk and A. Bulakh. *Minerals*. Cambridge University Press, Cambridge, UK, 2004.
- [128] P. Würfel. *Physics of Solar Cells. From Basic Principles to Advanced Concepts*. John Wiley & Sons, 2 edition, 2009.
- [129] K. Yanada, K. Chiba, Y. Yamaguchi, and H. Yamamoto. Characteristics of Dye-sensitized Solar Cells using Linear Szlfones as an Electrolyte Solvent. *Electrochimica acta*, 79(3):163–167, May 2012.
- [130] H. G. Yang, C. H. Sun, S. Z. Qiao, J. Zou, G. Liu, S. C. Smith, H.-M. Cheng, and G. Q. Lu. Anatase  $\text{TiO}_2$  single crystals with a large percentage of reactive facets. *Nature*, 453(7195):638–641, May 2008.
- [131] A. Yella. personal communication.
- [132] A. Yella, L.-P. Heiniger, P. Gao, M. K. Nazeeruddin, and M. Grätzel. Nanocrystalline Rutile Electron Extraction Layer Enables Low-Temperature Solution Processed Perovskite Photovoltaics with 13.7% Efficiency. *Nano Letters*, page 140402102617001, Apr. 2014.
- [133] A. Yella, H. W. Lee, H. N. Tsao, C. Yi, A. K. Chandiran, M. K. Nazeeruddin, E. W. G. Diau, C. Y. Yeh, S. M. Zakeeruddin, and M. Grätzel. Porphyrin-Sensitized Solar Cells with Cobalt (II/III)-Based Redox Electrolyte Exceed 12 Percent Efficiency. *Science*, 334(6056):629–634, Nov. 2011.
- [134] P. Y. Yu and M. Cardona. *Fundamentals of Semiconductors*. Springer, Heidelberg, 3rd edition, 2001.
- [135] S. Yu, S. Ahmadi, M. Zuleta, H. Tian, K. Schulte, A. Pietzsch, F. Hennies, J. Weissenrieder, X. Yang, and M. Göthelid. Adsorption geometry, molecular interaction, and charge transfer of triphenylamine-based dye on rutile  $\text{TiO}_2(110)$ . *The Journal of Chemical Physics*, 133(22):224704, 2010.
- [136] J.-H. Yum, E. Baranoff, F. Kessler, T. Moehl, S. Ahmad, T. Bessho, A. Marchioro, E. Ghadiri, J. E. Moser, C. Yi, M. G. a. tzel, and M. K. Nazeeruddin. A cobalt complex redox shuttle for dye-sensitized solar cells with high open-circuit potentials. *Nature Communications*, 3:631–8, Jan. 2012.

## Bibliography

---

- [137] J. H. Yum, T. W. Holcombe, Y. Kim, K. Rakstys, and T. Moehl. Blue-Coloured Highly Efficient Dye-Sensitized Solar Cells by Implementing the Diketopyrrolopyrrole Chromophore : Scientific Reports : Nature Publishing Group. *Scientific Reports*, 2013.
- [138] S. M. Zakeeruddin, M. K. Nazeeruddin, R. Humphry-Baker, P. Pechy, P. Quagliotto, C. Barolo, G. Viscardi, and M. Grätzel. Design, Synthesis, and Application of Amphiphilic Ruthenium Polypyridyl Photosensitizers in Solar Cells Based on Nanocrystalline TiO<sub>2</sub> Films. *Langmuir*, 18(3):952–954, Feb. 2002.

# Acknowledgements

First of all, I want to thank Prof. Michael Grätzel for giving me the opportunity to conduct my doctoral studies in his group. I enjoyed very much the freedom and independence I was given. I appreciated the discussions we had and I am grateful for the opportunities and the support I was offered.

I further thank Prof. Bengt H. Kasemo for hosting me at Chalmers University for an introduction to the QCM-D technique, for his active interest in my research, and for his kind assistance and expertise in numerous discussions.

My earlier work with Prof. Ullrich Steiner has sparked my interest in research, which prompted me to pursue a doctorate. I thank him for his continuous support. I am glad that Prof. Henry Snaith encouraged me to apply for a PhD at EPFL. I thank Prof. Alfred Leitenstorfer for teaching me how to look for fundamental solid-state physics on the sidelines of any experiment. I am grateful to Prof. Jian Zi, Prof. Günter Schatz and Prof. Ulrich Rüdiger for support and encouragement.

Over the course of my doctoral studies, I had the pleasure to visit several institutions and groups for collaboration on experimental work. I thank all of the people involved, in particular Dr. Kislou Voïtchovski, Prof. Francesco Stellacci, Negar Ashari Astani and Prof. Ursula Röthlisberger for collaboration within EPFL on atomic force microscopy and molecular dynamics simulations on adsorbed dye molecules. Further, I thank Dr. Christopher Kley and Prof. Klaus Kern at the Max Planck Institut für Festkörperphysik in Stuttgart for collaboration on scanning tunnelling microscopy. Many thanks for their hospitality to Dr. Ruipeng Li, Dr. Kui Zhao and Prof. Aram Amassian at KAUST for hosting me and for joint experiments on QCM-D and ellipsometry.

Within the laboratory of photonics and interfaces, I wish to thank all of the present and previous group members who helped me during my doctorate, and the list of names in this paragraph is not meant to be complete. I thank Nicolas Tétreault for helping me in writing consistent articles and abstracts, for experimental support and encouragement. Thanks to David, Kevin, Aswani, Julian and Simon for valuable scientific advice and discussions. Further thanks to Robin Humphry-Baker, Shaik M. Zakeeruddin, Pascal Comte, and Guido Rothenberger for help with measurements, materials, advice, and coursework. It was always a pleasure to go for lunch, coffee, or beer in good company, and the good social atmosphere

## Acknowledgements

---

was generated by a great mix of people, including the aforementioned and, exemplary for many, Jelissa, Arianna, Maurin, Florian, Jérémie, Takeru, Takashi, Adrianna, Marcel, Jingshan, Matt, Joël, Angela, Jan, and John Meschter. A big thanks to my colleagues in office, Leo-Philipp, Ludmilla and Fabrizio. I wish to pay an additional tribute to the people who helped proofread my thesis: Jan, Aswani, Arianna, Fabrizio, Amalie, David, Kislon and Goldie.

In a careful balance to work, I always found inspiration by spending time in the mountains. I wish to thank the people who shared this time with me, in particular my most long-term climbing partners Dieter, Flo, Goldie, Gregor, Nikolaus, Myrtille and Fred. Further thanks to Florian, Christelle and Anurag for being nice people and good flatmates.

I sincerely thank Assia for her love and understanding. Throughout my studies, it was essential for me to have the support of my entire family. I thank my father Heino and my late mother Almuth, as well as my sister Inka.



# Hauke Arne HARMS

---

Address: EPFL, Laboratory of Photonics and Interfaces  
Station 6  
CH-1015 Lausanne, Switzerland

Email: hauke.harms@epfl.ch

Date and place of birth: 01.12.1983 in Wilhelmshaven, Germany

Nationality: German



## EDUCATION

---

2010 to 2014 **PhD student in Chemistry** with Prof. M. Grätzel, EPFL, Switzerland

2004 to 2010 **Master in Physics**, University of Constance, Germany

1990 to 2003 Grammar School *Mariengymnasium Jever*, Germany

## EXPERIENCE and PROJECTS

---

2010 to 2014 **PhD project on dye-sensitized solar cells, EPFL, Switzerland**  
Implementation of a new technique to measure changes in thin films that determine the performance of a new, cheap type of solar cells. Close collaboration with the manufacturer *Biolin Scientific*, including webinar presentations for the company. Responsibility for various collaborative projects with partners at the MPI Stuttgart, Germany, with Chalmers University, Sweden, and with King Abdullah University of Science and Technology, Saudi Arabia. Providing of technical advice to the solar cell manufacturer *G24i Power*.

2009 to 2010 **Diploma Thesis on Nano-Photonics** with Prof. A. Leitenstorfer, **University of Constance, Germany**  
Microfabrication and characterization of optical cavities for quantum computing.

2007 to 2008 **Scholarship exchange student at Fudan University, Shanghai, China**  
Major in Chinese language; Internship at the physics department.

2007 **Internship with Prof. U. Steiner, University of Cambridge, UK**  
Continuation of a PhD work on superhydrophobic *non-stick* coatings for surfaces in specific applications in medical equipment and naval architecture. Presentation to investing companies.

2003 to 2004 **Social service with the Red Cross, Munich, Germany**

## MORE

---

Languages Fluent in **English, French** and **German**; basic knowledge of Spanish and Chinese.

Commitment Engagement for the German Alpine Association by establishing and leading a student group of 25 people from 2009 to 2010.

Lausanne, 5 July 2014

## Acknowledgements

---

### List of publications

Hauke A. Harms, Nicolas Tétreault, Viktoria Gusak, Bengt Kasemo and Michael Grätzel, In situ investigation of dye adsorption on TiO<sub>2</sub> films using a quartz crystal microbalance with dissipation technique, *Phys. Chem. Chem. Phys.* **14**, 9037-9040 (2012).

Hauke A. Harms, Nicolas Tétreault, Kislun Voïtchovsky, Francesco Stellacci, and Michael Grätzel, In-situ investigation of dye adsorption on TiO<sub>2</sub> films using QCM-D, fluorescence and AFM techniques, *Proc. SPIE 8811, Physical Chemistry of Interfaces and Nanomaterials XII, 88110C*, (September 11, 2013).

Philippe Labouchere, Aravind Kumar Chandiran, Thomas Moehl, Hauke Arne Harms, Sudam Chavhan, Ramon Tena-Zaera, Mohammad Khaja Nazeeruddin, Michael Graetzel and Nicolas Tetreault, Passivation of ZnO Nanowire Guests and 3D Inverse Opal Host Photoanodes for Dye-Sensitized Solar Cells, *Advanced Energy Materials*, DOI:10.1002/aenm.201400217, (2014).

Kislun Voïtchovsky, Hauke A. Harms, Negar Ashari-Astani, Ivano Tavernelli, Basile Curchod, Nicolas Tétreault, Ursula Röthlisberger, Francesco Stellacci and Michael Grätzel, In-situ mapping of the molecular arrangement of amphiphilic molecules at the TiO<sub>2</sub> surface of dye sensitized solar cells, In situ mapping of the molecular arrangement of amphiphilic molecules for dye sensitized solar cells, *manuscript in preparation* (2014).

Hauke A. Harms, Nicolas Tétreault, Norman Pellet, Michaël Besimon and Michael Grätzel, Mesoscopic photosystems for light harvesting and conversion: Facile and reversible transformation of metal-halide perovskites, *Faraday Discussions*, submitted (2014).

### Conference contributions

Fall Meeting of the Swiss Chemical Society at EPFL (2011). Abstract publication in *CHIMIA* **65**(7-8), 591 (2011), poster presentation.

QCM-D Scientific World Tour, Bensheim, Germany (2011), oral presentation.

QUANTSOL Winter workshop, Bad Gastein, Austria (2012), oral presentation.

Conference for Hybrid and Organic Photovoltaics (HOPV), Uppsala, Sweden (2012), poster presentation.

Fall Meeting of the Swiss Chemical Society at ETHZ (2012). Abstract publication in *CHIMIA* **66**(7-8), 586 (2012), poster presentation.

Global Young Scientist Summit (GYSS), Singapore (2013). White paper: Photovoltaics in the Third Dimension: Cheap Technology Using Vertical Surfaces for Electric Power Generation in Sustainable Smart Grid Cities.

## Acknowledgements

---

SPIE Optics and Photonics, *Physical Chemistry of Interfaces and Nanomaterials*, San Diego, United States (2013), oral presentation.

International Colloquium on Flexible Electronics and Photovoltaics, KAUST, Saudi Arabia (2013), poster presentation.

Conference for Hybrid and Organic Photovoltaics (HOPV), Lausanne, Switzerland (2014), 3rd poster prize for perovskite solar cells.